Plasmonic superradiance in metallo-dielectric nanohybrids

Pierre Fauché

université de BORDEAUX

THÈSE

présentée à

L'Université de Bordeaux

École Doctorale des Sciences Physiques et de l'Ingénieur

par **Pierre FAUCHÉ**

pour obtenir le grade de

DOCTEUR

Spécialité : Lasers, Matière et Nanoscience

Plasmonic superradiance in metallo-dielectric nanohybrids

Soutenue le 21 Novembre 2016

Après avis de :

Jean-Jacques Greffet	Professeur, Institut d'Optique Graduate School	Rapporteur
Yannick De Wilde	Directeur de Recherche, CNRS	Rapporteur

Devant la commission d'examen formée de :

Cécile Zakri	Professeur, Université de Bordeaux	Président
Jean-Jacques Greffet	Professeur, Institut d'Optique Graduate School	Rapporteur
Yannick De Wilde	Directeur de Recherche, CNRS	Rapporteur
Niek van Hulst	Professeur, ICFO	Examinateur
Renaud A. L. Vallée	Chargé de Recherche (HDR), CNRS	Directeur de thèse
Brahim Lounis	Professeur, Université de Bordeaux	Directeur de thèse

À ma famille, Elise, Marie-Laure et Michel

Remerciements

Ce manuscrit est la synthèse d'une aventure de 3 ans, une immersion dans le monde de la science mais aussi des rencontres avec des personnes passionnées et passionantes venues du monde entier. Je remercie ici toutes celles et ceux qui, de près ou de loin, ont contribué à ce travail et ont apporté leur soutien.

Je voudrais tout d'abord remercier l'ensemble de mon jury de thèse pour l'intérêt et la bienveillance qu'ils ont porté à mon travail. Merci à Jean-Jacques Greffet et Yannick De Wilde d'avoir rapporté ce manuscrit. Merci à Niek van Hulst d'avoir accepté d'examiner ce travail et merci à Cécile Zakri d'avoir présidé mon jury de thèse.

Je remercie le LabEx LAPHIA pour avoir financé cette thèse.

Ces travaux de thèse ont été effectués entre le CRPP et le LP2N. Je remercie Philippe Richetti et Cécile Zakri, directeurs successifs du CRPP, ainsi que Philippe Bouyer, directeur du LP2N de m'avoir accueilli au sein de leurs laboratoires.

Je remercie chaleureusement mes directeurs de thèse Renaud Vallée et Brahim Lounis pour leurs qualités humaines et scientifiques. Merci de m'avoir fait confiance et d'avoir toujours été disponibles. Ce travail doit beaucoup à leur intuition et méthodologie scientifique, mais aussi à leur pédagogie, leurs précieux conseils et leurs encouragements.

Dans le groupe MaFIC, j'ai particulièrement de la gratitude envers Serge Ravaine et Miguel Comesaña-Hermo qui ont eu la lourde tâche de synthétiser les nano-objets; merci pour leur confiance et leur optimisme. Dans le groupe Nanophotonics, un grand merci à Jean-Baptiste Trebbia et Philippe Tamarat qui ont toujours su trouver le temps et l'énergie pour me soutenir, partager et réaliser des expériences sur la superradiance.

J'ai eu la chance de travailler en collaboration avec d'autres groupes de recherche, créant un environnement riche et stimulant. Les nombreuses interactions m'ont permis de faire évoluer mon point de vue, et de découvrir d'autres façons de travailler. Je remercie chaleureusement Philippe Lalanne au LP2N de m'avoir accueilli comme un doctorant de son groupe, merci pour sa disponibilité et son enthousiasme. Un grand merci à Gabriela Olivíková, Ruben Esteban et Javier Aizpurua au DIPC, pour m'avoir accueilli à San Sebastian, pour leur optimisme et leur aide, même à distance. Enfin merci à Simona Moldovan et Ovidiu Ersen à l'IPCMS pour la caractérisation tridimensionelle des nano-objets en tomographie électronique.

Plus généralement, je remercie les stagiaires, doctorants, post-doctorants et membres permanents de l'équipe MaFIC au CRPP, mais aussi des équipes Nanophotonics et Light in Complex Nanostructures au LP2N. Je tiens également à remercier l'ensemble du personnel technique et administratif du CRPP, du LOMA et du LP2N pour sa bonne humeur et son aide.

J'ai une pensée particulière pour mes amis, doctorants ou pas, rencontrés ici et ailleurs, avec lesquels j'ai partagé de très bons moments et dont le soutien, les blagues, les sourires ont été précieux pour moi, merci à tous.

Enfin, je voudrais exprimer tout ma reconnaissance à ma famille que j'admire et qui m'a soutenu tout au long de mon parcours.

Floriane, je te dédie ces quelques lignes pour te remercier d'être aussi attentionnée et rafraîchissante. J'ai hâte de vivre de nouvelles aventures trépidantes à tes côtés.

Bordeaux, le 4 Janvier 2017

Pierre Fauché

Résumé long

Depuis la domestication du feu il y a plus de 400 000 ans, la lumière a eu une influence cruciale sur le développement de l'humanité [1]. L'interaction lumière-matière constitue donc est un sujet de recherche de longue date. Dans les années 1960, la compréhension de cette interaction a permis la conception et la fabrication de systèmes optiques avancés tels que des sources de lumière cohérentes [2], mais aussi des fibres, des commutateurs et des amplificateurs optiques [3]. Plus récemment, la miniaturisation des circuits et micropuces électroniques a permis d'augmenter considérablement la densité en composants, pour une plus faible consommation en énergie. Afin de réaliser des avancées similaires en photonique, un nouveau champ de recherche a émergé, la nanophotonique : il consiste en l'étude de systèmes optiques à l'échelle du nanomètre. L'objectif est d'utiliser les propriétés de la lumière, telles que la vitesse de propagation et la nature quantique, pour potentiellement interagir avec des nanocomposants électroniques.

Au cours de la dernière décennie, la superradiance, introduite par R. Dicke en 1954, s'est révélée être un processus intéressant pour la nano-optique. Dans ce travail pionnier [4], R. Dicke a montré qu'un ensemble d'atomes dont la population a été inversée, pouvait spontanément relaxer vers l'état fondamental en une durée qui est inversement proportionnellle au nombre d'atomes. Il s'agit de l'émission collective et spontanée de photons par un ensemble d'émetteurs quantiques. Cet effet est le résultat d'une interaction cohérente entre les atomes. Pour qu'il puisse avoir lieu, il est nécessaire que la distance séparant deux atomes soit petite devant leur longueur d'onde d'émission. La superradiance consiste donc en l'émission collective et spontanée de photons par un ensemble d'émetteurs quantiques. Ce phénomène a été largement étudié aussi bien théoriquement qu'expérimentalement [5–9]. Il a été démontré que la superradiance permet de modifier efficacement l'émission de lumière par un ensemble d'émetteurs à l'échelle nanométrique [10, 11]. Son complémentaire, l'effet de subradiance, pourrait, quant à lui, mener à de nouveaux systèmes pour stocker l'information quantique par exemple [12].

Dans une quête de traitement de l'information par des nanocomposants optiques, le con-

finement du signal dans les guide d'ondes diélectriques est limité par la diffraction, menant à un faible confinement pour des systèmes nanométriques et ainsi à des pertes considérables d'énergie pour les modes guidés. Depuis la fin du XXème siècle, une nouvelle quasi-particule, appelée plasmon polariton de surface (SPP), a suscité un grand intérêt. Prédit par R. Ritchie en 1957 [13], un SPP consiste en une onde électromagnétique couplée à une oscillation collective d'électrons libres aux interfaces métal/diélectrique. Il résulte de la réponse cohérente de ces électrons à une lumière incidente. En plus d'une dynamique subpicoseconde, la propriété la plus remarquable d'un SPP est le confinement de modes électromagnétiques à l'échelle sub-longueur d'onde [14, 15], qui contribue à un renforcement du champ électromagnétique local. Les applications les plus développés sont la diffusion Raman de surface exaltée (SERS) pour la détection moléculaire [16, 17] et la microscopie de champ proche [18–20]. Grâce aux récentes avancées en chimie et en nanolithographie, il est possible de concevoir et de synthétiser des nanostructures métalliques afin de contrôler les propriétés de propagation du SPP. De telles structures plasmoniques permettent de fabriquer des circuits optiques avec des domaines de résolution meilleurs que la limite de diffraction.

Des études récentes ont montré que les SPPs possèdent une cohérence spatiale et temporelle [21–25]. En 2003, D. Bergman et M. Stockman [26] ont prédit l'émission spontanée de SPP comme un moyen de générer un champ plasmonique intense, localisé et cohérent. Sur la base de ce travail, un nanolaser a été réalisé et caractérisé expérimentalement par M. Noginov *et al.* [27], où un milieu à gain a été placé autour d'une nanosphère métallique afin de compenser les pertes dans le métal. Ces travaux pionniers dans le domaine de la plasmonique quantique ont révélé qu'un émetteur peut interagir de manière cohérente avec un SPP. De plus, il a été montré qu'un mode plasmonique permet de transmettre des photons intriqués [28–30] et d'intriquer deux émetteurs quantiques [31, 32]. Ces propriétés uniques permettent de considérer la plasmonique pour le traitement quantique de l'information [33, 34]. La superradiance étant un phénomène quantique, il pourrait aussi bénéficier des propriétés sub-longueur d'onde du SPP. En particulier, le groupe de F. García-Vidal a récemment montré théoriquement qu'un guide d'onde plasmonique peut être utilisé pour améliorer l'interaction entre des émetteurs et réaliser une superradiance à longue distance [35]. La superradiance par l'intermédiaire d'un mode plasmonique - appelé superradiance plasmonique - a été introduite par V. Pustovit et T. Shahbazyan en 2009 [36], comme une extension de la superradiance de Dicke aux systèmes plasmoniques.

L'objectif de cette thèse est d'étudier la superradiance plasmonique dans des nanostructures métallo-diélectriques. Le système typique étudié consiste en un ensemble de molécules fluorescentes greffées en nombre contrôlé et à distance contrôlée, autour d'un coeur sphérique

en métal. La distance entre les émetteurs et le coeur plasmonique est ajustée en contrôlant l'épaisseur d'une écorce intermédiaire en silice. Le modèle publié par V. Pustovit et T. Shahbazyan [36, 37] a permis de mettre en évidence le mécanisme de la superradiance plasmonique. Cependant les auteurs se sont focalisés sur un cas simple : les émetteurs sont répartis uniformément et sont tous orientés perpendiculairement à la surface de la particule. Dans notre étude, nous avons tout d'abord étendu ce modèle pour étudier l'influence de la position et de l'orientation des émetteurs sur la superradiance plasmonique. Grâce à ce modèle nous avons pu déterminer les dimensions spatiales optimales du nanohybride pour une étude expérimentale. Ces nanohybrides furent synthétisés par une approche ascendante de la chimie colloïdale. Les mesures de déclin temporel de fluorescence ont mis en évidence de manière claire et directe les propriétés de la superradiance plasmonique à température ambiante. Cependant aucun accord quantitatif n'a été obtenu. Nous proposons alors un modèle semi-classique simple afin de discuter l'effet de décohérence - induite par la température - qui altère la superradiance plasmonique. Cette observation de la superradiance plasmonique à température ambiante ouvre des questions sur la robustesse d'un état superradiant contre des mécanismes de décohérence, qui présente un intérêt majeur pour des applications potentielles.

Le chapitre I commence par introduire le concept de la superradiance de Dicke. Nous présentons une discussion qualitative de l'émission collective par deux émetteurs couplés. Ensuite, après avoir introduit le formalisme semi-classique, nous soulignons les principales caractéristiques de la superradiance. Puis nous introduisons l'influence d'un environnement structuré sur l'émission et sur le couplage entre émetteurs. Finalement, une fois que ces concepts clés ont été introduits, nous mettons en perspective le travail effectué pendant cette thèse.

Le chapitre II a pour but d'étudier théoriquement la superradiance plasmonique dans le cas d'émetteurs répartis autour d'un nanohybride sphérique, consistant en un coeur-écorce métallo-diélectrique. Nous développons une approche classique, explicite et efficace pour calculer la réponse d'un grand ensemble de molécules placées à proximité d'un nanohybride. Ce modèle ne fait aucune hypothèse sur la position et l'orientation des émetteurs, et représente donc une extension du modèle proposé par V. Pustovit et T. Shahbazyan [36]. En utilisant la théorie de Mie, nous montrons que les propriétés optiques d'une nanosphère métallo-diélectrique sont gouvernées par la dynamique de modes SPP localisés (LSPP). Le nanohybride représente donc un environnement riche qui redéfinit l'interaction de champ proche entre les émetteurs. Nous discutons d'abord comment les dimensions du nanohybride et son environnement influencent ses propriétés optiques. Ensuite nous soulignons

l'influence des dimensions du nanohybride et des propriétés de l'émetteur sur l'interaction entre une seule molécule et le coeur plasmonique. Puis nous analysons la réponse collective d'émetteurs répartis autour du nanohybride. Nous montrons que les modes LSPP radiatifs et non-radiatifs contribuent tous les deux au couplage entre les émetteurs. En particulier les modes LSPP non-dipolaires participent principalement au couplage non radiatif. De plus ces modes d'ordre supérieur favorisent l'interaction entre émetteurs voisins. Par conséquent la formation d'états superradiants purs, avec la participation d'une grande partie des émetteurs, est attendue quand l'interaction émetter-émetteur est dominée par le mode LSPP dipolaire. Nous en déduisons que le diamètre optimal du coeur plasmonique pour observer expérimentalement la superradiance plasmonique est de 60 nm. Nous comparons alors nos résultats avec ceux publiés par V. Pustovit et T. Shahbazyan [37]. Nous prédisons que le taux de relaxation du mode superradiant est proportionnel au nombre d'émetteurs, et que ce taux de relaxation augmente d'autant plus que les émetteurs se rapprochent du coeur plasmonique. Notre modèle permet de souligner l'influence considérable de la position et de l'orientation des émetteurs sur les tendances prédites. Un optimum du taux de relaxation étant attendu pour la configuration symétrique qui a été étudiée par V. Pustovit et T. Shahbazyan [37]. Finalement nous montrons que ces tendances survivent après un moyennage sur la position et l'orientation des émetteurs, quoiqu'avec un taux de relaxation réduit.

Dans le chapitre III, nous généralisons le formalisme classique développé dans le chapitre II afin d'étudier l'émission collective induite par une cavité quelconque. À titre d'exemple, nous étudions la superradiance plasmonique dans le cas d'émetteurs répartis autour d'un nanobâtonnet métallique. La géométrie de la structure ainsi que le formalisme des modes quasi-normaux, permet d'avoir une meilleure compréhension du phénomène de superradiance plasmonique. En particulier nous distinguons la contribution de l'interaction entre émetteurs due au nanobâtonnet plasmonique et celle due à l'interaction directe émetteur-émetteur. Nous montrons clairement que les importants décalages en fréquence sont principalement dus à l'interaction directe entre émetteurs. Nous attribuons les larges taux de relaxation à l'interaction induite par la structure plasmonique. À partir de la distribution des moments dipolaires induits, nous montrons alors que la coopérativité des modes superradiants et subradiants est principalement due à l'interaction via la structure plasmonique. En revanche l'interaction directe mène à des états subradiants localisés, perturbant ainsi la formation de modes entièrement collectifs. Comme avec une structure sphérique, nous prédisons que le taux de relaxation est proportionnel au nombre d'émetteurs dans le cas d'un nanobâtonnet plasmonique. Ce résultat est encore valide après moyennage sur la position et l'orientation des émetteurs. Finalement nous proposons et vérifions une expression analytique pour le taux

de relaxation superradiant dans le cas d'un système purement coopératif, induit par une seule résonance électromagnétique. En particulier nous introduisons le facteur de Purcell moyen qui est une propriété intrinsèque de la cavité.

Le chapitre IV présente les matériaux et méthodes expérimentales développés afin d'étudier la superradiance plasmonique. Nous décrivons la synthèse chimique des nanohybrides sphériques décorés par des molécules fluorescentes, ainsi que la caractérisation de ces structures. Ensuite nous détaillons les techniques expérimentales utilisées pour mesurer le taux de déclin de fluorescence en mesure d'ensemble et à l'échelle de la particule unique.

Le chapitre V est consacré aux résultats expérimentaux sur la superradiance plasmonique à température ambiante. Nous présentons d'abord l'analyse des profils temporels de fluorescence, pour des nanohybrides avec différents nombres d'émetteurs et différentes épaisseurs d'écorce de silice. Ensuite nous montrons que le taux de relaxation mesuré est proportionnel au nombre d'émetteurs. Nous prenons un soin particulier à identifier et limiter l'influence de l'interaction directe émetteur-émetteur sur le signal de fluorescence observé. Ce résultat est une preuve claire et directe de la superradiance plasmonique. Il est important de noter que cette tendance a été observée pour deux systèmes : différentes molécules fluorescentes, proches de différentes tailles de coeur plasmonique, caractérisés avec deux approches différentes (mesure d'ensemble et mesure à l'échelle de l'objet unique). De plus, en variant l'épaisseur de l'écorce de silice, nous avons observé que la pente du taux de relaxation par rapport au nombre d'émetteurs augmente lorsque les émetteurs se rapprochent du coeur plasmonique. Bien que ces résultats expérimentaux soient en accord avec les tendances prédites par le modèle classique, un accord quantitatif n'a été obtenu que pour un seul émetteur. Comme l'expérience a été menée à température ambiante, nous proposons d'aller plus loin dans l'interprétation de ces résultats en discutant l'effet de la décohérence induite par la température. En se basant sur la littérature existante et sur un modèle semi-classique simple, nous montrons qu'un processus de décohérence pure perturbe la superradiance plasmonique. En particulier la pente du taux de relaxation avec le nombre d'émetteurs est nettement diminuée à cause du déphasage thermique.

Le chapitre VI aborde l'étude de modes hybrides plasmonique-photonique. Ces modes résultent de l'association de résonances plasmoniques et photoniques. En particulier, nous étudions l'effet du désaccord spectral entre un mode hybride et un émetteur sur la modification de son émission. Pour mener cette étude, un cristal photonique est une structure appropriée car certains modes optiques peuvent être accordés spectralement, en changent l'angle d'incidence ou la polarisation du faisceau incident par exemple. Ainsi nous caractérisons la dépendance spectrale du facteur de Purcell d'émetteurs placés sur un cristal

plasmonique-photonique bidimensionnel. Nous observons une évolution asymétrique, au lieu d'une résonance Lorentzienne qui est attendue pour le facteur de Purcell d'un seul mode faiblement dissipatif. Ces observations sont appuyées par des simulations de différences finies dans le domaine temporel (FDTD) et sont attribuées au couplage des émetteurs avec le mode hybride.

Contents

Introduction

Scientific context

Since the discovery of fire more than 400,000 years ago, light has had crucial influence on humankind's development [1]. Accordingly, the endeavor to understand how light interacts with matter has been a long-running research venture. In the 1960's, the comprehension of the light-matter interaction allowed the design and fabrication of advanced optical devices such as coherent light sources [2], as well as optical fibers, switches, amplifiers [3]. More recently, the miniaturization of electronic circuits and microchips allowed for smaller device footprint, yielding larger chip density and lower power consumption at lower price. In the drive to achieve similar benefits in photonics, a new research field named nanophotonics arose: it consists in the design of optical devices on the nanoscale. The aim is to take advantage of the properties of light, such as speed of propagation and quantum nature; and to potentially interface with electronic nanodevices.

In the last decades, a process of interest for nano-optics emerged as the superradiance, introduced by R. Dicke in 1954. In this pioneering work [4], R. Dicke showed that a collection of atoms with a population inversion could spontaneously relax to the ground state in a time inversely proportional to the number of atoms. It consists in the collective and spontaneous emission of photons from a collection of quantum emitters. This effect results from a coherent interaction between atoms. In the case of Dicke superradiance, it requires that the separation distance between two emitters is small compared to their emission wavelength. It was widely investigated both theoretically and experimentally [5–9]. This process has proven to be efficient to tune the emission of light from nanometric ensembles of emitters [10, 11]. It promises to lead to new devices for storing quantum information [12].

In the drive to perform information-processing with optical nanodevices, the confinement in dielectric waveguides is limited by diffraction, yielding weak confinement for nanoscale devices and thus considerable leakage for the guided modes. Since the end of the 20th century, a new quasi-particle called surface plasmon polariton (SPP) inspired great interest.

Predicted by R. Ritchie in 1957 [13], a SPP consists in an electromagnetic wave coupled to a collective oscillation of free electrons along metal/dielectric interfaces. It results from the resonant and coherent response of these electrons to an incident illumination. In addition to sub-picosecond dynamics, the most remarkable property of SPP is the confinement of electromagnetic modes at sub-wavelength scales [14, 15], and the associated significant local electromagnetic field enhancement. The most developed applications are surface enhanced Raman scattering (SERS) for molecular detection [16, 17] and near-field microscopy [18–20]. Thanks to recent advances in chemistry and nanolithography, it is possible to design and synthesize well-controlled metallic nanostructures in order to shape the SPP propagation properties. Such plasmonic structures allow for the fabrication of subwavelength optical circuits, thereby overcoming the diffraction limit of light. Nanoscale waveguiding based on the negative dielectric constant of the metal can be achieved, at the expense of Ohmic losses in the metal [15]. Accordingly, the propagation length L is relatively small, even for smooth crystalline structures: $L \approx 10\lambda$ [38], where λ is the operating wavelength.

It has been reported that SPP exhibit both spatial and temporal coherence [21–25]. In 2003, D. Bergman and M. Stockman [26] predicted the stimulated emission of SPP as a way to generate strong, localized and coherent plasmonic field. Based on this work, a nanolaser was later experimentally demonstrated by M. Noginov *et al.* [27], where a gain medium was placed in the vicinity of a metal nanosphere to overcome the losses in the metal. These pioneering works in the field of quantum plasmonics revealed that a quantum-emitter can coherently interact with a SPP. Furthermore, it has been shown that a plasmonic mode allows to transmit entangled photons [28–30] and to entangle two quantum emitters [31, 32]. These unique properties allow to consider plasmonics for quantum information processing [33, 34]. Superradiance being a quantum process, it may also benefit from the subwavelength properties of SPP. In particular, the group of F. García-Vidal recently showed theoretically that a plasmonic waveguide can be exploited to enhance the coupling between emitters and perform long-distance superradiance [35]. A model for plasmon-mediated superradiance - called plasmonic superradiance - was introduced by V. Pustovit and T. Shahbazyan in 2009 [36], as an extension of the Dicke superradiance phenomenon to plasmonic systems.

The objective of this doctorate thesis is to investigate the plasmonic superradiance in metallo-dielectric nanohybrids. Typically a collection of fluorescent molecules are distributed around a spherical metal core. The distance between the emitters and the plasmonic core is tuned by controlling the thickness of an intermediate silica shell. The model published by V. Pustovit and T. Shahbazyan [36, 37] allowed to highlight the mechanism of plasmonic superradiance. Yet it mainly focused on a simple case: the emitters are uniformly distributed and

they are all oriented normally to the particle surface. We thus extended this model to study the influence of the distribution in position and orientation of the emitters on the plasmonic superradiance. Furthermore this model allowed us to determine the optimal nanohybrid spatial dimensions for an experimental investigation. These nanohybrids were synthesized by bottom-up approach. The measurement of their fluorescence temporal decay profiles yielded a clear and direct evidence of plasmonic superradiance at room temperature. A simple semi-classical model allows to discuss the effect of the temperature-induced decoherence on the collective emission. This observation of plasmonic superradiance at room temperature opens questions about the robustness of plasmon-mediated superradiant states against decoherence mechanisms, which are of major interest for potential applications.

Outline of the thesis

This manuscript consists in 6 chapters.

Chapter I begins with an introduction to the concept of superradiance without nanohybrid by qualitatively discussing the collective emission of two interacting emitters. Then, after introducing the semi-classical formalism, we point out the main features of superradiance. Next we introduce the influence of a structured environment on the emission and on the coupling between emitters. Finally, once these central concepts are introduced, we further put into context the work conducted during this thesis.

Chapter II intends to theoretically investigate the plasmonic superradiance in the case of emitters distributed around a spherical metallo-dielectric core-shell nanohybrid. As an extension of the model from V. Pustovit and T. Shahbazyan [36], we develop an explicit and efficient classical approach to derive the response of large collection of molecules near the nanohybrid, with no assumption on the emitters position and orientation. We introduce the nanohybrid as a rich environment that redefines the near-field interaction between the emitters. We first discuss how the nanohybrid dimensions and environment influence its optical properties. Then we study the emission of one molecule near the nanohybrid. In particular we highlight the influence of the nanohybrid dimensions and emitters properties on the interaction between the molecule and the plasmonic core. Then we examine the collective response of emitters distributed around the nanohybrid. After describing the main features, we estimate the optimal nanohybrid dimensions for the experimental observation of plasmonic superradiance. Next we compare our results with the one published by V. Pustovit and T. Shahbazyan [37]. We then predict that the superradiant decay rate is proportional to the number of emitters and that the associated slope increases if the emitters get closer to

the plasmonic core. Our model allows us to emphasize the dramatic influence of the emitters position and orientation on the predicted trends. Finally we show that these trends survive after averaging over the emitters position and orientation.

In Chapter III we generalize the classical formalism developed in chapter II to study the collective emission mediated by an arbitrary cavity. As an example we investigate plasmonic superradiance in the case of emitters distributed around a metal nanorod. The geometry of the structure, along with the quasi-normal modes formalism, allow to get a better insight into the plasmonic superradiance phenomenon. In particular we discriminate the contribution of the plasmon-mediated interaction as compared to the direct emitter-emitter interaction. Then we study the cooperativity of the superradiant and the subradiant modes. We show that the direct emitter-emitter interaction impairs the formation of fully collective modes. Furthermore we predict that a decay rate scaling with the number of emitters is also expected for a nanorod-mediated superradiance. Finally we propose and verify an analytical expression for the superradiant decay rate in the case of a purely cooperative system, mediated by a single electromagnetic resonance.

Chapter IV presents the experimental materials and methods developed in order to investigate plasmonic superradiance. We describe the chemical synthesis of the spherical nanohybrids decorated with fluorescent molecules, supported by structural characterization. Then we detail the experimental techniques used to estimate fluorescent decay rates from ensemble and single particle measurements.

Chapter V is devoted to the experimental results on plasmonic superradiance at room temperature. We first present the analysis of fluorescence temporal decay profiles, for nanohybrids with different numbers of emitters and different silica shell thicknesses. We then report that the measured decay rate is proportional with the number of emitters. We take a particular care in identifying and limiting the influence of the direct emitter-emitter interaction on the observed fluorescence signal. It yields a direct and clear evidence of plasmonic superradiance. It is worth noticing that this trend is observed for two systems: different fluorescent molecules and plasmonic core sizes that were characterized with different approaches: ensemble and single object measurements. Besides, controlling the silica shell thickness allows us to observe that the slope of the decay rate with respect to the number of emitters increases as the emitters are closer to the plasmonic core. Even though these experimental results are in accordance with the trends predicted with the classical model, a quantitative agreement could only be obtained for one emitter. As the experiment was performed at room temperature, we propose a further interpretation of these results by discussing the effect of temperature-induced decoherence. In particular this discussion is based on the literature and

on a simple semi-classical model.

Chapter VI is dedicated to the investigation of hybridized plasmonic-photonic modes. These modes result from the association of plasmonic and photonic resonances. In particular, we investigate the effect of the detuning between an hybridized mode and an emitter on its emission's modification. To this end, a photonic crystal is a convenient structure since the supported optical modes can be readily tuned, by changing the illumination incidence angle or the polarization for instance. We therefore characterize the wavelength-dependence of the Purcell factor of emitters distributed on a two dimensional plasmonic-photonic crystal. We report an asymmetrical spectral line shape instead of a Lorentzian line shape, which is expected for the Purcell factor of a single mode with negligible leakage and absorption. These observations are supported by FDTD simulations and are attributed to the coupling of the emitters to a hybridized mode.

Finally we present a brief summary of the main results and discuss some outlooks with preliminary results.

Chapter I

Superradiance and effect of the near-field environment

Contents

In this chapter we introduce the reader to the concept of superradiance without nanohybrid and we discuss the effect of a structured environment. It is the opportunity to present the theoretical frameworks we used for both classical and semi-classical calculations. Both approaches will be further exploited in chapters II-III and V, respectively. Section I.1 briefly outlines the phenomenon of superradiance by discussing the case of two interacting emitters. Then section I.2 introduces the semi-classical formalism and points out the main features of superradiance. Next section I.3 considers a structured environment placed in the near-field of the emitters. We discuss the resulting modification of the spontaneous emission and of the coupling between emitters. Finally we emphasize some recently published results to further put our work into context.

I.1 Principle of superradiance

I.1.a Qualitative description of superradiance

I.1.a.i Spontaneous emission of a two-level system

In this work we investigate the fluorescence of organic molecules. These emitters show mainly one dipole transition between two electronic energy levels [39]: the lowest unoccupied molecular orbital (LUMO) and the highest occupied molecular orbital (HOMO). In the following, we thus approximate a molecule as a two-level system (TLS), with the excited state $|e\rangle$ and the ground state $|g\rangle$ which are separated by an energy $\hbar\omega_0$.

A TLS is represented by the dipole moment operator $\hat{\boldsymbol{\mu}}$

$$\hat{\boldsymbol{\mu}} = \boldsymbol{\mu}\hat{\sigma}^+ + \boldsymbol{\mu}^*\hat{\sigma}^- \tag{I.1}$$

where $\hat{\sigma}^+$ and $\hat{\sigma}^-$ are the TLS raising and lowering operators, respectively [40]

$$\begin{aligned} \hat{\sigma}^+ &= |e\rangle\langle g| \\ \hat{\sigma}^- &= |g\rangle\langle e| \\ \hat{\sigma}^+\hat{\sigma}^- &= |e\rangle\langle e| \end{aligned} \tag{I.2}$$

and $\boldsymbol{\mu}$ is the transition dipole moment

$$\boldsymbol{\mu} = \langle e|\,\hat{\boldsymbol{\mu}}\,|g\rangle \tag{I.3}$$

In order to discuss the build up of the superradiance phenomenon, we also quantize the electromagnetic field. Let us consider an excited TLS in vacuum, the system {TLS+field} is then in the state $|e\rangle \otimes |\emptyset\rangle$: the TLS is excited and no photon is in the continuum of modes of the vacuum electromagnetic field. Because the TLS is coupled to the vacuum modes, the system spontaneously evolves to the continuum of states $|g\rangle \otimes |1_l\rangle$: the TLS decayed to the ground state while one photon was emitted in one of the vacuum modes, denoted by l.

The resulting fluorescence signal that will be measured experimentally is proportional to the probability to find the TLS in its excited state, measured by [41]

$$\left\langle \hat{\sigma}^+ \hat{\sigma}^- \right\rangle = \mathrm{Tr}\{\rho \hat{\sigma}^+ \hat{\sigma}^-\} \tag{I.4}$$

where ρ is the density matrix describing the state of the molecular system.

We denote by γ_p the decay rate of the excited state population in vacuum, where p stands for *population*. The rate of photon emission at time t is then [7]

$$\xi(t) = \gamma_p \left\langle \hat{\sigma}^+ \hat{\sigma}^- \right\rangle \tag{I.5}$$

Energy conservation requires that the decrease of the TLS excitation should at any time be compensated by the increase of the photon number so that

$$\begin{aligned} \partial_t \left\langle \hat{\sigma}^+ \hat{\sigma}^- \right\rangle &= -\xi(t) \\ &= -\gamma_p \left\langle \hat{\sigma}^+ \hat{\sigma}^- \right\rangle \end{aligned} \tag{I.6}$$

where ∂_t designates the time derivative. Eq. I.6 can be integrated to yield

$$\left\langle \hat{\sigma}^+ \hat{\sigma}^- \right\rangle = e^{-\gamma_p t} \tag{I.7}$$

Hence during the so-called spontaneous emission, the excited state population $\langle \hat{\sigma}^+ \hat{\sigma}^- \rangle$ and the radiation rate both decay exponentially with the characteristic time $\tau_p = \gamma_p^{-1}$.

I.1.a.ii Superradiance of two TLS

Following the approach proposed in [7], we now consider two identical TLS 1 and 2 at positions $\mathbf{r}_1$ and $\mathbf{r}_2$, with the same population decay rate γ_p and transition frequency ω_0. We denote by $|e_1\rangle$ ($|e_2\rangle$) and $|g_1\rangle$ ($|g_2\rangle$) the excited and ground states of the TLS 1 (2), respectively. Figure I.1 shows a schematic diagram of the energy levels in the direct-product Hilbert space of the

two TLS. Furthermore $\hat{\sigma}_1^+$ ($\hat{\sigma}_2^+$) and $\hat{\sigma}_1^-$ ($\hat{\sigma}_2^-$) denote the raising and lowering operators of the TLS 1 (2), respectively. At initial time $t = 0$ both TLS are excited so that the molecular system is in the state $|e_1, e_2\rangle$, the vacuum field being in its ground state.

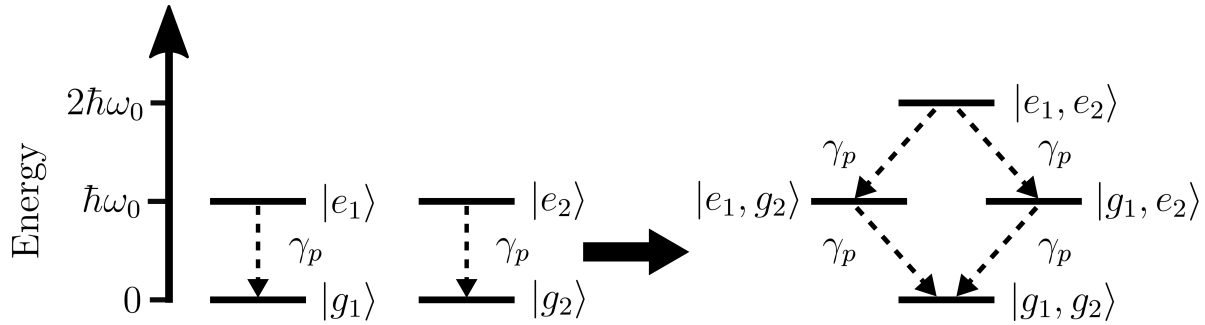

Figure I.1: Schematic diagram of the energy levels of 2 identical two-level systems, with resonance frequency ω_0. Left part: the solid lines are the electronic excited $|e\rangle$ and ground $|g\rangle$ states for each TLS. The right part shows the energies of the direct-product states. The $|e_1, e_2\rangle$ line corresponds to the state where both TLS are excited. The dashed lines represent the spontaneous emission with decay rate γ_p.

We define the collective operators

$$\begin{aligned} \hat{\sigma}^+ &= \hat{\sigma}_1^+ + \hat{\sigma}_2^+ \\ \hat{\sigma}^- &= \hat{\sigma}_1^- + \hat{\sigma}_2^- \end{aligned} \tag{I.8}$$

We assume that the TLS have parallel transition dipole moments and are separated by a distance $R_{12} = |\mathbf{r}_1 - \mathbf{r}_2|$ small compared with their resonance wavelength

$$R_{12} \ll \frac{2\pi c}{\omega_0} = \lambda_0 \tag{I.9}$$

where c is the light velocity.

The condition expressed in Eq. I.9 yields that the TLS are indiscernible in their interaction with the electromagnetic field fluctuations. Following the emission of the first photon, one cannot distinguish which TLS is still excited and which decayed to the ground state. The state of the molecular system is then in the coherent superposition

$$|\Psi_C\rangle = \frac{1}{\sqrt{2}}\Big(|e_1, g_2\rangle + |g_1, e_2\rangle\Big) \tag{I.10}$$

and one photon is emitted in a mode of the vacuum field.

Eq. I.9 allows us to consider the system as a point-like source resulting from the sum of the 2 individual TLS. We generalize the radiation rate for a single TLS from Eq. I.6 to

deduce the 2-TLS system radiation rate [7]

$$\tilde{\xi} = \gamma_p \left\langle \hat{\sigma}^+ \hat{\sigma}^- \right\rangle \tag{I.11}$$

The total radiation rate of the molecular system from the superposition $|\psi_C\rangle$ is then

$$\begin{aligned} \tilde{\xi} &= \gamma_p \left\langle \hat{\sigma}^+ \hat{\sigma}^- \right\rangle = \gamma_p \langle \psi_C | \, \hat{\sigma}^+ \hat{\sigma}^- \, | \psi_C \rangle \\ &= \gamma_p \Big(\left\langle \hat{\sigma}_1^+ \hat{\sigma}_1^- \right\rangle + \left\langle \hat{\sigma}_2^+ \hat{\sigma}_2^- \right\rangle + \left\langle \hat{\sigma}_1^+ \hat{\sigma}_2^- + \hat{\sigma}_2^+ \hat{\sigma}_1^- \right\rangle \Big) \\ &= 2\gamma_p \end{aligned} \tag{I.12}$$

Now we compare this rate to the total radiation rate obtained for two TLS emitting independently. After the emission of the first photon, the state is either $|g_1, e_2\rangle$ or $|e_1, g_2\rangle$. The radiation rate from each state is then

$$\tilde{\xi}^{(ind)} = \gamma_p \left\langle \hat{\sigma}^+ \hat{\sigma}^- \right\rangle = \gamma_p \tag{I.13}$$

For instance, Eq. I.13 corresponds to two TLS located at large distance from each other $R_{12} \gg \lambda_0$.

From Eqs. I.12 and I.13 , we deduce that the correlation between the TLS brings a coherent contribution to the total radiation rate. In term of phase, after the emission of the first photon, the transition dipole moments acquired a specific phase difference through their interaction with the electromagnetic field fluctuations, even though their respective phase remain random $\langle \hat{\boldsymbol{\mu}}_1 \rangle = \langle \hat{\boldsymbol{\mu}}_2 \rangle = 0$. The coherent contribution thus consists in an interference term depending on the relative phase between the TLS dipole moments.

If the dipole moments are in-phase then we observe constructive interference and the radiation rate is larger, as shown in Eq. I.12. It corresponds to the so-called superradiant emission.

On the contrary out-of-phase dipole moments result in destructive interference, resulting in the subradiant emission.

To conclude, superradiance consists in the collective spontaneous emission by a collection of atoms or molecules separated by a distance that is small compared with their emission wavelength. The cooperativity in this phenomenon results from the correlation between the TLS that build-up after the emission of the first photon. The relaxation of correlated TLS then consists in the interference of the fields emitted by the TLS. As such, the subsequent emission can be described using a classical approach. We demonstrate this in the next

paragraph I.1.b, which will be exploited in chapters II and III to describe the plasmonic superradiance phenomenon.

I.1.b Classical approach to superradiance

In the classical approach a fluorescent molecule is described as an electron-ion pair behaving as a harmonic oscillator, with frequency ω_0. It couples to the electromagnetic field via its electric dipole moment $\boldsymbol{\mu}$ [42]. In the so-called Lorentz oscillator model, losses of energy by the dipole correspond to a damping of the dipole oscillations at a rate γ_{cl}, where *cl* stands for *classical*. Here we assume that the dipole oscillation damping is only due to the radiation of electromagnetic energy.

In the following we consider values that are averaged over one period of the dipole oscillations. In order to discuss the time evolution of these averages, we assume that the damping is slow as compared to the period of the dipole oscillations, which will be verified in paragraph I.1.c

$$\gamma_{cl} \ll \omega_0 \tag{I.14}$$

I.1.b.i Power radiated by one Lorentz oscillator and energy conservation

In absence of a driving field, the equation of motion of the oscillating dipole is

$$\partial_t^2 \boldsymbol{\mu}(t) + \gamma_{cl} \partial_t \boldsymbol{\mu}(t) + \omega_0^2 \boldsymbol{\mu}(t) = 0 \tag{I.15}$$

The solution of Eq. I.15 is then [43]

$$\boldsymbol{\mu}(t) = \boldsymbol{\mu}_\omega e^{-i(\omega t - \phi)} e^{-\gamma_{cl} t/2} \tag{I.16}$$

where $\omega = \omega_0 \sqrt{1 - (\gamma_{cl}^2/(4\omega_0^2)}$ and ϕ is the phase. The dipole moment amplitude thus decays with the decay rate $\gamma_{cl}/2$.

Then the average power radiated by this dipole at time t is deduced from Larmor's formula [43]

$$\overline{P}(t) = \frac{\omega_0^4}{12\pi\epsilon_0 c^3} |\boldsymbol{\mu}(t)|^2 = \frac{\omega_0^4}{12\pi\epsilon_0 c^3} \boldsymbol{\mu}_\omega^2 e^{-\gamma_{cl} t} \tag{I.17}$$

where the average was taken over one period of the dipole oscillations $2\pi/\omega$. Hence the average radiated power decays with the spontaneous decay rate γ_{cl}.

Energy conservation then yields that the average radiated power must equal the average

power lost by the system

$$\overline{P}(t) = -\partial_t \overline{W} \tag{I.18}$$

where W is the kinetic and potential energy of the oscillating dipole. The average value of W at time t is [43]

$$\overline{W}(t) = \frac{m\omega_0^2}{2q^2}|\boldsymbol{\mu}(t)|^2 \tag{I.19}$$

where q and m are the electron charge and mass, respectively.

From Eqs. I.17, I.18 and I.19, we deduce the time evolution of the average dipole energy

$$\begin{aligned} \partial_t \overline{W}(t) &= -\frac{\omega_0^2}{12\pi\epsilon_0 c^3}\frac{2q^2}{m}\overline{W}(t) \\ &= -\gamma_{cl}\overline{W}(t) \end{aligned} \tag{I.20}$$

where we identify the classical decay rate of the dipole in vacuum [43]

$$\gamma_{cl} = \frac{\omega_0^2}{6\pi\epsilon_0 c^3}\frac{q^2}{m} \tag{I.21}$$

I.1.b.ii Collective radiation by 2 Lorentz oscillators

Here we consider two identical dipoles $\boldsymbol{\mu}_1$ and $\boldsymbol{\mu}_2$, with the same classical decay rate γ_{cl} and transition frequency ω_0, so that the total dipole moment is

$$\boldsymbol{\mu} = \boldsymbol{\mu}_1 + \boldsymbol{\mu}_2 = \boldsymbol{\mu}_\omega e^{-\gamma_{cl}t/2}(e^{-i(\omega t-\phi_1)} + e^{-i(\omega t-\phi_2)}) \tag{I.22}$$

where ϕ_1 and ϕ_2 are their respective phase.

We assume that the dipoles are separated by a distance small compared with their resonance wavelength, so that the system behaves as a point-like source resulting from the sum of the 2 individual dipoles. The average radiated power is then

$$\overline{P}(t) = \frac{\omega_0^4}{12\pi\epsilon_0 c^3} 2\boldsymbol{\mu}_\omega^2\Big(1 + cos(\Delta\phi)\Big)e^{-\gamma_{cl}t} \tag{I.23}$$

where $\Delta\phi = \phi_1 - \phi_2$ is the phase difference appearing in an interference term which clearly contributes to the average radiated power. As discussed in paragraph I.1.a.ii, this phase difference is determined by the interaction between the emitters.

For in-phase dipole moments i.e. $\Delta\phi = 0$, the constructive interference results in an

increased power

$$\overline{P}(t) = 4\frac{\omega_0^4}{12\pi\epsilon_0 c^3}\boldsymbol{\mu}_\omega^2 e^{-\gamma_{cl}t} \tag{I.24}$$

Energy conservation then yields (see Eq. I.18)

$$\begin{aligned}\partial_t\overline{W}(t) &= \overline{P}(t)\\ &= -2\gamma_{cl}\overline{W}(t)\end{aligned} \tag{I.25}$$

Whereas for non-interacting dipoles one obtains

$$\overline{P}(t) = 2\frac{\omega_0^4}{12\pi\epsilon_0 c^3}\boldsymbol{\mu}_\omega^2 e^{-\gamma_{cl}t} \tag{I.26}$$

and

$$\partial_t\overline{W}(t) = -\gamma_{cl}\overline{W}(t) \tag{I.27}$$

Therefore the interacting in-phase dipoles radiate twice as much power and twice as fast as non-interacting dipoles. This collective radiation corresponds to the superradiant case.

On the contrary out-of-phase dipoles i.e. $\Delta\phi = \pi$, lead to destructive interference

$$\overline{P} = -\partial_t\overline{W}(t) = 0 \tag{I.28}$$

In this situation the system does not couple to the electromagnetic field and the energy is trapped. This is the subradiant case.

I.1.c Relationship between population and dipole decay rates

In both quantum and classical approaches we introduced various decay rates. In this paragraph we clearly define each decay rate and explain how they are related to the optical properties of a fluorescent molecule observed experimentally.

In section I.1.a we saw that the temporal decay of the fluorescence signal is determined by the decay rate of the excited state population γ_p. The homogeneous linewidth of the fluorescence spectrum is given by [44] $\Delta\nu_{hom} = \gamma_d/\pi$, where γ_d is the decay rate of the coherence between the ground state and the excited state. It is given by

$$\gamma_d = \frac{\gamma_p}{2} + \gamma^* \tag{I.29}$$

where γ^* is due to pure dephasing processes. The distinction between γ_p and γ_d is thus

crucial.

For instance let us consider a single molecule in a polymer matrix at room temperature. The matrix phonon modes interact with the molecule, resulting in a dephasing of its dipole moment, yielding to a homogeneous broadening of the spectrum. However the population of the excited state is not affected. Hence the temporal decay profile of the fluorescence intensity is unchanged. At liquid helium temperature, pure dephasing processes vanish: $\gamma^* = 0$. The relaxation of the coherence is then solely due to the relaxation of the excited state population and the emission linewidth is $\Delta\nu_{hom} = \gamma_p/(2\pi)$.

In addition to the spontaneous emission of a photon, relaxation of the population from the excited to the ground state can occur by non-radiative processes. For instance the electronic energy can be converted into heat by the creation of phonons [39]. We denote by γ_p^r the radiative decay rate and γ_p^{nr} the non-radiative decay rate such that

$$\gamma_p = \gamma_p^r + \gamma_p^{nr} \tag{I.30}$$

The molecule quantum yield is then

$$\eta = \frac{\gamma_p^r}{\gamma_p} \tag{I.31}$$

For a fluorescent molecule as the one investigated experimentally in our work, $\gamma_p \approx$ 50 MHz and $\eta > 60\%$.

Concerning the classical decay rate γ_{cl}, it can be related to the population decay rate γ_p by [41]

$$\gamma_p^r = f\gamma_{cl} \tag{I.32}$$

where f is the oscillator strength of the transition. We emphasize that the classical model discussed in this manuscript is only valid in the absence of pure dephasing processes $\gamma^* = 0$. In this case $\gamma_{cl} \ll \omega_0$ as assumed in paragraph I.1.b.

I.2 Semi-classical approach

In this section we introduce a semi-classical approach to describe the main features of superradiance. Importantly, only the TLS are quantized in this "semi-classical" approach, not the electromagnetic field. Using this semi-classical approach, we neglect the intermediate build-up of correlation between TLS via the TLS-field interaction that was pointed out in paragraph I.1.a. This corresponds to the Born approximation. Furthermore, the TLS-field

correlation time is assumed to be small as compared with the evolution time of the system, according to the Markov approximation [7]. This model will be used to investigate the environment-mediated coupling between TLS in chapter V. We thus adopt a single-atom frame [45] rather than the historical collective description [4, 7, 46]. Furthermore we study the relaxation of excited TLS so we do not consider any external field.

I.2.a System derivation for two emitters

We investigate the interaction of 2 identical two-level systems, as introduced in paragraph I.1.a. The molecular system is described by the Hamiltonian [45, 47]

$$\hat{H} = \hat{H}_0 + \hat{H}_{dd} \tag{I.33}$$

where the atomic Hamiltonian $\hat{H}_0$ accounts for the energy of individual TLS. The origin of energy is taken at the state $|g_1, g_2\rangle$, as shown in Fig. I.1.

$$\hat{H}_0 = \hbar\omega_0(\hat{\sigma}_1^+\hat{\sigma}_1^- + \hat{\sigma}_2^+\hat{\sigma}_2^-) \tag{I.34}$$

Then $\hat{H}_{dd}$ describes the coherent interaction between the TLS [45]

$$\hat{H}_{dd} = \hbar \sum_{l=1,j\neq l}^{2,2} \frac{g_{lj}}{2}(\hat{\sigma}_l^+ + \hat{\sigma}_l^-)(\hat{\sigma}_j^+ + \hat{\sigma}_j^-) = \hbar g_{12}(\hat{\sigma}_1^+\hat{\sigma}_2^- + \hat{\sigma}_2^+\hat{\sigma}_1^-) \tag{I.35}$$

where only the resonant terms are kept. Accounting for the distance between the TLS $\mathbf{r}_{12} = \mathbf{r}_1 - \mathbf{r}_2 = R_{12}\hat{\mathbf{r}}_{12}$, the retarded coupling constant is

$$\begin{aligned} g_{12} = \frac{3}{2}\gamma_p\Big\{ & -[\mathbf{e}_1\cdot\mathbf{e}_2 - (\mathbf{e}_1\cdot\hat{\mathbf{r}}_{12})(\mathbf{e}_2\cdot\hat{\mathbf{r}}_{12})]\frac{cos(k_0R_{12})}{k_0R_{12}} \\ & +[\mathbf{e}_1\cdot\mathbf{e}_2 - 3(\mathbf{e}_1\cdot\hat{\mathbf{r}}_{12})(\mathbf{e}_2\cdot\hat{\mathbf{r}}_{12})][\frac{sin(k_0R_{12})}{(k_0R_{12})^2} + \frac{cos(k_0R_{12})}{(k_0R_{12})^3}]\Big\} \end{aligned} \tag{I.36}$$

where $k_0 = \omega_0/c$ and $\mathbf{e}_1$ ($\mathbf{e}_2$) is the dipole moment unitary vector of the TLS 1 (2), respectively.

The Hamiltonian in Eq. I.33 does not include energy dissipation due to spontaneous emission or interaction between TLS. Making the Born and Markov approximation, we describe these effects by introducing a dissipative part in the Lindblad form of the master equation [47]

$$\partial_t \rho = \frac{i}{\hbar}[\rho, \hat{H}] + \mathcal{L}\rho \tag{I.37}$$

where ρ is the density matrix describing the molecular system and $\mathcal{L}$ consists in the following Liouville operators

$$\mathcal{L} = \mathcal{L}^1_{sp} + \mathcal{L}^2_{sp} + \mathcal{L}^{12}_{dd} \tag{I.38}$$

where

$$\mathcal{L}^l_{sp}\rho = -\frac{\gamma_p}{2}(\hat{\sigma}^+_l \hat{\sigma}^-_l \rho + \rho \hat{\sigma}^+_l \hat{\sigma}^-_l - 2\hat{\sigma}^-_l \rho \hat{\sigma}^+_l) \tag{I.39}$$

describes the spontaneous emission with decay rate γ_p.

$\mathcal{L}^{12}_{dd}$ accounts for the incoherent exchange of excitation between the TLS. It is due to the absorption by a TLS of photons spontaneously emitted by the other TLS [47]

$$\mathcal{L}^{12}_{dd}\rho = -\frac{\gamma_{12}}{2}(\hat{\sigma}^+_1 \hat{\sigma}^-_2 \rho + \rho \hat{\sigma}^+_1 \hat{\sigma}^-_2 - 2\hat{\sigma}^-_2 \rho \hat{\sigma}^+_1 + \hat{\sigma}^+_2 \hat{\sigma}^-_1 \rho + \rho \hat{\sigma}^+_2 \hat{\sigma}^-_1 - 2\hat{\sigma}^-_1 \rho \hat{\sigma}^+_2) \tag{I.40}$$

with the cross-damping rate

$$\begin{aligned}\gamma_{12} = \frac{3}{2}\gamma_p \Big\{ &[\mathbf{e}_1 \cdot \mathbf{e}_2 - (\mathbf{e}_1 \cdot \hat{\mathbf{r}}_{12})(\mathbf{e}_2 \cdot \hat{\mathbf{r}}_{12})] \frac{sin(k_0 R_{12})}{k_0 R_{12}} \\ &+ [\mathbf{e}_1 \cdot \mathbf{e}_2 - 3(\mathbf{e}_1 \cdot \hat{\mathbf{r}}_{12})(\mathbf{e}_2 \cdot \hat{\mathbf{r}}_{12})][\frac{cos(k_0 R_{12})}{(k_0 R_{12})^2} - \frac{sin(k_0 R_{12})}{(k_0 R_{12})^3}] \Big\}\end{aligned} \tag{I.41}$$

I.2.b Characteristic features of two emitters superradiance

I.2.b.i Eigenstates and energy diagram

We solve the master equation from Eq. I.37 in the direct-product Hilbert space of the two TLS, in the orthonormal basis represented in the right part of figure I.1

$$\begin{cases} |e_1, e_2\rangle & \rightarrow & \rho_{ee} \\ |e_1, g_2\rangle & \rightarrow & \rho_{eg} \\ |g_1, e_2\rangle & \rightarrow & \rho_{ge} \\ |g_1, g_2\rangle & \rightarrow & \rho_{gg} \end{cases} \tag{I.42}$$

The diagonal elements $(\rho_{ee}, \rho_{eg}, \rho_{ge}, \rho_{gg})$ of the density matrix ρ in this uncoupled basis give access to the population of each TLS.

However $|e_1, g_2\rangle$ and $|g_1, e_2\rangle$ are not eigenvectors of the Hamiltonian $\hat{H}$ from Eq. I.33. Therefore we also solve the master equation from Eq. I.37 in the eigenbasis consisting in the

following coupled states [45]

$$\begin{cases} |e_1, e_2\rangle & \rightarrow \quad \rho_{ee} \\ |+\rangle = \dfrac{1}{\sqrt{2}}(|e_1, g_2\rangle + |g_1, e_2\rangle) & \rightarrow \quad \rho_{+} \\ |-\rangle = \dfrac{1}{\sqrt{2}}(|e_1, g_2\rangle - |g_1, e_2\rangle) & \rightarrow \quad \rho_{-} \\ |g_1, g_2\rangle & \rightarrow \quad \rho_{gg} \end{cases} \tag{I.43}$$

where $|+\rangle$ is the superradiant state and $|-\rangle$ is the subradiant state. Straightforward calculation of the associated populations leads to the following four coupled differential equations

$$\begin{aligned} \partial_t \rho_{ee} &= -2\gamma_p \rho_{ee} \\ \partial_t \rho_{+} &= (\gamma_p + \gamma_{12})\rho_{ee} - (\gamma_p + \gamma_{12})\rho_{+} \\ \partial_t \rho_{-} &= (\gamma_p - \gamma_{12})\rho_{ee} - (\gamma_p - \gamma_{12})\rho_{-} \\ \partial_t \rho_{gg} &= (\gamma_p + \gamma_{12})\rho_{+} + (\gamma_p - \gamma_{12})\rho_{-} \end{aligned} \tag{I.44}$$

where the decay rates are explicited.

Diagonalizing the Hamiltonian from Eq. I.33, we also deduce their energy $E_{ee} = 2\hbar\omega_0$, $E_{\pm} = \hbar(\omega_0 \pm g_{12})$ and . We give a representation of the coupled basis in figure I.2.

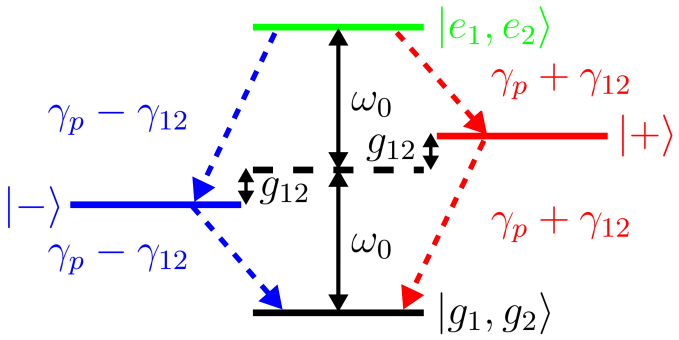

Figure I.2: Schematic representation of the coupled basis for the superradiance of 2 identical two-level systems, with energy and decay constants.

Note in Fig. I.2 that the energy shift between the superradiant and subradiant states is given by the coherent interaction g_{12}. Whereas the incoherent interaction γ_{12} increases the superradiant decay rate γ_+ and decreases the subradiant decay rate γ_-.

I.2.b.ii Time evolution of the population

Here we investigate the time evolution of the population in both the uncoupled and the coupled basis so as to get a better insight into the superradiance mechanism. We assume that initially TLS 1 is excited while TLS 2 is in the ground state, yielding $\rho_{ee}(t) = 0$. The two transition dipole moments are parallel, oriented orthogonally to the segment joining them: $\mathbf{r}_{12} \cdot \boldsymbol{\mu}_1 = \mathbf{r}_{12} \cdot \boldsymbol{\mu}_2 = 0$, as represented in the insets of Fig. I.3.

We consider two cases: large separation distance $R_{12} \gg \lambda_0$, yielding $g_{12} \approx \gamma_{12} \approx 0$; and intermediate separation distance $R_{12} = \lambda_0/10$, corresponding to $g_{12} = 2.5\gamma_p$ and $\gamma_{12} = 0.92\gamma_p$. Figure I.3 shows the time evolution of the states populations, in the uncoupled and the coupled basis.

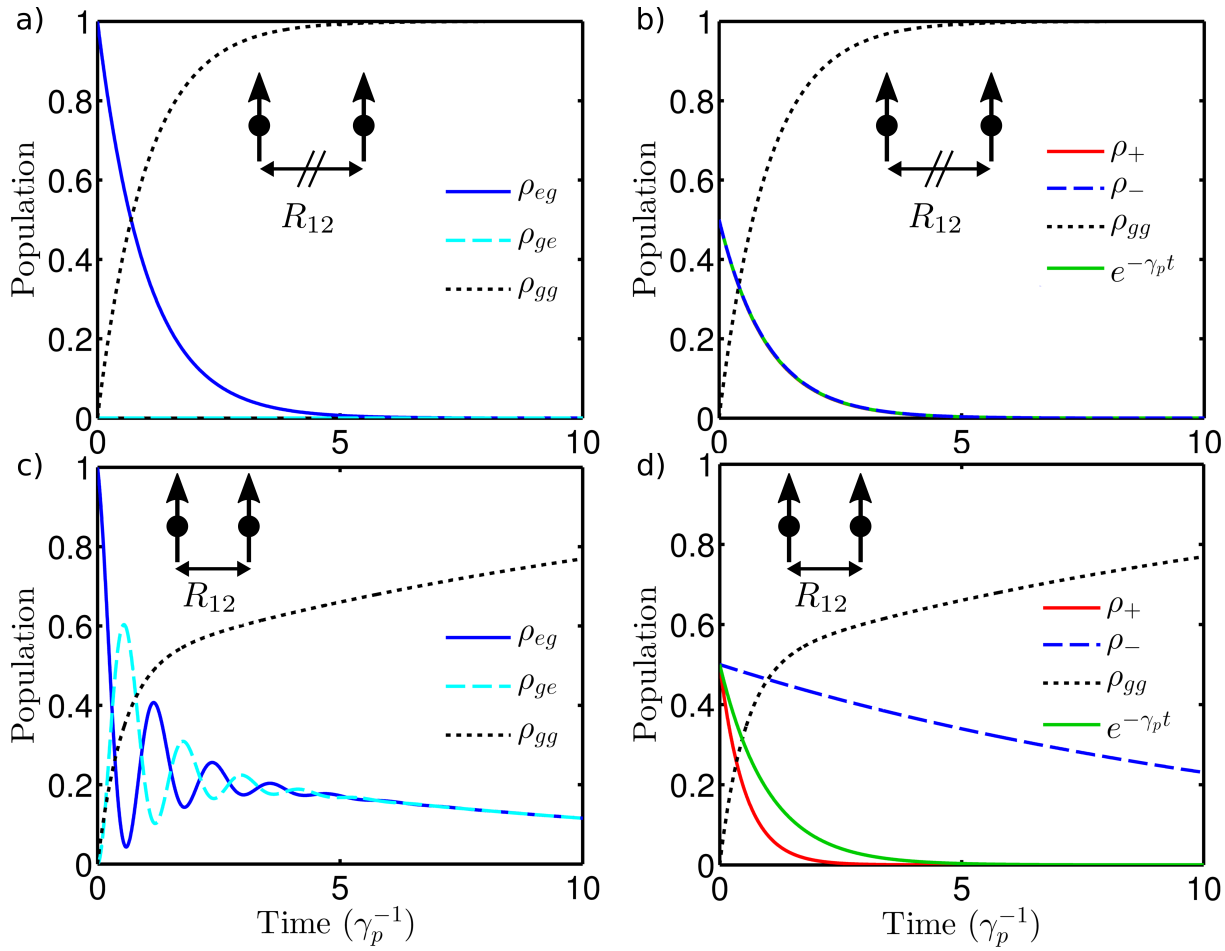

Figure I.3: Two identical and parallel TLS are separated by the distance R_{12}. As represented in the insets, we consider two cases: a) and b) $R_{12} \gg \lambda_0$ or c) and d) $R_{12} = \lambda_0/10$. a) and c) Time evolution of the population of the system states in the uncoupled basis: (solid blue line) ρ_{eg}, (dashed cyan line) ρ_{ge} and (dotted dark line) ρ_{gg}. b) and d) Time evolution of the population of the system states in the coupled basis: (solid red line) ρ_+, (dashed blue line) ρ_-, (dotted dark line) ρ_{gg}. The solid green line corresponds to the normalized decay of non-interacting TLS. The TLS 1 is initially excited while the TLS 2 is in the ground state, hence $\rho_{ee} = 0$.

For $R_{12} \gg \lambda_0$, we observe in figure I.3a that the TLS 1 population ρ_{eg} spontaneously decreases, and thus populates the ground state $|g_1, g_2\rangle$. On the contrary the TLS 2 remains in the ground state: $\rho_{ge}(t) = 0$. Accordingly, $\rho_+ = \rho_- = \rho_{eg}/2$ and Fig. I.3b shows that the population of both superradiant and subradiant states relax with decay rate γ_p, corresponding to non-interacting emitters.

For $R_{12} = \lambda_0/10$, we see in Fig. I.3c that the probability to find a single TLS in its excited state oscillates. The population is transferred back and forth from one TLS to the other, as a result of their interaction with each other. The frequency of these oscillations is given by the frequency shift between the superradiant and subradiant states $2g_{12}$, which is related to the coherent interaction between the TLS. During these oscillations, the TLS spontaneous emission progressively populates the ground state $|g_1, g_2\rangle$. We observe in Fig. I.3d that the decay of the superradiant state $|+\rangle$ is faster $\gamma_+ = \gamma_p + \gamma_{12}$ and the decay of the subradiant state $|-\rangle$ is slower $\gamma_- = \gamma_p - \gamma_{12}$ than the spontaneous emission of non-interacting emitters γ_p.

In the small separation limit, $\gamma_{12} \approx \gamma_p$ so that $\gamma_+ \approx 2\gamma_p$ and $\gamma_- \approx 0$. Note that the relative orientation of the transition dipole moments also strongly influences the coupling coefficients. In particular, orthogonal orientation may lead to non-interacting TLS, regardless of their separation distance.

I.2.b.iii Time evolution of the radiation rate

Now we discuss the time evolution of the fluorescence emitted by the molecules, which corresponds to what is detected experimentally. According to energy conservation, any emitted photon corresponds to an elastic relaxation in the diagram Fig. I.2 [48]. The total radiation rate $\xi(t)$, in photons per second, is then the product of the population of the relaxing states by the associated decay rates [49]

$$\xi(t) = -\sum_{\alpha} \partial_t \rho_\alpha = 2\gamma_p \rho_{ee} + \gamma_+ \rho_+ + \gamma_- \rho_- \tag{I.45}$$

Figure I.4 shows the time evolution of the total radiation rate for two identical and parallel TLS, separated by $R_{12} = \lambda_0/10$. We consider two different initial conditions: a) one TLS is excited or b) both TLS are excited. For comparison, we show the decay of two non-interacting TLS.

If one TLS is initially excited, we observe the decay shown in Fig. I.4a. As discussed in Fig. I.3d, the superradiant $|+\rangle$ and subradiant states $|-\rangle$ are equally populated and decay with decay rates γ_+ and γ_-, respectively. As a consequence, the two corresponding decay

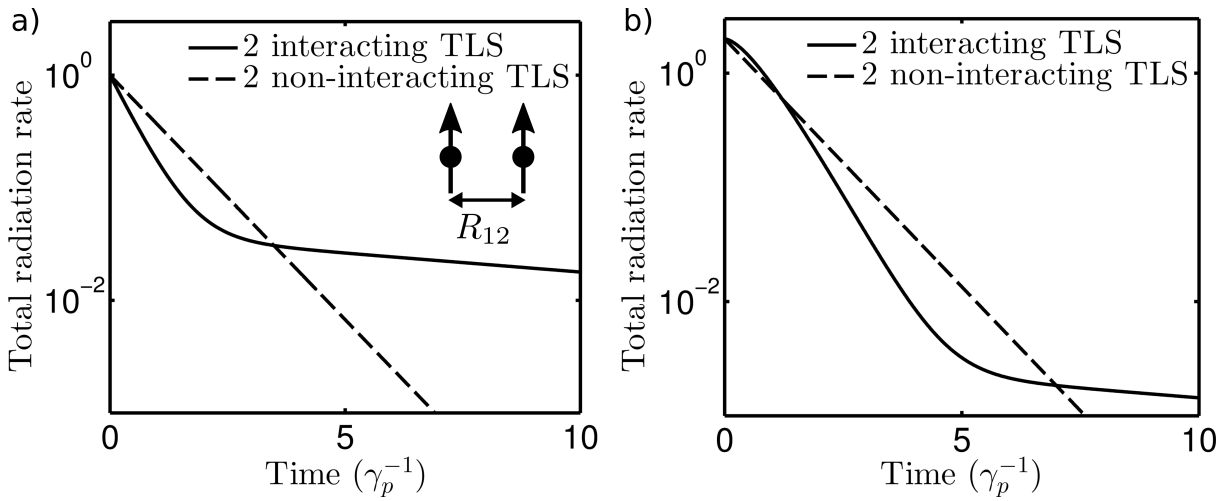

Figure I.4: Time evolution of the total radiation rate for a 2-TLS superradiant system. It consists in two identical and parallel TLS separated by $R_{12} = \lambda_0/10$ (solid line), as represented in the inset. a) One TLS or b) both TLS are initially excited. We use a log-scale to compare them with the decay of two non-interacting TLS (dashed line).

constants are observed. The short one is the superradiant mode and the long one is the subradiant mode.

If both TLS are initially excited then $\rho_{ee} = 1$ at time $t = 0$. We thus observe the decay shown in Fig. I.4b. First, the $|e_1, e_2\rangle$ state starts to decay. The superradiant state is populated faster than the subradiant state, as depicted in Fig. I.2. During this transition, both the superradiant and subradiant also contribute to the fluorescence signal. Hence the total radiation rate is larger than what is observed for 2 non-interacting TLS. The total radiated energy is conserved so this radiation burst is followed by a fast decay. Eventually, both $|+\rangle$ and $|-\rangle$ states contribute to the emission and we retrieve the superradiant and subradiant components observed in Fig. I.4a.

Experimentally, the molecules are embedded in a polymer matrix and characterized at room temperature. We will show in chapter V how this semi-classical approach can be adapted to describe the resulting collective emission.

I.2.c N emitters superradiance and simplification

The superradiance of 2 emitters thus shows promising features for the control of light emission. We now discuss the investigation of the superradiance by a collection of N emitters. It consists in solving the time evolution of the 2^N states where each TLS is either in the ground or the excited state, *e.g.* $|e_1, g_2, g_3, e_4, ..., g_N\rangle$. As a consequence, the dimension of the density matrix ρ rapidly diverges with the number of emitters. Therefore it is challenging to solve this N-body problem accounting for the interactions between the TLS. Furthermore,

the problem worsens if one accounts for their interaction with an external electromagnetic field, which is usually quantized [46].

Modern computation methods limit the study to approximately 10 TLS, using the density matrix approach [50] or Monte Carlo simulation [51, 52]. Experimentally, the sample usually consists in an ensemble of at least hundreds of atoms or molecules [53]. To describe them theoretically and then interpret the results, one usually considers a Hilbert subspace by making some simplifications.

In his pioneering paper [4], R. Dicke considered that, as the TLS are confined in a volume small compared to their emission wavelength, the TLS are indiscernible with respect to their interaction with the electromagnetic field [4]. It follows that the system is invariant by TLS permutation. All the states with N_e excited TLS can thus be gathered in a degenerated ($\binom{N}{N_e}$ degeneracy) state, denoted by $|N_e\rangle$ and known as Dicke state [7, 46]. We denote by "S" the "operator" generating a $|N_e\rangle$ state from the simple product states

$$|N_e\rangle = S\{|\underbrace{e, e, ..., e}_{N_e}\ \underbrace{g, g, ..., g}_{N-N_e}>\} \tag{I.46}$$

The corresponding Hilbert subspace is represented in figure I.5. Its dimension is then N+1 instead of 2^N, at the cost of the so-called mean-field approximation.

Another approach to reduce the Hilbert space dimension is to truncate the level of correlations between the TLS [54] or to consider a limited number of excited TLS. For instance one may assume that the system is excited by one photon so that only one TLS can be excited. The Hilbert space is then limited to the lower part of the ladder (red area) represented in figure I.5. It corresponds to the weak excitation regime, also known as the single photon superradiance [55]. Appendix B shows that, during the experiment reported in chapter IV and V, the excitation power was weak enough to consider that the system was characterized in this weak excitation regime.

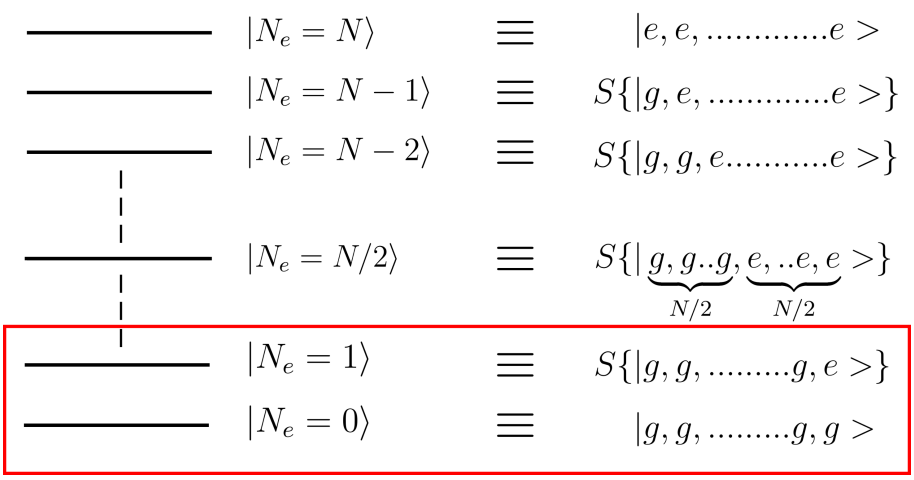

Figure I.5: Schematic representation of the N+1 symmetrical states introduced by R. Dicke [4]. Adapted from Ref. [7]. The red area corresponds to the Hilbert subspace considered in the weak excitation regime.

I.3 Near-field effect

As emphasized in the introduction, another key element of plasmonic superradiance is the plasmonic structure that is placed in the near-field of the emitters. In this section we identify the influence of a structured environment on the spontaneous emission and on the interaction between the emitters.

I.3.a Purcell effect

In a given environment, the decay rate of one TLS - with transition frequency ω_0 and transition dipole moment $\boldsymbol{\mu}$ - is given by Fermi's Golden Rule [43, 56] and can be approximated by [57]

$$\gamma_p = \frac{2\pi}{\hbar^2} \sum_f |\langle f| - \hat{\boldsymbol{\mu}} \cdot \hat{\mathbf{E}} |i\rangle|^2 \delta(\omega_0 - \omega_f) \tag{I.47}$$

where $\hat{\boldsymbol{\mu}}$ is the dipole moment operator defined in Eq. I.1. In the initial state $|i\rangle = |e\rangle \otimes |\emptyset\rangle$ the TLS is excited and no photon is in the electromagnetic modes of the environment. In the final state $|f\rangle = |g\rangle \otimes |1_{\omega_l}\rangle$ the TLS decayed to the ground state and one photon was emitted in one of the optical modes of the environment, denoted by l. Note that only the electric field modes that are resonant with the molecular transition contribute to the decay of the excited state population.

$\hat{\mathbf{E}}$ is the electric field operator at the TLS position $\mathbf{r_0}$. It is expressed in term of modes by [43]

$$\hat{\mathbf{E}} = \sum_l \left[\mathbf{E}_l \hat{a}_l + \mathbf{E}_l^* \hat{a}_l^\dagger\right] \tag{I.48}$$

where $\hat{a}_l^\dagger$ ($\hat{a}_l$) describes the creation (annihilation) of a photon in the mode l. $\mathbf{E}_l$ is then the complex amplitude of the field for the mode l at $\mathbf{r_0}$.

Assuming that the optical modes are orthogonal ($\left\langle 1_{\omega_l} \middle| 1_{\omega_j} \right\rangle = \delta_{lj}$), we introduce by $\rho_{\boldsymbol{\mu}}(\mathbf{r}_0, \omega_0)$ the local density of optical states (LDOS) provided by the environment at the position and frequency of the TLS, depending on the TLS orientation $\boldsymbol{\mu}$. The population decay rate is then given by [43, 58]

$$\gamma_p = \frac{\pi\omega_0}{3\hbar\epsilon_0}|\boldsymbol{\mu}|^2\rho_{\boldsymbol{\mu}}(\mathbf{r}_0, \omega_0) \tag{I.49}$$

As introduced by E. Purcell in 1946 [59], we notice in Eq. I.49 that the environment modifies the TLS deexcitation. This modification is usually estimated as compared to a reference medium γ_p^0. This reference is usually a homogeneous dielectric medium with refractive index $\sqrt{\epsilon_{host}}$, whose LDOS is $\rho_0 = \frac{\sqrt{\epsilon_{host}}\omega^2}{\pi^2 c^3}$. The Purcell factor is then defined as

$$F_P = \frac{\gamma_p}{\gamma_p^0} = \frac{\rho_{\boldsymbol{\mu}}(\mathbf{r}_0, \omega_0)}{\rho_0} \tag{I.50}$$

Notably in the absence of pure dephasing processes $\gamma^* = 0$ the classical decay rate is approximated by

$$\frac{\gamma_{cl}}{\gamma_{cl}^0} = F_P = \frac{\rho_{\boldsymbol{\mu}}(\mathbf{r}_0, \omega_0)}{\rho_0} \tag{I.51}$$

As a first experimental evidence of the Purcell effect, Drexhage *et al.* investigated in 1966 the influence of a planar silver surface on the spontaneous emission of europium (III) molecules [60]. We reproduce in figure I.6 the main experimental results (dots), that were successfully theoretically described (solid line) by Chance *et al.* in 1975 [61].

Figure I.6 shows an oscillation of the europium emission lifetime with the distance to the silver surface, tending to a stationary value far from the metal layer. These oscillations were qualitatively explained as the interaction between the dipole source and its image by the mirror, or as the interference between the light radiated by the dipole and its reflection on the mirror. As implied in these interpretation, the metal surface acts as a passive and polarizable interface. Therefore, as the dipole polarizes its environment, it induces electromagnetic modes which contribute to the LDOS $\rho_{\boldsymbol{\mu}}$.

In other words, the LDOS can be estimated from the field created by the dipole source $\boldsymbol{\mu}$ on itself $\mathbf{E}_{\boldsymbol{\mu}}(\mathbf{r}_0)$, due to the interaction with its environment. This induced field, at any

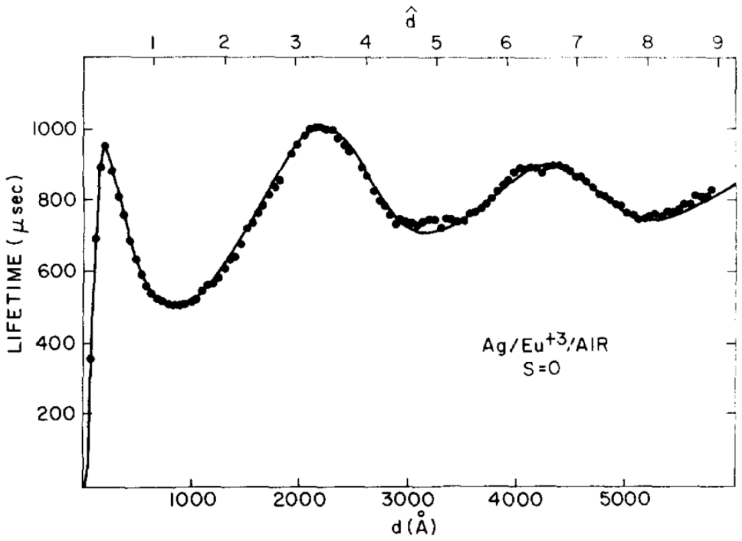

Figure I.6: Evolution of the fluorescence lifetime of Eu^{3+} complex with the distance d to a thick silver surface, measured (dots) by Drexhage et al. [60]. The solid curve represents the best fit to the data proposed by Chance et al. [61]. Reproduced from Ref. [61].

point $\mathbf{r}$, is elegantly described by the Green function $\overleftrightarrow{\mathbf{G}}$ [42]

$$\mathbf{E}_{\boldsymbol{\mu}}(\mathbf{r}) = \frac{\omega_0^2}{\epsilon_0 c^2} \overleftrightarrow{\mathbf{G}}(\mathbf{r}, \mathbf{r}_0, \omega_0) \cdot \boldsymbol{\mu} \tag{I.52}$$

Using the Green formalism, the LDOS is given by [43, 62]

$$\rho_{\boldsymbol{\mu}}(\mathbf{r}_0, \omega_0) = \frac{6\omega_0}{\pi c^2} \Big[\mathbf{e}_0 \cdot \mathrm{Im}\Big\{ \overleftrightarrow{\mathbf{G}}(\mathbf{r}_0, \mathbf{r}_0, \omega_0) \Big\} \cdot \mathbf{e}_0 \Big] \tag{I.53}$$

where $\mathbf{e}_0$ is the dipole orientation.

From a classical point of view, the power radiated by a dipole source $\boldsymbol{\mu}$ is [42]

$$P = \frac{\omega_0^3 |\boldsymbol{\mu}|^2}{2\epsilon_0 c^2} \Big[\mathbf{e}_0 \cdot \mathrm{Im}\Big\{ \overleftrightarrow{\mathbf{G}}(\mathbf{r}_0, \mathbf{r}_0, \omega_0) \Big\} \cdot \mathbf{e}_0 \Big] \tag{I.54}$$

Comparing Eqs. I.54 and I.53, we deduce that the Purcell factor can also be derived as the ratio between the power radiated by the dipole with the structured environment, P and without, P_0 [43]

$$F_P = \frac{\gamma_{cl}}{\gamma_{cl}^0} = \frac{P}{P_0} = \frac{\Big[\mathbf{e}_0 \cdot \mathrm{Im}\Big\{ \overleftrightarrow{\mathbf{G}}(\mathbf{r}_0, \mathbf{r}_0, \omega_0) \Big\} \cdot \mathbf{e}_0 \Big]}{\Big[\mathbf{e}_0 \cdot \mathrm{Im}\Big\{ \overleftrightarrow{\mathbf{G}_0}(\mathbf{r}_0, \mathbf{r}_0, \omega_0) \Big\} \cdot \mathbf{e}_0 \Big]} \tag{I.55}$$

where $\overleftrightarrow{\mathbf{G}_0}$ is the reference medium Green function. This relationship from Eq. I.55 is particularly convenient in Finite-Difference Time-Domain (FDTD) calculation as used in chapter

VI.

Finally, the sharp drop of the lifetime at small distance from the metal layer in Fig. I.6 was attributed to the efficient energy transfer to non-radiative modes in the metal. The transferred energy is then lost in heat dissipation since the metal is not a perfect conductor, it is the quenching effect [63]. As a result, only a part of the dipole energy will be radiated with the radiative decay rate γ_r while the remaining energy will decay through other processes with the non radiative decay rate γ_{nr}. We thus introduce the quantum yield η of the system {dipole+environment}

$$\eta = \frac{\gamma_r}{\gamma} = \frac{P_r}{P_r + P_{nr}} \tag{I.56}$$

where $\gamma = \gamma_r + \gamma_{nr}$ is the total decay rate, P_r is the radiated power and P_{nr} is the dissipated power.

In our work, the emitter environment consists in a metal nanometric particle (MNP). This object was found to be an optimal environment to enhance the spontaneous radiation of a dipole source [64, 65]. First, the metal conduction electrons can oscillate accordingly to the field radiated by the dipole, thus representing a strongly polarizable environment. Then, the nanometric dimension allows to efficiently couple out the dipole near-field to the far field. Finally, as a MNP introduces Ohmic losses, it shows broad resonance bands that allow for an efficient spectral overlapping with a fluorescent molecule at room temperature. If we consider it as a cavity with resonance frequency ω_r and bandwidth $\Delta\omega$, the quality factor $Q = \frac{\omega_r}{\Delta\omega}$ of a MNP is small, typically $Q \approx 10$. However it is compensated by a strong field confinement [66]. These features will be discussed in details in chapter II.

I.3.b Interaction enhancement

In this part, we discuss the effect of a structured environment on the interaction between two emitters placed in its vicinity. Such an investigation is usually carried out using the semi-classical approach for both weak [67, 68] and strong coupling regime [69, 70]. It consists in replacing the quantized field [71, 72], produced by a TLS, with an effective field expressed by the Green formalism [68, 73]. The fully quantum description was reported to be interesting in the strong coupling regime when the semi-classical approach shows chaotic behavior [74].

The expression of the field induced by a TLS source $\boldsymbol{\mu}_1$ on another TLS $\boldsymbol{\mu}_2$, via the environment is [42].

$$\mathbf{E}_{\boldsymbol{\mu}_1}(\mathbf{r}_2, \omega) = \frac{\omega^2}{\epsilon_0 c^2} \mathbf{e}_2 \cdot \overleftrightarrow{\mathbf{G}}(\mathbf{r}_2, \mathbf{r}_1, \omega) \cdot \boldsymbol{\mu}_1 \tag{I.57}$$

Therefore the coherent coupling constant between two TLS 1 and 2, with transition

frequency ω_0, is approximated [73] by

$$g_{21} = \frac{\omega_0^2}{\hbar\epsilon_0 c^2}\boldsymbol{\mu}_2^* \cdot \mathrm{Re}\Big\{\overleftrightarrow{\mathbf{G}}(\mathbf{r}_2, \mathbf{r}_1, \omega_0)\Big\} \cdot \boldsymbol{\mu}_1 \tag{I.58}$$

while the cross-damping rate is approximately

$$\gamma_{21} = 2\frac{\omega_0^2}{\hbar\epsilon_0 c^2}\boldsymbol{\mu}_2^* \cdot \mathrm{Im}\Big\{\overleftrightarrow{\mathbf{G}}(\mathbf{r}_2, \mathbf{r}_1, \omega_0)\Big\} \cdot \boldsymbol{\mu}_1 \tag{I.59}$$

Note that the coupling constants explicited in Eqs. I.36 and I.41 (in section I.2) were deduced from the free-space Green function.

Using this approach, the coupling, the superradiance and the entanglement of two TLS mediated by plasmonic waveguides were predicted [31,32,35]. The first experimental evidence of environment-mediated superradiance was reported by A. Goban *et al.* in 2015 [75]. In this pioneering work, the authors observed the collective emission of cesium atoms trapped near a photonic crystal waveguide. We reproduce from Ref. [75], in figure I.7, the schematic description of the experiment as well as the main results.

The structure is an "alligator" photonic crystal waveguide (APCW) supporting a TE-like guided mode [76], which is excited by the incidence field E_{in}. The reflection of a side-illumination (SI) beam forms an optical dipole trap to localize the atoms near the APCW (see the inset in Fig. I.7a). The inset of Fig. I.7a also shows the coupling rate of a single atom into the guided mode Γ_{1D} as a function of the atom position along the structure main axis. The peak value being $\Gamma_{1D}/\Gamma_0 = 1.1 \pm 0.1$ where Γ_0 is the free space decay rate. The number of trapped atoms $\overline{N}$ is adjusted by varying the trap hold time prior to measurement (red dots in Fig. I.7b) or by tailoring the atom density in the magneto-optical trap before their optical trapping near the APCW (blue dots in Fig. I.7b). We clearly see in figure I.7b that the total decay rate $\overline{\Gamma}_{tot}$ evolves linearly with the number of atoms $\overline{N}$, as an evidence of structure-mediated superradiance.

The experimental values in Fig. I.7b were fitted with a semi-classical model (solid line in Fig. I.7b). The superradiant decay rate evolves as $\overline{\Gamma}_{SR} = \eta \cdot \overline{N} \cdot \Gamma_{1D}$ with $\eta = 0.34 \pm 0.06$. The deviation from the ideal $\overline{N} \cdot \Gamma_{1D}$ slope was attributed to the random atom distribution near the photonic waveguide.

This work represents the first experimental evidence of a structure-mediated superradiance, based on a photonic mode. Concerning the plasmon-mediated superradiance, it was proposed to explain unexpectedly short decay times in silver aggregates [77] and quantum yield enhancement in quantum dots films [78]. However a clear and direct experimental

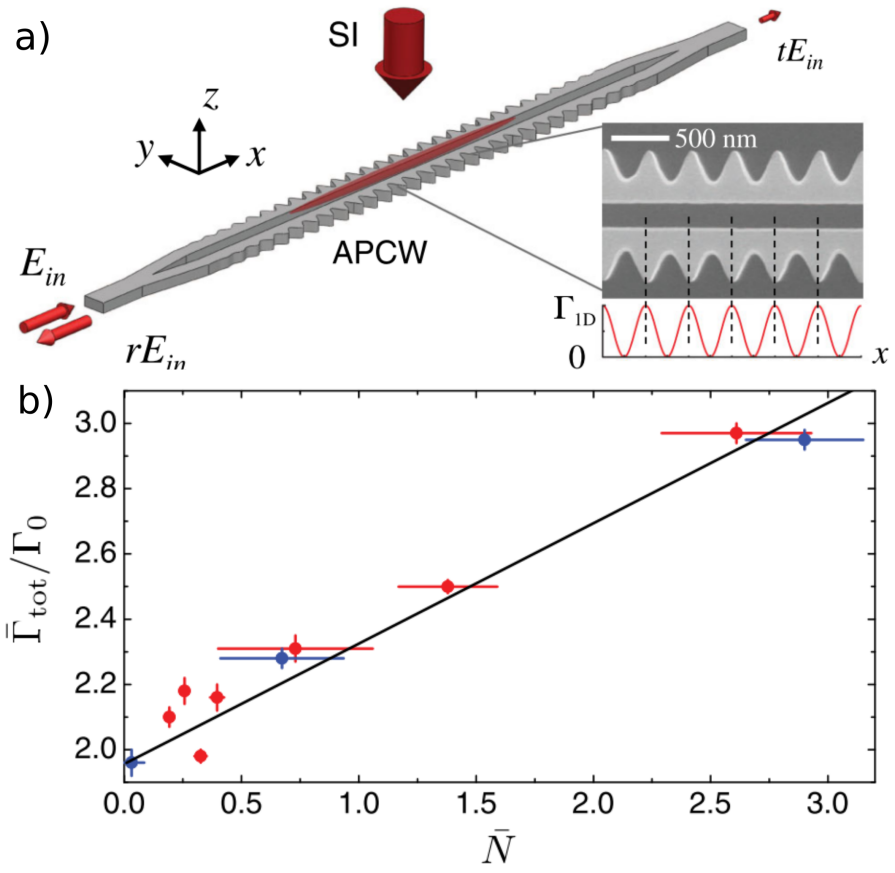

Figure I.7: a) A controlled number of cesium atoms (red shaded region) are optically trapped near an "alligator" photonic crystal waveguide (APCW). The inset shows a SEM image of the APCW and coupling rate of a single atom into the guided mode Γ_{1D}, along the x-axis at the center of the gap. The incident field E_{in} excites the TE-like mode supported by the structure. The side-illumination (SI) beam forms an optical trap near the APCW. b) Total decay rate $\overline{\Gamma}_{tot}$ normalized by the free space decay rate Γ_0 as a function of the mean number of trapped atoms $\overline{N}$. $\overline{N}$ is adjusted by changing the trap hold time (red dots) or the atom density (blue dots). The black line is a linear fit from a semi-classical model. Reproduced from [75].

demonstration of plasmon-mediated superradiance is still lacking. This is the aim of this work.

I.4 Conclusion

In this chapter we showed that superradiance is a longstanding topic of great interest. It consists in the collective spontaneous emission by a collection of TLS whose transition dipole moments are correlated. The cooperativity results from this correlation between emitters that builds up after the emission of the first photon. A characteristic feature of superradiance is the modification of the TLS emission rate. The quantum treatment of the TLS allows for a complete description of the superradiance phenomenon, but may require important computation resources for complex systems. To overcome this issue, it is usual to use a semi-classical model and to make further assumptions such as the weak excitation approximation. The semi-classical approach is convenient to account for the influence of the near-field environment, using the Green formalism. Finally, recent works revealed that the interaction between TLS can be enhanced by the photonic or plasmonic resonances supported by the environment. Therefore systems comprising many quantum objects coupled to an electromagnetic resonance represent a critical platform in modern nanophotonics, for the design of nanolasers [52] or to achieve long-range qubit entanglement for instance [21, 32].

Chapter II

Classical theory of plasmonic superradiance with a metal nanosphere

Contents

The mechanism of plasmon-mediated superradiance was first identified by V. Pustovit and T. Shahbazyan in 2009 [36]. They developed a classical approach to investigate the collective radiation of dipole sources distributed around a gold nanosphere [37]. In order to discuss the underlying mechanism, they focused on a fully symmetrical configuration: the dipoles were regularly distributed and oriented normally to the particle surface. However the position and orientation of the fluorescent molecules are not controlled experimentally, as it will be discussed in chapter IV. As a consequence we extended the model published by V. Pustovit and T. Shahbazyan to describe all the possible configurations; in close collaboration with the group of Philippe Lalanne in the LP2N (Bordeaux, France). In particular this model was developed to calculate the average response of an ensemble of plasmonic nanohybrids by averaging over many configurations as it is performed experimentally. Besides experimentally the distance between the emitters and the metal sphere is controlled by an intermediate silica shell. Hence our model also accounts for this dielectric layer surrounding the metal core.

This chapter aims at introducing this theoretical model. To depict the dipole-dipole coupling induced by the spherical metallo-dielectric nanohybrid, we describe the latter as an effective polarizability in section II.1. In particular we show how the nanohybrid dimensions and environment influence its optical properties. Then section II.2 explains how we put in equation the interaction between each dipole and the nanohybrid, as well as the interaction between the dipoles via the nanohybrid. Next section II.3 outlines how the radiation of a single dipole is modified by the presence of the nanohybrid. Finally the collective radiation of N dipoles distributed around the nanohybrid is discussed in section II.4. In particular it will be the opportunity to determine what is the optimal nanohybrid dimensions for the experimental observation of plasmonic superradiance.

II.1 Optical properties of a core-shell spherical nanohybrid

In the aim of describing the optical properties of a core-shell gold-silica nanohybrid, we first discuss the optical properties of a bare gold sphere in a homogenous host medium. In particular we need to estimate the local field induced by the particle, at the position of the molecules. We thus derive the particle polarizability.

II.1.a Theoretical description of a metal nanosphere

II.1.a.i Bulk dielectric permittivity of a noble metal

Noble metals such as gold are made of atoms which exhibit the same electronic structure: the orbital d is full and the orbital s has one electron. The electrons in the s orbitals are delocalized in the atomic crystal and form a conduction electron sea. An incident electromagnetic field at frequency ω induces an oscillation of the conduction electrons and thus a polarization. The collective oscillation of the electrons is called plasmon. The optical response of a bulk metal is then determined by the relation between the incident field and the resulting polarization. This is given by the dielectric permittivity ϵ whose expression in the case of a bulk metal is

$$\epsilon(\omega) = \epsilon^{(D)}(\omega) + \epsilon^{(IB)}(\omega) \tag{II.1}$$

The first term $\epsilon^{(D)}$ is related to the optical transition of the conduction electrons between the levels within the conduction band. This term is well described by the Drude model and is thus denoted by a D.

In practice the Drude model is only valid for frequencies below the allowed interband transition edge, in the visible range for gold. Indeed in the near UV region noble metals support interband transitions. The lowest energy transitions mainly occur between the d band of the valence bands and the unoccupied states in the conduction band, near the Fermi level [79]. The second term $\epsilon^{(IB)}$ in Eq. II.1 accounts for these interband transitions.

Contribution of the intraband transitions

The model introduced by Drude in 1900 [80] is based on the kinetic theory of gases. The dynamics of one electron with charge q, mass m, at position $\mathbf{r}$ and driven by the polarizing field $\mathbf{E}_{inc}(\mathbf{r}, t)$ at frequency ω, is described by the following equation of motion

$$\partial_t^2 \mathbf{r}(t) + \gamma_{bulk} \partial_t \mathbf{r}(t) = \frac{q}{m} \mathbf{E}_{inc}(\mathbf{r}, t) \tag{II.2}$$

where γ_{bulk} is the damping rate of the electron movement in the bulk material. It introduces, in a phenomenological way, the collision with other electrons (e-e), with phonons (e-ph) and with impurities (e-imp) in the structure [81]. Considering that these processes are independent, the damping rates are then simply added : $\gamma_{bulk} = \gamma_{e-e} + \gamma_{e-ph} + \gamma_{e-imp}$.

Furthermore, the Drude model considers that the N_e electrons are independent so that the macroscopic polarization $\mathbf{P}$ is

$$\mathbf{P} = N_e q \mathbf{r} = -\frac{\epsilon_0 \omega_p^2}{\omega^2 + i\gamma_{bulk}\omega} \mathbf{E}_{inc} \tag{II.3}$$

where $\omega_p = \sqrt{N_e q^2 / m\epsilon_0}$ is the plasma frequency.

Then, as $\mathbf{P} = \epsilon_0 \Big(\epsilon(\omega) - 1\Big)\mathbf{E}_{inc}$, we deduce the dielectric permittivity in the free electron model

$$\epsilon^{(D)}(\omega) = 1 - \frac{\omega_p^2}{\omega^2 + i\gamma_{bulk}\omega} \tag{II.4}$$

The Drude parameters are assumed to be independent from ω. They are usually obtained by fitting tabulated experimental data, from Ref. [82] for instance. Typically $\hbar\omega_p \approx 9.0\ eV$ and $\hbar\gamma_{bulk} \approx 70\ meV$ [83] for gold.

Contribution of the interband transitions

The interband transitions are described as bound-electrons. They are thus depicted as Lorentz resonances. The interband contribution $\epsilon^{(IB)}$ is then introduced as independent from the intraband contribution $\epsilon^{(D)}$, by adding a set of Lorentz resonances in the permittivity [83]. Therefore the Drude-Lorentz model is written as

$$\epsilon(\omega) = \epsilon^{(D)}(\omega) + \epsilon^{(IB)}(\omega) = \epsilon^{(D)}(\omega) + \sum_l \frac{f_l \omega_p^2}{\omega^2 - \omega_l^2 + i\gamma_l \omega} \tag{II.5}$$

where f_l, ω_l and γ_l are the oscillator strength, resonance frequency and damping rate of the Lorentz resonance l. These parameters are fitted from experimental data.

The model from Eq. II.5 allows to correctly describe the bulk optical properties of noble metals. However when no analytical expression is required, one may directly use tabulated experimental data. The most commonly used are from Refs. [82, 84]. In the here presented calculations, the metal permittivity is taken from P. Johnson and R. Christy experimental data [82].

II.1.a.ii Polarizability of a metal nanosphere

Now we consider a metal nanosphere (MNP) with diameter D and permittivity ϵ_P, embedded in a homogeneous host medium with permittivity ϵ_{host}. For simplicity we consider that a homogeneous field $\mathbf{E}_{inc}$, at frequency ω, illuminates the MNP so that the induced polarization $\mathbf{P}$ is uniform over the MNP volume. In the dipolar approximation, each volume element dV of the MNP then behaves as a dipole moment generating a field $d\mathbf{E}_{dep}$. As a result the polarized MNP generates a depolarization field $\mathbf{E}_{dep}$ which is the sum of all these dipolar contributions.

Accounting for the retardation effect, $\mathbf{E}_{dep}$ at the center of the MNP is expressed by [85]

$$\mathbf{E}_{dep} = \left(-1 + (\sqrt{\epsilon_{host}}\frac{\omega}{c}\frac{D}{2})^2 + i\frac{2}{3}(\sqrt{\epsilon_{host}}\frac{\omega}{c}\frac{D}{2})^3\right)\frac{\mathbf{P}}{3\epsilon_0\epsilon_{host}} \tag{II.6}$$

where the retarded dipole field has been expanded up to power ω^3. Note that the electrostatic case is then obtained from the the zero order term of Eq. II.6.

Then the polarization $\mathbf{P}$ is expressed by [42]

$$\mathbf{P} = \epsilon_0(\epsilon_P(\omega) - \epsilon_{host})(\mathbf{E}_{inc} + \mathbf{E}_{dep}) \tag{II.7}$$

and it is related to the induced dipole moment $\boldsymbol{\mu}_P$ of the MNP by

$$\boldsymbol{\mu}_P = \frac{4}{3}\pi(\frac{D}{2})^3\mathbf{P} = \epsilon_0\epsilon_{host}\alpha^P\mathbf{E}_{inc} \tag{II.8}$$

where we introduced the MNP polarizability α^P that relates the induced dipole moment and the incident field. α^P thus describes the optical response of the MNP

From Eqs. II.6, II.7 and II.8 we deduce the MNP polarizability in the dipolar approximation [86]

$$\alpha^P_{dip} = 4\pi(\frac{D}{2})^3\frac{\epsilon_P(\omega) - \epsilon_{host}}{\epsilon_P(\omega) + 2\epsilon_{host} - (\epsilon_P(\omega) - \epsilon_{host})(\sqrt{\epsilon_{host}}\frac{\omega}{c}\frac{D}{2})^2 - i\frac{2}{3}(\epsilon_P(\omega) - \epsilon_{host})(\sqrt{\epsilon_{host}}\frac{\omega}{c}\frac{D}{2})^3} \tag{II.9}$$

Even though this expression assumes a dipole response of the MNP, it gives reliable results for diameters smaller than 40 nm [86, 87]. For such a small size, the extinction of the transmitted power due to the MNP is approximated by [88]

$$P_{ext} = \frac{\omega}{2}\mathrm{Im}\{\alpha^P_{dip}\}|\mathbf{E}_{inc}|^2 \tag{II.10}$$

and the scattered power is approximately

$$P_{sca} = \frac{\omega k^3\sqrt{\epsilon_{host}}}{12\pi}|\alpha^P_{dip}|^2|\mathbf{E}_{inc}|^2 \tag{II.11}$$

Then according to energy conservation the absorbed power is [89]

$$P_{abs} = P_{ext} - P_{sca} = \frac{\omega}{2}\left[\mathrm{Im}\{\alpha^P_{dip}\} - \frac{k^3\sqrt{\epsilon_{host}}^3}{6\pi}|\alpha^P_{dip}|^2\right]|\mathbf{E}_{inc}|^2 \tag{II.12}$$

Note that the extinction power evolves as the volume D^3 of the MNP while the scattered power evolves as the squared volume D^6.

Let us now take a close look at Eq. II.9:

- the term in power ω^2 in the denominator is the dynamic depolarization term [87]. It describes the fact that the depolarization field locally decreases the incident field, resulting in a smaller particle polarization.
- the term in power ω^3 corresponds to the spontaneous emission of radiation by the induced dipole moment [90–92]. In other words this term introduces the scattering of light by the MNP.

For diameters small compared to the field wavelength λ: $D \ll \lambda$, the retardation effect can be neglected and one may assume that the MNP response is only due to the absorption of light $P_{ext} \approx P_{abs}$. It corresponds to the Rayleigh scattering limit and the polarizability becomes

$$\alpha^P = 4\pi(\frac{D}{2})^3 \frac{\epsilon_P(\omega) - \epsilon_{host}}{\epsilon_P(\omega) + 2\epsilon_{host}} \tag{II.13}$$

Considering that the real part of a noble metal permittivity $\epsilon_P(\omega)$ can reach negative values in the visible range, this simple expression shows that the polarizability exhibits a dipole resonance. This resonance consists in a coupled state between the incident photon and a plasmon; and is thus called a plasmon polariton. Then for a nanometric structure it is a localized surface plasmon polariton (LSPP) resonance.

In their model V. Pustovit and T. Shahbazyan [36] neglected the dynamic depolarization term, making the quasi-static approximation. The polarizability of the dipole LSPP resonance is then

$$\alpha^P = 4\pi(\frac{D}{2})^3 \frac{\epsilon_P(\omega) - \epsilon_{host}}{\epsilon_P(\omega) + 2\epsilon_{host} - i\frac{2}{3}(\epsilon_P(\omega) - \epsilon_{host})(\sqrt{\epsilon_{host}}\frac{\omega}{c}\frac{D}{2})^3} \tag{II.14}$$

II.1.a.iii Mie theory

In this work, we experimentally investigate MNP that can be approximated as spheres with 60 nm or 90 nm diameters, see chapter IV. The field wavelength is typically 500 nm so the phase of the incident field is not constant in the MNP volume and thus the quasi-static approximation does not stand.

At the beginning of the 20$^{\text{th}}$ century, G. Mie rigorously solved Maxwell equations to describe the interaction of light with a spherical particle comparable to the wavelength [93].

More precisely, the Mie theory consists in analytical solutions of the Helmholtz equation in spherical coordinates [88]. Considering the spherical symmetry, the electric and magnetic fields can be expressed by infinite sums over a basis of vectorial spherical harmonics. These vectorial harmonics consist in the product of spherical Bessel j_l or Hankel h_l functions for the radial dependency, and associated Legendre polynomials $cos(m\phi)P_l^m(cos\theta)$ and $sin(m\phi)P_l^m(cos\theta)$ for the angular dependency. For instance, the field scattered by a sphere, under illumination by a plane wave $\mathbf{E}_{inc} = E_0 e^{i\mathbf{k}\cdot\mathbf{r}}\mathbf{e}_{inc}$, is [88]

$$\mathbf{E}_s^P(\mathbf{r}) = \sum_{l=1}^{\infty}\sum_{m=0}^{l}\sum_{\sigma=0}^{1} i^l \frac{2l+1}{l(l+1)} E_0\Big(ia_l\frac{1}{k}\nabla\times\mathbf{M}_\sigma(\mathbf{r}) - b_l\mathbf{M}_\sigma(\mathbf{r})\Big) \tag{II.15}$$

where a_l and b_l are the scattering Mie coefficients and

$$\begin{aligned}\mathbf{M}_0(\mathbf{r}) &= \nabla\times\Big[\mathbf{r}cos(m\phi)P_l^m(\theta,\phi)h_l(kr)\Big]\\ \mathbf{M}_1(\mathbf{r}) &= \nabla\times\Big[\mathbf{r}sin(m\phi)P_l^m(\theta,\phi)h_l(kr)\Big]\end{aligned} \tag{II.16}$$

The mode expansion in Eq. II.15 reveals that the optical response of a sphere can be decomposed in poles, denoted by the index l. The first pole $l = 1$ dominates for $D < 30\ nm$ and corresponds to the dipole resonance. The contribution of other LSPP modes can not be neglected for the MNP size observed experimentally. We notice that the summation of three poles is usually sufficient for spheres with diameter smaller than 200 nm [94].

The quasi-static polarizability from Eq. II.14 can be derived using the Mie theory, by expanding the spherical functions for $l = 1$. V. Pustovit and T. Shahbazyan accounted for the higher order mode l by making a similar approximation [37]

$$\alpha_l^P(\omega) = \frac{\alpha_{l0}^P(\omega)}{1 - is_l\sqrt{\epsilon_{host}}^{2l+1}k^{2l+1}\alpha_{l0}^P(\omega)} \tag{II.17}$$

where

$$\alpha_{l0}^P(\omega) = \frac{\pi D^{2l+1}}{2^{2l-1}}\frac{\epsilon_P(\omega) - \epsilon_{host}}{\epsilon_P(\omega) + (1+\frac{1}{l})\epsilon_{host}} \tag{II.18}$$

and

$$s_l = \frac{l+1}{4\pi l(2l+1)[(2l-1)!!]^2} \tag{II.19}$$

In the here presented calculations, we consider the exact Mie solutions.

II.1.b Optical response of a metallo-dielectric nanohybrid

II.1.b.i Size effect

To discuss the advantage of introducing higher order ($l \geq 2$) modes, we compare in figure II.1 the scattering, absorption and extinction cross sections of a 10 nm diameter and a 150 nm diameter gold sphere, calculated from Mie theory. The MNP is embedded in a homogeneous host medium of refractive index $\sqrt{\epsilon_{host}} = 1.5$. It is illuminated by a plane wave propagating along the X-axis and polarized along the Z-axis, as represented in Fig. II.1c.

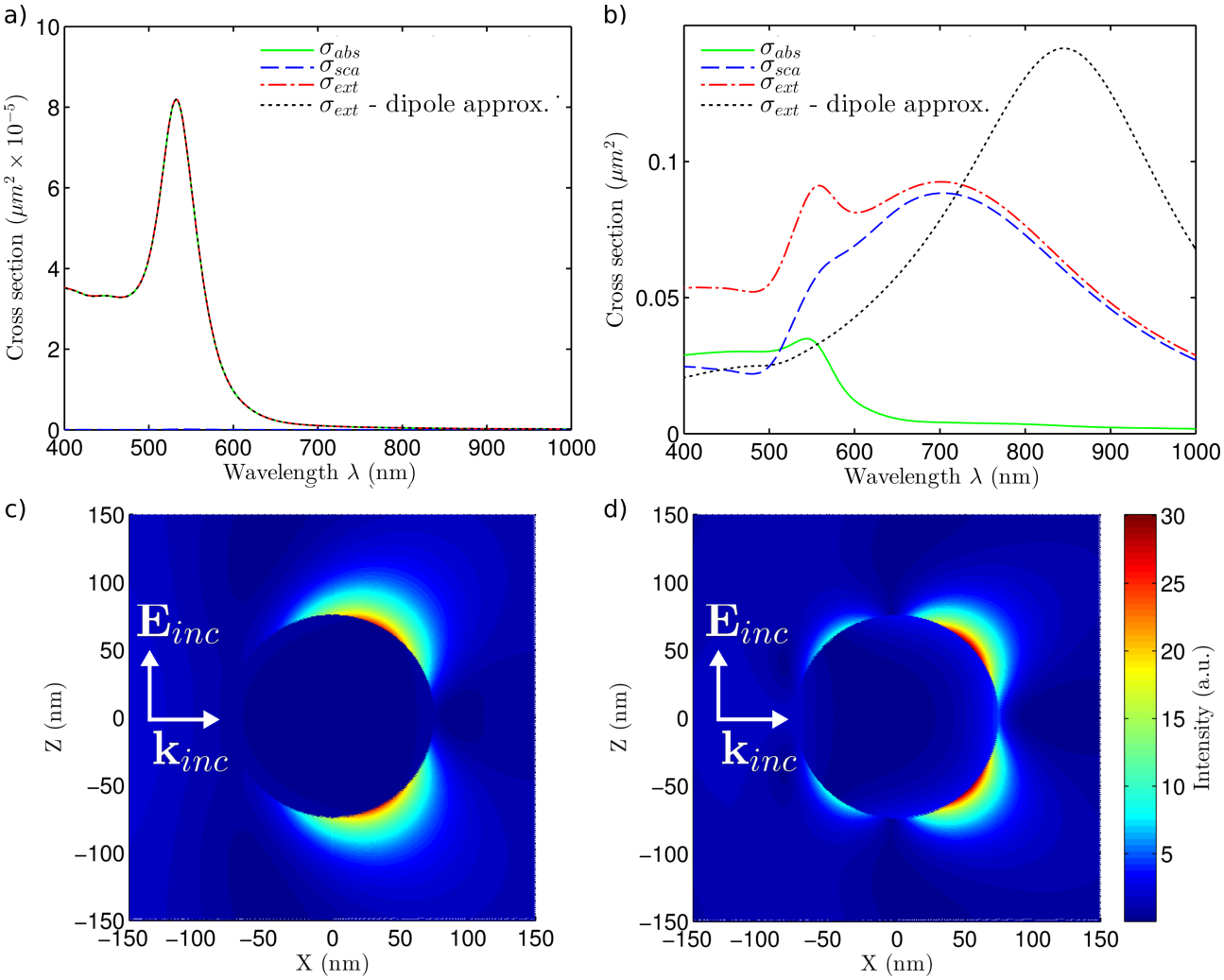

Figure II.1: Absorption (solid green line), scattering (dashed blue line) and extinction (dash-dotted red line) cross-sections, calculated from the Mie theory, of a) a 10 nm and b) a 150 nm diameter gold sphere, illuminated by a linearly polarized plane wave. Extinction cross sections derived from the dipolar approximation (Eq. II.9) are shown (dotted black line) for comparison. Electric field intensity distribution calculated for the illumination of a 150 nm diameter gold sphere by a plane wave ($\mathbf{E}_{inc}$,$\mathbf{k}_{inc}$), at c) $\lambda = 702$ nm and d) $\lambda = 558$ nm.

For the 10 nm diameter MNP, we observe in Fig. II.1a that the extinction is mainly due

to absorption and that it consists in one resonance ($\lambda_{l=1} = 533\ nm$): the dipole LSPP mode. Then, we see that the extinction cross section in the dipolar approximation (derived from Eqs. II.9 and II.10) nicely reproduces the result from the complete Mie theory, as expected since $\lambda \approx 50D$.

For the 150 nm diameter MNP we observe two peaks in the cross sections in Fig. II.1b. We show in Fig. II.1c the electric field intensity map corresponding to the broad peak on the long wavelength side ($\lambda_{l=1} = 702\ nm$). It exhibits two poles, revealing the excitation of the dipole LSPP mode. Comparing Fig. II.1a and Fig. II.1b, we clearly see that increasing the particle size causes a broadening and a shift of the dipole LSPP mode to longer wavelength as well as an increase of the extinction cross section amplitude. As opposed to the 10 nm diameter MNP, $\lambda \approx 3D$ for the 150 diameter MNP. Accordingly the dipolar approximation does not stand in Fig. II.1b, even though the radiative and the depolarization terms in Eq. II.9 introduce a shift, a broadening and an increase of the dipole LSPP resonance as the MNP size is increased.

To go further, we express the dipole mode $l = 1$ from the Mie theory. Approximating the relative magnetic permeability of the MNP and the surrounding by one, the associated Mie coefficient is expressed as [88]

$$T_{E1} = \frac{j_1(\rho_D)\sigma_1 - [\rho_D j_1(\rho_D)]'\nu_1}{h_1(\rho_D)\sigma_1 - [\rho_D h_1(\rho_D)]'\nu_1} \tag{II.20}$$

where $\rho_i = \sqrt{\epsilon_i}kD/2$, the prime denotes differentiation with respect to ρ_i and

$$\begin{aligned} \sigma_1 &= \epsilon_{host}[\rho_P j_1(\rho_P)]' \\ \mu_1 &= \epsilon_P(\omega) j_1(\rho_1) \end{aligned} \tag{II.21}$$

Expanding the spherical functions to the first three orders, we deduce the following polarizability as a good approximation for the diameters of interest [86]

$$\begin{aligned} \alpha^P_{Mie} &= -i\frac{3}{2k^3\sqrt{\epsilon_{host}}^3}T_{E1} \\ &= \frac{\pi D^3}{2}\frac{\epsilon_P(\omega) - \epsilon_{host}}{\epsilon_P(\omega) + 2\epsilon_{host} - \frac{3}{5}(\epsilon_P(\omega) - 2\epsilon_{host})(\sqrt{\epsilon_{host}}\frac{\omega}{c}\frac{D}{2})^2 - i\frac{2}{3}(\epsilon_P(\omega) - \epsilon_{host})(\sqrt{\epsilon_{host}}\frac{\omega}{c}\frac{D}{2})^3} \end{aligned} \tag{II.22}$$

Comparing Eq. II.22 and Eq. II.9 we observe that the radiative term is similar while the dynamic depolarization term is overestimated in Eq. II.9. In the following we will use the polarizability from Eq. II.22 to describe the dipole LSPP mode.

Next, a second peak is observed in figure II.1b, at shorter wavelength ($\lambda_{l=2} = 558\ nm$), i.e. higher frequency. Figure II.1d illustrates this resonance and shows four poles at the surface of the particle. This intensity distribution corresponds to a LSPP quadrupole resonance that is not modeled in the dipolar approximation. We note that the poles at $\lambda_{l=1}$ (Fig. II.1c) are more spatially extended than the poles at $\lambda_{l=2}$ (Fig. II.1d). Actually, as the mode order increases, the corresponding field is more confined at the surface. Therefore the dipole LSPP mode is the most efficiently coupled to the external fields. For $D < 50\ nm$, the coupling of the higher order modes ($l \geq 2$) to external radiative modes is usually neglected, so that the dipole mode is the only mode radiating in far field [95]. Accordingly, figure II.1b shows that for $D = 150\ nm$, the dipole LSPP mode is mainly due to scattering, confirming the efficient coupling to the far field. Whereas the absorption clearly contributes to the quadrupole resonance, showing non negligible Ohmic losses in the metal. This may be attributed to a better field confinement at the surface of the particle, as well as a larger imaginary part of the dielectric function at higher frequencies [82].

II.1.b.ii Environment effect

The approximated expression of the LSPP modes in Eq. II.17 shows that their resonance frequencies depend on the host medium permittivity ϵ_{host}. This remarkable property is widely used to perform high sensitivity biological and chemical sensing [96]. In the Rayleigh limit, see Eq. II.13, the dipole LSPP position is simply given by the Fröhlich condition [97]

$$-\mathrm{Re}\{\epsilon_P(\omega)\} = 2\epsilon_{host} \tag{II.23}$$

Even though the quasi-static approximation is not valid for our samples, the Fröhlich condition already describes the main features due to the host medium permittivity. For usual noble metals, such as gold and silver, $-\mathrm{Re}\{\epsilon_P\}$ increases with increasing wavelength nearby the dipole resonance. Therefore an increase in ϵ_{host} leads the dipole LSPP peak to shift to longer wavelengths. Besides the resonance linewidth is determined by $\mathrm{Im}\{\epsilon_P\}$ which also increases with increasing wavelength so the LSPP resonance broadens as ϵ_{host} increases.

Using the Mie solution expressed in Eq. II.22, the position of the dipole LSPP resonance is approximately given by the condition [86]

$$\mathrm{Re}\{\epsilon_P(\omega)\} = -2\epsilon_{host} - \frac{24\epsilon_{host} + \mathrm{Im}\{\epsilon_P(\omega)\}^2}{40} k^2 D^2 \epsilon_{host} - \frac{\mathrm{Im}\{\epsilon_P(\omega)\}}{12} k^3 D^3 \sqrt{\epsilon_{host}}^3 - \frac{3}{56} k^4 D^4 \epsilon_{host}^2 \tag{II.24}$$

We show in figure II.2a the evolution of the dipole LSPP position with the host refractive

index for a 60 *nm* diameter gold sphere. We observe that the dipole resonance wavelength

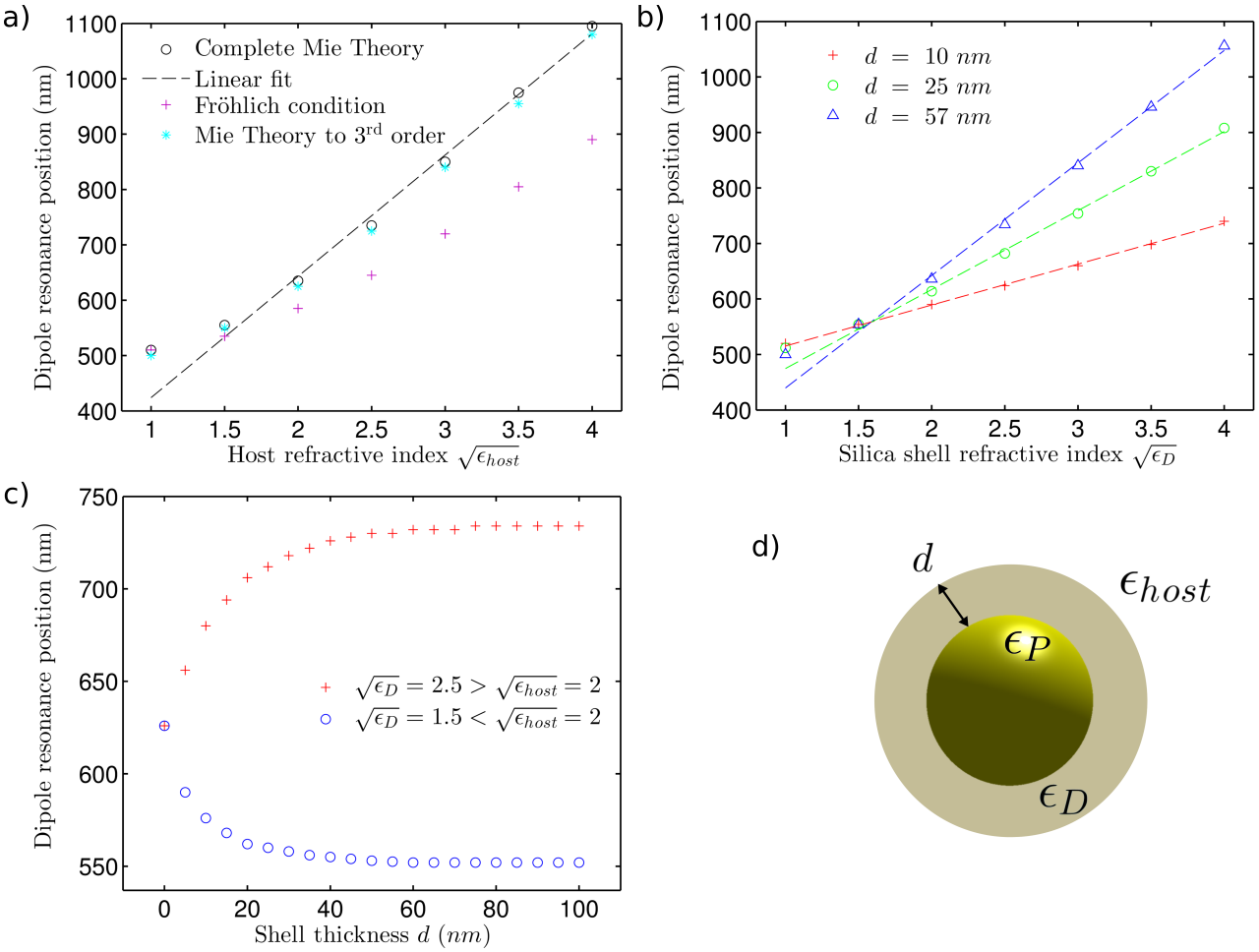

Figure II.2: A spherical nanohybrid is embedded in a homogeneous host medium with permittivity ϵ_{host}, as represented in d). The system is illuminated by a linearly polarized plane wave. The dipole LSPP resonance wavelength is deduced from the extinction cross section calculated using the complete Mie theory. a) Evolution of the dipole LSPP wavelength for a 60 nm diameter gold sphere as a function of the host medium refractive index $\sqrt{\epsilon_{host}}$. We show results from the complete Mie theory (black circles), fitted with a line (dashed black line) (as a guide for the eyes), compared to the Fröhlich condition from Eq. II.23 (magenta pluses) and the dipole Mie eigenmode approximated to the third order from Eq. II.24 (cyan asterisks). The 60 nm diameter gold sphere is then coated with a shell of thickness d and permittivity ϵ_D, as represented in d). The nanohybrid is embedded in a host medium with refractive index $\sqrt{\epsilon_{host}} = 1.5$. b) Evolution of the dipole resonance wavelength for d = 10 nm (red pluses), d = 25 nm (green circles) and d = 57 nm (blue triangles) as a function of the shell refractive index $\sqrt{\epsilon_D}$. Dashed lines are linear fits as a guide for the eyes. c) Evolution of the dipole resonance wavelength for $\sqrt{\epsilon_D} = 2.5$ (red pluses) or $\sqrt{\epsilon_D} = 1.5$ (blue circles) as a function of the shell thickness d. The nanohybrid is embedded in a host medium with refractive index $\sqrt{\epsilon_{host}} = 2$.

evolves roughly linearly with the host refractive index $\sqrt{\epsilon_{host}}$, in agreement with the experimental observations reported in Ref. [98]. Then, as expected, the resonance condition from Eq. II.24 gives a good approximation as compared to the Fröhlich condition from Eq. II.23.

Experimentally the gold nanosphere is coated by a silica shell, with permittivity ϵ_D, whose thickness d varies between 10 and 60 nm, as represented in Fig. II.2d. If the shell and the

host medium have different permittivities, the shell results in a modification of the effective permittivity of the MNP environment. An extension of the Fröhlich condition to the coated case is [88]

$$\epsilon_P(\omega) = -2\epsilon_D\left[\frac{\epsilon_D(1-f)+\epsilon_{host}(2-f)}{\epsilon_D(1+2f)+2\epsilon_{host}(1-f)}\right] \tag{II.25}$$

where f is the fraction of the particle volume occupied by the gold core. This expression shows that both the shell thickness and permittivity influence the LSPP position and linewidth. However it does not allow an immediate reading of the main features. A more intuitive description is the effective permittivity picture: depending on the shell thickness, the environment permittivity varies continuously between ϵ_{host} ($d = 0$) and ϵ_D ($d = \infty$).

Figure II.2b shows the evolution of the dipole LSPP resonance position, for a 60 nm diameter gold nanosphere, as a function of the shell refractive index $\sqrt{\epsilon_D}$, for three different shell thicknesses. These results are determined using the complete Mie theory with $1 \leq l \leq 3$. However they can be approximated from Eq. II.20 since the σ_1 and μ_1 coefficients admit analytical expressions in the coated-sphere case [99].

We observe in Fig. II.2b that for all thicknesses, the dipole resonance wavelength evolves roughly linearly with the shell refractive index. An increase of the shell refractive index thus results in an increase of the effective permittivity seen by the particle. Then note that the effect is greater as the shell is thicker. It confirms that a thicker shell implies a larger modification of the effective permittivity. This is in accordance with the experimental observations reported in Ref. [100].

To go further, the evolution of the dipole resonance wavelength with the shell thickness is represented in figure II.2c. We distinguish two cases : $\sqrt{\epsilon_D} = 2.5 > \sqrt{\epsilon_{host}} = 2$ and $\sqrt{\epsilon_D} = 1.5 < \sqrt{\epsilon_{host}} = 2$. We observe that if $\epsilon_D > \epsilon_{host}$ then an increase of the shell thickness increases the effective permittivity and leads to a shift to longer wavelengths. While if $\epsilon_D < \epsilon_{host}$ then the dipole resonance shifts to shorter wavelengths. For shell thicknesses above the core radius (30 nm in Fig. II.2c), the resonance shift saturates because the plasmon oscillations are no longer sensitive to the hosting medium, as reported in Ref. [101].

II.2 Classical model of emitter-nanohybrid interaction

The main system investigated during this work consists in the radiation of N identical dipole sources close to a metallo-dielectric nanohybrid. This system was theoretically investigated by V. Pustovit and T. Shahbazyan for a silver and a gold nanosphere without shell [36, 37]. In this section we introduce the formalism employed by V. Pustovit and T. Shahbazyan,

which is also used in our classical model. We consider molecular dipole sources so the dipole $\boldsymbol{\mu}_l = \mu_l \mathbf{e}_l$ can oscillate only in the direction of its orientation $\mathbf{e}_l$. In the presence of a driving field $\mathbf{E}_d$ at frequency ω, the equation of motion of of the dipole l is then [43]

$$\partial_t^2 \mu_l(t) + \gamma_l \partial_t \mu_l(t) + \omega_l^2 \mu_l(t) = \frac{q^2}{m} \mathbf{E}_d(\mathbf{r}_l, t) \cdot \mathbf{e}_l \tag{II.26}$$

where ω_l and $\mathbf{r}_l$ are the dipole resonance frequency and position. The damping rate γ_l is a classical decay rate as introduced by γ_{cl} in section I.1.c. Using a scattered-field formulation, the driving field $\mathbf{E}_d$ is written as a sum of the background incident field $\mathbf{E}_{inc}$ and the field $\mathbf{E}_{inc}^s$ scattered by the environment under illumination: $\mathbf{E}_d(\mathbf{r}, t) = \mathbf{E}_{inc}(\mathbf{r}, t) + \mathbf{E}_{inc}^s(\mathbf{r}, t)$.

To solve Eq. II.26, it is convenient to work in the Fourier domain and we adopt the $exp(-i\omega t)$ convention so that Eq. II.26 becomes

$$\mu_l(\omega) = -\frac{q^2/m}{\omega^2 - \omega_l^2 + i\gamma_l \omega} \mathbf{E}_d(\mathbf{r}_l, \omega) \cdot \mathbf{e}_l \tag{II.27}$$

We deduce the dipole polarizability α_l as the relation between the driving field and the induced dipole moment, such that $\mu_l(\omega) = \alpha_l(\omega) \mathbf{E}_d(\mathbf{r}_l, \omega) \cdot \mathbf{e}_l$.

$$\alpha_l(\omega) = -\frac{6\pi\epsilon_0 \gamma_l^0 c^3}{\sqrt{\epsilon_{host}}\omega_l^2} \frac{1}{\omega^2 - \omega_l^2 + i\gamma_l \omega} \tag{II.28}$$

where we introduced the decay rate γ_l^0 of the emitter l in the reference medium: a homogeneous medium with refractive index $\sqrt{\epsilon_{host}}$, see Eq. I.21 in chapter I. Since the dipoles are described by a polarizability, their radiation is depicted as a scattering of the driving field. Therefore both the dipoles and the nanohybrid are scatterers in this formalism.

To go further, one usually considers excitation close to the dipole frequency $(\omega - \omega_l)/\omega_l \ll 1$, so that

$$\alpha_l(\omega) = -\frac{3\pi\epsilon_0 \gamma_l^0 c^3}{\sqrt{\epsilon_{host}}\omega_l^3} \frac{1}{\omega - \omega_l + i\frac{\gamma_l}{2}} = -\frac{|\boldsymbol{\mu}_l^0|^2}{\hbar} \frac{1}{\omega - \widetilde{\Omega}_l} \tag{II.29}$$

where $\widetilde{\Omega}_l = \omega_l - i\frac{\gamma_l}{2}$ is the dipole complex transition frequency. We introduced in Eq. II.29 the transition dipole moment in the reference medium $|\boldsymbol{\mu}_l^0|$

$$|\boldsymbol{\mu}_l^0| = \sqrt{\frac{3\pi\epsilon_0 \gamma_l^0 \hbar c^3}{\sqrt{\epsilon_{host}}\omega_l^3}} \tag{II.30}$$

According to Maxwell's equation, the electron movement results in a dipole current that

feeds back to the electric field [42]

$$\boldsymbol{\nabla} \times \boldsymbol{\nabla} \times \mathbf{E}(\mathbf{r},\omega) - \epsilon(\mathbf{r})\epsilon_0 \frac{\omega^2}{c^2}\mathbf{E}(\mathbf{r},\omega) = -\frac{\omega^2}{\epsilon_0 c^2}\sum_{l=1}^{N} \mu_l(\omega)\delta(\mathbf{r}-\mathbf{r}_l)\mathbf{e}_l \tag{II.31}$$

where $\epsilon(\mathbf{r})$ is the relative permittivity of the material at location $\mathbf{r}$. We assume in Eq. II.31 that the relative magnetic permeability of the environment is close to unity at optical frequencies, since gold and silver show weak diamagnetism [102].

A solution of the inhomogeneous equation from Eq. II.31 can be elegantly written in the Green formalism, where we define the Green dyadic $\overleftrightarrow{\mathbf{G}}$ such that [43]

$$\boldsymbol{\nabla} \times \boldsymbol{\nabla} \times \overleftrightarrow{\mathbf{G}}(\mathbf{r},\mathbf{r}',\omega) - \epsilon(\mathbf{r})\epsilon_0 \frac{\omega^2}{c^2}\overleftrightarrow{\mathbf{G}}(\mathbf{r},\mathbf{r}',\omega) = \overleftrightarrow{\mathbf{I}}\,\delta(\mathbf{r}-\mathbf{r}') \tag{II.32}$$

In our typical system, $\overleftrightarrow{\mathbf{G}}$ can be split into two parts: $\overleftrightarrow{\mathbf{G}} = \overleftrightarrow{\mathbf{G}}_0 + \overleftrightarrow{\Delta\mathbf{G}}$. Where $\overleftrightarrow{\mathbf{G}}_0$ is the free space Green dyadic which describes the system in a homogeneous and isotropic host medium. $\overleftrightarrow{\Delta\mathbf{G}}$ accounts for the modifications of the Green dyadic due to the presence of the nanohybrid.

Equations II.26 and II.31 form a closed system coupling the dipoles $\boldsymbol{\mu}_l$ with the electric field at the dipoles positions $\mathbf{E}(\mathbf{r}_l)$. Using the Green formalism, this coupled system can be written as

$$\mu_l(\omega) = \alpha_l(\omega)\mathbf{e}_l \cdot \Big\{\mathbf{E}_d(\mathbf{r}_l,\omega) + \frac{\omega^2}{\epsilon_0 c^2}\overleftrightarrow{\Delta\mathbf{G}}(\mathbf{r}_l,\mathbf{r}_l,\omega)\cdot\boldsymbol{\mu}_l + \frac{\omega^2}{\epsilon_0 c^2}\sum_{j\neq l}\overleftrightarrow{\mathbf{G}}(\mathbf{r}_l,\mathbf{r}_j,\omega)\cdot\boldsymbol{\mu}_j\Big\} \tag{II.33}$$

where the first term is the driving field at the position of the dipole l. The second term describes the field radiated by the dipole l and scattered back to the dipole l by the nanohybrid, it corresponds to the Purcell effect. The last term accounts for the field radiated by the other dipoles j on the dipole l, directly (free space) and after scattering by the nanohybrid.

Separating the direct and the nanohybrid contributions, Eq. II.33 becomes

$$\mu_l(\omega) = \alpha_l(\omega)\mathbf{e}_l \cdot \Big\{\mathbf{E}_d(\mathbf{r}_l,\omega) + \frac{\omega^2}{\epsilon_0 c^2}\sum_{j\neq l}\overleftrightarrow{\mathbf{G}}_0(\mathbf{r}_l,\mathbf{r}_j,\omega)\cdot\boldsymbol{\mu}_j + \frac{\omega^2}{\epsilon_0 c^2}\sum_{j=1}^{N}\overleftrightarrow{\Delta\mathbf{G}}(\mathbf{r}_l,\mathbf{r}_j,\omega)\cdot\boldsymbol{\mu}_j\Big\} \tag{II.34}$$

Finally, solving Eq. II.34 gives access to the excitation and radiation properties of each dipole in the system. This approach thus allows to study the collective emission in the presence of the plasmonic nanohybrid.

II.3 Single dipole radiation close to a metallo-dielectric nanosphere

Here we investigate the radiation of a single dipole close to a core-shell gold-silica spherical nanohybrid. As discussed in chapter I and commonly admitted since the work of E. Purcell [59], the decay rate of a dipole source is not intrinsic. It is modified as the near-field environment provides new relaxation channels for the dipole. Hence the nanohybrid leads to an enhancement of the radiated power and to non-radiative losses as heat dissipation in the metal. These features have been extensively investigated in the case of a single dipole coupled to a nanosphere [67, 92, 95, 103–117].

Let us consider a single dipole $\boldsymbol{\mu} = \mu \mathbf{e}_0$, with resonance frequency ω_0 and decay rate $\gamma^0 = \gamma_r^0 + \gamma_{nr}^0$ in a homogeneous reference medium. This dipole is placed at $\mathbf{r}_0$ close to a nanohybrid. Eq. II.34 is then

$$\mu = \alpha(\omega)\mathbf{e}_0 \cdot \left\{ \mathbf{E}_d(\mathbf{r}_0, \omega) + \mu \frac{\omega^2}{\epsilon_0 c^2} \overleftrightarrow{\Delta \mathbf{G}}(\mathbf{r}_0, \mathbf{r}_0, \omega) \cdot \mathbf{e}_0 \right\} \tag{II.35}$$

Solving for μ, we obtain

$$\mu = \left\{ 1 - \alpha(\omega) \frac{\omega^2}{\epsilon_0 c^2} \mathbf{e}_0 \cdot \overleftrightarrow{\Delta \mathbf{G}}(\mathbf{r}_0, \mathbf{r}_0, \omega) \cdot \mathbf{e}_0 \right\}^{-1} \alpha(\omega) \mathbf{E}_d(\mathbf{r}_0, \omega) \cdot \mathbf{e}_0 \tag{II.36}$$

We then deduce an effective polarizability so that $\mu = \alpha_{\text{eff}}(\omega)\mathbf{E}_d(\mathbf{r}_0, \omega) \cdot \mathbf{e}_0$

$$\alpha_{\text{eff}}(\omega) = -\frac{|\boldsymbol{\mu}_0|^2}{\hbar} \frac{1}{\omega - (\omega_0 + \Delta) + i\frac{\gamma}{2}} \tag{II.37}$$

where

$$\begin{aligned} \Delta &= -\frac{|\boldsymbol{\mu}_0|^2 \omega^2}{\hbar \epsilon_0 c^2} \text{Re}\{\mathbf{e}_0 \cdot \overleftrightarrow{\Delta \mathbf{G}}(\mathbf{r}_0, \mathbf{r}_0, \omega) \cdot \mathbf{e}_0\} \\ \gamma &= \gamma^0 + 2\frac{|\boldsymbol{\mu}_0|^2 \omega^2}{\hbar \epsilon_0 c^2} \text{Im}\{\mathbf{e}_0 \cdot \overleftrightarrow{\Delta \mathbf{G}}(\mathbf{r}_0, \mathbf{r}_0, \omega) \cdot \mathbf{e}_0\} \end{aligned} \tag{II.38}$$

Hence the dipole response has a new complex eigenfrequency in the presence of the nanohybrid $\tilde{\omega} = \omega_0 + \Delta - i\frac{\gamma}{2}$. We clearly see in Eq. II.38 that the resonance frequency is shifted by the real part of the Green function, while the linewidth is modified by the imaginary part. The dipole total decay rate in the presence of the nanosphere is then [92]

$$\frac{\gamma}{\gamma^0} = 1 + \frac{6\pi c}{\omega_0} \Big[\mathbf{e}_0 \cdot \text{Im}\Big\{ \overleftrightarrow{\Delta \mathbf{G}}(\mathbf{r}_0, \mathbf{r}_0, \omega_0) \Big\} \cdot \mathbf{e}_0 \Big] \tag{II.39}$$

Note that this expression can be directly deduced from the definitions in Eqs. I.49, I.53 and II.30. The advantage of considering a spherical resonator is that its optical response is fully described by the Mie theory [88, 93] so that $\overleftrightarrow{\Delta \mathbf{G}}(\mathbf{r}_0, \mathbf{r}_0, \omega_0)$ is rigorously known.

The decay rate enhancement would lead to a different application depending whether the radiative or non radiative relaxation is boosted. Indeed, a nanoantenna would enhance the radiated signal [65, 118]. On the contrary a nanolaser based on the stimulated emission of surface plasmon requires the emitters to generate plasmon oscillations [27]. It is then interesting to enhance the transfer of energy to the non-radiative modes of the plasmonic core.

One thus need to distinguish the radiative γ_r and the non radiative decay rates γ_{nr}. In the following, γ_{nr} is deduced from the absorbed power

$$\gamma_{nr} = \frac{\gamma_r^0}{P_0}\Big(\frac{1-\eta_0}{\eta_0} P_0 + P_{abs}^P\Big) \tag{II.40}$$

where η_0 is the dipole quantum yield and P_0 is the power emitted by the dipole in the reference medium, given by Eq. I.17 in chapter I. The first term in Eq. II.40 accounts for the dipole internal non-radiative relaxation, e.g. internal conversion. Then P_{abs}^P is the power absorbed by the MNP, which is described as a polarizability α_{Mie}^P from Eq. II.22. Using Eq. II.12, the power absorbed by the MNP is then deduced from the field emitted by the dipole at the particle position $\mathbf{E}_{\boldsymbol{\mu}}(\mathbf{r}_P)$

$$\begin{aligned} P_{abs}^P &= \frac{\omega}{2}\Big[\mathrm{Im}\{\alpha_{Mie}^P\} - \frac{k^3\sqrt{\epsilon_{host}}^3}{6\pi}|\alpha_{Mie}^P|^2\Big]|\mathbf{E}_{\boldsymbol{\mu}}(\mathbf{r}_P)|^2 \\ &= \frac{\omega^3}{2\epsilon_0 c^2}\Big[\mathrm{Im}\{\alpha_{Mie}^P\} - \frac{k^3\sqrt{\epsilon_{host}}^3}{6\pi}|\alpha_{Mie}^P|^2\Big]|\overleftrightarrow{\mathbf{G}}(\mathbf{r}_P, \mathbf{r}_0, \omega)\cdot\boldsymbol{\mu}|^2 \end{aligned} \tag{II.41}$$

Finally γ_r is simply

$$\gamma_r = \gamma - \gamma_{nr} \tag{II.42}$$

II.3.a Influence of the nanohybrid dimensions and the emitter orientation

We first investigate the influence of the system geometry on the interaction between the emitter and the nanosphere, and thus on the resulting optical properties. We take the parameters from the experiment reported in chapters IV and V: the plasmonic core is a gold nanosphere and the distance between the emitter and the core surface d is set by a spherical silica shell $\sqrt{\epsilon_{SiO_2}} = 1.48$ [119] that acts as a spacer. The system is embedded in a polymer

matrix with refractive index $\sqrt{\epsilon_{host}} = 1.5$. The reference medium is the hosting medium without nanohybrid. The emitter quantum yield in the reference medium is $\eta_0 = 90\%$ and its resonance wavelength is $\lambda_0 = 553\ nm$, which matches the dipole LSPP resonance observed in Fig. II.1.

Figure II.3 shows the evolution of the radiative and non-radiative decay rates as a function of both the plasmonic core diameter D and the shell thickness d. We show results for normal and tangential orientations of the dipole with respect to the particle surface. All the decay rates are normalized by the dipole radiative decay rate in the reference medium γ_r^0.

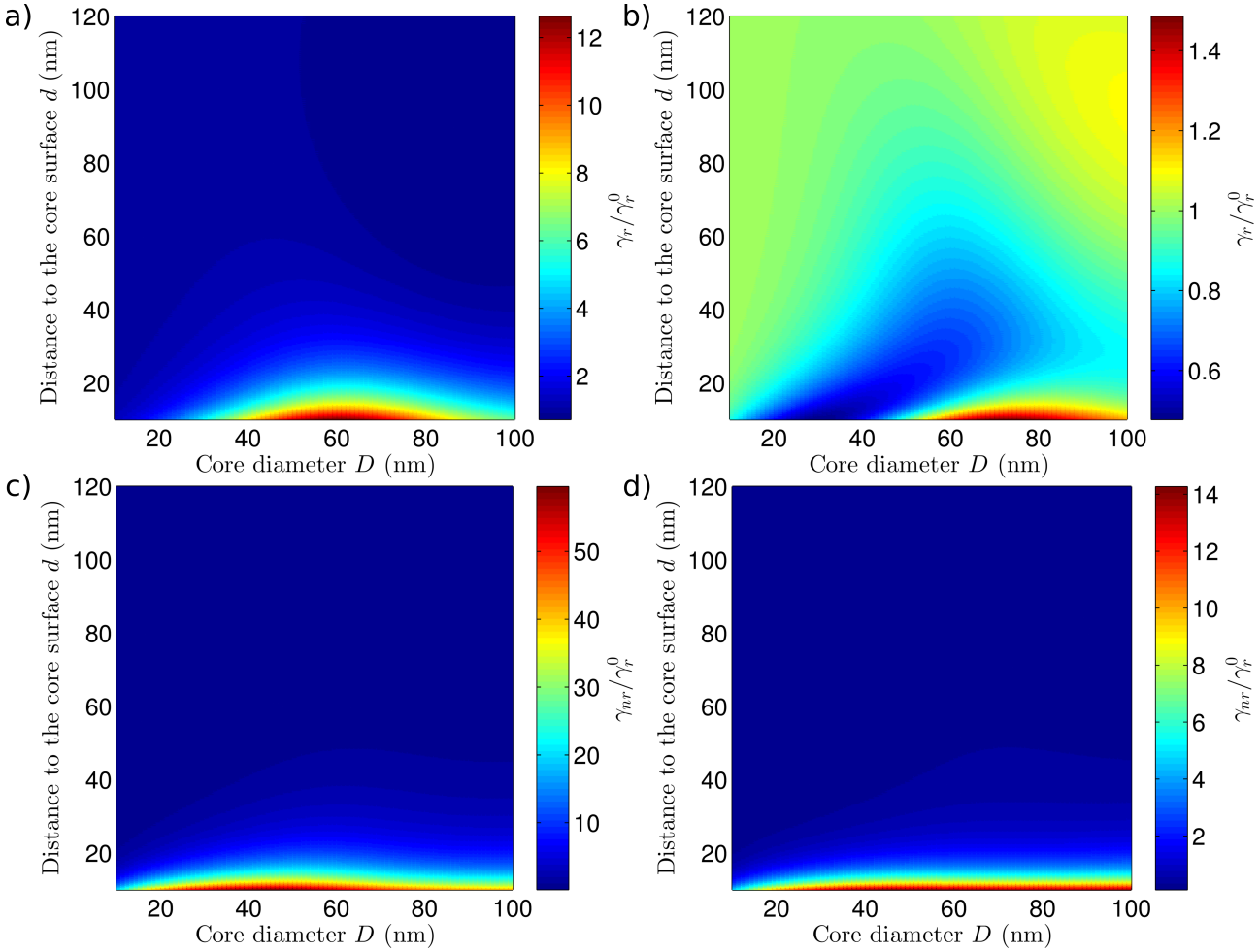

Figure II.3: A dipole with a $\eta_0 = 90\%$ quantum yield is placed close to a gold nanosphere with diameter D, coated by a silica shell with thickness d. The system is embedded in a host medium with refractive index 1.5. The dipole orientation is normal to the particle surface in a) and c) while it is tangential in b) and d). We show the evolution of the a) and b) radiative decay rate γ_r, c) and d) non-radiative decay rate γ_{nr}, as a function of i) the diameter D of the plasmonic core and ii) the distance d between the dipole and the core surface. The decay rates are normalized by the radiative decay rate of the dipole in the host medium γ_r^0.

First we note in Fig. II.3 that both the radiative and the non-radiative decay rates are larger for a normal orientation than for a tangential orientation of the emitter. It shows

that a normally oriented dipole yields to a better dipole-plasmon coupling. Nevertheless one should keep in mind that the spectral maximum of γ_r and γ_{nr} depend on the dipole orientation [111, 120].

For short distances d, typically below 15 nm, we can see that, for both orientations, the decay is dominated by non-radiative relaxation in the metal, leading to the quenching effect [107]. The quenching is dominated by higher-order modes $l \geq 2$ since they weakly couple to the far field and mainly lead to Ohmic losses, as discussed in figure II.1. Therefore the non-radiative decay rate increases with decreasing distance d for both dipole orientations, as observed in Figs. II.3c and II.3d.

Accordingly the main radiating mode is the dipole mode. The plasmonic core then acts as an dipolar antenna enhancing the radiation. The radiation enhancement can thus be qualitatively described as a coupling between the dipole and the induced dipole in the MNP. On the one hand, if the emitter is oriented normally to the sphere surface, then the system is equivalent to two aligned dipoles radiating in phase, resulting in an enhanced radiation due to constructive interference. As a consequence we observe in Fig. II.3a that the radiative decay rate increases as the distance d decreases. On the other hand, if the emitter orientation is tangential to the particle surface, the MNP dipole mode oscillates out-of-phase with respect to the dipole source. The resulting destructive interference yields to a smaller emitted power so that γ_r is reduced. Accordingly we observe in Fig. II.3b that γ_r decreases with d for $D < 50\ nm$ and in the $d > 20\ nm$ range for $D > 50\ nm$. It shows that for $D > 50\ nm$ the particle is so large that the coupling of the higher order modes to the far field cannot be neglected.

Finally note that, at a given distance $d < 60\ nm$ and for both orientations, the coupling of the dipole to the radiative mode is optimal for $D \approx 60\ nm$. Indeed a smaller plasmonic core exhibits a less intense dipole mode. Whereas a larger core yields to a non negligible contribution of the higher order modes.

II.3.b Influence of the emitter quantum yield

Experimentally we consider fluorescent molecules with two different quantum yields 60% and 90%. We thus investigate how the dipole quantum yield influences the modification of its radiation close to the nanohybrid. We consider a dipole oriented tangentially to the particle surface, as represented in the inset of figure II.4a.

Figures II.4a and II.4b show the evolution of the radiative γ_r, non radiative γ_{nr} and total decay rates γ with the distance d to the core surface for $\eta_0 = 90\%$ and $\eta_0 = 1\%$, respectively. To go further we also show the evolution of the quantum yield with the distance d, in figures

II.4c and II.4d for $\eta_0 = 90\%$ and $\eta_0 = 1\%$, respectively.

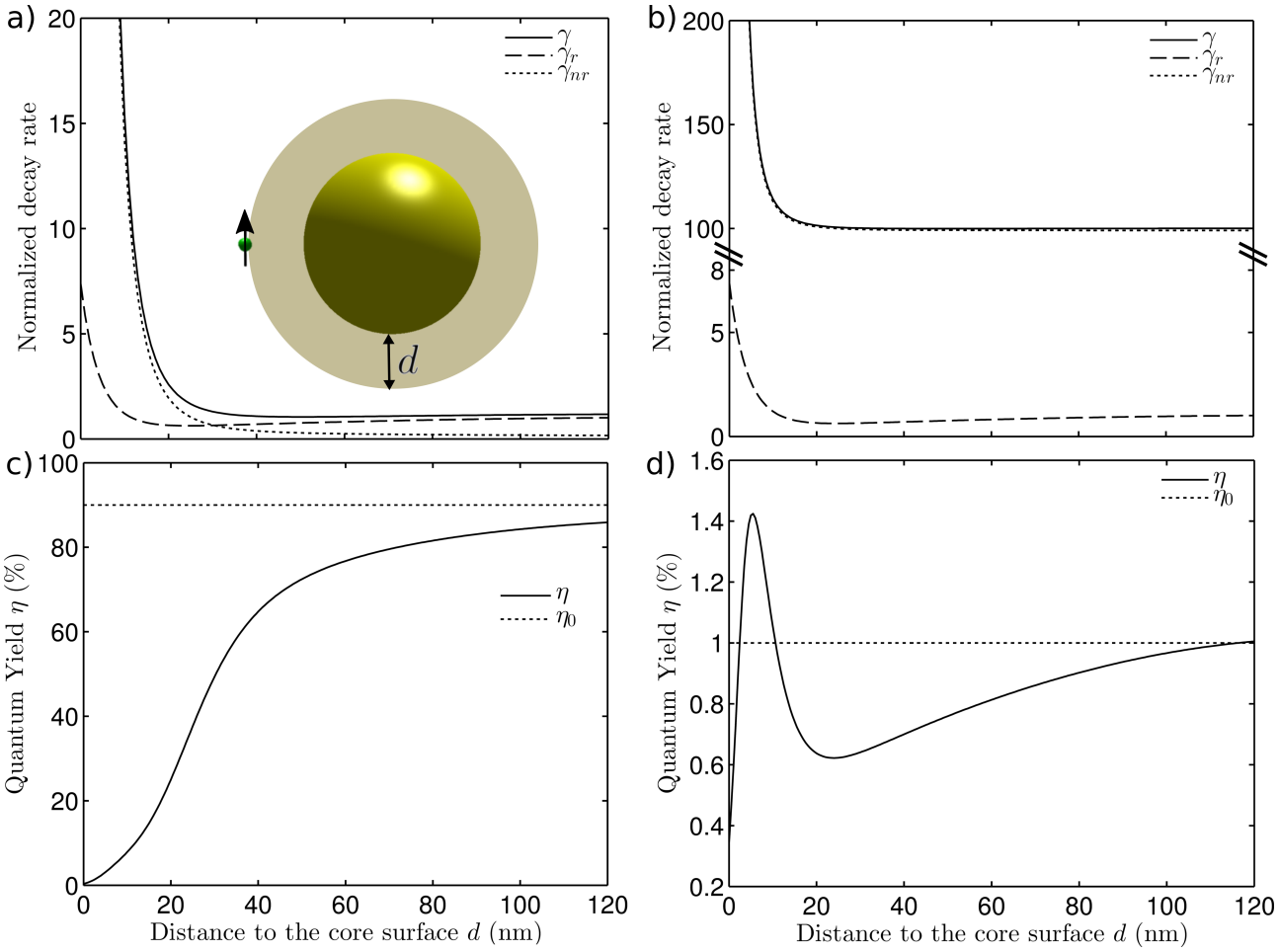

Figure II.4: A dipole is placed at a distance d from the surface of a 60 nm diameter gold sphere, coated with a silica shell. The dipole is oriented tangentially to the particle surface as represented in the inset of a). The system is embedded in a host medium with refractive index 1.5. The dipole quantum yield in the host medium is $\eta_0 = 90\%$ in a) and c) or $\eta_0 = 1\%$ in b) and d). a) and b) Evolution of the total decay rate γ (solid line), the radiative decay rate γ_r (dashed line) and the non-radiative decay rate γ_{nr} (dotted line) with the distance d between the dipole and the gold core surface. c) and d) Evolution of the quantum yield η with the distance d. The dipole quantum yield in the host medium η_0 (dotted line) is shown for comparison. The decay rates are normalized by the radiative decay rate of the dipole in the host medium γ_r^0.

First, we see in Figs. II.4a and II.4b that the radiation enhancement γ_r/γ_r^0 does not depend on the dipole quantum yield η_0. More precisely the radiative decay rate increases with d for $d > 20\ nm$. Note that, for $d > 30\ nm$, the non-radiative decay rate is weakly affected by the nanohybrid. Hence the quantum yield also increases with d in this range, as observed in both Figs. II.4c and II.4d. Far from the particle the radiative decay rate tends to $\eta_0\gamma_0$, the non-radiative decay rate tends to $(1-\eta_0)\gamma_0$ and η tends to η_0.

Then we observe that, regardless of the dipole quantum yield η_0, the total decay rate increases for decreasing distance d. The steep rise of the non-radiative decay rate for $d <$

15 nm, is due to the quenching effect. This is confirmed by the fact that the quantum yield tends to zero as d decreases, for both $\eta_0 = 90\%$ and $\eta_0 = 1\%$.

For $\eta_0 = 90\%$ Fig. II.4a shows that γ_{nr} rises for $d < 20nm$ while γ_r rises for $d < 15nm$. As a consequence the quantum yield observed in Fig. II.4c decreases as the dipole gets closer to the core surface. On the contrary for $\eta_0 = 1\%$ γ_{nr} rises only for $d < 10nm$, leading the quantum yield to show a maximum at $d \approx 5$ nm. Furthermore note that at $d = 10$ nm, $\gamma_{nr}/\gamma_{nr}^0 = 14$ for $\eta_0 = 90\%$ while $\gamma_{nr}/\gamma_{nr}^0 = 1.14$ for $\eta_0 = 1\%$. As a consequence, a dipole with high quantum yield η_0 experiences a large enhancement of the non-radiative decay rate with respect to its radiation enhancement, resulting in a low quantum yield. On the contrary a dipole with small quantum yield η_0 experiences a small enhancement of the non-radiative decay rate [110] that can lead to an enhancement of the quantum yield, as observed in Fig. II.4d.

II.4 Collective radiation close to a metal nanosphere

II.4.a Numerical implementation

We consider the radiation of N dipoles distributed around a metal nanosphere. This N+1-body problem is described by Eq. II.34, reproduced here

$$\alpha_l(\omega)\mathbf{E}_d(\mathbf{r}_l,\omega)\cdot\mathbf{e}_l = \Big\{\mu_l(\mathbf{r}_l) - \alpha_l(\omega)\frac{\omega^2}{\epsilon_0 c^2}\sum_{j\neq l}\mathbf{e}_l\cdot\overleftrightarrow{\mathbf{G}}_0(\mathbf{r}_l,\mathbf{r}_j,\omega)\cdot\boldsymbol{\mu}_j - \alpha_l(\omega)\frac{\omega^2}{\epsilon_0 c^2}\sum_{j=1}^{N}\mathbf{e}_l\cdot\overleftrightarrow{\Delta\mathbf{G}}(\mathbf{r}_l,\mathbf{r}_j,\omega)\cdot\boldsymbol{\mu}_j\Big\} \tag{II.43}$$

This coupled system can be casted in matrix form, which is convenient for a numerical implementation. Denoting by $\overrightarrow{\boldsymbol{\mu}}$ the vector formed by the μ_l's, $l \in [\![1, N]\!]$, we obtain

$$\boldsymbol{\alpha}(\omega)\vec{\mathcal{E}}(\omega) = \Big\{\mathcal{I} - \boldsymbol{\alpha}(\omega)\mathcal{G}_0(\omega) - \boldsymbol{\alpha}(\omega)\Delta\mathcal{G}(\omega)\Big\}\vec{\boldsymbol{\mu}} \tag{II.44}$$

where $\mathcal{I}$ is the $N \times N$ identity matrix, $\boldsymbol{\alpha}$ is the $N \times N$ diagonal polarizability-matrix with $\boldsymbol{\alpha}_{ll} = \alpha_l$ and $\vec{\mathcal{E}}$ a N-vector formed from the driving laser field: $\vec{\mathcal{E}}_l(\omega) = \mathbf{E}_d(\mathbf{r}_l,\omega)\cdot\mathbf{e}_l$. The $N \times N$ free-space interaction matrix is $\mathcal{G}_0$, where $\mathcal{G}_0^{lj}(\omega) = \frac{\omega^2}{\epsilon_0 c^2}\mathbf{e}_l\cdot\overleftrightarrow{\mathbf{G}}_0(\mathbf{r}_l,\mathbf{r}_j,\omega)\cdot\mathbf{e}_j$ if $j \neq l$ and 0 otherwise. The $N \times N$ nanohybrid-mediated interaction matrix $\Delta\mathcal{G}$ is given by $\Delta\mathcal{G}^{lj}(\omega) = \frac{\omega^2}{\epsilon_0 c^2}\mathbf{e}_l\cdot\overleftrightarrow{\Delta\mathbf{G}}(\mathbf{r}_l,\mathbf{r}_j,\omega)\cdot\mathbf{e}_j$.

For a given incident field $\vec{\mathcal{E}}(\omega)$, the induced dipole moments are obtained through a matrix inversion

$$\vec{\boldsymbol{\mu}} = \Big\{\mathcal{I} - \boldsymbol{\alpha}(\omega)\mathcal{G}_0(\omega) - \boldsymbol{\alpha}(\omega)\Delta\mathcal{G}(\omega)\Big\}^{-1}\boldsymbol{\alpha}(\omega)\vec{\mathcal{E}}(\omega) \tag{II.45}$$

and the radiation properties of the whole system are given by solving the system of Eq. II.44. Each eigenstate corresponds to a decay channel of the molecular ensemble. The associated eigenfrequency $\tilde{\omega}$ is complex, as noted already for a single dipole in Eq. II.37. The real part specifies the resonance frequency $\mathrm{Re}\{\tilde{\omega}\}$ and the imaginary part indicates the resonance linewidth $\gamma = -2\mathrm{Im}\{\tilde{\omega}\}$. Therefore the computation of all complex eigenfrequencies of the molecular ensemble gives access to the resonance frequency and the linewidth of all decay channels. Hence the above analysis has led to a simple yet elegant way to rigorously and quantitatively evaluate the optical properties of a collection of emitters.

In a general case, Eq. II.44 is a non-linear eigenproblem that may not be diagonalizable. So even for the simple case of steady-state studies, the numerical modeling of coupled systems with large collections of emitters represents a major challenge in computational electrodynamics [36, 121]. The challenge worsens when studying the dynamics which requires to iteratively solve coupled equations for the Maxwell's fields and the carriers-population operators [51, 54]. Computing ensemble-averaged responses over a statistical distribution of emitters (positions, orientations, resonance frequencies) may also be demanding [70, 122]. However it can be required to interpret experiments for which the exact location and orientation of the emitter is approximately known [78, 123, 124]. In this doctorate thesis, we focus on the steady-state study.

First a rigorous but tedious approach to solve Eq. II.44 is to calculate the determinant for each frequency of the complex plane. Zeros of the determinant then correspond to the problem eigenfrequencies. This method requires good initial guess values and large computation power to re-calculate the new Green-tensor at each iteration. Furthermore N eigenfrequencies are expected for N coupled emitters, resulting in a non-negligible computational burden.

In order to avoid scanning the complex plane, we propose some simplifications to make the problem (Eq. II.44) diagonalizable. First the free space interaction is known analytically [43]

$$\overleftrightarrow{\mathbf{G}}_0(\mathbf{r}_l, \mathbf{r}_j, \omega) = \frac{exp(ikR_{lj})}{4\pi R_{lj}} \Big[\Big(1 + \frac{ikR_{lj} - 1}{k^2 R_{lj}^2}\Big) \overleftrightarrow{\mathbf{I}} + \frac{3 - 3ikR_{lj} - k^2 R_{lj}^2}{k^2 R_{lj}^2} \frac{\mathbf{R}_{lj} \otimes \mathbf{R}_{lj}}{R_{lj}^2} \Big] \quad \text{(II.46)}$$

where $k = \sqrt{\epsilon_{host}}\omega/c$, $\overleftrightarrow{\mathbf{I}}$ is the 3×3 unit dyad, $\mathbf{R}_{lj} = \mathbf{r}_l - \mathbf{r}_j$ and $\mathbf{R}_{lj} \otimes \mathbf{R}_{lj}$ is the outer product of $\mathbf{R}_{lj}$ with itself.

Then the dipole resonances are spectrally very narrow ($\gamma_l \approx 50$ MHz $\ll \omega_l \approx 500$ THz). Hence all the modified decay channels are expected to occur in a narrow energy interval. If we consider that all the dipoles have the same resonance frequency $\widetilde{\Omega}_l = \widetilde{\Omega} = \omega_0 - i\frac{\gamma_0}{2}$ and are distributed in a subwavelength volume, we can assume that $|\frac{\sqrt{\epsilon_{host}}(\tilde{\omega} - \widetilde{\Omega})}{c}| R_{lj} \ll 1$. In this limit, we may expand the exponential term of the free space Green-tensor $\overleftrightarrow{\mathbf{G}}_0$ from Eq. II.46

in a fast-converging power series [125]

$$exp(i\sqrt{\epsilon_{host}}R_{lj}\frac{\tilde{\omega}}{c}) = exp(i\sqrt{\epsilon_{host}}R_{lj}\frac{\tilde{\Omega}}{c})\Big(1 + i\sqrt{\epsilon_{host}}R_{lj}\frac{\tilde{\omega}-\tilde{\Omega}}{c} + ...\Big) \tag{II.47}$$

For instance when the dipole-dipole separations are smaller than 200 nm, an expansion of the exponential term up to the first order is sufficient.

Concerning the nanohybrid-mediated interaction $\Delta\mathcal{G}$, the LSPP resonance linewidth is typically 25 THz, which is about 6 orders of magnitude larger than the dipole linewidth. Therefore the plasmonic resonance may be considered as flat nearby the dipole resonance frequency. As a consequence we assume that $\Delta\mathcal{G}$ is frequency independent.

The problem from Eq. II.44 then becomes

$$(\frac{\tilde{\omega}}{\tilde{\Omega}} - 1)(\frac{\tilde{\omega}}{\tilde{\Omega}})^3\mathcal{I} + \frac{4\pi\epsilon_0\rho}{\tilde{\kappa}^3}\Delta\mathcal{G} + \rho(\mathcal{S}(\frac{\tilde{\omega}}{\tilde{\Omega}})^3 + \mathcal{T}(\frac{\tilde{\omega}}{\tilde{\Omega}})^2 + \mathcal{U}\frac{\tilde{\omega}}{\tilde{\Omega}} + \mathcal{V}) \tag{II.48}$$

where we introduced $\rho = 3\gamma^0/(4\tilde{\Omega}\sqrt{\epsilon_{host}})$ and $\tilde{\kappa} = \tilde{\Omega}/c$. where the first term corresponds to the inverse of the polarizability. The second and third terms are the nanohybrid-mediated and direct interaction matrices, respectively. The free space contribution is written as a polynomial expansion where $\mathcal{S}, \mathcal{T}, \mathcal{U}$ and $\mathcal{V}$ are dimensionless matrices.

$$\begin{aligned}
\mathcal{S}_{lj} &= i\sqrt{\epsilon_{host}}\Big(\delta_{lj} - \mathbf{e}_l \cdot \frac{\mathbf{R}_{lj}\otimes\mathbf{R}_{lj}}{R_{lj}^2}\cdot\mathbf{e}_j\Big)exp(i\sqrt{\epsilon_{host}}\tilde{\kappa}R_{lj}) \\
\mathcal{T}_{lj} &= \Big[i\sqrt{\epsilon_{host}}\Big(-\delta_{lj} + \mathbf{e}_l \cdot \frac{\mathbf{R}_{lj}\otimes\mathbf{R}_{lj}}{R_{lj}^2}\cdot\mathbf{e}_j\Big) + 2\frac{c}{\tilde{\Omega}}\mathbf{e}_l \cdot \frac{\mathbf{R}_{jl}\otimes\mathbf{R}_{lj}}{R_{lj}^3}\cdot\mathbf{e}_j\Big]exp(i\sqrt{\epsilon_{host}}\tilde{\kappa}R_{lj}) \\
\mathcal{U}_{lj} &= \frac{1}{\tilde{\kappa}R_{lj}}\Big(\delta_{lj} - 3\mathbf{e}_l \cdot \frac{\mathbf{R}_{lj}\otimes\mathbf{R}_{lj}}{R_{lj}^2}\cdot\mathbf{e}_j\Big)exp(i\sqrt{\epsilon_{host}}\tilde{\kappa}R_{lj}) \\
\mathcal{V}_{lj} &= \Big(\frac{1}{\epsilon_{host}\tilde{\kappa}^3R_{jl}^3} + \frac{1}{i\sqrt{\epsilon_{host}}\tilde{\kappa}^2R_{lj}^2}\Big)\Big(-\delta_{lj} + 3\mathbf{e}_l \cdot \frac{\mathbf{R}_{lj}\otimes\mathbf{R}_{lj}}{R_{lj}^2}\cdot\mathbf{e}_j\Big)exp(i\sqrt{\epsilon_{host}}\tilde{\kappa}R_{lj})
\end{aligned} \tag{II.49}$$

Hence Eq. II.48 is a polynomial eigenproblem of degree 4 which can be solved using modern eigensolver libraries. We use the MATLAB function *polyeig.m*. To validate the diagonalization approach, we compare the exact poles estimated by scanning the complex plane with the approximated eigenfrequencies obtained by diagonalizing Eq. II.48.

For instance we consider two identical dipoles separated by 20 nm and placed at 10 nm from the surface of a 60 nm diameter gold sphere, as represented in figure II.5a. The system is embedded in a homogeneous host medium with refractive index $\sqrt{\epsilon_{host}} = 1.5$. We denote by $\tilde{\Omega}$ and γ_0 the dipoles complex frequency and decay rate in the host medium without the MNP, respectively. Without the gold sphere, these two dipoles are weakly coupled in

this specific configuration: $g_{12} \approx \gamma_{12} \approx 0$. Hence any coupling between the dipoles is due to the plasmonic particle. Figure II.5b shows the rigorously calculated determinant of the non-linear problem from Eq. II.44 in the complex plane $\tilde{\omega}$. In comparison the white dots are the eigenfrequencies obtained by diagonalizing the polynomial eigenproblem from Eq. II.48.

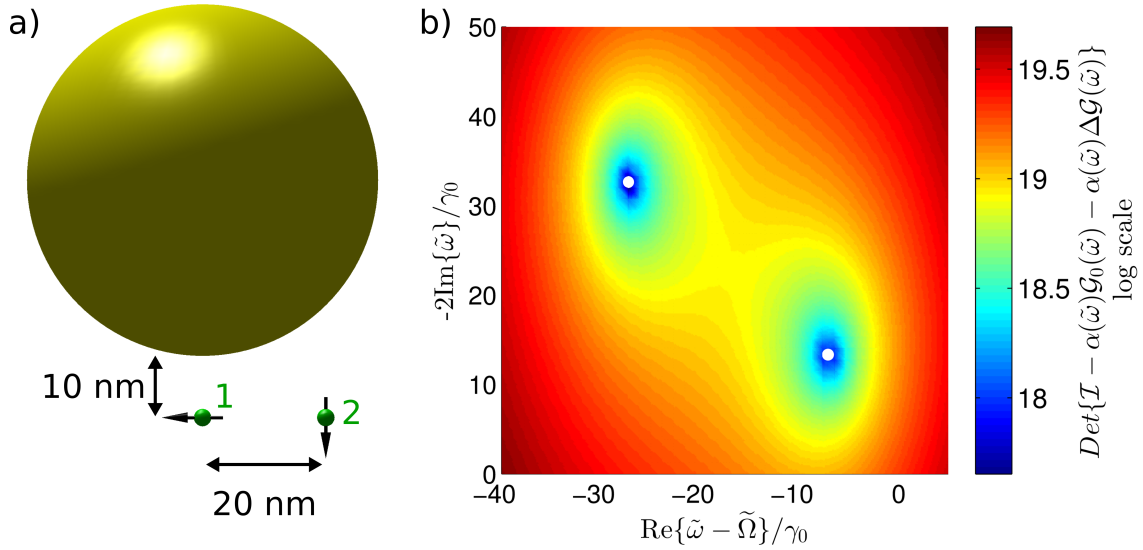

Figure II.5: Two identical dipoles separated by 20 nm are placed at 10 nm from the surface of a 60 nm diameter gold sphere, as represented in a). b) Rigorously calculated determinant of the non-linear problem from Eq. II.44 in the complex plane $\tilde{\omega}$. The colorbar is in log scale. The white dots show the eigenfrequencies obtained by diagonalizing the polynomial eigenproblem from Eq. II.48. $\tilde{\Omega}$ and γ_0 denote the dipoles complex frequency and decay rate in the host medium without the particle, respectively.

First we observe that the determinant shows two zeros, as expected for a two emitters system. We note a good agreement between the rigorously calculated and approximated eigenfrequencies. Using the rigorous approach, the accuracy on the poles is determined by the scan grid resolution, giving a rough estimation within a reasonable computation time. From this first guess, we use the bisection method [126] which is faster and more robust to estimate the pole. The eigenfrequencies are then similar with the two methods, up to the 3$^{\text{rd}}$ decimal: $\tilde{\omega}_{sub} - \omega_0 = (-7.108 - i13.341/2)\gamma_0$ and $\tilde{\omega}_{sup} - \omega_0 = (-27.255 - i32.643/2)\gamma_0$.

We compare these eigenfrequencies to the dipoles respective properties due to the Purcell effect: $\tilde{\omega}_1 - \omega_0 = (-21.886 - i19.248/2)\gamma_0$ and $\tilde{\omega}_2 - \omega_0 = (-12.477 - i26.730/2)\gamma_0$. We clearly see that both the resonance position and the linewidth are modified, showing that the dipoles are coupled via the plasmonic sphere.

II.4.b N dipoles radiation near a spherical nanohybrid

In this section we consider the radiation of N dipoles distributed around a 60 nm diameter gold sphere coated by a silica shell. The system is embedded in a polymer matrix with

refractive index $\sqrt{\epsilon_{host}} = 1.5$. The dipoles are identical with same resonance frequency $\tilde{\Omega} = \omega_0 - i\gamma_0/2$ and same quantum yield $\eta_0 = 90\%$ in the reference medium, i.e. the hosting medium without nanohybrid.

II.4.b.i Influence of the distance to the metal core surface

Here we investigate the influence of the distance to the metal core surface. For simplicity the dipoles are uniformly distributed at the nanohybrid surface and they are all normally oriented to the particle surface, as represented in the inset of figure II.6a. We implemented and diagonalized the problem from Eq. II.48 so to observe the evolution of the eigenstates decay rate $\gamma = -2\text{Im}\{\tilde{\omega}\}$ and energy shift $\Delta = \text{Re}\{\tilde{\omega} - \widetilde{\Omega}\}$ with the distance to the core surface. Figures II.6a and II.6b describe the system with a silica shell between the dipoles and the gold core. To study the effect of the shell on the plasmonic superradiance, we will discuss in the next paragraph II.4.b.ii the results without shell shown in Figs. II.6c and II.6d. It will be the opportunity to compare the model presented here with the model published by V. Pustovit and T. Shahbazyan [37] which are also presented in Figs. II.6c and II.6d.

In figure II.6a we first observe that all the decay rates increase for decreasing distance d, as a result of a more efficient dipole-plasmon coupling as the dipoles get closer. Correlating Figs. II.6a and II.6b, we identify three main behaviors and thus sort the eigenvalues into three groups.

One state (blue dashed line in Fig. II.6a and II.6b) shows the smallest decay rate, but the largest positive energy shift with a peak at $d = 10\ nm$. In particular, beyond the quenching distance $d > 10\ nm$, the small decay rate indicates a weak contribution of the plasmonic core, corresponding to the darkest subradiant state. Then the large frequency shift allows us to deduce that this mode is mainly due to the direct dipole-dipole interaction between neighbor emitters.

Then three states (red dash-dotted lines in Figs. II.6a and II.6b) exhibit the largest decay rate for all distances and are thus called the superradiant states. Each superradiant state corresponds to a dimension of the structure, explaining why we observe three states for a sphere [37]. In a perfectly symmetrical system, these three eigenvalues are degenerate. However they are not perfectly degenerate in Figs. II.6a and II.6b because the dipoles distribution slightly breaks the symmetry. The large decay rate shows an efficient coupling via the plasmonic core. Nevertheless their energy shift shows a small peak at about $d = 15\ nm$, revealing the contribution of the direct dipole-dipole interaction. The observations in figure II.3 showed that each dipole is preferentially coupled to the dipole LSPP mode for $d > 20\ nm$. Since the dipole LSPP mode is mainly radiative, we deduce that these superradiant states

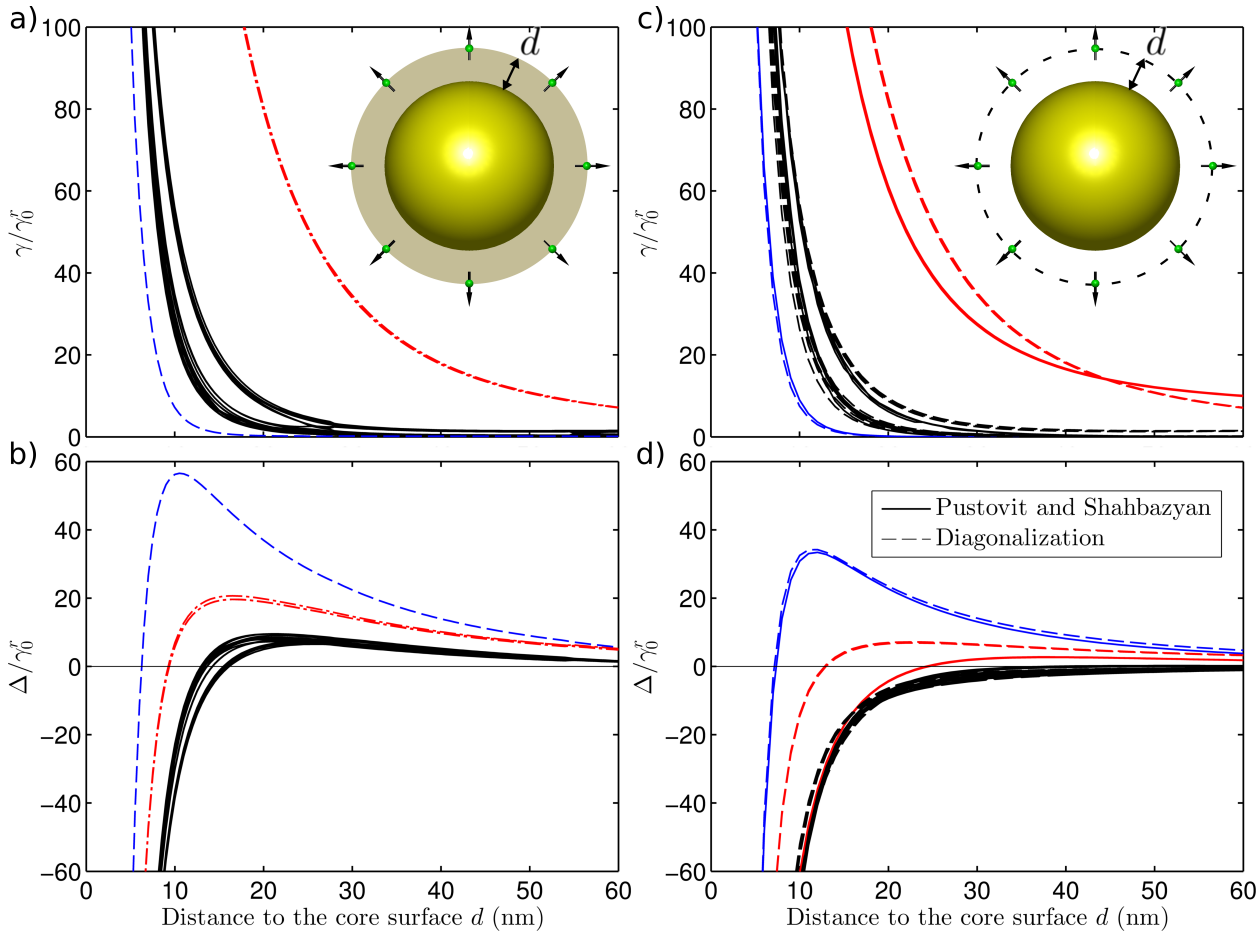

Figure II.6: 20 *dipoles are uniformly distributed around a 60 nm diameter gold sphere a) and b) with or c) and d) without a silica shell. The dipoles have a* $\eta_0 = 90\%$ *quantum yield and are normally oriented to the particle surface, as represented in the insets. We show the evolution of the eigenvalues a) and c) decay rates and b) and d) energy shifts with the distance to the gold core. Each line represents an eigenstate and is similarly marked in all graphs. In a) and b) we identify the three superradiant decay rates (red dash-dotted lines), the darkest subradiant state (dashed blue line) and the other subradiant states (black solid lines). In c) and d), the superradiant (red), darkest subradiant (blue) and other subradiant (dark) states obtained with our model (dashed lines) is compared with the results calculated using V. Pustovit and T. Shahbazyan model (solid lines) [37]. All the decay rates and energy shifts are normalized by the radiative decay rate of a dipole* γ_0^r *in the host medium without hybrid.*

are dominated by plasmon-enhanced radiative coupling through the dipole plasmon mode for $d > 20\ nm$.

The remaining subradiant states (black solid lines in Figs. II.6a and II.6b), have the smallest energy shift without clear peak and are thus weakly affected by the direct dipole-dipole interaction. For $d > 20\ nm$ the coupling through the dipole plasmon mode also dominates and the associated decay rates are small, yielding to pure subradiant states.

The sharp rise (decrease) of γ (Δ) below $d = 10\ nm$ is attributed to the quenching effect. In this range the dipole-dipole interaction is dominated by non-radiative coupling via the higher order plasmon oscillations. As a consequence both the superradiant and subradiant states are weakly coupled to the far field. This leads the superradiant and subradiant states to admixture through the higher order plasmon modes. Below 5 nm, the quenching dominates and cooperative radiation is destroyed [36]. Note that the admixture between superradiant and subradiant states is relatively weak for $d > 10\ nm$, even though the higher order modes contribute to the dipole-dipole coupling.

To conclude the free-space interaction mainly contributes to the large collective energy shifts [127], and plays an important role in the subradiant radiation [128]. Then the plasmon-mediated interaction is responsible for the formation of superradiant states with large decay rates [36], even for a small number of dipoles. These features will be further evidenced in the case of a nanorod in chapter III. Next the dipole LSPP mode allows for a radiative plasmon-mediated interaction, leading to pure superradiant and subradiant states. Whereas the higher order modes yield to a non-radiative interaction, that leads to an admixture between superradiant and subradiant states.

The experimental work carried out in this doctorate thesis aims at observing the superradiant states. Therefore the nanohybrid dimensions should allow for the formation of pure superradiant and subradiant states. As a consequence we choose a plasmonic core size that promotes the coupling of each dipole to the dipole LSPP mode, while limiting the contribution of the higher order modes. We observed in Fig. II.3 that a single dipole near the nanohybrid shows such a situation in the range $15\ nm < d < 60\ nm$ and for $D \approx 60\ nm$. These optimal dimensions will be investigated experimentally in chapter V.

II.4.b.ii Comparison with V. Pustovit and T. Shahbazyan model

Very similar features were reported by V. Pustovit and T. Shahbazyan for a 32 nm diameter gold sphere [36] and a 40 nm diameter silver sphere [37], without silica shell. The dipoles were uniformly distributed and oriented normally to the particle surface, as represented in figure II.6c. Similarly to our approach, they made the long-wave approximation to both the

free-space and the sphere Green functions. However they neglected the frequency dependency of the free-space interaction while we considered a first order polynomial expansion of the exponential term in Eq. II.46. Furthermore, they considerably simplified both the free-space and plasmon-mediated Green functions in order to introduce analyticity in the published discussion and thus outline the underlying mechanism. In particular the nanoparticle polarizability was taken from Eq. II.17, accounting for the radiation damping while neglecting the depolarization effect. The latter was discussed in paragraph II.1.b.i and contributes to the plasmon resonance spectral shape and position for $D = 60\ nm$. Finally, they considered that the radiative coupling is only due to the dipole plasmon mode, neglecting the contribution of the higher order modes.

In figures II.6c and II.6d, we compare these two models for the system discussed in figures II.6a and II.6b but without shell, as represented in Fig. II.6c. The solid lines represent the eigenvalues derived using the model from V. Pustovit and T. Shahbazyan [37], while the solutions obtained by diagonalization of Eq. II.48 are shown as dashed lines. The colors indicate the three groups of modes: superradiant, darkest subradiant and other subradiant states.

First we see in both Figs. II.6c and II.6d that the darkest subradiant state, which is dominated by the direct interaction, is very similar. Indeed the main features are observed for $d < 30\ nm$, therefore the dipole-dipole separations are small enough to neglect the frequency dependency of the free-space contribution. Then note that the other subradiant states are also quite similar. We deduce that the depolarization effect, which slightly reduces the particle response and is neglected in V. Pustovit and T. Shahbazyan approach, weakly influences both the decay rates and the energy shifts. The main difference is observed for the superradiant states: our diagonalization approach yields to a larger decay rate and energy shift for $d < 45\ nm$. This difference may be due to the contribution of the higher order modes to the radiative coupling, which is neglected in V. Pustovit and T. Shahbazyan model. Nevertheless no more than 20% difference could be observed and the features are similar, thus justifying the approximations proposed by V. Pustovit and T. Shahbazyan.

Unlike V. Pustovit and T. Shahbazyan model, the model we developed in this doctorate thesis accounts for the silica shell. We observe the influence of the silica shell by comparing Figs. II.6a and II.6b with Figs. II.6c and II.6d. We see that adding the silica shell barely modifies the decay rates while the energy shift is increased for all the eigenstates. We deduce that the direct dipole-dipole interaction is enhanced in the presence of the shell. Indeed the silica shell creates a new interface where the light is scattered since $\epsilon_{SiO_2} \neq \epsilon_{host}$. However the silica shell and polymer dielectric permittivities are close so the shell weakly affects the

plasmon resonance and thus the plasmon-mediated interaction.

II.4.b.iii Influence of the dipoles distribution in position and orientation

As observed in section II.3, the emitter orientation strongly influences the interaction between one dipole and the nanohybrid. Therefore we expect it to also affect the plasmon-mediated dipole-dipole coupling. We study here how the dipoles distribution and orientation affects the eigenvalues.

To this end we perform statistics on the dipoles position and orientation. In the experimental study of chapter V, the emitters are randomly distributed around the nanohybrid and their orientation is preferentially tangential to the particle surface. Here we consider $N = 50$ dipoles placed on a $d = 18\ nm$ thick silica shell. We perform statistics on their position and orientation in the plane tangential to the nanohybrid, for 1000 configurations. From each configuration, we estimate 3 superradiant states and $N - 3 = 47$ subradiant states which are represented in figure II.7.

Furthermore in our model the free-space interaction in Eq. II.46 does not account for the Förster resonance energy transfer (FRET) [129] which is a non-radiative energy transfer between the molecules due to van der Waals interactions. For the molecules studied experimentally the FRET is efficient for molecules separated by less than 5 nm, see chapter V. We thus set a 5 nm minimum separation between the dipoles.

We first see in Fig. II.7 that both the superradiant states (red dots) and the subradiant states (black pluses) can exhibit either positive or negative energy shifts, depending on the configuration. Note that the subradiant energy shifts can reach large values as compared to the superradiant energy shifts. In accordance with the discussion paragraph II.4.b.i, we identify the states exhibiting the largest shifts as the darkest subradiant states.

Then we observe that the distinction between the superradiant and the subradiant states is not as clear as for the fully symmetrical case. Indeed in Fig. II.7 the dipoles orientation and position strongly alter the system symmetry. In particular we observe that the average superradiant state has a decay rate of about $< \gamma >= 8.8\gamma_0^r$ and varies between $6.9\gamma_0^r$ and $12.2\gamma_0^r$ with a standard deviation of 8.8%. As expected a larger standard deviation (16%) was observed when the statistics includes non-tangential orientations. In particular each dipole experiences a different Purcell effect and thus a different coupling to the plasmonic modes, depending on its orientation. We deduce that the position and orientation of the dipoles strongly influence the collective optical properties.

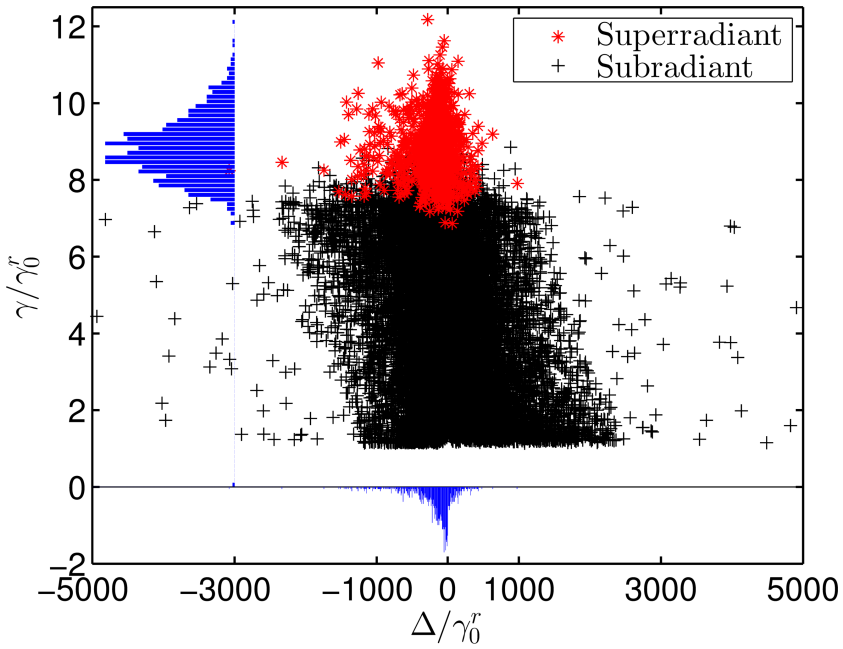

Figure II.7: 50 *dipoles are randomly distributed around a 60 nm diameter gold sphere coated by a* $d = 18$ *nm thick silica shell. The dipoles have a quantum yield of* $\eta_0 = 90\%$ *and are randomly oriented in a plane tangential to the particle nanohybrid. The minimum separation distance between the dipoles is* 5 *nm. A statistics over 1000 configurations was performed. The superradiant (the 3000 red dots) and subradiant (black pluses) modes are shown as a function of their normalized energy shift* Δ/γ_0^r *and normalized decay rate* γ/γ_0^r*. The histograms of the superradiant decay rates and energy shifts are shown in blue b).*

II.4.b.iv Influence of the number of emitters for different distances to the metal core

In Ref. [37] V. Pustovit and T. Shahbazyan reported that the superradiant decay rate scales with the number of emitters in the fully symmetrical configuration. This trend is a signature of a collective emission and is thus expected in plasmon-mediated superradiance. In this last section we investigate whether this trend survives when one averages over the emitters position and orientation, as it is performed experimentally.

To this end we derive the average superradiant decay rate for the system that will be investigated experimentally in chapter V. Figure II.8 shows the evolution of the average superradiant decay rate as a function of the number of dipoles N, for different distances to the plasmonic core surface d. The plotted values are the average of the three superradiant decay rates, averaged over the dipoles position and orientation in a plane tangential to the particle surface. A minimum separation distance of 5 nm was set between the dipoles.

First we observe in Fig. II.8 that whatever the distance to the core, the superradiant decay rate scales with the number N of dipoles. This signature of superradiance thus survives in average. Then as the dipoles are closer to the metal core the slope with N increases. This shows that the interaction between dipoles is enhanced as the dipole-plasmon coupling

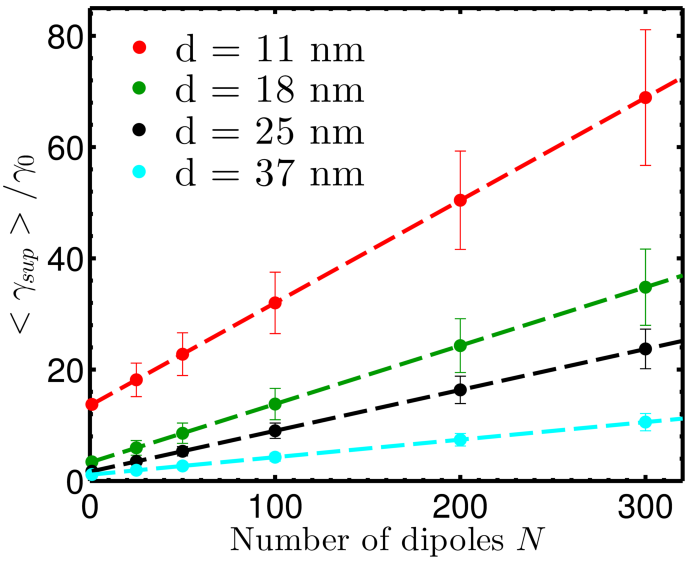

Figure II.8: N dipoles are randomly distributed around a 60 nm diameter gold sphere coated by a d thick silica shell. The dipoles have a quantum yield of $\eta_0 = 90\%$ and are randomly oriented in a plane tangential to the nanohybrid surface. The minimum separation distance between the dipoles is 5 nm. For each case (N, d), a statistics over the dipoles position and orientation was performed. We show the evolution of the average superradiant decay rate (dots with error bar) as a function of the number of dipoles N and the distance to the core surface d. Dashed lines are linear fits, as guides for the eyes.

increases.

II.5 Conclusion

To conclude we developed an explicit and efficient classical approach to derive the response of large collections of molecules near a spherical metallo-dielectric nanohybrid.

The optical properties of a metal nanosphere are fully described by the Mie theory and are depicted by plasmon modes. The higher the order of the mode, the more confined is the electric field at the particle surface. Hence the dipole mode is mainly a radiative mode while the contribution of the higher order modes is mainly non-radiative. The position and bandwidth of the plasmon modes are strongly affected by the MNP environment, and notably by the presence of a shell.

The radiation of a single dipole close to a nanohybrid consists in an enhancement of the radiated power as it couples to the dipole plasmon mode while the coupling to the higher order modes mainly leads to Ohmic losses. Below 5 nm from the metal surface all the energy is lost in heat dissipation (quenching effect). The Purcell effect is optimal when the dipole is oriented normally to the particle surface.

The collective radiation of N emitters distributed near a metal sphere is characterized by 3 superradiant modes, exhibiting the largest decay rate, and N-3 subradiant states. The 3 superradiant states correspond to the 3 dimensions of the sphere. The system decay channels strongly depend on the dipoles position and orientation. The largest decay rates being observed for a fully symmetrical configuration: the dipoles are uniformly distributed and oriented normally to the particle surface. We identified that the formation of pure superradiant states is observed when the dipole-dipole interaction is dominated by the dipole LSPP mode. Then the higher order plasmon modes mainly contribute to promote the interaction between neighbor dipoles, via non-radiative coupling. We deduced that the optimal plasmonic core diameter for the observation of superradiant states is 60 nm. We saw that the superradiant decay rate is proportional to the number of emitters and predicted that this trend survives when averaging over the emitters position and orientation. Furthermore we showed that the associated slope increases if the emitters get closer to the plasmonic core.

The here presented model makes no assumption on the emitters position and orientation. Furthermore it introduces the complete Mie theory, accounting for the depolarization effect and the presence of a dielectric layer between the dipoles and the metal core. This model is thus an extension of V. Pustovit and T. Shahbazyan model [37]. However the free-space interaction does not describe the FRET between neighbor dipoles. The dipole-dipole separation distance is thus limited to 5 nm minimum. Besides we assumed that the dipoles are identical. Finally this classical model does not account for pure dephasing processes.

Chapter III

Plasmonic superradiance with a metal nanorod

Contents

The numerical modeling of coupled systems with large collections of classical oscillators represents a major challenge in computational electrodynamics [36,121]. We showed in chapter II that the repeated calculation of the Green function at different frequencies may be avoided by diagonalizing the problem from Eq. II.44. This diagonalization was feasible thanks to some simplifications: we proposed to expand the free-space contribution while neglecting the frequency dependency of the nanohybrid-mediated interaction. The latter approximation may not be valid for cavities with high quality factor (or similarly oscillators with low quality factor). However an analytical expression of the Green dyadics would allow to identify more suitable simplifications. As a consequence the formalism, that was introduced in chapter II, may be used to efficiently analyze collective effects in ensemble of dipoles that are coupled by any electromagnetic cavity.

In this chapter, we aim at providing a more general formalism without making any hypothesis on the electromagnetic cavity, which could be photonic cavities or plasmonic nanoresonators, possibly with an overlapping of several resonances. To this end section III.1 introduces the concept of Quasi-Normal Modes as a way to describe an arbitrary cavity. In particular we show how this approach enriches the theory developed in chapter II. As an example we then consider a metal nanorod. The simple case of dipole doublets near the nanorod is treated in section III.2. This system allows us to clearly distinguish the contribution of the free-space interaction and the plasmon-mediated interaction. We also show how the scattering and absorption spectra are related to the eigenvalues. Section III.3 investigates the cooperativity of the superradiant and subradiant states by studying the induced dipole moments distribution for 100 dipoles. Finally we investigate how the predictions made for the nanosphere in section II.4.b.iii of chapter II are valid in the case of a metal nanorod.

This work was performed in close collaboration with the group of Philippe Lalanne in the LP2N, and in particular with Spyridon Kosionis during his postdoctoral fellowship. I was involved in studying how the non-linear eigenproblem may be diagonalized as well as performing the calculation and analyzing the results.

III.1 Generalization of the theoretical formalism using Quasi-Normal Modes

III.1.a Quasi-Normal Modes

An efficient and intuitive method for the analysis of the optical properties of a given cavity is the modal expansion. Illuminating the cavity with an incident wave and tuning its frequency, we find some intrinsic resonances. If the cavity is absorptionless and sufficiently confines the field to prevent leakage, then these resonances are the eigenstates of Hermitian time-evolution operators. They are known as normal modes ω_m and form a complete orthonormal basis, with infinite lifetimes and real eigenfrequencies [130]. The LDOS can then be explicited as a sum over all normal modes.

Now when the cavity is dissipative and/or leaky, e.g. a plasmonic system, the observed resonances do not form a complete orthonormal basis. Then an intuitive approach consists in solving for the modes of the cavity with outgoing-wave boundary conditions far from the cavity. The completeness and the orthogonality of these modes has been shown only for spherical or 1D open dielectric systems [131]. Nevertheless, it has been reported that, close to resonance, accurate predictions for leaky [132] and lossy cavities [133] can be obtained with expansions based on a few dominant modes only. To distinguish them from the normal-modes, these modes are called Quasi-Normal Modes (QNM). Since they show energy dissipation, they are characterized by complex frequencies $\tilde{\omega}_m$, similarly to the dipole polarizability from Eq. II.37 in chapter II. More precisely, a QNM is a pole of the cavity Green function and shows a non-zero linewidth $\gamma_m = -2\mathrm{Im}\{\tilde{\omega}_m\}$ while its spectral position is given by $\mathrm{Re}\{\tilde{\omega}_m\}$. The associated quality factor is then [134]

$$Q = \mathrm{Re}\{\tilde{\omega}_m\}\frac{\text{Stored energy}}{\text{Power loss}} = -\frac{\mathrm{Re}\{\tilde{\omega}_m\}}{2\mathrm{Im}\{\tilde{\omega}_m\}} \tag{III.1}$$

It gives access to the ratio of the time-averaged energy stored in the cavity to the energy loss per cycle [42]. A plasmonic nanoresonator is lossy and leaky, yielding to a typical quality factor of 10, while it can reach 10^4 for a designed photonic crystal [135, 136].

III.1.b Generalization of the theoretical formalism

Hereafter we adopt the approach developed in Refs. [132,137], in which reciprocity arguments allow to normalize the QNMs and to define an orthogonality relationship. The force of the QNM formalism resides in the fact that, once the QNMs are identified and properly

normalized, one may analytically derive the electromagnetic response for various excitations and frequencies, yielding to a considerably lower computational burden.

Using a scattered-field formulation [137], the driving field $\mathbf{E}_d$ (introduced in Eq. II.34, chapter II) at frequency ω is written as a sum of the incident laser field $\mathbf{E}_{inc}$ and the field $\mathbf{E}^s_{inc}$ scattered by the cavity under illumination by the laser. $\mathbf{E}^s_{inc}$ represents the nanoresonator response to the laser field and, as such, can be expanded in the QNM basis [137]

$$\mathbf{E}_d(\mathbf{r},\omega) = \mathbf{E}_{inc}(\mathbf{r},\omega) + \mathbf{E}^s_{inc}(\mathbf{r},\omega) = \mathbf{E}_{inc}(\mathbf{r},\omega) + \sum_m \beta_m(\omega)\tilde{\mathbf{E}}_m(\mathbf{r}) \tag{III.2}$$

where $\tilde{\mathbf{E}}_m$ denotes the electric-field distribution of the m$^{\text{th}}$ QNM. The coupling coefficient $\beta_m(\omega)$ is expressed as a spatial overlap integral between the incident laser field $\mathbf{E}_{inc}$ and the QNM field $\tilde{\mathbf{E}}_m$ [137]

$$\beta_m(\omega) = \frac{\omega}{\tilde{\omega}_m - \omega} \iiint_{V_{cav}} \Delta\epsilon(\omega,\mathbf{r})\mathbf{E}_{inc}(\omega,\mathbf{r}) \cdot \tilde{\mathbf{E}}_m \tag{III.3}$$

where the integral runs over the volume of the cavity V_{cav} since $\Delta\epsilon(\omega,\mathbf{r})$ denotes the difference between the cavity permittivity and the background permittivity.

We arrive at the most important factor responsible for the collective coherent response: the third term in Eq. II.34 in chapter II: $\overleftrightarrow{\Delta\mathbf{G}}(\mathbf{r}_l,\mathbf{r}_j,\omega)\cdot\boldsymbol{\mu}_j$. It represents the field scattered at $\mathbf{r}_l$ by the cavity illuminated by a dipole $\boldsymbol{\mu}_j$ at $\mathbf{r}_j$. Using a QNM expansion [137] the scattered field at $\mathbf{r}_l$ due to dipole j reads as

$$\frac{\omega^2}{\epsilon_0 c^2}\overleftrightarrow{\Delta\mathbf{G}}(\mathbf{r}_l,\mathbf{r}_j,\omega)\cdot\boldsymbol{\mu}_j = \sum_m \frac{\omega}{\tilde{\omega}_m - \omega}\Big(\tilde{\mathbf{E}}_m(\mathbf{r}_j)\cdot\boldsymbol{\mu}_j\Big)\tilde{\mathbf{E}}_m(\mathbf{r}_l) \tag{III.4}$$

The $N \times N$ matrix $\Delta\mathcal{G}$ is then given by $\Delta\mathcal{G}(\omega) = \sum_m \omega(\tilde{\omega}_m - \omega)^{-1}\mathbf{u}_m \otimes \mathbf{u}_m$ where $\mathbf{u}_m$ is the column vector such that $\mathbf{u}_{m,l} = \tilde{\mathbf{E}}_m(\mathbf{r}_l)\cdot\mathbf{e}_l$. A great advantage is that the dependency on ω of every elements $\vec{\mathcal{E}}$, $\Delta\mathcal{G}$ or $\mathcal{G}_0$ is now known analytically, allowing for a direct computation of all the eigenfrequencies $\tilde{\omega}$ of the dipole ensemble.

As $\Delta\mathcal{G}$ is naturally cast into a polynomial expansion in $\tilde{\omega}$, the linear system of Eq. II.44 in the absence of driving field ($\vec{\mathcal{E}} = 0$) can be formulated as a polynomial eigenproblem of degree $4 + N_{\text{QNM}}$, where N_{QNM} is the number of QNMs retained in the expansion. Equation II.48 from chapter II becomes

$$(\frac{\tilde{\omega}}{\tilde{\Omega}}-1)(\frac{\tilde{\omega}}{\tilde{\Omega}})^3\mathcal{I}+\frac{4\pi\epsilon_0\rho}{\tilde{\kappa}^3}\frac{\tilde{\omega}}{\tilde{\omega}_m-\tilde{\omega}}\mathbf{u}_m\otimes\mathbf{u}_m+\rho(\mathcal{S}(\frac{\tilde{\omega}}{\tilde{\Omega}})^3+\mathcal{T}(\frac{\tilde{\omega}}{\tilde{\Omega}})^2+\mathcal{U}\frac{\tilde{\omega}}{\tilde{\Omega}}+\mathcal{V}) \tag{III.5}$$

The system from Eq. II.44 can thus be solved as a polynomial eigenvalue problem

$$\begin{aligned}(\frac{\tilde{\omega}}{\tilde{\Omega}})^5\mathcal{I}-\Big[(1+\frac{\tilde{\omega}_m}{\tilde{\Omega}})\mathcal{I}+\rho\mathcal{S}\Big](\frac{\tilde{\omega}}{\tilde{\Omega}})^4+\Big[\frac{\tilde{\omega}_m}{\tilde{\Omega}}\mathcal{I}+\rho(\mathcal{T}-\frac{\tilde{\omega}_m}{\tilde{\Omega}}\mathcal{S})\Big](\frac{\tilde{\omega}}{\tilde{\Omega}})^3+\rho(\mathcal{U}-\frac{\tilde{\omega}_m}{\tilde{\Omega}}\mathcal{T})(\frac{\tilde{\omega}}{\tilde{\Omega}})^2\\+\Big[\frac{4\pi\epsilon_0\rho}{\tilde{\kappa}^3}\mathbf{u}_m\otimes\mathbf{u}_m+\rho(\mathcal{V}-\frac{\tilde{\omega}_m}{\tilde{\Omega}}\mathcal{U})\Big]\frac{\tilde{\omega}}{\tilde{\Omega}}-\rho\frac{\tilde{\omega}_m}{\tilde{\Omega}}\mathcal{V}\end{aligned} \tag{III.6}$$

III.1.c Example of a metal nanorod

As an example, we consider in the following a gold nanorod (diameter $D = 30\ nm$, length $L = 100\ nm$) in a host medium of refractive index $\sqrt{\epsilon_{host}} = 1.5$. This cavity was extensively studied in Refs. [133, 137, 138]. In order to have an analytical expression of the gold permittivity for complex frequencies, we assume that it follows a classical Drude model, $\epsilon_P = 1 - \frac{\omega_p^2}{\omega^2+i\gamma\omega}$, with $\omega_p = 1.26 \cdot 10^{16}$ Hz and $\gamma = 1.41 \cdot 10^{14}$ Hz. These values were fitted in Ref. [137] from tabulated data in Ref. [84]. The incident laser field $\mathbf{E}_{inc}$ is assumed to be a plane wave polarized parallel to the rod axis, as represented in Fig. III.1. The dipoles are described as classical oscillators with a resonant wavelength at 920 nm and a natural linewidth of $\gamma_0 = 75$ MHz in the host medium without the nanorod.

The electromagnetic response of the nanorod is dominantly driven by the fundamental z-polarized electric-dipole resonance mode. This dipole-like QNM frequency is $2\pi c/\tilde{\omega}_m = 920 + i47\ nm$ [137], which matches the dipole transition frequency. The quality factor of this QNM is about 10. To calculate the resonance-mediated interaction matrix $\Delta\mathcal{G}$, the QNM should be normalized. The normalization procedure of resonance modes with complex frequencies is subtle [139–141]. It was performed by using the general method described in [137]. We show in figure III.1 the normalized electric-field along the rod axis ($|\tilde{E}_z|$) of this QNM mode.

III.2 Dipole doublets near a metal nanorod

Before analyzing the electromagnetic properties of a large collection of dipoles, we start with the simpler case of a dipole doublets. As represented in Fig. III.1 we consider doublets that are placed in the bright spots of the rod near field and that are well aligned with the QNM field: along the rod axis. To distinguish the impact of free-space interaction and Purcell

effects on the doublet properties, we consider two distinct configurations.

In the first case the dipoles are placed on the same side of the rod, at a distance d from the rod surface. The transverse separation distance between the dipoles is $t = 10\ nm$. In the second case the dipoles are placed on the opposite sides of the rod, keeping the same distance to the rod surface and the same transverse dipole-dipole separation t. In this way we keep unchanged the interaction of the dipoles with the localized plasmon, but we considerably reduce the direct interaction between the dipoles.

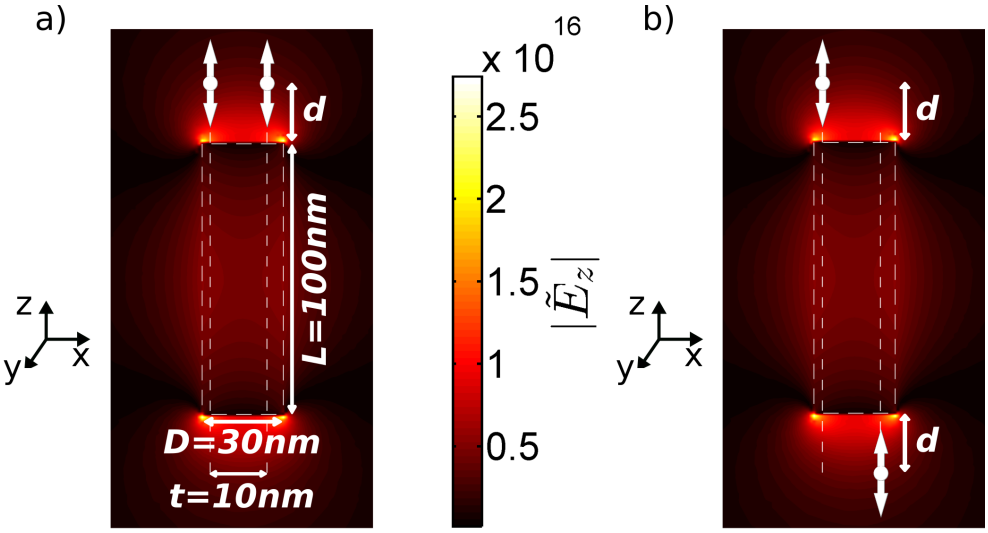

Figure III.1: A gold nanorod (diameter $D = 30\ nm$, length $L = 100\ nm$) is embedded in a host medium of refractive index 1.5. Normalized electric-field distribution along the rod axis $|\tilde{E}_z|$ of the dipole-like QNM with complex frequency $2\pi c/\tilde{\omega}_m = 920+47i\ nm$. Two dipoles, shown with white arrows, are oriented parallel to the nanorod long-axis and located at separation distance d from the nanorod surface. The transverse separation distance between the dipoles is $t = 10\ nm$. The dipole pair is shifted by 1 nm from the nanorod axis so that the asymmetric mode can be excited by the incident plane impinging normally to the plane of the figure with a polarization along the rod axis. We consider two configurations : the dipoles are located a) on the same side or b) on the opposite poles of the nanorod so that the interaction mediated by the QNM is the same while the direct dipole-dipole interaction is dramatically different.

III.2.a System eigenfrequencies

For each case the doublet eigenstates are formed by an asymmetric (dark/subradiant) mode denoted by "a" and a symmetric (bright/superradiant) mode denoted by "s" in figures III.2 and III.3. Fig. III.2 shows the evolution of the corresponding eigenfrequencies $\tilde{\omega}_a$ and $\tilde{\omega}_s$ with the distance d between the dipoles and the rod surface. These figures carry important hints that will be helpful for the analysis of systems with many dipoles.

First, the frequency shifts Δ (black lines) weakly depends on the distance d, but highly depends on the dipole-dipole separation distance $d_{dip-dip}$, increasing as $(kd_{dip-dip})^{-3}$ for small

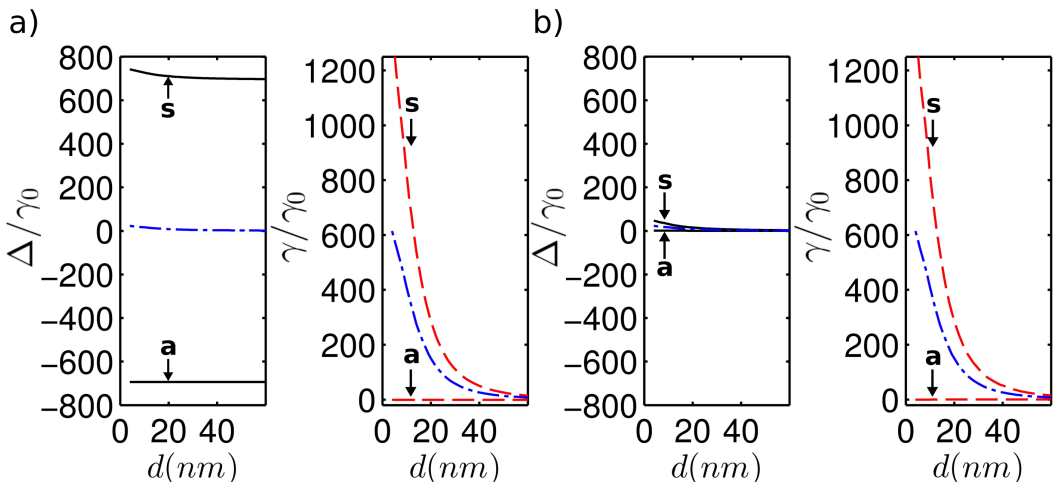

Figure III.2: We consider the two configurations shown in Fig. III.1: the dipoles are located a) on the same side or b) on the opposite poles of the nanorod so that the interaction mediated by the QNM is the same while the direct dipole-dipole interaction is dramatically different. We show the evolution of the frequency shift $\Delta/\gamma_0 = Re\{\tilde{\omega} - \widetilde{\Omega}\}/\gamma_0$ *and the linewidths* $\gamma/\gamma_0 = -2Im\{\tilde{\omega}\}/\gamma_0$ *of doublets as a function of the separation distance d from the nanorod surface, for the symmetric ("s") and asymmetric ("a") modes. For comparison we show the frequency shift and linewidth of one emitter placed and oriented along the rod axis (blue dash-dotted).*

$d_{dip-dip}$. Second, the linewidth $-2\text{Im}\{\tilde{\omega}\}$ (red dashed lines) of the subradiant eigenstate remain almost null for all distances to the rod: increasing from $0.1\gamma_0$ to γ_0. This is because the asymmetric mode weakly couple to the localized electric-dipole QNM for symmetry reasons. Third, the linewidth of the "s" eigenstate strongly increases for small d's, to become as large as $1200\gamma_0$ for distance $d < 10\ nm$. Note that in reality both linewidths dramatically increase at small distance $d < 10\ nm$ due to quenching, but this cannot be modeled with our single-QNM-expansion approximation. Finally we check that far from the nanorod the Purcell effect is weak while the frequency shift due to direct dipole-dipole interaction remains.

Comparing with the frequency shift and linewidth of a single dipole placed and oriented along the rod axis (blue dash-dotted line in Figs. III.2a and III.2b), we notice that the features due to the rod are about twice larger for the doublets. Hence the decay-rate acceleration that preferentially impacts the superradiant mode is the analogue for doublets of the traditional Purcell effect.

III.2.b Spectral analysis

To illustrate how these eigenfrequencies affect the optical response of the system {dipole doublet+nanorod}, we now investigate the scattering and absorption cross sections. We illuminate the system with an incident plane wave impinging normally to the plane of the figure III.1 with a polarization along the rod axis. We set each dipole at $d = 15\ nm$ from

the rod surface. The resulting scattering and absorption cross sections of the ensemble are shown in figure III.3.

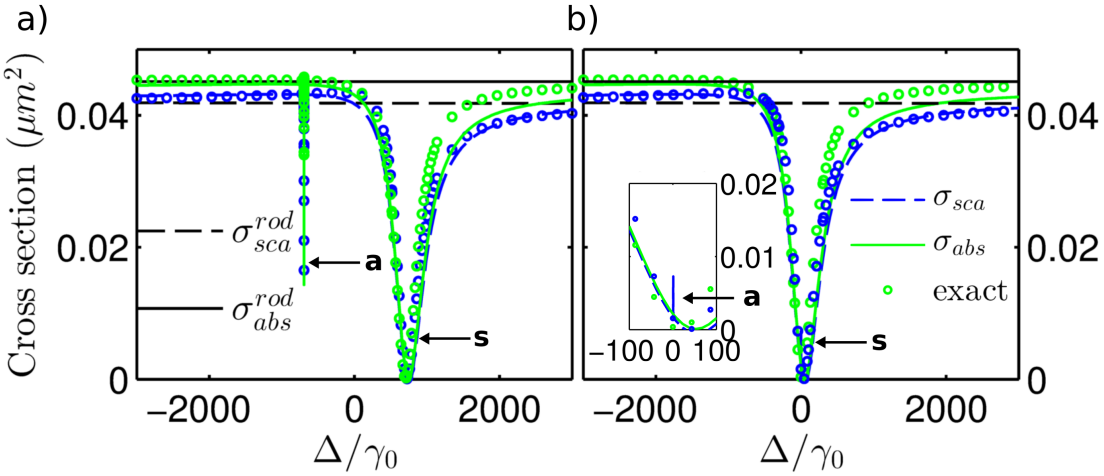

Figure III.3: We consider the two configurations shown in Fig. III.1: the dipoles are located a) on the same side or b) on the opposite poles of the nanorod so that the interaction mediated by the QNM is the same while the direct dipole-dipole interaction is dramatically different. We set each dipole at $d = 15$ nm from the rod surface and we illuminate the system with an incident plane wave impinging normally to the plane of the figure III.1 with a polarization along the rod axis. We show the scattering (blue dashed line) and absorption (solid green line) cross sections of the system as a function of the normalized frequency detuning Δ from the dipole resonance at 920 nm. Circles represent the exact cross sections derived using a finite element method (COMSOL software). The scattering (dashed black line) and absorption (solid black line) cross sections of the nanorod without dipoles is shown for comparison. The resonance due to the symmetric (asymmetric) mode is designated with "s" ("a"). The inset in b) shows a zoom around $\Delta = 0$ to reveal the subradiant mode.

As each eigenvalue is a decay channel of the system, the observed spectra are directly correlated with the previous analysis. The broad dip, with a large linewidth, corresponds to the superradiant mode while the narrow peak is the subradiant mode. When the dipoles are close to each other (case shown in Fig. III.1a), the large frequency shifts observed in Fig. III.2a are recognized in Fig. III.3a: to higher energy for the superradiant "s" and to lower energy for the subradiant "a" state. When the dipoles are poorly interacting via free-space (case shown in Fig. III.1b), the resulting small shift makes it difficult to observe the subradiant state which is shown in the inset of Fig. III.3b.

Comparing with the scattering and absorption cross sections of the nanorod without dipoles (black lines in Fig. III.3a), we check that the dipoles only affect the optical properties close to their resonance. We further notice that the coupling of the dipoles with the nanorod results in dips in both scattering and absorption. These dips are due to a specific type of resonance resulting from the interference of a discrete state (superradiant or subradiant mode here) with a continuum of modes (QNM here), as proposed by U. Fano in 1961 [142]. Actually a large diversity of Fano resonances can be observed when a dipole is placed in the vicinity of a MNP [138]. For instance, we notice that the subradiant mode "a" in Fig. III.3b

results in a peak in both scattering and absorption. In the case of the dips observed in Fig. III.3, it may be explained as the result of a destructive interference, at the nanorod position, between the incident wave and the field scattered by the dipoles [143]. The dipoles thus efficiently dull the field in the nanorod, so that the latter weakly absorbs and scatters light. Furthermore the dipoles quantum yield was unitary $\eta_0 = 1$, yielding that all absorption is due to losses in the metal.

We emphasize that in a fully symmetrical dipole arrangement with respect to the nanorod symmetries, the incident field does not couple to the asymmetric state and only one dip would be observed in both scattering and absorption spectra. This is why we chose to shift the molecular system by 1 nm away from being completely symmetric. Therefore we do observe a narrow feature for both cases in Fig. III.3, although the cross section modifications are weak as the system is almost symmetric.

III.3 100-dipoles radiation near a metal nanorod

Here we investigate the cooperativity of the superradiant and subradiant states by studying the induced dipole moments distribution. Let us consider a collection of 100 dipoles randomly distributed and oriented within a 15 nm-thick cylindrical shell around the nanorod. As we consider the dipole-like QNM, the mode does not account for quenching so we set a 15 nm minimum distance between the dipoles and the rod surface. For the sake of clarity, we set a 10 nm minimum separation between neighboring dipoles so to avoid eigenstates with large frequency shifts.

III.3.a Spectra and eigenfrequencies

We first identify the superradiant and subradiant states by studying the cross sections spectra as well as the eigenvalues. Figure III.4a shows the scattering (σ_{sca}, dashed blue) and absorption (σ_{abs}, solid green) cross-section spectra of the decorated nanorod under illumination by a plane-wave polarized along the rod z-axis. Both spectra exhibit a series of sharp peaks superimposed on a spectrally broad ($\sim 10^3\gamma_0$) dip background. Various Fano-like responses are observed among the sharp peaks, due to the specific geometry of each mode. Note that the absorption and scattering cross-sections of the nanorod alone (without dipoles) are almost constant in this spectral range and are both approximately equal to 0.04 μm^2 (see Fig. III.2).

To help analyzing the spectra, we have also calculated the eigenstates of the system, shown

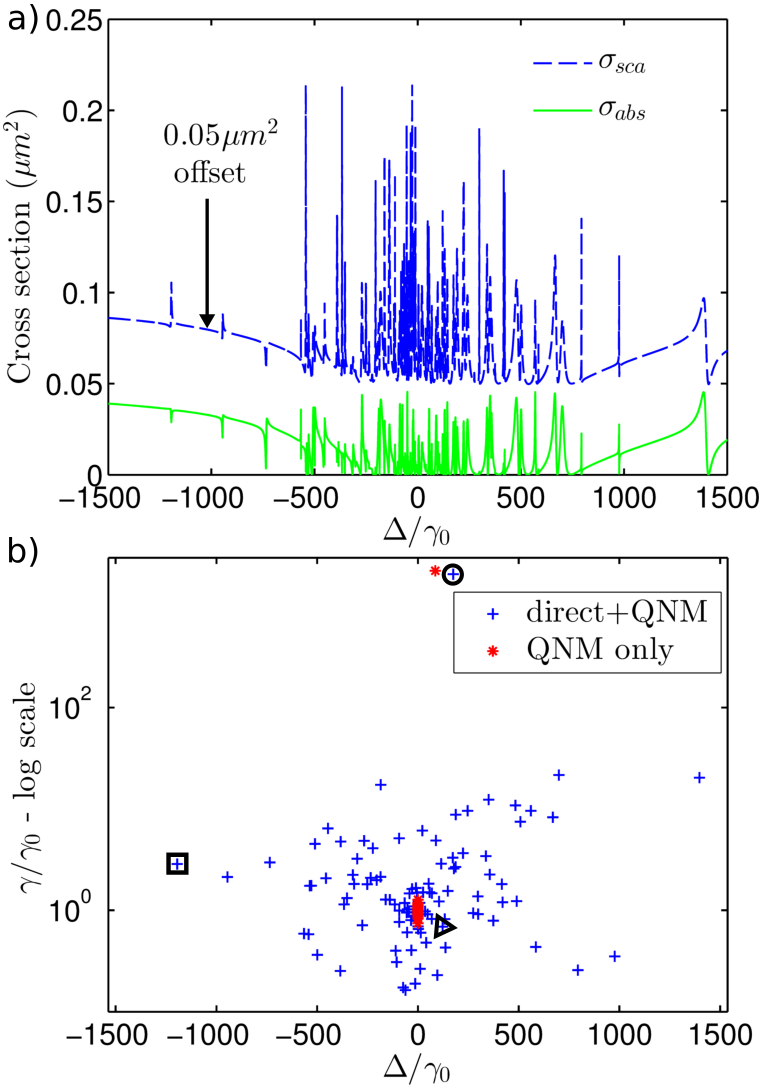

Figure III.4: A gold nanorod (diameter $D =$ 30nm, length $L = 100$ nm) embedded in a host medium of refractive index 1.5 is decorated with 100 dipoles, randomly distributed and oriented. a) Scattering (dashed blue line, shifted in y-scale for convenience) and absorption (solid green line) cross sections of the decorated nanorod under illumination by a plane wave polarized along the rod axis. b) The 100 corresponding eigenvalues $\tilde{\omega}$ are distributed according to their real and imaginary parts with y-log scale. Blue pluses correspond to the total interaction : direct dipole-dipole and QNM-mediated. Red dots correspond to QNM-mediated interaction only, without the direct interaction. Black square, triangle and circle designate the eigenstates discussed in figure III.5.

in Fig. III.4b with blue pluses in a log scale. We find a single superradiant state accompanied by a myriad of subradiant states. Careful inspection evidence a one-to-one correspondence between the sharp peaks in Fig. III.4a and the eigenfrequencies in Fig. III.4b. The broad background dip in Fig. III.4a is attributed to the superradiant state, which shows a large linewidth ($\sim 10^3\gamma_0$).

III.3.b Induced dipole-moments distributions

To investigate the cooperativity of the eigenstates, we estimate the induced dipole-moments distribution, by inverting the system from Eq. II.45 in chapter II. For each eigenstate, the calculated eigenvector $\vec{\boldsymbol{\mu}} = (\overline{\mu_1}, ..., \overline{\mu_N})$ describes the normalized induced dipole moments distribution in the system ($\sum_{l=1}^{N} |\overline{\mu_l}|^2 = 1$). Figure III.5 represents the dipole-moments distribution for 3 eigenstates that are characteristic of the variety of observed modes in this very case and in all similar configurations. Each dipole l is colored according to its normalized dipole moment $|\overline{\mu_l}|$.

We consider that an optically involved dipole shows a non-zero dipole moment amplitude $|\overline{\mu_l}|$. We then define the participation number of each mode $p = (\sum_{l=1}^{N} |\mu_l|^4)^{-1}$ [144]. This variable $1 \leq p \leq N$ not only estimates the collectivity of the mode but also its spatial extension [145].

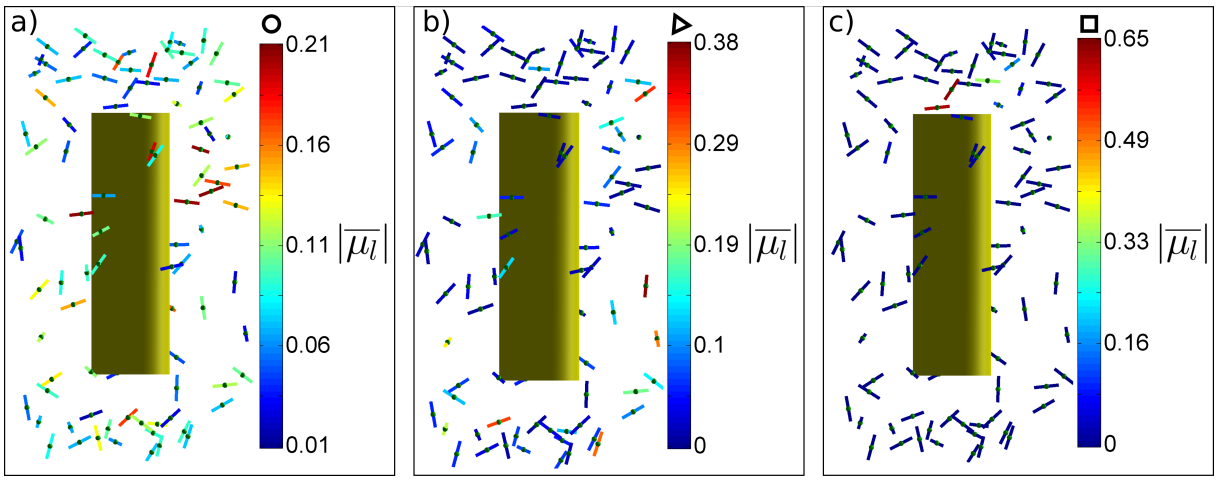

Figure III.5: A gold nanorod (diameter $D =$ 30nm, length $L = 100$ nm) embedded in a host medium of refractive index 1.5 is decorated with 100 dipoles, randomly distributed and oriented. Schematic representation of the induced dipole-moment distribution $\vec{\boldsymbol{\mu}} = (\overline{\mu_1}, ..., \overline{\mu_N})$, under illumination by a plane wave polarized along the rod axis, for a) the superradiant mode, b) an extended subradiant mode and c) a localized subradiant mode. Each dipole l is colored according to its normalized dipole moment $|\overline{\mu_l}|$, which is estimated by inverting Eq. II.45. The corresponding eigenfrequencies are designated in figure III.4b by a a) circle, b) triangle or c) square symbol.

The schematic shown in Fig. III.5a represents the distribution of the dipole moments

$(\overline{\mu_1}, ..., \overline{\mu_N})$ for the superradiant state : $-2\text{Im}\{\tilde{\omega}\} \approx 1030\gamma_0$. We observe that a large proportion of dipoles ($p = 47$) sustain a significant dipole-moment and are thus optically active in the mode, revealing strong cooperativity and spatial extension of the superradiant state.

Among the subradiant modes, approximately 69% have a participation of at least 5 dipoles. They are similar to the subradiant mode shown in figure III.5b ($p = 15$). Therefore these subradiant modes are spatially extended over tens of nanometers and are designated as extended subradiant modes [146]. We notice that these collective subradiant states involve up to 21 of the dipoles. Still, none of the subradiant states is as collective/extended as the superradiant state. On the contrary 31% of the subradiant states are similar to the one represented in Fig. III.5c ($p = 3$), with the participation of two to five dipoles. These modes involve neighbor dipoles and are thus spatially localized modes with low cooperativity. Actually in the case shown in Fig. III.5c, the active dipoles are about 10 nm away from each other and the two most active dipoles are roughly collinear. As a result, their dipole-dipole interaction dominates the system response, as confirmed by the large frequency shift: $\Delta \approx -1200\gamma_0$. We emphasize that the proportion of extended and localized subradiant modes depends on the dipole distribution.

We represent the cooperativity of the subradiant states in figure III.6. We clearly see

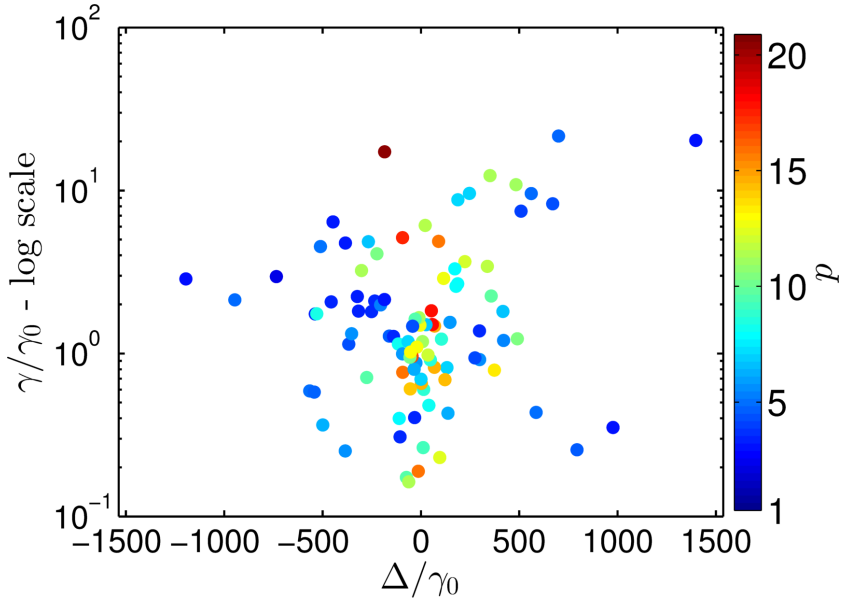

Figure III.6: A gold nanorod (diameter $D =$ 30nm, length $L =$ 100 nm) embedded in a host medium of refractive index 1.5 is decorated with 100 dipoles, randomly distributed and oriented. The 100 corresponding eigenvalues $\tilde{\omega}$ are distributed according to their real and imaginary parts with y-log scale. Each dot is colored according to the participation number p of the respective eigenmode.

that the subradiant modes with a large frequency shift Δ are localized modes: $p \leq 5$. It confirms that the direct dipole-dipole interaction is responsible for these strongly shifted

modes. However a localized subradiant mode can show a small frequency shift, it depends on the relative position of the neighbor dipoles that are involved in the mode.

Finally we have performed the system diagonalization but neglecting the direct interaction : $\mathcal{G}_0 = 0$. The obtained eigenfrequencies are shown with red dots in Fig. III.4b. As expected, the superradiant state weakly depends on the direct interaction. In contrast the cloud of subradiant states becomes degenerate with small shifts, confirming that the direct dipole-dipole interaction is responsible for the large shifts. We have verified that the cooperativity of all subradiant states then increases, with 15 to 36 of active dipoles.

III.4 Ensemble average

In experimental systems with atoms or molecules coupled to micro or nanocavities, the exact positions and orientations of the emitters are usually not precisely known. Thus it is important to study the effective optical properties that remain when averaging over the emitter positions and orientations. In section II.4.b.iii of chapter II we predicted that, for a spherical nanohybrid, the average of the 3 superradiant decay rates scales with the number of dipoles and that this trend survives in average. Here we perform the same investigation for the nanorod and see how this trend is affected by the cavity properties.

The dipoles are randomly distributed and oriented within a 15 nm-thick cylindrical shell around the nanorod. We set a 15 nm minimum distance between the dipoles and the rod surface. As the nanorod is described by the dipole-like QNM only, a given configuration exhibits one superradiant state. We thus estimate the average decay rate $< \gamma_{sup} >$ of this superradiant state by averaging over the dipoles position and orientation.

We show in figure III.7 the evolution of $< \gamma_{sup} >$ as a function of the number N of dipoles. We propose to compare three cases: QNM-mediated interaction only (red triangles) and both direct and QNM-mediated interactions with $t_{min} = 10\ nm$ (blue squares) or $t_{min} = 2\ nm$ (cyan circles) minimum separation distance. Note that the case where we consider only the QNM-mediated interaction does not corresponds to a physical situation since we set $\mathcal{G}_0 = 0$. However it allows to clearly identify what is due to the plasmon-mediated interaction.

In all cases Fig. III.7 evidences that the average decay rate of the superradiant state scales with N for a nanorod-mediated interaction. We deduce that the properties reported in Fig. III.7 are general, as they were observed in chapter II and are expected to be observed with any nanohybrid. The existence of a superradiant state (or several in case of degeneracy, e.g. sphere) is an intrinsic property of the cavity, not of the exact position of the dipoles. Indeed, the dominant effect of the electromagnetic resonance is a renormalization of the interaction

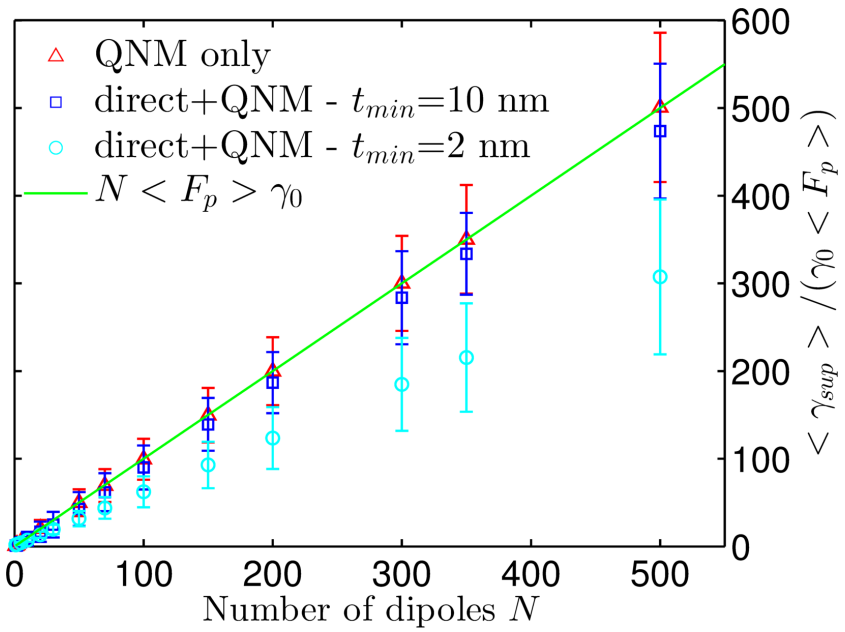

Figure III.7: A gold nanorod (diameter $D =$ 30nm, length $L = 100$ nm) embedded in a host medium of refractive index 1.5 is decorated with N dipoles, randomly distributed and oriented. Evolution of the normalized average decay rate of the superradiant state with the number N of dipoles. The model accounts for the QNM-mediated interaction only (red triangles) or for both direct and QNM-mediated interaction with $t_{min} = 10$ nm (blue squares) or $t_{min} = 2$ nm (cyan circles) minimum dipole-dipole separation distance.

between the dipoles. The reinforcement of the interactions helps observing collective effects, such as spasing in nanohybrids [27] or superradiance for atoms trapped in the near field of a photonic waveguide [75].

Because the dipoles are randomly oriented and placed at different distances from the rod surface, they do not experience the same Purcell effect, we thus consider the averaged Purcell factor $< F_P > \approx 20$, which is an intrinsic property of the nanohybrid geometry. Strikingly, without the direct interaction, $< \gamma_{sup} >$ is equal to the product of $N\gamma_0$ (like in the classical Dicke effect) by the Purcell factor $< F_P >$.

$$< \gamma_{sup} > = N < F_P > \gamma_0 \tag{III.7}$$

Equation III.7 is shown with the solid-green line in figure III.7 and perfectly fits the red triangles.

It was reported that cooperative radiation is altered for small dipole-dipole separation and may even be destroyed for extremely close dipoles [37]. Accordingly we observe in Fig. III.7 that, when the model accounts for the free-space interaction, the smaller the dipole-dipole separation the more the decay rate deviates from the law introduced in Eq. III.7. This is a clear evidence that the excitation of localized subradiant states, where dipole-dipole interac-

tion dominates, prevents the realization of hybrid states with large decay rates by combining Dicke and Purcell effects. In this perspective it would be interesting to study microcavities with larger mode volumes and larger quality factors, which may allow to investigate situations with a larger number of dipoles experiencing identical Purcell factors F_P.

III.5 Conclusion

We have proposed an explicit and efficient approach to derive the response of large ensembles of atoms or molecules near an engineered optical resonance. The use of the Quasi-Normal modes formalism allowed to analytically solve arbitrary systems while considerably lower the computational burden. Taking advantage of the introduced formulation, we have demonstrated that large frequency shifts are mainly due to the direct dipole-dipole interaction while large decay rates were attributed to the plasmon-mediated interaction. Then we showed that the direct interaction is responsible for localized subradiant modes, that alter the cooperative radiation.

We recovered the fact that the decay rate of a superradiant mode scales with the number of dipoles and evidenced that this trend survives after averaging over the dipoles position and orientation. Furthermore we introduced the averaged Purcell factor as an intrinsic property of the cavity. Finally we proposed and verified an analytical expression for the superradiant decay rate in the case of a purely cooperative system, mediated by a single electromagnetic resonance.

To go further the model may be improved by considering dipoles with different resonant frequencies. Besides the cavity is described using the Green function formalism, without including the modification of its resonance frequency due to the presence of dipoles.

Chapter IV

Materials and methods

Contents

The aim of this chapter is to introduce the experimental materials and methods that were developed to investigate plasmonic superradiance. The theoretical investigation carried out in chapter II revealed that a relevant way to study plasmonic superradiance is to characterize the fluorescence decay rate of the system. Therefore section IV.1 briefly depicts the fluorescence process. Then section IV.2 describes the chemical synthesis of the nanohybrids, supported by structural characterization. Finally section IV.3 presents the experimental methods used to measure fluorescence decay rates from ensemble and single particle measurements.

IV.1 Principle of fluorescence by a molecule

As introduced in chapter I, we describe a fluorescent molecule as a two-level system. The 1st electronic excited state S_1 and the ground state S_0 are represented in the Jablonski diagram in figure IV.1a. The absorption (green arrow) and fluorescence (orange arrow) of a photon corresponds to a transition (in energy) between these electronic levels, upwards and downwards, respectively. We show in figure IV.1b the typical absorption and emission spectra of a solution of Rhodamine B (RhB) molecules in ethanol, acquired with a commercial spectrofluorometer (JASCO FP-8300).

In addition to the electronic states, a molecule has vibrational degrees of freedom. As a consequence, both electronic states show a manifold of vibrational states at room temperature, as represented in figure IV.1a. Typically, a short laser pulse ($\approx$ 100 fs width) excites a molecule in one of these vibrational states of the electronic excited state (green arrow Fig. IV.1a). It results in additional wings on the blue side of the absorption peak (see Fig. IV.1b). Once excited, the emitter first relaxes non-radiatively in the lowest vibrational state of S_1 ($\nu' = 0$) (solid black arrow Fig. IV.1a) within few picoseconds. Then the decay to the ground state S_0 occurs via the emission of a photon (radiative recombination: orange arrow Fig. IV.1a) or via non-radiative processes (dashed arrow Fig. IV.1a) within few nanoseconds, with respective probabilities γ_r and γ_{nr}. The decay time of the electronic excited state is then

$$\tau = \frac{1}{\gamma_r + \gamma_{nr}} \tag{IV.1}$$

Here we consider small and rigid fluorescent molecules having a large probability to fluoresce: the quantum yield is typically larger than 50%. The radiative decay often ends up in a vibrational state, so the emitted photon energy is smaller than the excitation energy. In other words the fluorescence peak is red-shifted as compared to the absorption, as observed

in Fig. IV.1b. This red-shift is called the Stokes shift. Finally the emitter relaxes to its ground state ($S_0, \nu' = 0$) by the creation of phonons in the hosting medium (solid black arrow Fig. IV.1a).

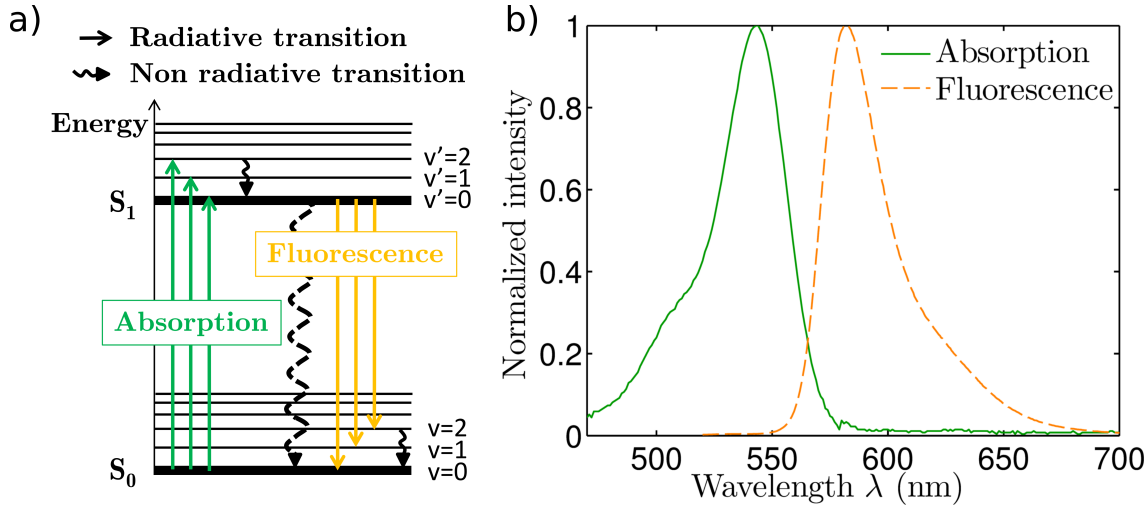

Figure IV.1: a) Jablonski diagram of a two-level system showing the steps involved in fluorescence. The thick lines are the lowest energy levels of each electronic state. The thin lines indicate the vibrational levels. b) Absorption (solid green line) and fluorescence (dashed orange line) spectra of Rhodamine B isothiocyanate in ethanol.

IV.2 Materials

The nanohybrids consist in a gold nanosphere surrounded by a silica shell. Two core diameters were studied during this doctorate thesis.

- $D_2 = 86 \pm 8\ nm$ for preliminary results based on previous investigations by Mélanie Ferrié during her doctorate thesis [147], as well as Sébastien Dupuy and Cédric Laval during their internships in 2011 and 2012, respectively.
- $D_1 = 57 \pm 3\ nm$ corresponding to the optimal plasmonic core size found from the theoretical study performed in chapter II.

The "bottom-up" synthesis procedure, performed by Miguel Comesaña-Hermo, is largely inspired from the doctorate thesis of Mélanie Ferrié and is briefly described in this part.

IV.2.a Core-shell nanohybrid synthesis

IV.2.a.i Synthesis of gold metal sphere

The gold nanospheres are grown in aqueous solution using a seed-mediated approach according to the procedure described in [148,149]. It first consists in reducing hydrogen tetrachloroaurate (III) $HAuCl_4$ (393.83g/mol) in the presence of a stabilizing agent: the sodium citrate $Na_3C_6H_5O_7.2H_2O$ (294.1g/mol, Aldrich). This step is carried out at T=127°C to produce seeds with small dispersion in size distribution. Then the reaction was finished by cooling to 105°C and diluting the solution. We thus obtain a seed solution (typically 46 ± 4 nm diameter) where 2mL of Na citrate and 1mL of $HAuCl_4$ are introduced sequentially to progressively grow the nanoparticles size.

Figures IV.2a and IV.2b show Transmission Electron Microscopy (TEM) micrographs of the synthesized objects for the two diameters $D_1 = 57 \pm 3$ nm and $D_2 = 86 \pm 8$ nm. We also show the corresponding size distribution histograms in Fig. IV.2c. Note that 57 nm diameter spheres show a smaller dispersion of size distribution (5% relative width) and smoother surface than 86 nm diameter particles (10% relative width). Furthermore the extinction spectra of the gold nanoparticles dispersed in ethanol (Fig. IV.2d) show a shift of the plasmon resonance to the long-wavelength side for increasing diameter [88]. This shift is in accordance with the theoretical discussion in chapter II and is mainly due the dynamic depolarization effect. Extinction spectra were acquired using a commercial UV-Vis spectrometer (Perkin Elmer Lambda 950).

IV.2.a.ii Coating with silica

The spherical gold particles are then coated with a silica shell according to the process published by Graf et al. [150]. In order to make the core surface vitriophilic (affinity for glass), poly(vinylpyrrolidone) (PVP) is first absorbed as a coupling agent. Then the system is transferred to ethanol prior to homogeneous silica growing by addition of silica precursor (tetraethylorthosilicate, TEOS). The thickness is controlled by varying the amount of TEOS. The coating consists in a sol-gel processing, using ammonia as a catalyst [151,152].

86 ± 8 nm diameter cores are coated with 15 ± 2 nm silica shell. Figure IV.3 shows the corresponding TEM micrograph, histogram and extinction spectra. Note the uniform and smooth silica shells, with relatively small dispersion in size (6% relative with) (Figs. IV.3a and b). We observe in Fig. IV.3c the dipole LSPP resonance of the gold nanoparticles at 556 nm. The silica shell shifts this LSPP resonance to the red (572 nm), as discussed in chapter II. In particular, since $\sqrt{\epsilon_{SiO_2}} = 1.48 > \sqrt{\epsilon_{EtOH}} = 1.36$ [153], the silica shell results

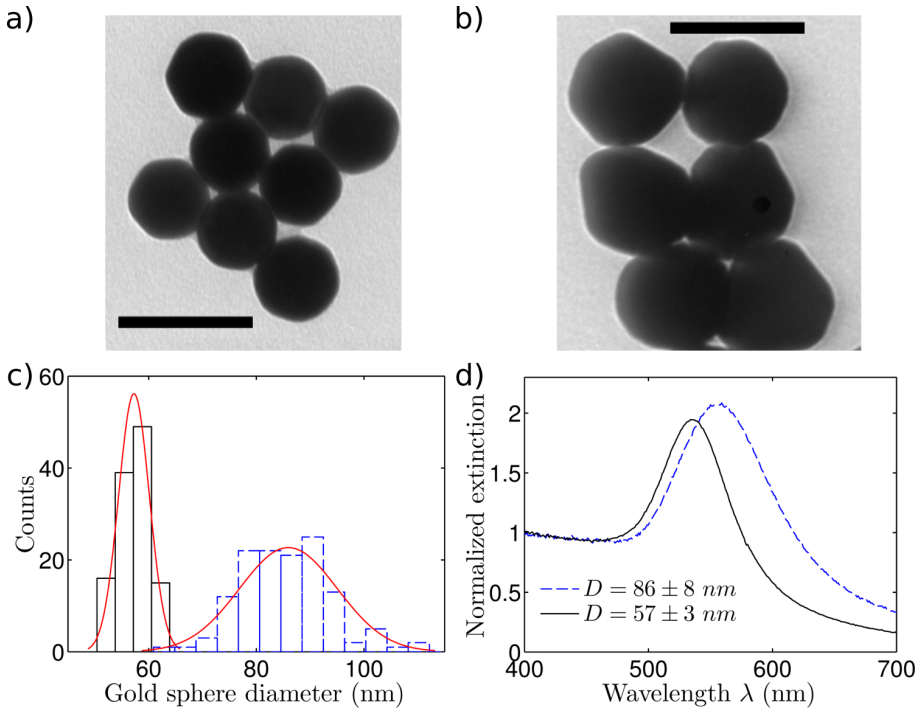

Figure IV.2: TEM images of the synthesized gold nanospheres with diameter a) $D = 57 \pm 3$ nm and b) $D = 86 \pm 8$ nm. Scale bar in both images: 100 nm. c) Histogram showing the gold nanosphere diameter distribution. Red lines are fits to a normal distribution. d) Extinction spectra of the synthesized gold nanospheres dispersed in ethanol. Dark solid line corresponds to $D = 57 \pm 3$ nm and dashed blue line to $D = 86 \pm 8$ nm.

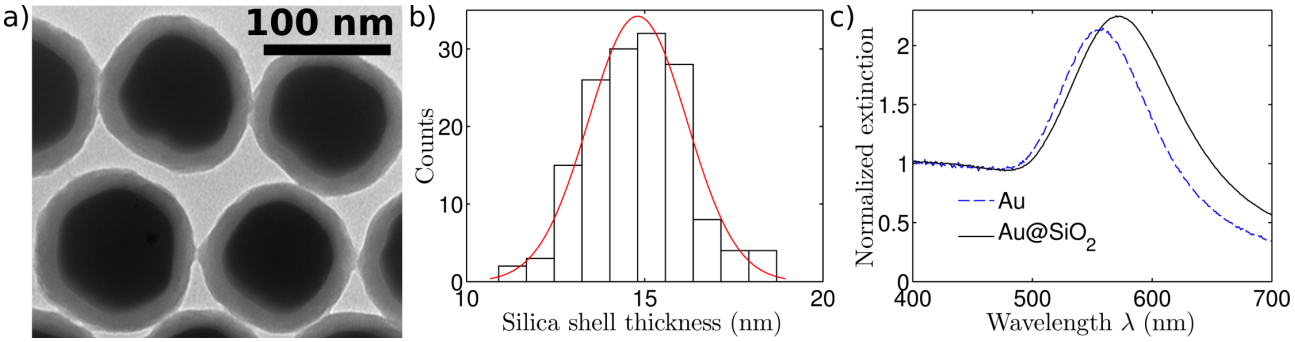

Figure IV.3: a)TEM images of the synthesized core-shell nanohybrids with $D = 86 \pm 8$ nm core diameter and $d = 15 \pm 2$ nm shell thickness. Scale bar: 100 nm. b) Histogram showing the corresponding silica shell thickness distribution: $d = 15 \pm 2$ nm. The red line is a fit to normal distribution. c) Extinction spectra of the synthesized $D = 86 \pm 8$ nm diameter gold nanospheres (blue dashed line) and silica coated gold nanospheres (dark solid line), dispersed in ethanol.

in an increase of the effective permittivity. We further note that the plasmon resonance is broadened by the coating: 73 THz without and 85 THz with the silica shell. This broadening is mainly due to the dispersion in size and shape of the silica shell. Indeed each of the hybrid shows a specific extinction spectrum due to its dimensions, yielding to an inhomogeneous broadening in ensemble measurements.

57 nm diameter cores are coated with varying silica shell thickness : $[11 \pm 3; 13 \pm 2; 18 \pm 2; 25 \pm 3; 37 \pm 3; 57 \pm 6]$ nm. Corresponding TEM micrographs and histograms are shown in figure IV.4. We observe uniform silica shells with relatively small dispersion in size for all thicknesses.

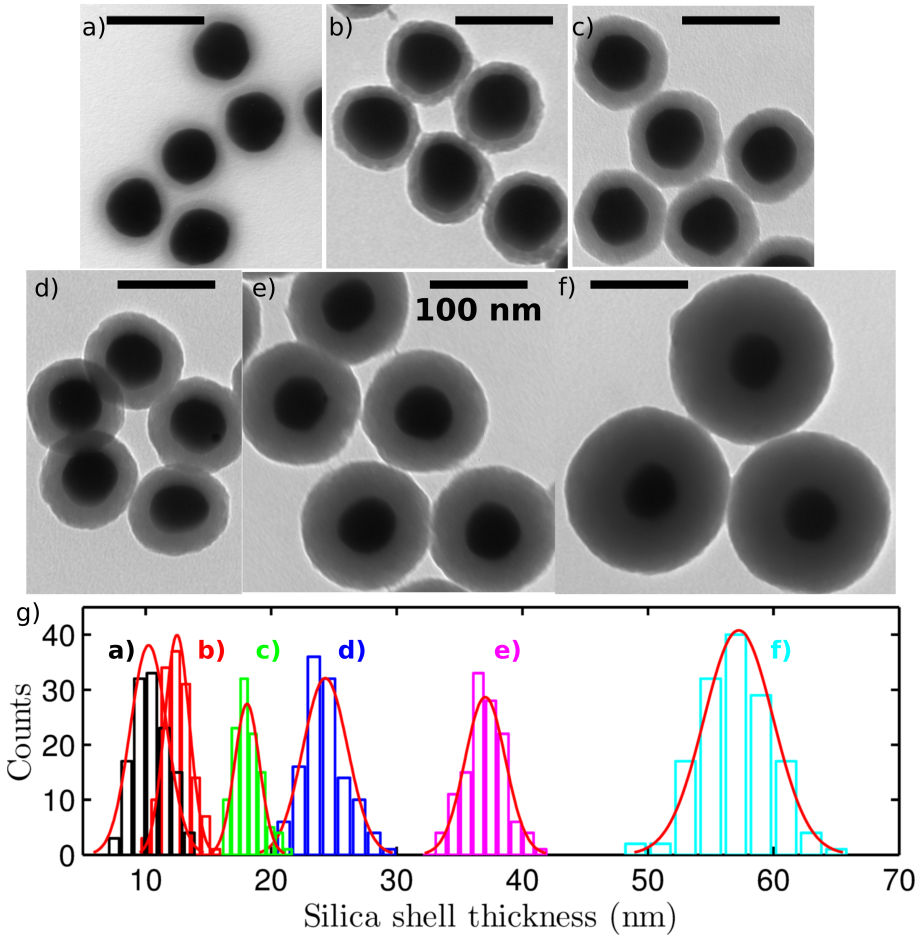

Figure IV.4: TEM images of the synthesized core-shell nanohybrids with $D = 57 \pm 3$ nm core diameter and a) 11 ± 3 nm, b) 13 ± 2 nm, c) 18 ± 2 nm, d) 25 ± 3 nm, e) 37 ± 3 nm, f) 57 ± 6 nm shell thickness. Scale bar: 100 nm. g) Histogram showing the silica shell thickness distributions for a $D = 57 \pm 3$ nm gold core .

IV.2.b Emitters grafting

The goal of this work is to study the coupling of emitters mediated by a plasmonic nanostructure. It is thus important that each emitter efficiently couples to the plasmon resonance. It implies an overlap between the plasmon resonance and both absorption and emission lines of the emitter [154]. Then another crucial requirement is the compatibility to grafting on silica surface. Eventually a decent quantum yield (larger than 50%) is required to collect sufficient fluorescence signal during the optical measurements. Following previous investigations [147], Rhodamine B isothiocyanate (RhB) is chosen to couple with 86 ± 8 *nm* diameter cores. While N-hydroxysuccinimide (NHS)-modified Atto532 (Atto-Tec) is coupled with 57 ± 3 *nm* diameter cores. RhB quantum yield in ethanol is 70% [155] and Atto532 quantum yield in water is 90% [156].

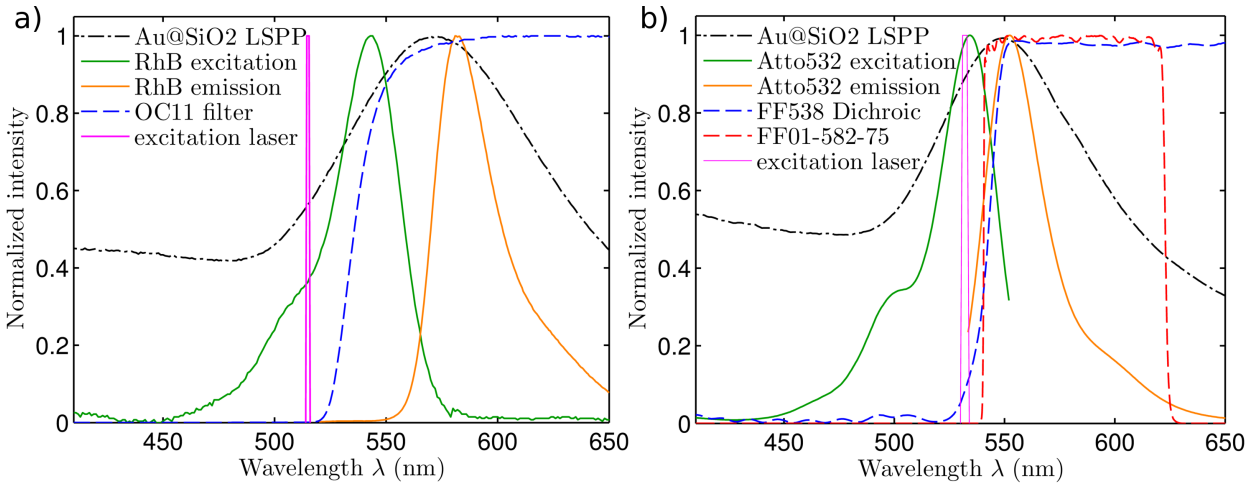

Figure IV.5: a) Au(D=86nm)@SiO_2(d=15nm) plasmon resonance spectrum in ethanol (black dash-dotted line), absorption and emission spectra of RhB in ethanol (dark green and orange solid lines), OC11 filter transmission spectrum (blue dashed line) and excitation line (magenta solid line) used experimentally. b) Au(D=57nm)@SiO_2(d=57nm) plasmon resonance spectrum in ethanol (black dash-dotted line), absorption and emission spectra of Atto532 (dark green and orange solid lines) in ethanol, FF538-Di01 Dichroic and FF01-582-75-25 filters transmission spectra (blue and red dashed lines) and excitation line (magenta solid line) used experimentally.

Excitation and emission spectra of the emitters are compared with their corresponding LSPP resonance in figure IV.5. We also show the transmission spectra of the spectral filters, as well as the excitation laser lines, used in the two experimental set-ups (see section IV.3). In order to perform single object study, the Atto-based samples will be embedded in a polymer matrix. We thus compare the Atto532 spectra with the LSPP resonance of hybrids having a 57 nm thick silica shell in ethanol. Indeed the solvent weakly affects the plasmon resonance at such a large distance from the plasmonic core, see chapter II. We check that absorption and emission of fluorescent molecules both overlap with the associated plasmon resonance.

Note in Fig. IV.5 that plasmon resonances are much broader than absorption and emission peaks of fluorescent molecules. We estimate the FWHM of the plasmon resonance $\mathrm{FWHM}_{LSPP} \approx 100$ THz, which is in agreement with the values discussed in chapter II. Note that the dispersion in size of the colloidal dispersion may also contribute to the spectrum broadening.

We now estimate the Full Width at Half Maximum (FWHM) of Atto532 absorption spectrum, ignoring the vibrational wing: $\mathrm{FWHM}_{em} \approx 30$ THz. We first emphasize that this value is 6 orders of magnitude larger than the typical excited state decay rate of these molecules in ethanol $\gamma_p \approx 50$ MHz. This observation clearly shows how crucial is the distinction between the dephasing rate γ_d and the population decay rate of the excited state γ_p, see I. In particular the molecule is dispersed in ethanol at room temperature so the emission linewidth observed in Fig. IV.5 is affected by the homogeneous broadening. Besides each molecule interacts with its immediate surrounding through the solvation process. As the local host environment varies from one molecule to another, the transition frequencies of the molecules are statistically distributed, yielding to an inhomogeneous broadening of the ensemble fluorescence spectrum [157]. For molecules like RhB or Atto, the homogeneous and inhomogeneous broadening are typically 20 THz [158–160]. This value is in agreement with the linewidth observed experimentally.

IV.2.b.i Grafting of the fluorescent molecules

The functionalization performed for both fluorescent molecules is adapted from van Blaaderen's paper [161]. The coupling agent between emitters and silica is the 3-aminopropyltriéthoxysilane (APTES). For RhB the molecules are first functionalized with APTES that will covalently attach to the silica surface. For Atto532 the core-shell nanohybrids are functionalized with APTES before adding the Atto molecules. In both cases the fluorescent solution is added to the nanohybrid solution under sonication to fastly homogenize the concentration and thus perform an uniform binding [123]. The procedure is carried out under ambient conditions. The objects are dispersed in ethanol and stored in a fridge to ensure a better colloidal stability [162]. All the vessels were protected from light with aluminium foil to avoid photobleaching of the fluorescent molecules during the chemical reactions. 7 centrifugation steps (4000 rpm, 20min) were carried out to separate decorated nanoparticles and free fluorescent molecules. According to TEM images and extinction spectra, the emitters grafting did not have an observable effect on the silica shell thickness and plasmon resonance.

We noted that Atto532 molecules have a reactive NHS-group that is hydrolyzed in the presence of oxygen. Stock solutions are thus handled and diluted under nitrogen atmosphere

in dimethyl sulfoxyde. Afterwards prepared fluorescent solutions and Atto-based nanohybrids dispersions are diluted in an ethanoic solution of Tween20 (0.05 $wt\%$) because the hydrolysis of the reactive NHS part is much slower in ethanol than in water [123].

IV.2.b.ii Estimation of the number of emitters per nanohybrid

Estimating the number of emitters that are attached to one hybrid is probably the most challenging part of this synthesis. Indeed the fluorescent molecules size is less than 1 nm, making the emitters difficult to observe and count under TEM observation. To our knowledge the only way to determine the number of emitters bound to a NP is to control the emitters quantity that is initially introduced and then to estimate the quantity remaining free in solution [123]. To do so we estimate the concentration of core shell particles from extinction spectra and deduce the needed amount of emitters. From the 7 centrifugation steps performed to extract free fluorescent molecules, the supernatants with the remaining molecules I_{sup} are compared to a reference sample containing the concentration of emitters that was added to the nanohybrids for grafting I_{ref}. The ratio of the integrated fluorescence intensities gives an estimation of the grafting yield η_{bind} :

$$\eta_{bind} = 1 - \frac{I_{sup}}{I_{ref}} \tag{IV.2}$$

The yields of fluorescent molecule attachment could be determined for all Atto-based samples and values above 70% were obtained. We show in appendix A a list of all the samples with the estimated binding yield, number of Atto532 per nanohybrid and deduced average distance between emitters.

In contrast, the binding yield could not be measured for RhB-based samples. In fact RhB molecules are so sensitive to pH that they may be used as pH sensors [163]. In the basic pH ethanol where the NPs are dispersed, RhB pH sensitivity is expressed by a deprotonation of the COOH-group that strongly affects the aromatic part - which is responsible for the emission of light - and results in a self-quenching of the fluorescence [155, 163]. Therefore the fluorescence intensity is not reliable and the estimation of the number of emitters cannot be performed with RhB-based samples.

IV.3 Experimental methods

IV.3.a Decay time measurement

An established method to estimate the decay time is the Time Correlated Single Photon Counting (TCSPC), as proposed by L. Bollinger and G. Thomas in 1961 [164]. This technique is based on the measurement of the delay between a pulsed optical excitation and the detection of the resulting emitted photon. In practice part of the excitation pulse is detected by a fast photodiode as a trigger. Then the system waits for the detection of a fluorescence photon by a sensitive detector: an avalanche photodiode (APD), a streak camera or a Photomultiplier (PM). The resulting time-lag is recorded and this experiment is repeated many times to build a reliable histogram, called fluorescence decay profile. In order to properly measure the evolution of the probability to decay with time, the excitation should be weak enough so that a single photon is detected per pulse. Otherwise only early photons are counted and the estimated decay time is biased.

The measured temporal decay profile $M(t)$ is then described as the convolution product of the Instrumental Response Function of the detection set-up $IRF(t)$ and the fluorescent system response $I(t)$

$$M(t) = IRF(t) * I(t) \tag{IV.3}$$

The decay of a single molecule corresponds to $I(t) = e^{-\gamma_p t}$. By fitting the experimental data with this model from Eq. IV.3, γ_p is obtained.

IV.3.b Ensemble measurement

IV.3.b.i Sample preparation

An ensemble measurement consists in characterizing a large number of objects. In this work, the objects of interest are core-shell nanoparticles decorated with fluorescent molecules, dispersed in ethanol. The measured solutions are so diluted (1 nanohybrid per 100 μm^3) that the nanohybrids freely diffuse without aggregating. This approach thus allows to directly estimate the average response of a single object. Notably the colloidal suspension is stable during hours at room temperature and the sample is stored in a fridge. Before fluorescence measurements we performed sonication during 30 seconds in order to separate aggregates that might be formed when the dispersion settles to the bottom of the containing tube.

IV.3.b.ii Optical set-up for ensemble measurements

The set-up that was used to perform ensemble measurements is represented in figure IV.6. A diode-pumped ytterbium oscillator from Amplitude System (t-Pulse 200) provides pulses

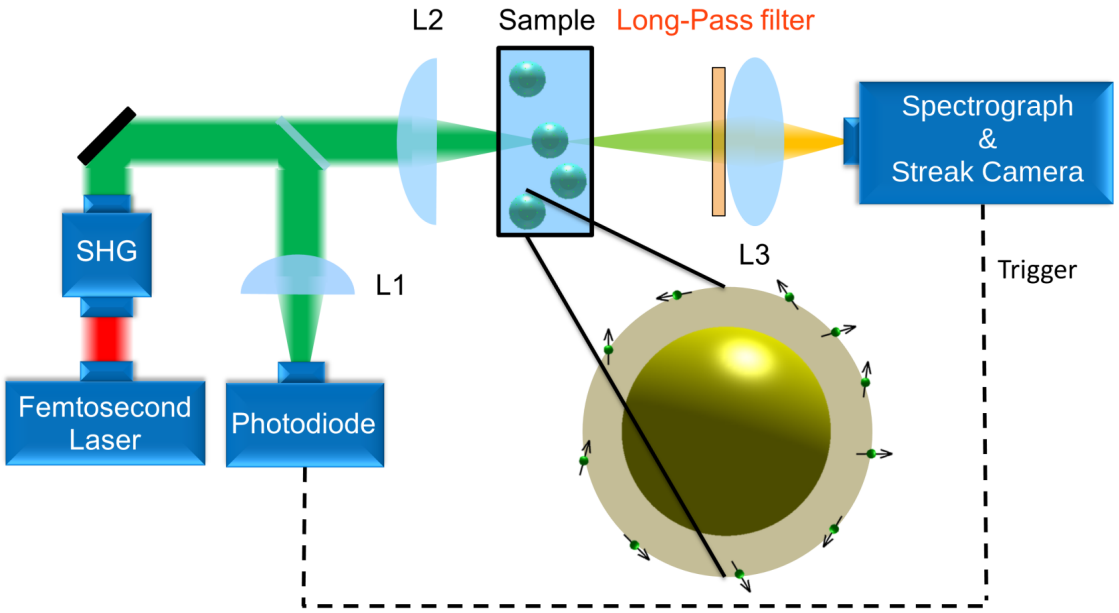

Figure IV.6: Diagram of the experimental set-up used to perform ensemble measurements. A femtosecond laser pulse excites nanohybrids in a colloidal dispersion. The resulting fluorescence signal is analyzed spectrally and temporally by a spectrograph coupled to a streak camera.

of 300 fs with a 10 MHz repetition rate at 1030 nm. Using a Second Harmonic Generation (SHG) crystal, we double the frequency to generate pulses at $\lambda_{exc} = 515$ nm. Part of the incident laser beam is focused ($f'_{L1} = 100\ mm$) onto a fast photodiode to generate the trigger signal. The remaining beam is then focused ($f'_{L2} = 50\ mm$) to a 1.5 mW, 100 µm-diameter spot that excites nanohybrids freely diffusing in ethanol in a 1 cm-thick quartz cuvette.

The resulting fluorescence signal is filtered by a 530 nm long-pass colored glass filter (OC11, see spectrum Fig. IV.5), before a lens ($f'_{L3} = 50mm$) collects it into a Czerny-Turner type spectrograph from Princeton Instruments (C11119-02). The signal is analyzed using a 150 lines/mm grating, corresponding to a 70 nm spectral range with 1 nm resolution. The spectrograph is coupled to a streak camera (Hamamatsu Streak scope C10627) that deflects the signal over time to generate temporal decay profiles. The temporal resolution is approximately 17 ps. We notice that the spectral selection performed by the grating filters out most of the laser beam, even in transmission configuration. Still the long pass filter is necessary for scattering samples such as nanoparticles.

IV.3.b.iii Streak plot

The coupling of a spectrograph with a streak camera allows to sort detected photons according to their wavelength and their arrival time, resulting in a streak plot. An example is given in figure IV.7 for RhB in ethanol. Integrating the signal over the wavelength (time), we observe

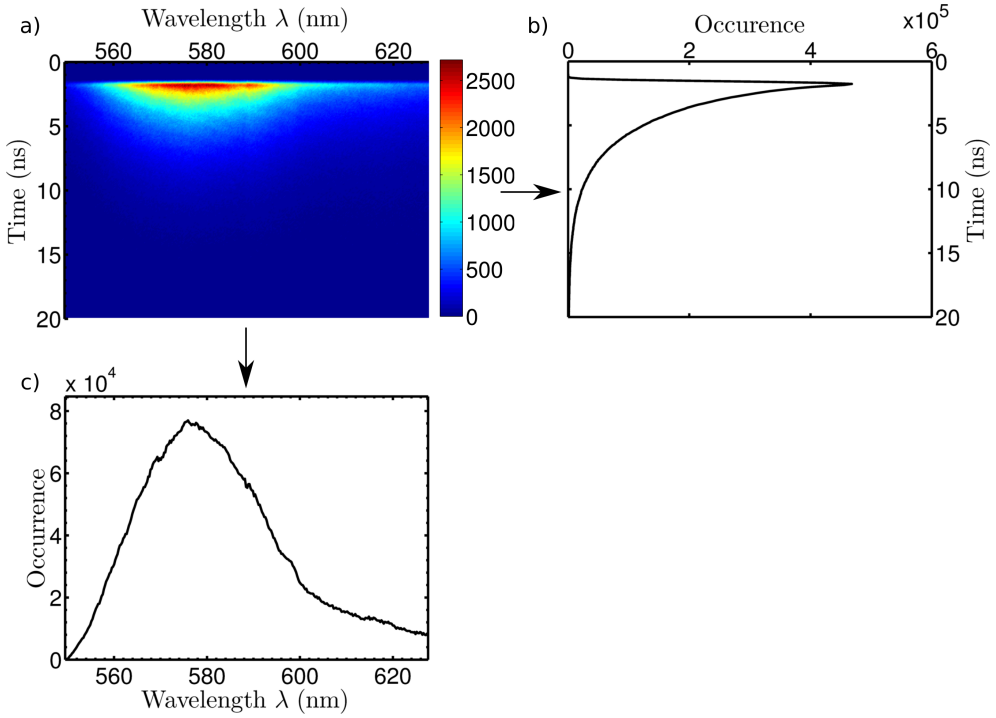

Figure IV.7: a) Spontaneous emission resolved in time and in energy (wavelength), for RhB molecules dispersed in ethanol. b) Temporal decay profile obtained by integrating over the whole spectrum. c) Fluorescence spectrum obtained by integrating from 0 to 10 ns.

the fluorescence temporal decay profile (spectrum) as shown in figure IV.7b (c). Furthermore, one may integrate over a selected part of the spectrum to deduce the decay profile for photons emitted within a specific energy window [165].

Besides photons are sorted along two dimensions, we thus have to accumulate the signal for 1 hour even though the streak camera is a sensitive device (typically 10% quantum efficiency). Eventually a time window larger than 5 times the expected decay time was set in order to allow an appropriate fit during the analysis. As a consequence only 30% of the lines Fig. IV.7a contain significant signal for the fluorescence spectrum. The spectrum is then obtained by integrating over a reduced time window, so to avoid excessive noise in the curve.

IV.3.b.iv Analysis of the fluorescence temporal decay profile

In ensemble measurements the signal is emitted by an ensemble of fluorescing systems. In the configuration represented in Fig. IV.6, the excitation volume is approximately 10^8 μm^3. So for a typical colloidal dispersion of nanohybrids (10^{10}nanohybrid/mL concentration), the streak plot is the result of the fluorescence of 10^6 nanohybrids. The fluorescence decay profile corresponds to the population relaxation and is thus not affected by the homogeneous and inhomogeneous broadening previously discussed. Therefore if all emitters have the same relaxation properties, the average decay profile appears as a monoexponential decay. For instance this is the case for RhB molecules dispersed in ethanol (figure IV.7). On the contrary each emitter grafted at the surface of a nanohybrid experiences a specific LDOS. As discussed in the previous section IV.2, nanohybrids show non-negligible dispersion in the sizes and shapes of the gold cores and the silica shells. Furthermore the number of grafted emitters is approximately known while their orientation is not controlled. The simulation performed in chapter II showed that the decay rate dramatically depends on each of these parameters. As a consequence the ensemble response of nanohybrids results in a non-exponential decay [166–168].

The possible configurations are so numerous that it is difficult to quantify the involved decay rates in a discrete way. The luminescence decay is then commonly described with a continuous distribution of decay rates

$$I(t) = I(0) \int_{\gamma=0}^{\infty} \phi(\gamma) e^{-\gamma t} \, \mathrm{d}\gamma \tag{IV.4}$$

where $\phi(\gamma)$ is a probability density function. The choice of the distribution $\phi(\gamma)$ should ideally be based on a theoretical model, using Monte-Carlo simulations for instance, making sure that there is a physical underlying distribution [169]. In the absence of a model, recovering the distribution without assumptions turns out to be an ill-conditioned problem, that is very sensitive to data quality [170, 171].

In the present system the decay time is highly sensitive to all the listed parameters, hence we do not expect to retrieve the distribution from our measurements. Still we are interested to estimate a non-biased average decay rate. We make the choice to use the stretched exponential [166], that has proven to be a flexible and successful fitting function [172]. The Kohlrausch-Williams-Watts (KWW) mathematical distribution, or stretched exponential, was introduced by R. Kohlrausch in 1854 [173] and applied to dielectric relaxation in 1970 [174]. It is usually defined by

$$I(t) = I(0) e^{-(\gamma_K t)^{\beta}} \tag{IV.5}$$

where $0 < \beta \leq 1$ is the stretching exponent, giving information about the variance of the underlying distribution: the latter gets broader as β decreases. For $\beta = 1$ we recover the monoexponential model. If $0.7 < \beta < 1$ one usually considers that the distribution is narrow enough to admit the average decay rate as representative of the system relaxation. The average decay rate [175] is given by

$$< \gamma >= \gamma_K \beta \frac{1}{\overline{\Gamma}(\frac{1}{\beta})} \tag{IV.6}$$

where $\overline{\Gamma}$ is the mathematical gamma function. The uncertainty on the estimated decay rate is then

$$\delta < \gamma >= \gamma \sqrt{(\frac{\delta\gamma_K}{\gamma_K})^2 + (1 - \frac{1}{\beta^3}\psi_0(\frac{1}{\beta}))\frac{\delta\beta^2}{\beta^2}} \tag{IV.7}$$

where $\overline{\psi_0}$ is the derivative of $\overline{\Gamma}$.

IV.3.c Single object measurement

As discussed in the previous part, ensemble measurement allows to estimate the average decay rate over a large population. Still the analysis does not provide reliable information on the other parameters of the decay times distribution. Besides results might be biased by unwanted emitting objects such as non-grafted emitters, or less probably by aggregated nanohybrids. A burdensome but very instructive alternative is to make statistics on single objects. It not only gives access to the decay time distribution but also insures the true nature of the single object signal which is measured. A tool of choice to achieve such measurement is the confocal microscope that was designed in 1955 by Minsky [176]. This technique aims at selecting a thin cross-section of the sample by rejecting the signal coming from out-of-focus planes (detailed in paragraph IV.3.c.iii).

IV.3.c.i Sample preparation

Confocal microscopy is a far field characterization technique so its resolution is limited by diffraction. The sample thus has to be sufficiently diluted in order to separate single objects once deposited in the hosting medium. To this end, we prepare a nanomolar solution with about 10^{11} nanohybrids per mL. In order to characterize a single nanohybrid, we enclose it in a homogeneous medium consisting in a polymer matrix, so that the nano-object stands still. For instance Polyvinyl Alcohol (PVA) offers a stable and non luminescent environment [177] that allows homogeneous dispersion of the nanohybrids, and is thus a support of choice for

single object spectroscopy [178]. In practice we add 10% (in volume fraction) of a 6.4 $wt\%$ PVA solution (0.79 g in 50 mL of highly purified - milli-Q grade - water) to the nanohybrid solution. The resulting mixture is spin-coated on a plasma-cleaned glass coverslip (2000 rpm, 2 min). The sample thus consists in single hybrids dispersed in an approximately 150 nm thick polymer matrix, with a density of about $0.1 NP/\mu m^2$.

To make sure that hybrids are characterized in a homogeneous medium, an additional polymer layer is spin-coated on the sample. Indeed the PVA-air interface would probably alter the emission properties since the nanohybrids diameter goes from 80 nm to 174 nm, especially for emitters located near the interface. To make sure that the hybrids remain in the PVA matrix which is hydrophilic, we choose an hydrophobic polymer : Poly(methyl methacrylate) (PMMA). Its thickness is about 600 nm (500 rpm, 1 min, 6 $wt\%$ in toluene), in accordance with Ref. [179].

The polymer thicknesses are estimated by making a scratch in the sample before measuring its depth using an Atomic Force Microscope. For example the image of a PVA layer spin coated on a glass substrate is given figure IV.8. We observe the deep due to a razor blade scratch and the polymer accumulated on either sides of the strip. Note that the polymer layer is homogeneous.

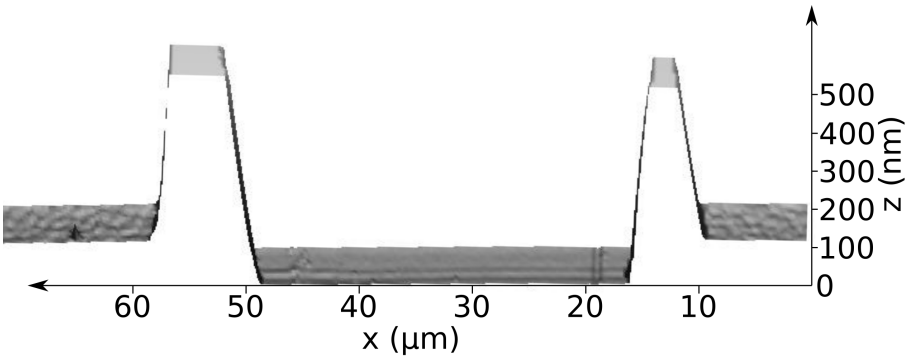

Figure IV.8: Atomic Force Microscope image of a PVA layer spin coated on a glass substrate. The PVA thickness is revealed by a scratch made with a razor blade and is estimated to be 169±2 *nm. This measurement was performed by Hassan Saadaoui in the CRPP.*

Noteworthy there is a refractive index matching between the silica shell, the polymer matrices and the coverslip at $\lambda_{em} = 553\ nm$: $n_{SiO_2} = 1.48$ [119], $n_{PVA} = 1.50$ [180], $n_{PMMA} = 1.49$ [181] and $n_{coverslip} = 1.51$. From the hybrid to the collection optics, this index matching avoids reflection and scattering of light at interfaces, thus helping to optimize the detection of the fluorescence.

IV.3.c.ii Single object imaging

If the probability to aggregate has proven to be negligible in a colloidal dispersion, the evaporation of solvent during the spin coating leads nanohybrids to form some aggregates in the polymer matrix. However the characterization of single nanohybrids requires the ability to identify non-aggregated particles.

In the Atto-based nanohybrids, the particles diameter is so large - 80 nm at minimum - that they can directly be observed in transmission bright field microscopy. In order to optimize the image contrast, we applied the widely used Köhler illumination [182, 183] that provides a homogeneous illumination of the sample.

Nevertheless, under light exposure, absorption-emission cycles of a fluorescent molecule cause chemical photoreaction that makes it unable to fluoresce, permanently. This phenomenon, called photobleaching, depends on the molecule structure and the surrounding environment. For instance it was reported that Atto532 photobleaching can be reduced by lowering the rate of the absorption-emission cycles using an excitation rate below 1 MHz [184]. As the decay rate of the nanohybrids is expected to be sensitive to the number of emitters, we need to avoid the photobleaching effect during the identification of single particles. Therefore we set a 610 nm long-pass colored filter (RG610 Schott) right after the light source, so that the fluorescent molecules are not excited during the observation in bright field microscopy. The observation wavelength is thus beyond 610 nm. The image of a single 80 nm diameter nanohybrid is then limited by the diffraction and has a 550 nm radius. It is then difficult to distinguish single nanohybrids from aggregates. The only difference thus lays in the image contrast. The silica shell and the hosting polymer have close refractive indexes, the contrast is thus mainly due to the extinction of the transmitted light by the gold core.

We show in figure IV.9b the calculated extinction cross section - using the Mie Theory - of a single monomer and compare it to the response of dimers with different silica shell thicknesses d. The system is embedded in a $\sqrt{\epsilon_{host}} = 1.5$ homogeneous medium and is illuminated by a plane wave, as represented in figure IV.9a. The gold core diameter is $D = 57\ nm$ so that the monomer exhibits a dipole LSPP resonance at 552 nm, in accordance with the experimental spectrum shown in figure IV.5b.

Concerning the dimers, we first observe that an aggregate of two gold nanospheres without silica shell exhibits two resonances at 546 nm and 680 nm, in accordance with the experimental observations in Ref. [185]. The optical properties of this dimer can be qualitatively described as two coupled springs or two interacting dipoles [186]. It shows a transverse (546 nm) and a longitudinal (680 nm) eigenmodes. Both modes are observed in Fig. IV.9b because the incident plane wave is polarized at 45° with respect to the dimer long axis, see

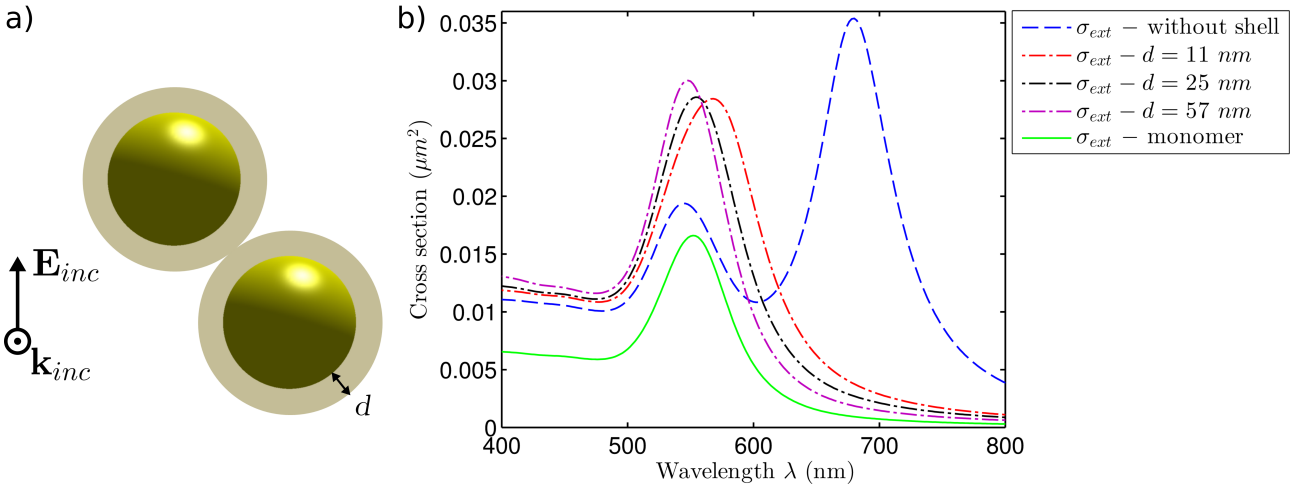

Figure IV.9: Two identical 57 nm diameter gold spheres, coated with a d thick silica shell, are aggregated and embedded in a homogeneous medium of refractive index $\sqrt{\epsilon_{host}} = 1.5$. *The system is illuminated by a plane wave impinging normally to the plane of the figure a) and linearly polarized* $\mathbf{E}_{inc}$. *b) Extinction cross sections of the dimer are calculated using the Mie theory without silica shell (dashed blue line) and for different silica shell thicknesses:* $d = 11$ *nm (dash-dotted red line),* $d = 25$ *nm (dash-dotted black line) and* $d = 57$ *nm (dash-dotted magenta line). For comparison we show the extinction cross section of a single core-shell particle with a* $d = 57$ *nm thick shell (solid green line).*

Fig. IV.9a.

As we increase the size of the silica shell d, the distance between the gold cores rapidly increases and the plasmon hybridization vanishes [187, 188]. As a result the extinction cross section for $d = 11$ nm consists in a slightly red shifted peak at 568 nm with a barely visible wing on the blue side. As d increases, the plasmon resonance shifts to lower wavelength to finally recover the resonance frequency of a monomer. We emphasize that, for the distances corresponding to the Atto-based nanohybrids ($11\ nm \leq d \leq 57\ nm$), the extinction cross section of a dimer is only slightly shifted as compared to the monomer.

Nevertheless notice in Fig. IV.9b that for wavelengths beyond 610 nm, the extinction cross section is at least 3 times larger for a dimer than for a monomer. This yields to a better contrast for a dimer than for a monomer in transmission bright field microscopy, and let us expect a larger contrast for bigger aggregates.

In order to validate this approach, we correlated bright field images with TEM micrographs. Hence we chose a support that allows to observe the same area with both techniques such as silicon nitride Si_3N_4 grids. These substrates are indeed compatible with electronic microscopy and transparent at optical frequency. A droplet of the smallest hybrids ($11 \pm 3\ nm$) is deposited on the grid and dries under ambient conditions. Figure IV.10 shows images of the same area for comparison. We observe monomers and dimers on the TEM image in Fig. IV.10b and notice that the corresponding contrasts in bright field microscopy, in

Fig. IV.10a, are different enough to distinguish monomers from dimers.

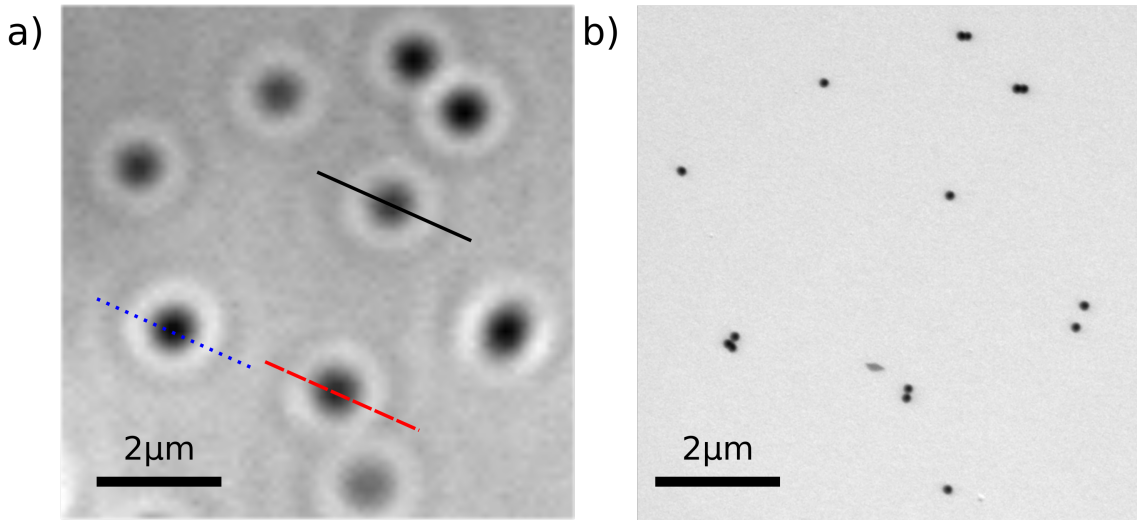

Figure IV.10: Nanohybrids deposited on a Si_3N_4 grid and observed in a) transmission bright field microscopy under Köhler illumination with 610 nm red filter and b) transmission electron microscopy. The core-shell nanohybrids consist in a 57 ± 3 nm diameter gold core with a 11 ± 3 nm thick silica shell. The solid dark line, dashed red line and dotted blue line indicate what intensity profiles are shown in figure IV.11, for a monomer, a dimer and a trimer, respectively.

To go further we compare the intensity profiles observed for a monomer, a dimer and a trimer in figure IV.11. We clearly see that the contrast allows to estimate the number of nanohybrids in an aggregate and thus to distinguish isolated nanohybrids.

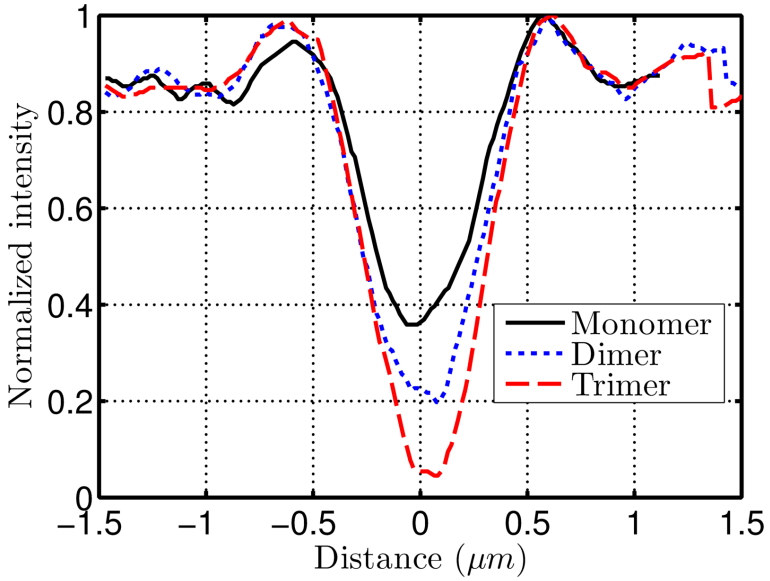

Figure IV.11: Normalized intensity profile for a monomer (solid dark line), a dimer (dotted blue line) and a trimer (dashed red line), observed in transmission bright field microscopy under Köhler illumination with a 610 nm red filter. The plotted profiles are pointed out by straight lines in figure IV.10a.

Finally we noted that the proportion of aggregates is much larger on the grid than in

the polymer matrix because particles are brought together as the solvent evaporates under ambient conditions while spin coating in a PVA matrix allows to obtain more homogeneous samples [178].

IV.3.c.iii Confocal lifetime measurement

The set-up that was built to perform confocal lifetime measurement of nanohybrids at the single object level is represented in figure IV.12.

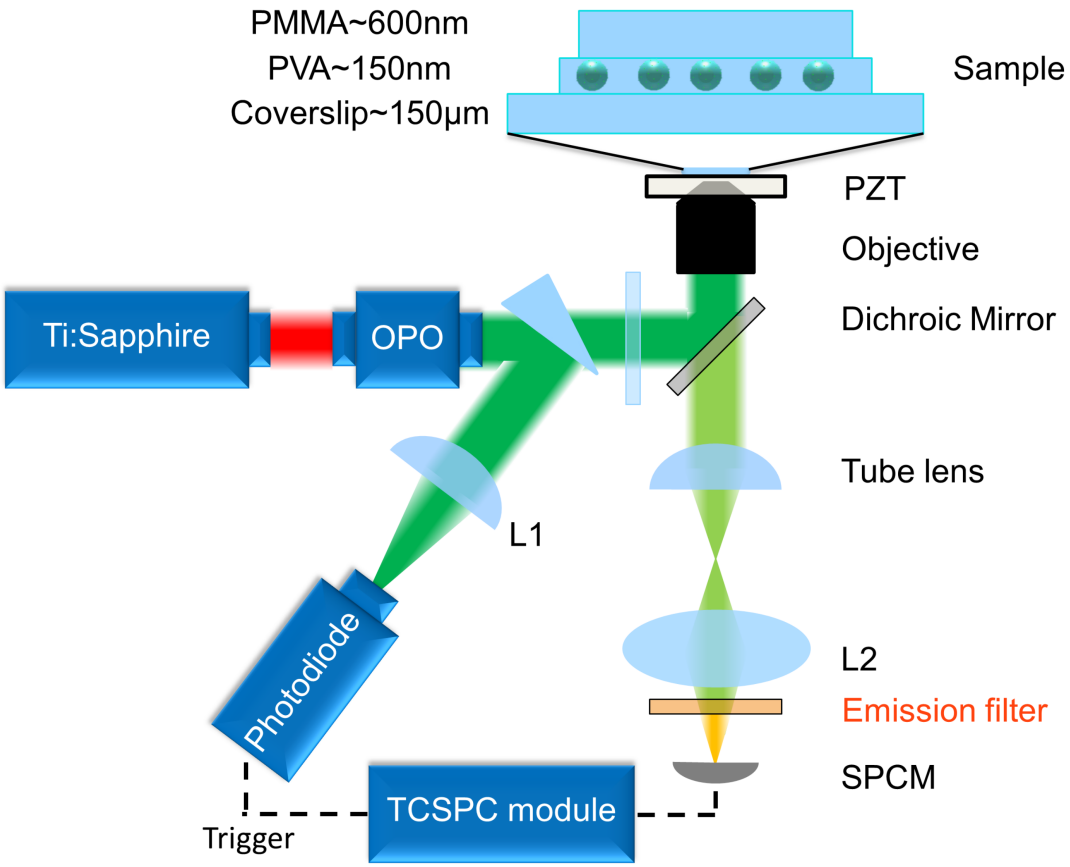

Figure IV.12: Diagram of the experimental set-up used to perform single object measurements. A femtosecond laser pulse excites a single nanohybrid embedded in a polymer matrix. The resulting fluorescence is collected by the objective, spectrally filtered by a dichroic mirror and an emission filter before reaching a SPCM. The fluorescence signal is analyzed by a TCSPC module that generates the temporal decay profile.

A Ti:Sapphire laser (Chameleon Coherent) provides pulses of 140 ± 20 fs with a 80.5 MHz repetition rate at 850 nm, to pump an optical parametric oscillator (OPO, Chameleon Compact OPO-Vis Coherent), which is tuned to deliver excitation pulses at $\lambda_{exc} = 532\ nm$. First the p-polarized beam is sent to a wedge prism that, close to the Brewster angle, reflects approximately 10% towards a fast photodiode, to generate a trigger signal. The excitation power is adjusted, while keeping the same linear polarization, by a combination of a zero-

order half-wave plate, mounted in a rotation holder, and a polarizer. Next the 850 nm laser component is filtered by a colored filter (BG39 Schott). Then the beam is expanded using a telescope (50 mm and 300 mm focal lengths) and sent to an inverted microscope (Nikon Eclipse Ti-U). The resulting beam, with a 150 nW average power, overfills the rear aperture of the microscope objective and is thus focused on a diffraction limited volume, called PSF. We use a 100x oil immersion objective with high numerical aperture (NA = 1.45) so that the excitation PSF is $W = \frac{1.22\lambda_{exc}}{2\mathrm{NA}} = 224\ nm$ perpendicular to the direction of propagation [189, 190].

The resulting fluorescence is collected by the same objective, then spectrally filtered by a dichroic mirror (FF538-Di01 Semrock, $\mathrm{OD}_{\lambda=532nm}$=1) and an interferential emission filter (FF01-582/75-25 Semrock, $\mathrm{OD}_{\lambda=532nm}$=7) to efficiently reject the excitation laser (see spectra Fig. IV.5). The fluorescence is finally focused on a Single Photon Counting Module (SPCM, MPD) based on an APD, with an achromatic lens ($f'_{L2} = 75\ mm$). We use a SPCM whose photon detection efficiency is 49% at $\lambda_{em} = 553\ nm$, dark count is about 25 Hz and time resolution is 50 ps at FWHM.

The main advantage of confocal microscopy is to significantly enhance the spatial resolution along the direction of propagation. A pinhole is usually placed in a Fourier plane before the detector to reject the out-of-focus fluorescence. In our sample the PVA matrix thickness is comparable to the hybrids dimension, so that the objects are distributed in a 2D-plane. Therefore we do not expect any out-of-focus signal. Nevertheless the APD sensitive area is 50 μm diameter, which is small enough to directly perform the spatial filtering without using a pinhole. The detection volume in the sample is imaged by the objective (x100), the tube lens (x1.5) and the lens L2 onto the detector. The lens L2 is only used to transport the image to the APD without magnification. The lateral size of the detection volume is thus about 330 nm. This is slightly larger than the diffraction limit (290 nm for the largest nanohybrids) so that we collect all the available photons.

Finally the sample holder is mounted onto a XY piezo-electric (P-517 Physik Instrumente) device (denoted PZT Fig. IV.12) to precisely place a single nanohybrid in the confocal volume.

When the excitation pulse is detected by the fast photodiode, the resulting analog signal is sent to a TCSPC module (PicoHarp300 PicoQuant) which records the arrival time using a Time to Digital Converter (TDC). When a fluorescence photon is then detected, the SPCM module generates an analog signal to the TCSPC module. The arrival time is then recorded using another TDC. The delay between the excitation and the detection is finally used to increment the histogram and build the temporal decay profile. Before the TDC circuits, a Constant Fraction Discriminator (CFD) rejects spurious pulses. The thresholds are set to 50

mV for the APD signal and 250 mV for the trigger signal.

IV.4 Conclusion

In conclusion, thanks to the work of Miguel Comesaña-Hermo in Serge Ravaine's team, we have access to uniform and smooth spherical silica-gold core-shell nanoparticles whose dimensions are nicely controlled with small dispersion in size. The emitters are fluorescent molecules grafted at the surface of the nanohybrid, so that their distance to the plasmonic core is tuned by changing the silica shell thickness.

Following previous investigations, a 86 ± 8 nm diameter gold core with a 15 ± 2 nm silica shell is decorated with RhB fluorescent molecules. These RhB-based nanohybrids are dispersed in ethanol to investigate their response in ensemble measurements.

Unfortunately the RhB pH sensitivity prevents a proper estimation of the number of emitters per nanohybrid. A better emitter is then the Atto532 fluorescent molecule which is not pH sensitive, shows good photostability and a 90% quantum yield. These emitters are grafted to a 57 ± 3 nm diameter gold core with various silica shell thicknesses (between 11 nm and 57 nm) to study the influence of the distance between the emitters and the core. Concerning the optical characterization, a single nanohybrid is clearly identified using red-filtered transmission bright field microscopy. Once identified its fluorescence temporal decay profile is recorded in standard confocal microscopy.

Chapter V

Experimental evidence of plasmonic superradiance

Contents

In this chapter we report the experimental observation of plasmonic superradiance and discuss the evolution of the system decay rate with the number of emitters and their distance to the plasmonic nanoparticle. In order to characterize the plasmon-mediated cooperative fluorescence, we measure the decay rate of core-shell gold-silica spherical nanohybrids decorated by a controlled number of emitters, as described in chapter IV. Section V.1 shows results for Rhodamine B-based nanohybrids in ethanol that are studied in ensemble measurements. Then section V.2 is dedicated to Atto532 nanohybrids that are studied at the single object level.

V.1 Rhodamine B-based nanohybrids: Ensemble measurements

We first investigate the fluorescence of RhB-based nanohybrids dispersed in ethanol, in ensemble measurements. Rhodamine B molecules are commonly used as a textile dye [191] or laser dye [192]. The quantum yield of RhB in ethanol is about 60 %. Such a quantum yield is quite low and thus yields a good Purcell enhancement, as discussed in section II.3.b of chapter II. Yet it allows for a decent fluorescence signal since it is larger than 50 %. We tune the gold core size to 86 ± 8 nm diameter so that the plasmon resonance matches the RhB absorption and emission bands at 580 nm. These plasmonic cores are coated with a 15 ± 2 nm silica shell and decorated with different concentrations of RhB molecules. The distance between the emitters and the plasmonic core surface $d = 15 \pm 2$ nm was chosen to ensure an efficient coupling to the plasmon oscillations, as discussed in chapter II.

Further information about these hybrids can be found in chapter IV: corresponding histograms of the system dimensions are given in Figs. IV.2 and IV.3 and the characteristic spectra are shown in Fig. IV.5a. These objects were characterized in ensemble measurements using the set-up represented in Fig. IV.6. The RhB fluorescence signal turned out to be unreliable, preventing an estimation of the number of RhB actually grafted per nanohybrid. We will thus discuss in term of concentration of RhB that was initially introduced in the solution to perform the grafting: $C = C_0,\ 2\ C_0,\ 10\ C_0,\ 20\ C_0,\ 55\ C_0,\ 110\ C_0$. Assuming that the binding yield is similar for all the samples, as it was observed for Atto532 samples in chapter III (see appendix A), the number of RhB molecules per nanohybrid is proportional to the introduced concentration C.

If we normalize the smallest concentration of RhB C_0 by the number of nanohybrids in solution, it corresponds to approximately $N_{guessed} = 8 \cdot 10^3$ $RhB/nanohybrid$ for a 100 %

binding yield. Or to about 0.2 RhB/nm^2 in term of surface density.

V.1.a Fluorescence decay in absence of plasmonic core

We first investigate the fluorescence of RhB in absence of plasmonic core. As a reference system, the RhB molecules are grafted on a 104 *nm* diameter silica sphere, without gold core. This system is denoted by SiO_2@RhB. To focus on the RhB fluorescence signal, we integrate the measured streak plots over the 560-590 nm wavelength range, see Fig. IV.7 in chapter IV. The resulting temporal decay profiles are shown in Fig. V.1.

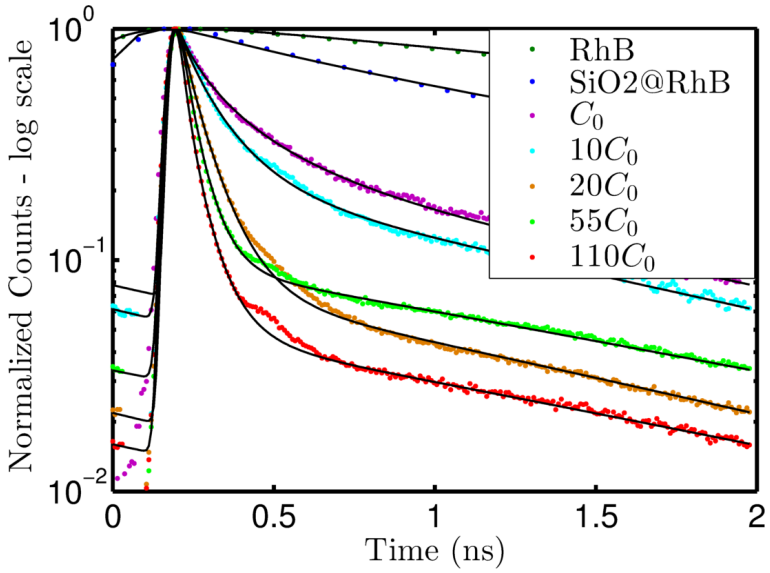

Figure V.1: Fluorescence temporal decay profiles for RhB molecules (dark green dots), SiO_2(D=104nm)@RhB particles (blue dots) and RhB-based nanohybrids in ethanol for different concentrations of RhB: C_0 (magenta dots), 10 C_0 (cyan dots), 20 C_0 (orange dots), 55 C_0 (green dots) and 110 C_0 (red dots). The emission wavelength was selected in the 560-590 nm range. Black solid lines are fits.

We first observe that the decay of the RhB molecules (dark green dots) in ethanol is monoexponential. A fit with a single exponential model on a 20 ns time window, as discussed in section IV.3.b.iv of chapter IV, estimates the RhB decay time in ethanol to be $\tau_{RhB} = 2.8 \pm 0.1\ ns$.

Then the blue dots in figure V.1 represent the temporal decay profile of RhB molecules grafted to the silica sphere in absence of gold core. The decay is monoexponential and clearly exhibits a shorter decay time than the RhB molecules in ethanol. Fitting the temporal decay profile on a 20 ns time window, we estimate $< \tau_{SiO_2@RhB} >= 1.5 \pm 0.2\ ns = 1/\gamma_{SiO_2@RhB}$.

First the silica sphere modifies the effective permittivity ϵ_{host} surrounding the molecules. As such the RhB decay time is approximately modified as $\tau_{SiO_2@RhB} \approx \tau_{RhB}\sqrt{\epsilon_{EtOH}}/\sqrt{\epsilon_{host}}$. Since $\sqrt{\epsilon_{SiO_2}} = 1.48$ [119] and $\sqrt{\epsilon_{EtOH}} = 1.36$ [153], the decay time is shortened by less

than 0.2 ns. Even though the modification of the permittivity contributes to the observed shortening, it is clearly not enough to explain this result.

Assuming a 100% binding yield, the concentration of RhB C_0 would correspond to $N_{guessed} = 8 \cdot 10^3$ $RhB/nanohybrid$, yielding a small separation distance between neighbor molecules: about $R_{RhB-RhB} \approx 2$ nm. Therefore this shortening may be due to the direct non radiative energy transfer between molecules, called homo-Förster Resonance Energy Transfer (homo-FRET) [193]. The FRET efficiency η_{FRET} decreases as the sixth of the RhB-RhB separation distance and is related to the decay time τ by [129, 194] :

$$E = 1 - \frac{\tau}{\tau_{RhB}} = \frac{R_0^6}{R_0^6 + R_{RhB-RhB}^6} \tag{V.1}$$

where R_0 is the separation for which $\eta_{FRET} = 50\%$. It is called the Förster radius and is $R_0 = 5.2$ nm in the case of RhB [195]

To check if the observed shortening is due to homo-FRET, we increased by 5.5 times the concentration in RhB introduced for the same 104 diameter silica spheres without gold core. The corresponding average RhB-RhB separation is $R_{RhB-RhB} \approx 1$ nm. Strikingly no change in the decay time was observed. We deduce that the decay time weakly depends on the concentration of RhB that we introduced. Hence the corresponding number of RhB per nanohybrid is much smaller than expected. Roughly, the average RhB-RhB separation is at least larger than R_0, yielding a binding yield smaller than 30%.

We deduce that the decay time modification is mainly due to chemical grafting to the silica shell. Indeed the covalent bond between the RhB and the silica surface may open an extra relaxation channel.

V.1.b Evolution of the decay rate with the number of emitters

Here we investigate the fluorescence temporal decay profile of RhB molecules distributed around a 86 nm diameter spherical gold core. In particular we study how the system decay rate depends on the number of RhB per nanohybrid. Integrating the streak plots over the 560-590 nm wavelength range, we obtain the temporal decay profiles shown in Fig. V.1.

Compared to the decay of RhB in ethanol, the decays of RhB-based nanohybrids clearly show a dramatic shortening of the decay time. This increase of the fluorescence decay rate due to the presence of the gold is in accordance with the theoretical discussion carried out in chapter II.

For all concentrations except C_0, we fist notice that there is a small bump at about 0.5

ns. This might be due to a reflection of the excitation laser on the colored filter that would excite the hybrids a second time, resulting in a second fluorescence burst.

The decays of RhB-based nanohybrids are multiexponential. We observe two main components: a short component which changes with the number of RhB per nanohybrid and a long component. The long one is fitted with a monoexponential τ_{long} while the short component requires a stretched exponential (τ_K, β). Following the expression of a temporal decay profile (see Eq. IV.3, in chapter III), we fit these decay profiles with the model

$$M(t) = IRF(t) * I(t) \quad \text{with} \quad I(t) = I_1 e^{-(t/\tau_K)^\beta} + I_2 e^{-t/\tau_{long}} \tag{V.2}$$

where IRF is the Instrumental Response Function of the set-up. Estimating the long component on a 2 ns time window is inaccurate. Furthermore there may be a balancing between the fitting parameters of the two components, that may disrupt the estimation of the short component. Therefore the long one is first assessed by adjusting the tail of the decay, before fitting the whole decay with the model Eq.V.2, so that the stretched component is adjusted using as few parameters as possible. The resulting parameters are shown in the table V.1.

RhB/NP (C_0)	τ_{long} (ns)	τ_K (ps)	β (%)	$<\tau>$ (ps)	$<\gamma>/\gamma_{SiO_2@RhB}$
1	1.4 ± 0.4	134 ± 8	94 ± 9	138 ± 8	11 ± 1
2	1.4 ± 0.4	121 ± 10	79 ± 8	137 ± 10	11 ± 2
10	1.5 ± 0.3	97 ± 6	88 ± 5	103 ± 6	15 ± 1
20	1.4 ± 0.3	76 ± 5	95 ± 7	78 ± 5	20 ± 1
55	1.8 ± 0.3	40 ± 6	90 ± 5	42 ± 6	36 ± 5
110	1.6 ± 0.3	20 ± 7	70 ± 5	26 ± 10	57 ± 21

Table V.1: Fit parameters τ_{long}, τ_K, β and corresponding average decay time $<\tau>$ and average normalized decay rates $<\gamma>/\gamma_{SiO_2@RhB}$ for different concentrations of RhB.

Even though this estimation is inaccurate because of the too short time window, notice that the long component is similar for all the concentrations and is approximately $\tau_{long} = 1.4 \pm 0.5\ ns$. We thus attribute this long component to the fluorescence of RhB molecules freely diffusing in solution.

Whereas the stretched component reveals that the average decay time decreases as the concentration of RhB increases. We plot in Fig. V.2 the evolution of the corresponding average decay rate, normalized by the decay rate of SiO_2@RhB particles, as a function of the introduced concentration of RhB.

We observe that the average decay rate scales with the number of RhB per nanohybrid. This proportionality with the number of emitters is a signature of superradiance, as discussed

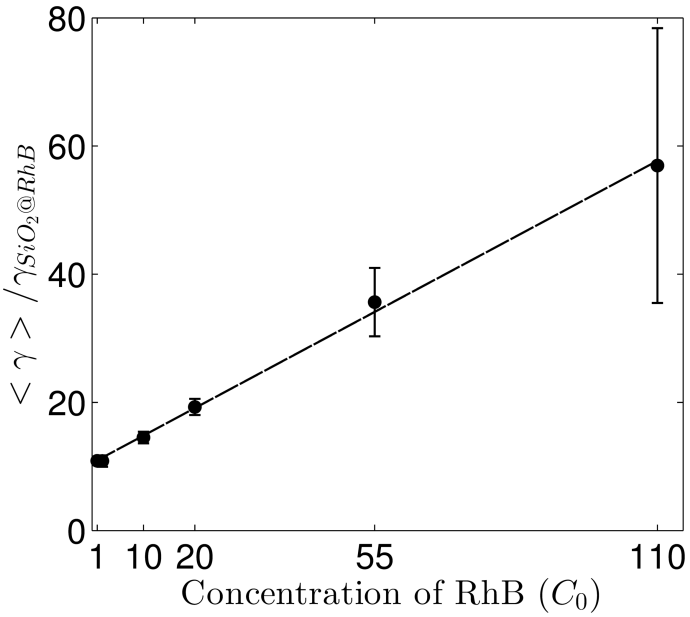

Figure V.2: Evolution of the average decay rate of RhB-based nanohybrids normalized by the decay rate of SiO_2@RhB particles, for different concentrations of RhB. The emission wavelength was selected in the 560-590 nm range. The line is a linear fit as a guide for the eyes.

in chapter II. Furthermore we showed in section V.1.a that the decay rate of RhB molecules grafted to a silica sphere does not depend on the concentration of RhB in our samples. This proportionality with the number of emitters is thus due to the presence of the gold core. Hence it is a first signature of a plasmon-mediated superradiance.

To go further we compare the experimental decay rates with the expected Purcell factor of the nanohybrid. Using the model described in chapter II, we consider one dipole located on a 15 nm thick silica shell grown around a 86 nm diameter gold sphere, embedded in ethanol. We take $\sqrt{\epsilon_{SiO_2}} = 1.48$ [119], $\sqrt{\epsilon_{Au}} = 0.30 + 2.84i$ [82] and $\sqrt{\epsilon_{EtOH}} = 1.36$ [196] at $\lambda = 582\ nm$. The theoretical Purcell factor is $P^{\parallel}_{N=1} = 4.2$ for a dipole oriented tangentially to the hybrid surface. And $P^{\perp}_{N=1} = 25.8$ for normal orientation. A priori the RhB molecules do not have a specific orientation so we derive the average value, likely to be observed for 1 RhB/nanohybrid

$$< P_{N=1} >= \frac{1}{3}P^{\perp}_{N=1} + \frac{2}{3}P^{\parallel}_{N=1} = 11.4 \tag{V.3}$$

Strikingly this value corresponds to the decay rate measured for the concentration C_0. It confirms that the actual number of RhB per nanohybrid is much smaller than the value initially guessed : $N_{guessed} = 8 \cdot 10^3 RhB/NP$. We deduce that the binding yield during the synthesis is very small.

V.1.c Evolution of the decay rate with the emission wavelength

To go further we study how the observed trend with the concentration of RhB depends on the emission wavelength. We thus perform the decay rate analysis for different wavelength windows, as published in Ref. [197]; for 560 $nm < \lambda < 570$ nm, 570 $nm < \lambda < 580$ nm and 580 $nm < \lambda < 590$ nm. We recall that the dipole LSPP resonance of the hybrid was observed at 556 nm in Fig. IV.3.

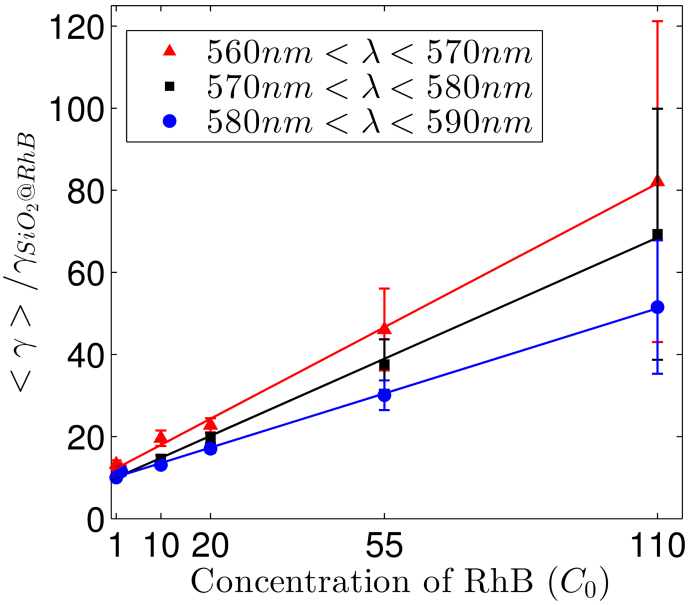

Figure V.3: Evolution of the average decay rate of RhB-based nanohybrids normalized by the decay rate of SiO_2@RhB particles, for different concentrations of RhB. The emission wavelength was selected in the 560-570 nm (red triangles), 570-580 nm (black squares) and 580-590 (blue dots) range. The lines are linear fits.

First figure V.3 shows that, at each concentration of RhB, the decay rate enhancement decreases for a larger detuning between the emission wavelength and the plasmon resonance. Indeed the LDOS of the nanohybrid is larger close to the plasmon resonance. Hence a smaller detuning leads to a more efficient molecule-plasmon coupling.

Then we observe in Fig. V.3 that the slope of $< \gamma >$ with the concentration in RhB increases as the selected emission wavelength range is closer to the plasmon resonance. This result evidences a larger cooperativity for a smaller detuning from the plasmon resonance. We deduce that the coupling between the molecules, which is mediated by the plasmon, is also more efficient.

V.2 Atto-based nanohybrids: Single object measurements

In order to confirm the preliminary results observed with RhB-based nanohybrids, we investigate Atto-based nanohybrids in single object measurements. Atto 532 is a fluorescent molecule related to the Rhodamine 6G, used as a tracer in biology and for single molecule spectroscopy [198]. It shows a 90% quantum yield with a good photostability. More importantly Atto532 molecules are not pH sensitive and so their fluorescence intensity is reliable. It thus allowed us to take a particular care in controlling the number of emitters per nanohybrid. A similar quantification of the number of grafted Atto molecules was reported in Ref. [123].

A Atto-based nanohybrid consists in a $D = 57 \pm 3\ nm$ diameter gold sphere surrounded by a silica shell that was decorated with Atto 532 molecules. The distance between the emitters and the core surface was controlled by tuning the silica shell thickness d. Several spacer thicknesses were thus synthesized : $d = [11 \pm 3\ nm, 13 \pm 2\ nm, 18 \pm 2\ nm, 25 \pm 3\ nm, 37 \pm 3\ nm, 57 \pm 6\ nm]$. Further information about these hybrids can be found in chapter IV: histograms of the core diameter and shell thicknesses are given in Figs. IV.3 and IV.4, characteristic spectra are shown in Fig. IV.5. In order to perform single object measurements, Atto-based nanohybrids were dispersed in a solution with Polyvinyl Alcohol (PVA). Then this solution was spin-coated to obtain a 150 nm thick PVA matrix with embedded nanohybrids. The sample was then covered with a 600 nm Poly(methyl methacrylate) (PMMA) layer so that the hybrids were characterized in a homogeneous medium. The refractive index of PVA (1.50 [180]) and silica (1.48 [119]) are close at the emission wavelength $\lambda_{em} = 553\ nm$ so the LSPP extinction peak does not depend on the shell thickness. It assures that the molecule-plasmon spectral overlap is similar for all silica shell thicknesses. Finally, because some nanohybrids were aggregated in the PVA matrix, isolated single nanohybrids were pinpointed using bright field microscopy. The fluorescence temporal decay profiles of single nanohybrids were then recorded in a confocal configuration at room temperature.

V.2.a Fluorescence decay in absence of plasmonic core

We first investigate the fluorescence decay of Atto 532 molecules in absence of plasmonic core. As a reference system, Atto molecules are grafted on a 104 nm diameter silica shell, without gold core. These SiO_2@Atto532 objects are also studied at the single object level. Figure V.4 compares the fluorescence decay profile of a Atto532 molecule in PVA with the decay profile of about 70 Atto532 molecules grafted on a silica sphere.

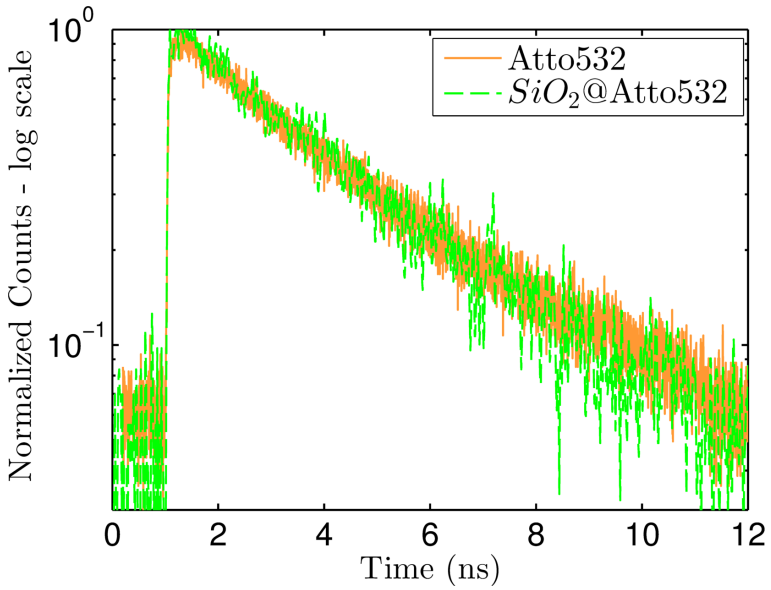

Figure V.4: Normalized fluorescence decay of a single Atto532 molecule in PVA matrix (solid orange line) and for a 104 nm diameter silica sphere decorated with about 70 Atto532 molecules (dashed green line, denoted by SiO_2@Atto532).

We observe in Fig. V.4 that the fluorescence temporal decays are similar. A statistics over 20 single Atto532 molecules in PVA yields a $\tau_{Atto} = 2.9 \pm 0.2\ ns = 1/\gamma_{Atto}$ average lifetime. A statistics over 50 single silica spheres decorated with about 70 Atto532 molecules yields a $2.7 \pm 0.2\ ns$ average lifetime.

First the modification of the permittivity due to the silica sphere has a weak influence on the Atto532 decay rate. Indeed the silica permittivity is close to the surrounding PVA permittivity.

Then a number of 70 Atto532 per nanohybrid corresponds to an average molecule-molecule separation of about 22 nm. This distance is about 4 times larger than Atto532 Förster radius $R_0 = 5.8nm$ [156]. The homo-FRET is thus negligible for these SiO_2@Atto532 objects. Therefore we attribute the slight shortening of Atto532 decay time to the covalent bond used to graft Atto532 molecules to the silica shell. The reference decay time is then $\tau_s = 2.7 \pm 0.2\ ns = 1/\gamma_s$.

To go further a similar single object study was performed on 104 nm diameter decorated silica spheres for different numbers N of emitters per nanohybrid. Figure V.5 shows the evolution of the average decay time $< \tau >$ - normalized by the decay time of single Atto532 in PVA τ_{Atto} - as a function of the corresponding average molecule-molecule separation. Noteworthy the average decay times obtained from statistics on single SiO_2@Atto532 objects were confirmed by ensemble measurements of these objects dispersed in ethanoic solution.

The average molecule-molecule separation was deduced from N by considering a random

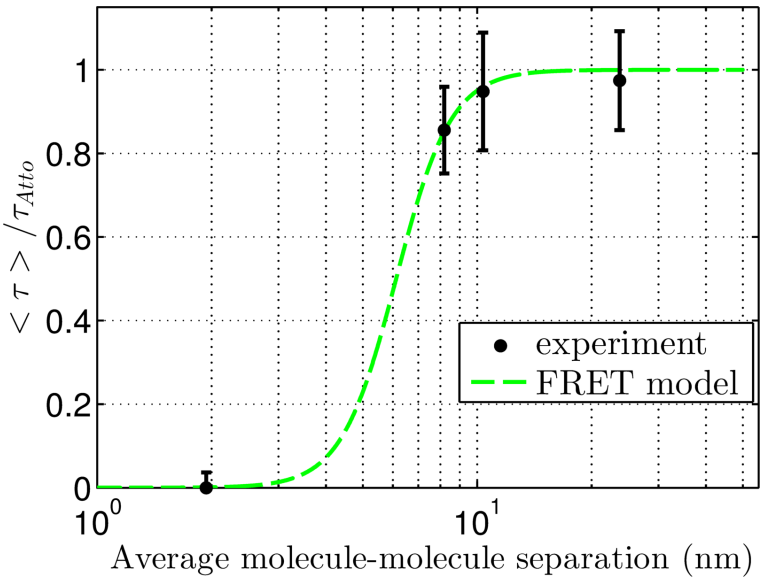

Figure V.5: a) Experimental average decay time $< \tau >$ of SiO_2(104 nm)@Atto532(N) particles (black dots), normalized to the unperturbed decay time of a single Atto532 in PVA τ_{Atto}, as a function of the average molecule-molecule separation distance. Green dashed line represents a fit using the FRET model, from Eq.V.1.

distribution of the emitters at the surface of a sphere S_{sph}: $R_{Atto-Atto} = \sqrt{S_{sph}/N}$. Fitting the experimental data with the FRET model from Eq. V.1, we estimate a Förster radius of about $R_0 = 6.2\ nm$. This value is in accordance with the one given by the molecule supplier: 5.8 nm [156]. This result shows that the estimation of the number of Atto532 molecules per nanohybrid is correct.

In all the investigated Atto-based nanohybrids, the average emitter-emitter separation was kept larger than 8 nm, limiting the homo-FRET efficiency below 10% and thus allowing us to focus on the plasmon-mediated superradiance.

V.2.b Direct evidence of plasmonic superradiance

Here we investigate the fluorescence temporal decay profile of Atto532 molecules distributed around a 57 nm diameter spherical gold core. In particular we study how the system decay rate depends on the number of Atto532 per nanohybrids and on the distance between a molecule and the plasmonic core.

Figure V.6 shows typical fluorescence decays of Atto-based nanohybrids. First, each Atto-based nanohybrid shows a monoexponential decay. We deduce that the decays observed in ensemble measurements for RhB-based nanohybrids are multiexponential because of the distribution of objects and not because of the nanohybrid intrinsic properties. Then, for all configurations, the decay time of a Atto-based nanohybrid is shorter than the decay time of Atto532 molecules grafted to a silica sphere in absence of plasmonic core.

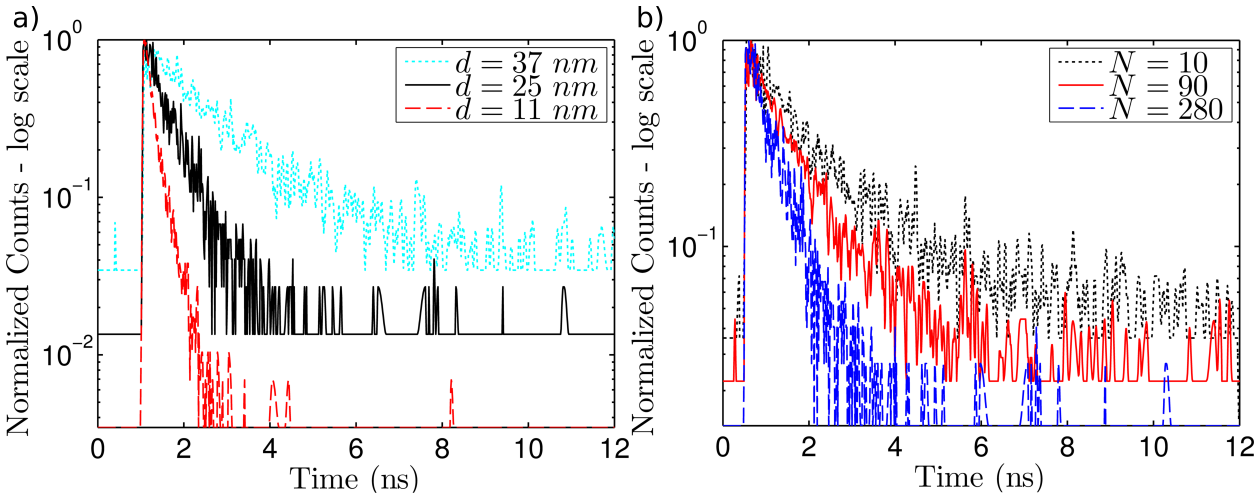

Figure V.6: a) Normalized fluorescence decay profile of Atto-based nanohybrids with a similar number of emitters per nanohybrid $N \approx 280$ but different silica shell thicknesses: $d = 37\ nm$ (dotted cyan line), $d = 25\ nm$ (solid black line) and $d = 11\ nm$ (dashed red line). b) Normalized fluorescence decay profile of Atto-based nanohybrids with a similar silica shell thickness $d = 25 \pm 3\ nm$ and decorated with about 10 (dotted black line), 90 (solid red line) and 280 (dashed blue line).

In Fig. V.6a the number of Atto532 per nanohybrid is kept nearly constant: $N \approx 280$ and the different decays correspond to different silica shell thicknesses. Whereas N varies in Fig. V.6b but for the same distance between the emitters and the core surface: $d = 25 \pm 3\ nm$. We observe that the molecules relaxation gets faster as the emitters are closer to the core and as the number of emitters increases.

For each configuration, the average decay rate $< \gamma >$ and its uncertainty were deduced from statistics over 50 single objects and normalized by the decay rate of a Atto532 molecule grafted to a silica sphere without gold core, γ_s. Figure V.7 shows the histograms of Atto-based nanohybrids for different silica shell thicknesses (Fig. V.7a) and different numbers of emitters per nanohybrid N (Fig. V.7b).

We observe in figure V.7a that a difference of only 2 nm in the emitter-core distance yields to a $5\gamma_s$ shift of the decay rate distribution, for $N \approx 280$ emitters. Then we observe in figure V.7b that at $d = 13\ nm$ from the gold core, multiplying the number of emitters by 10 yields to a shift of the decay rate distribution by about $3\gamma_s$. Hence the decay rate of Atto-based nanohybrids is influenced by both the number of emitters and the distance between the emitters and the plasmonic core.

The average decay rates $< \gamma >$ deduced from histograms are reported in figure V.8, as a function of the number N of emitters per nanohybrid and for different silica shell thicknesses d.

First, for all distances to the core surface, the average decay rate scales with the number of emitters, as a clear evidence of a collective emission. In the case of silica spheres without

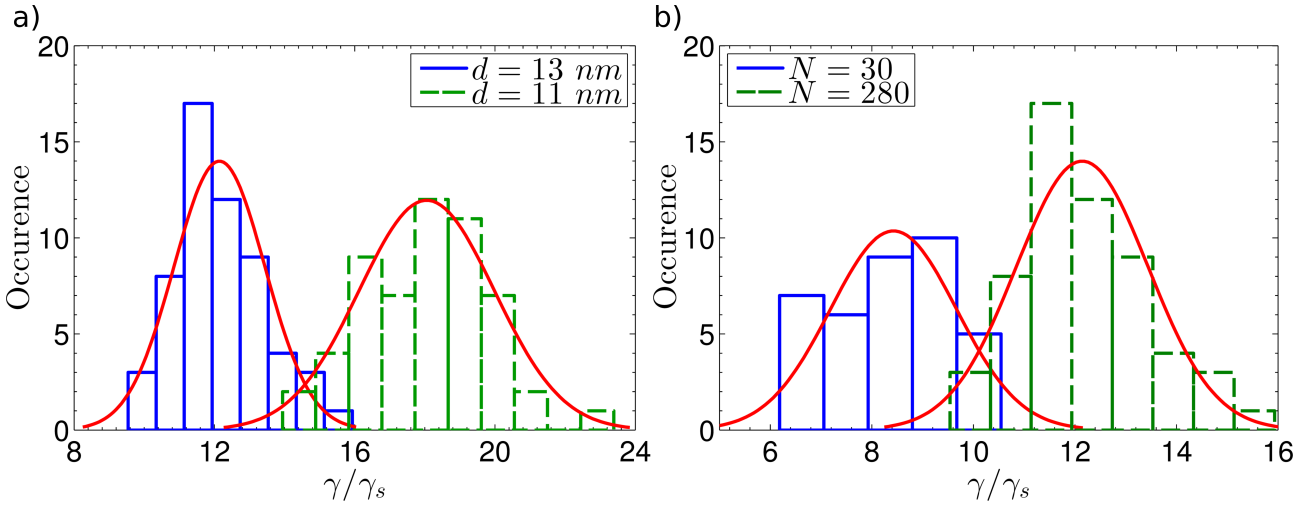

Figure V.7: a) Histogram showing the decay rate of Atto-based nanohybrids with a similar number of emitters per nanohybrid ($N \approx 280$) but different silica shell thicknesses: $d = 13$ nm (solid blue line) and $d = 11$ nm (dashed green line). b) Histogram showing the decay rate of Atto-based nanohybrids with a similar silica shell thickness $d = 13 \pm 2$ nm and decorated with about 30 (solid blue line) and 280 (dashed green line) molecules. In both figures the red lines are fits to a normal distribution, used to estimate the average decay rate and its uncertainty. The decay rates are normalized by the decay rate of a Atto532 molecule grafted to a silica nanosphere in absence of plasmonic core, γ_s.

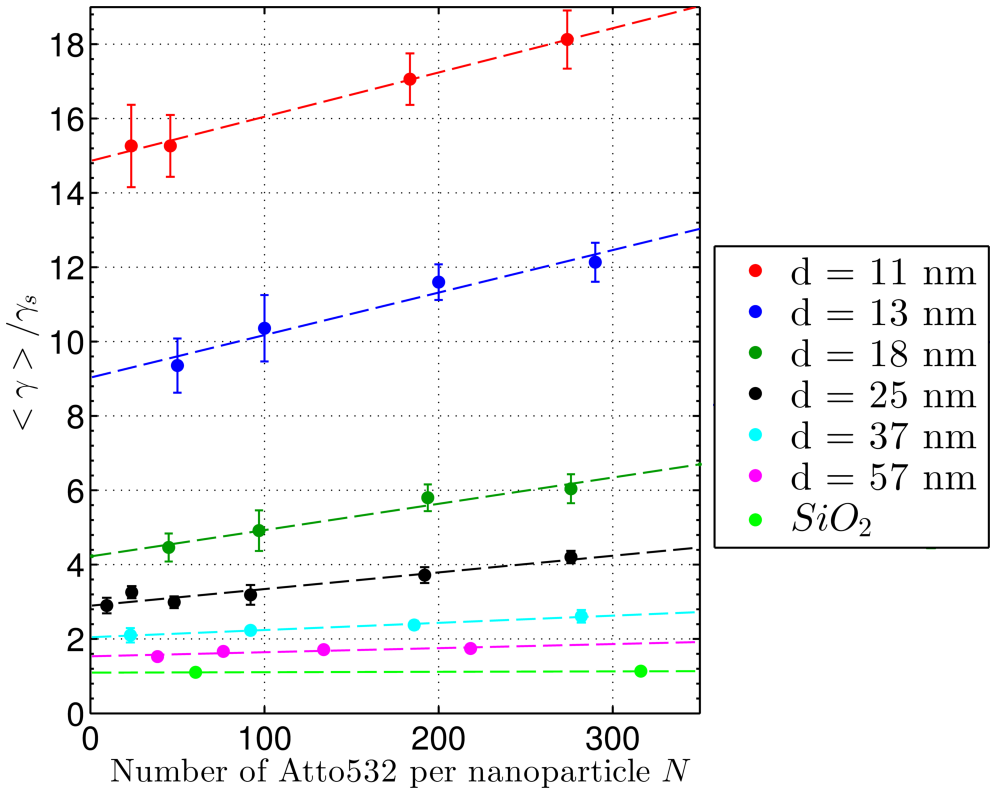

Figure V.8: Experimental average decay rate of Atto-based nanohybrids (dots) as a function of the number N of Atto532 per nanohybrid and for different distances d to the gold core surface. Dashed lines are linear fits, as guides for the eyes. The decay rates are normalized by the decay rate of a Atto532 molecule grafted to a silica nanosphere in absence of plasmonic core γ_s.

plasmonic core (green dots in Fig. V.8), the number of emitters does not influence the average decay rate. We deduce that the collective emission observed for Atto-based nanohybrids is due to the presence of the gold core, as a clear and direct demonstration of collective emission mediated by plasmonic oscillations.

V.2.c Further discussions on plasmonic superradiance results

V.2.c.i Purcell effect

First, we discuss the contribution of the Purcell effect for $N = 1$ emitter. For each distance in Fig. V.8, we estimate the average experimental Purcell factor $< F_P >$ by extrapolating the linear fits (dashed lines) to $N = 1$. Figure V.9 compares these experimental values with the theoretical model of spontaneous emission close to a spherical nanohybrid, introduced in chapter II. This model considers a classical dipole, with a 90% quantum yield, located at the surface of a spherical core-shell nanohybrid. The nanohybrid dimensions and permittivities are taken from the experimental conditions. The dipole orientation is normal (dotted line) or tangential (dashed line) to the nanohybrid surface.

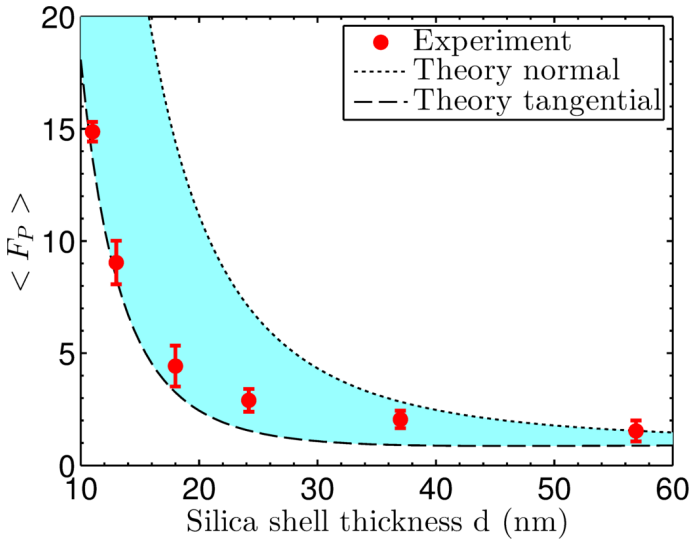

Figure V.9: Experimental (red dots) and theoretical (black lines) results for the average Purcell factor $< F_P >$ of N=1 Atto532 at the surface of a core-shell nanohybrid. The core is a 57 nm diameter gold sphere and the shell is a silica layer with thickness d. Experimental values are deduced from the linear fits in Fig. V.8. Theoretical values are estimated for normal (dotted line) and tangential (dashed line) dipole orientation with respect to the nanohybrid surface.

We see in figure V.9 that the experimental average decay rates are in good agreement with the theoretical calculations for tangentially oriented molecules. We deduce that the Atto532 molecules are preferentially oriented tangentially to the nanohybrid surface. This

observation is in agreement with ensemble measurements in ethanoic solution reported by P. Reineck *et al.* [123]. The authors attributed this preferred orientation to the formation of hydrogen bonds between the primary amine side groups of Atto 532 and the primary amines of the binding molecule (APTES).

V.2.c.ii Analysis of the slope with the number of emitters

We then see in Fig. V.8 that the slope with N increases as the emitters get closer to the plasmonic core. This trend shows that decreasing the distance d results into the improvement of the cooperativity of the plasmonic superradiance phenomenon.

The fact that the slope with N increases as the emitters get closer to the core was observed theoretically in chapter II. We reproduce in Fig. V.10 the calculated evolution of the average superradiant decay rate with the number of dipoles per nanohybrid for a 18 nm thick silica shell, from Fig. II.8 in chapter II. The represented values are the result of a statistics on the classical dipoles position and orientation over 1000 configurations. In accordance with the previous observation for $N = 1$, the dipole orientation was kept tangential to the nanohybrid surface.

We observe in figure V.10 that the calculated slope with N is roughly one order of magnitude larger than the slope observed experimentally.

Superradiance is a collective emission process. As such it is determined by the coherence between the molecules, as it has been demonstrated both theoretically and experimentally for Dicke superradiance [199–204]. The experiment was performed at room temperature and for molecules in a polymer matrix so the coherence between the emitters is affected by the temperature-induced dephasing. However the theoretical model developed in chapter II does not account for pure dephasing mechanisms. Furthermore the superradiance properties may also be affected by the fact that the molecules have different resonance frequencies. First there is a static disorder in the molecule resonances due to the inhomogeneous broadening. Besides a molecule can spontaneously change its conformation, resulting in a shift of its resonance frequency. This dynamical process is called spectral diffusion. These three processes yield to a disrupted collective emission, as studied both theoretically [205–207] and experimentally [200, 208] for Dicke superradiance. We may thus attribute the disagreement observed in Fig. V.10 to these processes.

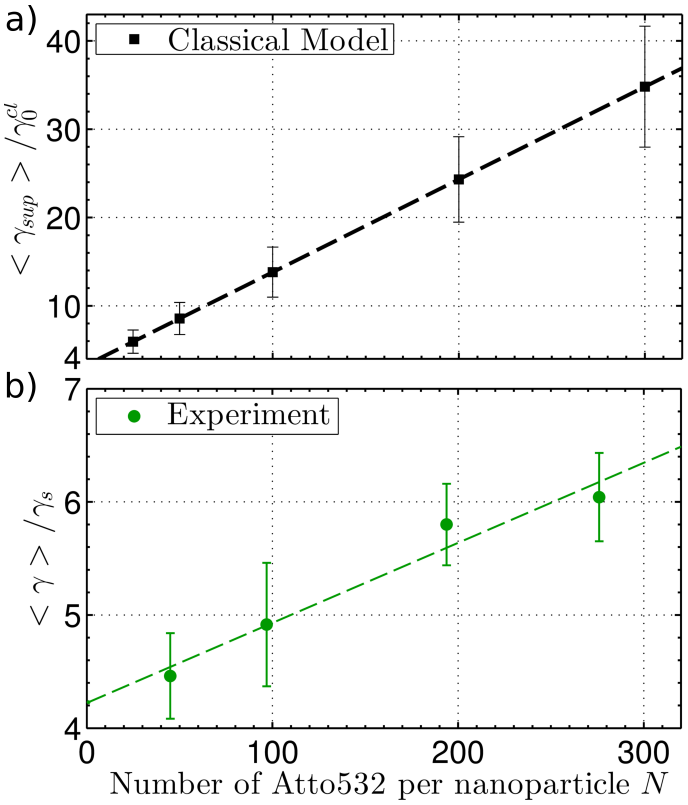

Figure V.10: A number N of emitters are distributed on a $d = 18$ nm thick silica shell that is grown around a 57 nm diameter gold sphere. The dipoles orientation is preferentially parallel to the nanohybrid surface. a) Calculated (black squares) evolution of the average superradiant decay rate $< \gamma_{sup} >$ with the number of classical dipoles per nanohybrid. $< \gamma_{sup} >$ is normalized by the decay rate of the classical dipole γ_0^{cl} in a homogeneous medium of refractive index $\sqrt{\epsilon_{host}} = 1.5$. b) Experimental (green circles) evolution of the average decay rate $< \gamma >$ with the number of Atto532 per nanohybrid. $< \gamma >$ is normalized by the decay rate of Atto532 molecules grafted onto a silica shell nanosphere in absence of plasmonic core and embedded in a PVA matrix γ_s. The dashed lines are linear fits, as guides for the eyes.

V.2.d Effect of thermal dephasing on plasmonic superradiance

To go further in the interpretation of the experimental results, we qualitatively describe the effect of thermal dephasing on plasmonic superradiance. To help the discussion, we neglect the spectral diffusion and the inhomogeneous broadening, even though these assumptions are a priori not valid.

V.2.d.i Case of two molecules

The aim of this paragraph is to outline the effect of thermal dephasing on the plasmonic superradiance phenomenon. To this end we consider two molecules placed at $d = 18\ nm$ from the plasmonic core surface and oriented tangentially to this surface. The theoretical Purcell factor is then $F_P = 3.3$. We assume that the molecules are identical, with the same population decay rate γ_p in the host medium without the nanohybrid and the same resonance frequency ω_0.

To introduce the interaction with a thermal bath, we extend the semi-classical model developed in chapter I. The molecules are thus described as Two-Level Systems (TLS). Following the model introduced by H. Haken and G. Strobl [209], the thermal dephasing is introduced by assuming that the electronic transition frequency of each molecule is undergoing rapid fluctuations at a dephasing rate γ^*, according to a Markovian process. To this end we add a new Liouville operator to the Lindblad form of the master equation, see Eq. I.37 in chapter I

$$\mathcal{L}^l_{th,d}\rho = -\gamma^*(\hat{\sigma}_l^+\hat{\sigma}_l^-\rho + \rho\hat{\sigma}_l^+\hat{\sigma}_l^- - 2\hat{\sigma}_l^+\hat{\sigma}_l^-\rho\hat{\sigma}_l^+\hat{\sigma}_l^-) \tag{V.4}$$

To account for the plasmonic nanohybrid we use the Green function formalism, that was also introduced in chapter I. In particular we introduce the nanohybrid Green function in Eqs. I.58 and I.59 in chapter I to deduce the coherent g_{12} and incoherent γ_{12} coupling constants between the two TLS. Therefore the nanohybrid is introduced as a way to modify the coupling between the TLS. As a consequence the evolution of the molecular density matrix, as formulated by the Eq. I.37 in chapter I, is still valid.

In chapter II we have seen that plasmonic superradiance strongly depends on the emitters position as well as their orientation with respect to the nanohybrid and with respect to each other. To go further figure V.11 shows the distribution of the coupling strength between two TLS at the surface of the nanohybrid, in spherical coordinates (θ, ϕ). Both TLS are placed at $d = 18\ nm$ from the core surface and oriented tangentially to this surface. We set the TLS 1 at the position $(\theta = 0°, \phi = -90°)$ and calculate the values of g_{12} and γ_{12} at each position of

the TLS 2 (θ, ϕ), as represented in Fig. V.11a. The values plotted in Fig. V.11 are obtained by averaging over the second TLS orientation, keeping it parallel to the surface. Hence Fig. V.11 allows to see how the two TLS are coupled depending on their relative position on the nanohybrid. Furthermore we discriminate the part of the coupling due to the plasmonic core (Figs. V.11c and V.11e), from the part due to the direct interaction (free-space and silica shell) (Figs. V.11b and V.11d).

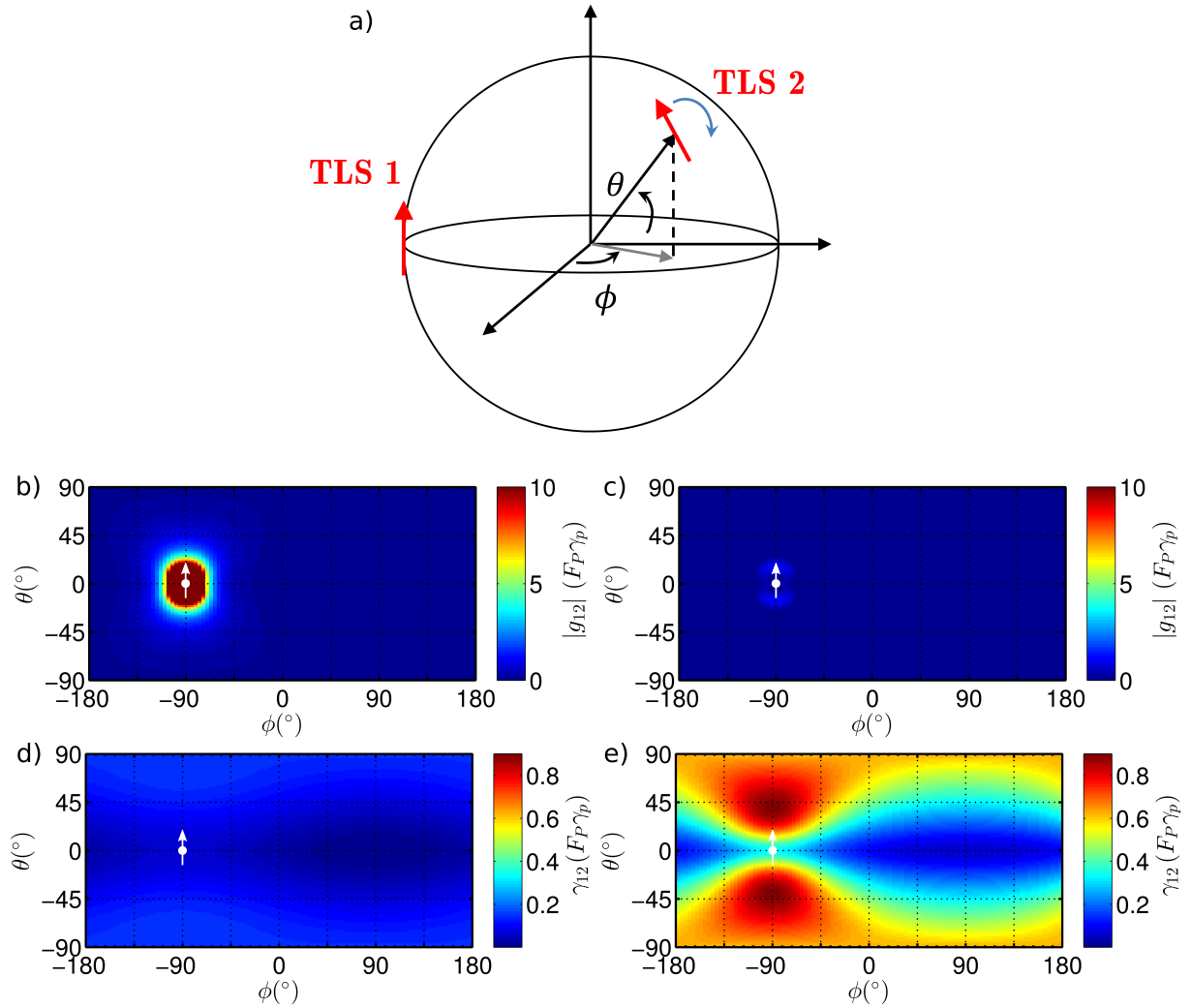

Figure V.11: Two TLS are placed at the surface of a $d = 18$ nm thick silica shell, coating a 57 nm diameter gold core. They are oriented tangentially to the nanohybrid surface. We consider here spherical coordinates. As shown in a), TLS 1 is set at the position $(\theta = 0°, \phi = -90°)$ and the TLS 2 is moving on the particle surface. For each position of the TLS 2 (θ, ϕ), we average $|g_{12}|$ and γ_{12} over the orientation of the TLS 2, keeping it tangentially oriented to the particle. We show the calculated distribution of $|g_{12}|$ in b) and c) and of γ_{12} in d) and e). b) and d) correspond to the part of the coupling due to the free-space and the silica shell. c) and e) correspond to the part of the coupling due to the plasmonic core.

First, by comparing Figs. V.11b and V.11d with Figs. V.11c and V.11e, we see that the direct interaction dominates the coherent coupling g_{12}, while the plasmon-mediated interac-

tion dominates the incoherent coupling γ_{12}. These observations are in accordance with the demonstration made in chapter III for a plasmonic nanorod.

Then we see in Fig. V.11e that γ_{12} exhibits two lobes at $\theta = \pm 90°$ due to the dipole mode of the plasmonic core. Furthermore when γ_{12} is due to the plasmon-mediated interaction (Fig. V.11e), we observe two intense spots close to the TLS 1. These spots show that the higher order plasmonic modes promote the coupling to neighbor emitters. Besides, these coupling distributions clearly show that the plasmonic spherical nanohybrid does not allow a homogeneous coupling between the emitters distributed at its surface. For simplicity we average the coupling constants over the TLS position, yielding to $g_{12} = 9F_P\gamma_p$ and $\gamma_{12} = 0.6F_P\gamma_p$. These values of the coupling constants are used in the following.

During the experiment, the excitation power was small enough to consider that the laser pulse excites only one emitter of the nanohybrid, see appendix B for details. We thus assume that the system is in the weak excitation regime. Hence only one TLS is excited at time t=0, after excitation by the laser pulse.

To summarize, this semi-classical model accounts for the thermal dephasing, the plasmonic nanohybrid and the initial condition. Now we investigate the influence of thermal dephasing on the plasmon-mediated superradiance of two TLS. At time $t = 0$, TLS 1 is excited and TLS 2 in the ground state. Figure V.12 shows the time evolution of the TLS population ρ_{eg} for the TLS 1 and ρ_{ge} for the TLS 2. We denote by ρ_{gg} the population of the ground state: when both TLS are de-excited. Besides we also calculate the time evolution of the total radiation rate which is proportional to what is measured experimentally. These quantities are estimated for different dephasing rates γ^*.

First, for $\gamma^* = 0$ we retrieve the characteristic features of superradiance in Figs. V.12a and V.12d: oscillation of the TLS population and two components (superradiant and subradiant) in the decay of the radiation rate. Note that the temporal axis is normalized by $F_P\gamma_p$, showing that the nanohybrid results in an enhanced superradiance and subradiant decay rates. Hence the nanohybrid acts as a communication bus enhancing the emitter-emitter interaction, as expected from chapters II and III.

Then we observe in Fig. V.12b that a dephasing rate similar to $F_P\gamma_p$ yields to a damping of the TLS population oscillation. Accordingly, the components of the radiation rate decay in Fig. V.12e get closer to the decay rate of one TLS experiencing the Purcell effect. This is a clear evidence that the thermal dephasing disrupts the superradiance phenomenon. Finally we see in Figs. V.12c and V.12f that if the dephasing rate is larger than $F_P\gamma_p$ by one order of magnitude, then superradiance is almost destroyed and the system emits almost like two independent TLS experiencing the Purcell effect. More precisely, the oscillations are

completely damped for $\gamma^* \gg 2g_{12}$ [199], the interaction is then incoherent. On the contrary, if $\gamma^* \gg \gamma_{12}$ the superradiant and subradiant decay rates are both equal to the decay rate of a single TLS $F_P\gamma_p$ [199].

We emphasize that plasmon-mediated superradiance may survive a larger dephasing rate than Dicke superradiance if either g_{12} or γ_{12} are enhanced by a plasmonic structure. Noteworthy, for a sufficiently large coupling between the emitters, in molecular aggregates for instance, Dicke superradiance could be observed at room temperature in Refs. [9, 208, 210, 211].

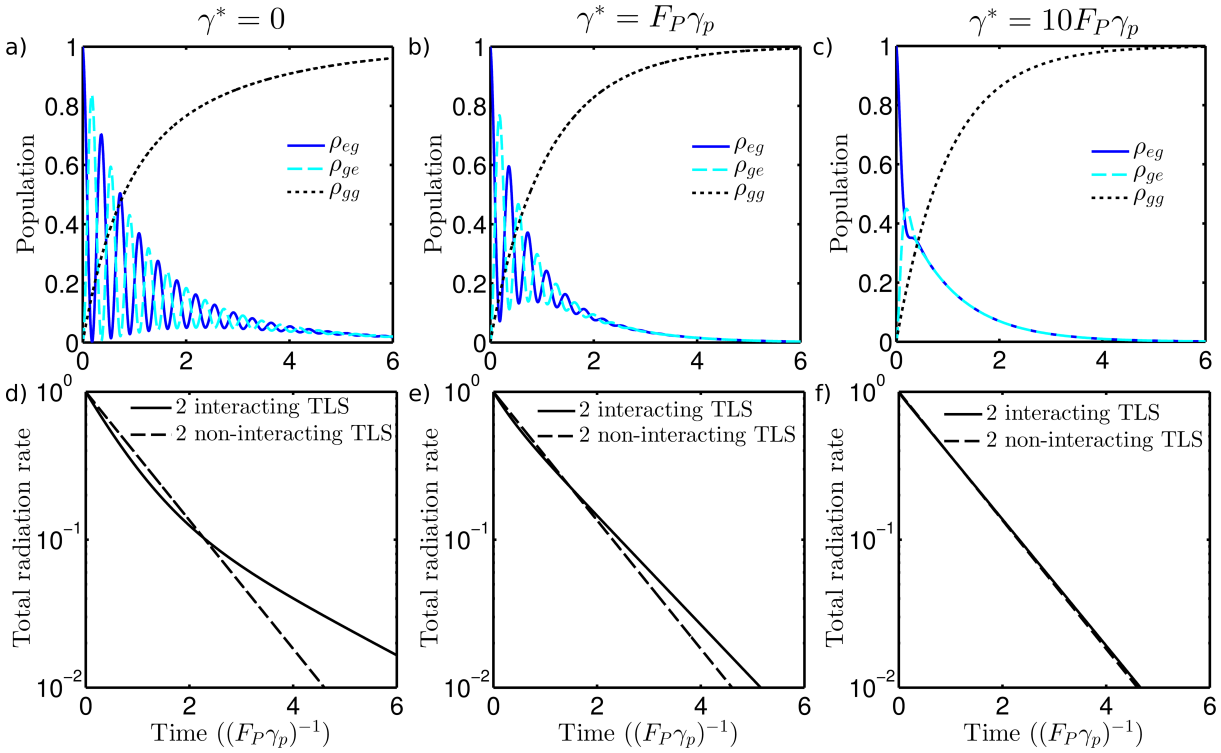

Figure V.12: Two TLS are placed at the surface of a $d = 18$ nm thick silica shell, coating a 57 nm diameter gold core. They are oriented tangentially to the nanohybrid surface. Initially, TLS 1 is excited while TLS 2 is in the ground state. a), b) and c) Calculated evolution of the TLS population with time for $\gamma^* = 0$, $\gamma^* = F_P\gamma_p$ and $\gamma^* = 10F_P\gamma_p$, respectively. d, e) and f) Corresponding calculated evolution of the total radiation rate as a function of time.

V.2.d.ii Case of N molecules

We now discuss how thermal dephasing influences the plasmonic superradiance of N molecules. In the case of Dicke superradiance the effect of thermal dephasing has been widely studied both theoretically and experimentally [199–204].

The effect of the coupling to phonon modes on Dicke superradiance has been introduced theoretically by the group of S. Mukamel [199, 201, 202]. They considered a cyclic chain of N identical TLS evenly separated, oriented parallel to each other and perpendicular to the chain

axis. Typically this system corresponds to a molecular aggregate [200]. Such a configuration allows to consider identical coupling constants between all the TLS and thus, along with the weak excitation approximation, to considerably simplify the equations [199].

In order to qualitatively discuss the effect of thermal dephasing in our system, we consider a perfectly symmetrical case in the weak excitation regime. We thus assume that all the TLS are identically coupled to each other via the plasmonic oscillations. Obviously the coupling distributions shown in Fig. V.11 invalidate this last approximation. However this rough assumption allows to simplify the calculation as well as the discussion of whether the temperature may explain the discrepancy between the experiment and the theory, observed in Fig. V.10.

We define $\chi_e(t)$ as the probability that one molecule is excited at time t, after excitation by the laser pulse at time $t = 0$. It is proportional to the exponential decay measured experimentally. Then a measure of the average decay rate is provided by [199]

$$\Gamma = \left[\int_0^\infty dt \chi_e(t)\right]^{-1} \tag{V.5}$$

Exploiting the system symmetry in the Heisenberg picture, $\chi_e(t)$ is analytically derived in appendix C. We deduce the average decay rate of N identical TLS that are identically coupled in the weak excitation regime

$$\Gamma = F_P\gamma_p + (N-1)\gamma_{12}\left(\frac{F_P\gamma_p - \gamma_{12}}{F_P\gamma_p - \gamma_{12} + 2\gamma^*}\right) \tag{V.6}$$

In the limit case $\gamma^* \ll \gamma_{12}$, we retrieve the superradiant mode $\Gamma \approx F_P\gamma_p + (N-1)\gamma_{12}$ and notably, $\gamma_{12} \approx F_P\gamma_p$ leads to $\Gamma \approx NF_P\gamma_p$. On the other hand, for $\gamma^* \gg \gamma_{12}$, the N TLS are decoupled and they all undergo the same Purcell effect so that $\Gamma \approx F_P\gamma_p$. The expression in Eq. V.6 explicits that the average decay rate is an affine function with the number of emitters, in agreement with the experimental results in Fig. V.8 and the theoretical predictions in chapters II and III. Moreover the thermal dephasing clearly lowers the slope with N, confirming that the loss of coherence disrupts the plasmonic superradiance phenomenon.

In figure V.13, we compare the simple model from Eq. V.6 with the experimental results from Fig. V.8 for $d = 18\ nm$. We take the average coupling constant γ_{12} estimated in the previous section V.2.d. The dephasing rate is typically $\gamma^* \approx 30$ THz $\approx 10^5\ F_P\gamma_p$, as estimated from the emission spectra in chapter IV and confirmed by the literature [158].

We see in figure V.13 that the theoretical slope is two orders of magnitude smaller than the experimental one. This difference is emphasized by the fact that the system is considered

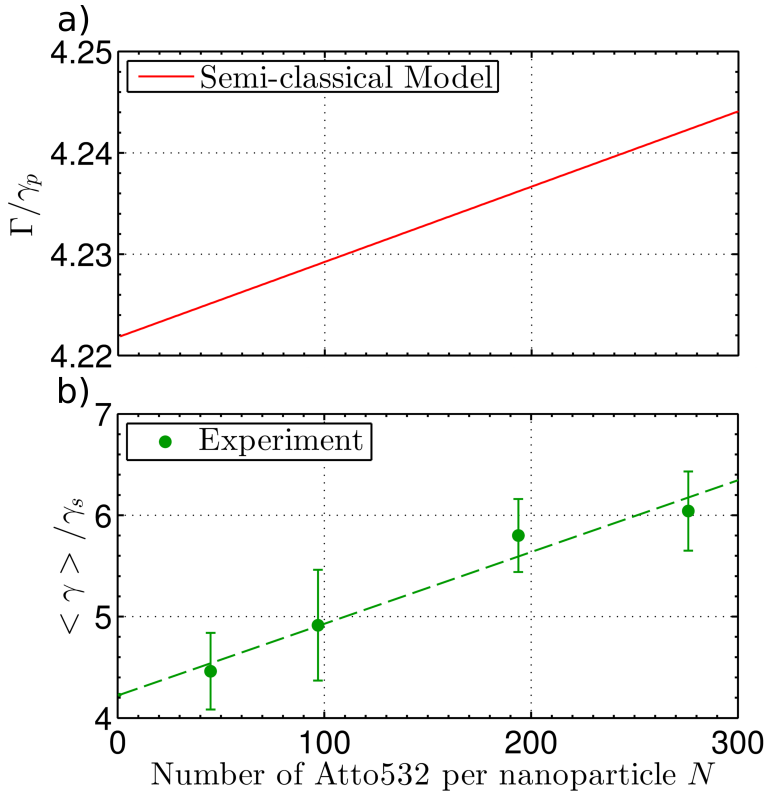

Figure V.13: A number N of emitters are distributed on a $d = 18$ nm thick silica shell coating a 57 nm diameter gold sphere. The TLS are oriented tangentially to the nanohybrid surface. a) Calculated evolution of the average decay rate Γ with the number of TLS per nanohybrid, for $\gamma^* = 10^5 F_P \gamma_p$. This curve was obtained from Eq .V.6. b) Experimental (green dots) evolution of the average decay rate with the number of Atto532 per nanohybrid. The dashed line is a linear fit, as a guide for the eyes.

fully symmetrical in the semi-classical model, yielding to the largest possible superradiant decay rate according to chapter II. We deduce that the Haken-Strobl model, which assumes that each molecule undergoes independent and rapid perturbations, is too strong to describe the effect of dephasing on the observed plasmonic superradiance.

In 1990 S. de Boer and D. Wiersma reported an experimental investigation on the influence of thermal dephasing on the superradiance of J-aggregated pseudoisocyanine bromide (PIC-Br) molecules [200]. They observed a non-disrupted superradiant decay rate up to 50 K, which corresponds to $\gamma^* \approx 10\gamma_p$. Beyond 50 K, they showed that the radiative decay rate is inversely proportional to the temperature. Because these observations cannot be explained with the Haken-Strobl model, the group of S. Mukamel proposed to account for the details of the interaction with phonon modes in a microscopic description [201, 202]. In particular, instead of using a Liouville operator [199], an interaction Hamiltonian was introduced. It describes dipole dephasing as well as population transfer due to the interaction with phonons. Interestingly, this model introduces a temporal memory that can maintain the coherence between the emitters. This new approach allowed to successfully explain the results from S. de Boer and D. Wiersma.

Hence it appears relevant to go beyond the Haken-Strobl model to explain our experimental results. For instance a more microscopic model would allow to incorporate the phonon modes supported by the hybrid structure after the absorption of the excitation pulse [212–215].

V.3 Conclusion

In conclusion we presented an experimental demonstration of plasmonic superradiance with a clear demonstration of cooperativity at room temperature. Plasmon-mediated cooperative emission was shown to be reproducible for two different combination of emitters and plasmonic nanostructures: RhB-based and Atto-based nanohybrids.

RhB molecules were grafted to 86 nm diameter gold sphere coated with a 15 nm thick silica shell. The pH sensitivity of RhB molecules prevented a proper estimation of the number of emitters per nanohybrid. However we observed in ensemble measurements that the average decay rate scales with the concentration of emitters introduced during the RhB binding process. This observation constituted preliminary results. Besides we showed that the number of RhB actually grafted to the nanohybrid was much smaller than expected. This allowed us to neglect the influence of the homo-FRET between neighbor molecules.

A better emitter was then Atto532 fluorescent molecules which is not pH sensitive, shows

good photostability and a 90% quantum yield. These emitters were grafted to a 57 nm diameter gold core with various silica shell thicknesses to study the influence of the distance to the core. A statistical study on single object measurements showed that the average decay rate scales with the number of emitters N. Furthermore we observed that the slope with N increases as the emitters are closer to the plasmonic core. These trends qualitatively validated the prediction proposed in chapter II and thus the model of V. Pustovit and T. Shahbazyan [37]. These last results represent a direct experimental demonstration of plasmonic superradiance at room temperature. Noteworthy the number of emitters per nanohybrid was set below 300 so to dismiss the contribution of the direct interaction between neighbor emitters on the observed effects. This last point was confirmed by ensemble and single object measurements on decorated silica nanoparticles in absence of plasmonic core.

Even though a good agreement was observed between the experiment and the classical theory for $N = 1$, no quantitative accordance was observed concerning the slope with N. Since the superradiance phenomenon results from the coherence between emitters, it is disrupted by pure dephasing mechanisms. The experiment was performed at room temperature and on molecules embedded in a polymer matrix. We thus expect that the plasmonic superradiance in our experiment was affected by the thermal dephasing, the spectral diffusion and the inhomogeneous broadening. To go further we developed a semi-classical model accounting for thermal dephasing and plasmon-mediated interactions between identical emitters. For simplicity, this model assumed negligible spectral diffusion and inhomogeneous broadening. Furthermore it considered a perfectly symmetrical configuration, with an identical coupling between the emitters. This rough model allowed us to confirm that a pure dephasing process such as thermal dephasing yields to a disrupted plasmonic superradiance with a decreased slope with N.

To go further, it would be interesting to develop a microscopic theory accounting for thermal dephasing, spectral diffusion and inhomogeneous broadening. Besides the inhomogeneous coupling between the TLS at the surface of the nanohybrid may also play a key role in the formation of plasmonic superradiance.

Chapter VI

Emitters as probes of a complex plasmo-photonic mode

Contents

In the sought for intermediate quality factor and effective volume, the association of plasmonic and photonic resonances leads to the formation of hybridized modes. In this chapter we investigate the effect of the detuning between an hybridized mode and an emitter on its emission's modification.

As the optical modes of a Photonic Crystal (PhC) can be readily tuned, by changing the illumination incidence angle or the polarization for instance [216], we studied the Purcell factor of emitters distributed on a two dimensional (2D) plasmonic-photonic crystal. The results were published in 2014 [217]. This work is the product of a collaboration with Simona Ungureanu in the CRPP (Bordeaux, France) and Branko Kolaric in the Influx Lab (Mons, Belgium). I was specifically involved in the transmission, reflection and lifetime measurements as a function of angle as well as the corresponding analysis.

Section VI.1 consists in an introduction to hybrid plasmo-photonic crystals. A description of the optical properties specific to the 2D hexagonal close-packed (hpc) PhC is proposed. Then the effect of the deposition of a plasmonic metal overlayer is discussed. In the other sections, the published results are reproduced.

VI.1 Optical properties of a 2D plasmo-photonic hexagonal close-packed crystal

VI.1.a 2D photonic crystal

VI.1.a.i Definition

In general a PhC consists in a basic scheme of modulation of the permittivity: a given unit cell is repeated infinitely periodically. The spatial arrangement of the unit cell forms a lattice with translational symmetry. Thanks to the periodicity, the structure is invariant by any vector that is a linear superposition of the primitive vectors of the unit cell. Hence a PhC is fully described by these primitive vectors. In the present work we are interested in a 2D hexagonal lattice formed by polystyrene (PS) ($\epsilon_{PS} = 2.53$ [218]) spheres closely packed on a glass substrate (about 5 mm thick), as represented in figure VI.1a. The corresponding hexagonal unit cell is represented in figure VI.1b where $(\mathbf{a}_1, \mathbf{a}_2)$ are the primitive vectors whose lengths are given by the beads diameter D. We studied two sphere diameters: 457 nm and 505 nm with a small dispersity in size distribution.

Since the permittivity constant is periodically distributed, the propagation of electromagnetic waves through the PhC is analogous to the motion of electrons in a crystalline

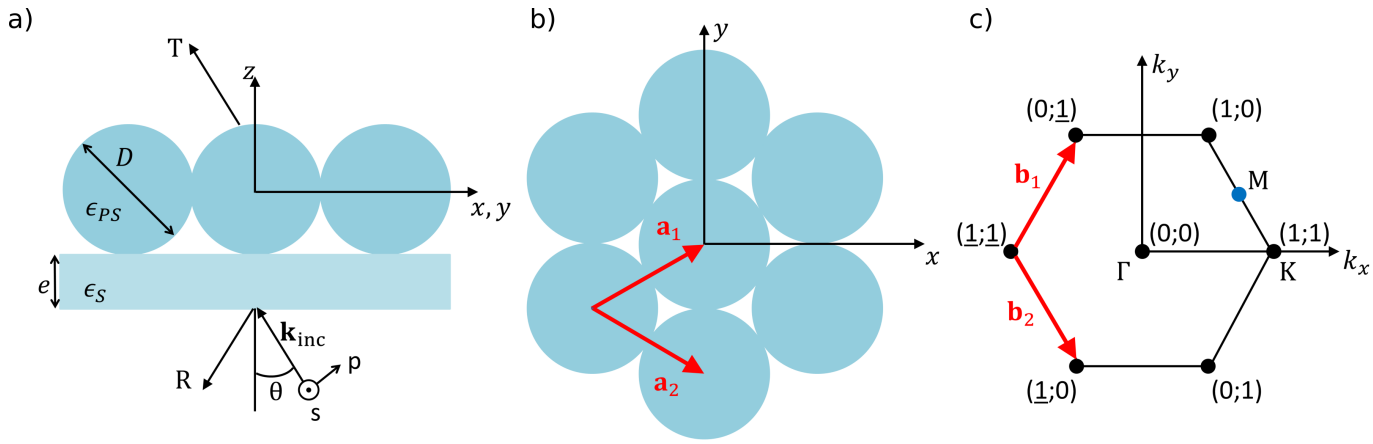

Figure VI.1: a) Diagram of a 2D periodic assembly of polystyrene (PS) spheres on a glass substrate (thickness $e \approx 5$ mm and $\epsilon_S = 2.3$). Typically $D = 500$ nm diameter spheres are closely packed to form a hexagonal close-packed (hcp) lattice in the xy plane. A s or p-polarized plane wave with wavevector $\mathbf{k}_{inc}$ is incident through the substrate with incidence angle θ. Reflection and transmission spectra are then collected as represented by R and T. b) Real and c) reciprocal space of the hcp lattice, with respective primitive vectors $(\mathbf{a}_1, \mathbf{a}_2)$ and $(\mathbf{b}_1, \mathbf{b}_2)$, respectively. In c), numbers indicate the lattice sites, Γ is the centre, K and M are the symmetry points of the Brillouin zone.

solid [216]. The solution $\psi_{\mathbf{k}}(\mathbf{r})$ of the wave equation can then be expressed as a Bloch state, i.e. the product of a periodic function in the x-y plane $u(x, y)$ and a plane wave $e^{i\mathbf{k}\cdot\mathbf{r}}$ [219]. The corresponding wavevector eigenvalues are periodic and form a reciprocal space. Accordingly one usually builds a primitive Wigner-Seitz cell in the reciprocal space, known as the first Brillouin zone (BZ). The reciprocal space of the 2D hexagonal PhC under study is represented in figure VI.1c where $(\mathbf{b}_1, \mathbf{b}_2)$ are the primitive reciprocal lattice vectors. They are expressed by

$$\begin{aligned} \mathbf{b}_1 &= 2\pi \frac{\mathbf{a}_1}{\mathbf{a}_1 \times \mathbf{a}_2} = \frac{4\pi}{\sqrt{3}D}\mathbf{e}_{b_1} \\ \mathbf{b}_2 &= 2\pi \frac{\mathbf{a}_2}{\mathbf{a}_1 \times \mathbf{a}_2} = \frac{4\pi}{\sqrt{3}D}\mathbf{e}_{b_2} \end{aligned} \tag{VI.1}$$

Note that eigenstates with wavevectors differing by a linear superposition of the vectors $(\mathbf{b}_1, \mathbf{b}_2)$ are degenerate. Hence the reciprocal space is fully described by these primitive vectors.

VI.1.a.ii Bragg scattering

The optical response of the structure represented in figure VI.1a is the result of the complex interplay of light scattering by each PS sphere. When the incident wave has his k-vector in phase with the periodic structure, the light scattered in reflection (transmission) construc-

tively (destructively) interfere and one observes a peak (dip) in the far field spectrum. The structure thus supports a standing wave and the propagation through the PhC is forbidden for a range of frequencies, called the photonic bandgap (PBG). Constructive interference of scattered waves was first described in the study of X-rays reflection from a crystal by W. Bragg in 1913 [220], and is thus called Bragg scattering. This phenomenon is a dominant feature in PhC and is involved in the optical mode that is investigated in the published paper.

Let us explicit the condition for Bragg scattering using the reciprocal space formalism. As shown in figure VI.1a, we consider an incident wavevector $\mathbf{k}_{inc}$ whose projection in the sample plane is $\mathbf{k}_{inc}^{\parallel} = \frac{2\pi}{\lambda} sin(\theta)\mathbf{e}_k$ where λ is the incident wavelength and θ is the incidence angle with respect to the sample plane's normal. As we are in the Mie scattering regime, we suppose that light scattering is an elastic process. Therefore any reflected or refracted electromagnetic wave also has the wavelength λ. Then momentum conservation implies that the associated in-plane effective wavevector $\mathbf{k}_{\text{eff}}$ satisfies the relation

$$\mathbf{k}_{\text{eff}} = \frac{2\pi}{\lambda}\sqrt{\epsilon_{\text{eff}}}\mathbf{e}_{k_{\text{eff}}} = \mathbf{k}_{inc}^{\parallel} + \mathbf{G}_{n,p} \tag{VI.2}$$

where ϵ_{eff} is the structure effective permittivity and $\mathbf{G}_{n,p} = n\mathbf{b}_1 + p\mathbf{b}_2 = \mathrm{G}_{n,p}\mathbf{e}_G$ is a reciprocal lattice vector supported by the structure. The condition from Eq. VI.2 is represented in the reciprocal plane in figure VI.2a. For a 2D hcp monolayer of PS spheres, ϵ_{eff} is defined on a filling factor basis : $\epsilon_{\text{eff}} = \epsilon_{PS} f + \epsilon_{air}(1-f) \approx 1.93$ where $f = \pi/3\sqrt{3} \approx 0.61$ [221].

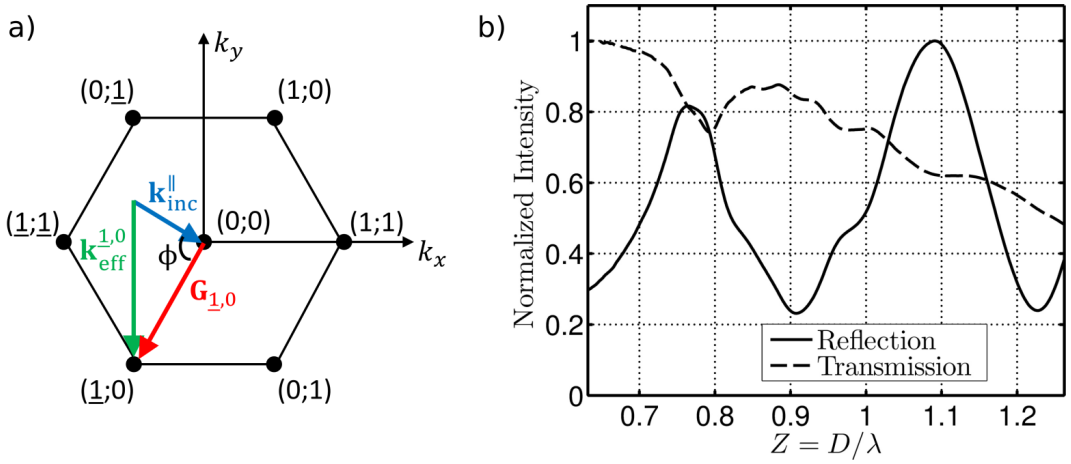

Figure VI.2: a) Reciprocal space of a 2D hexagonal lattice with lattice sites. An incident plane wave $\mathbf{k}_{inc}$ is scattered at the lattice vector $\mathbf{G}_{1,0}$ to result in an effective guided mode $\mathbf{k}_{\text{eff}}^{1,0}$. ϕ denotes the azimuthal angle between $\mathbf{k}_{inc}$ and $\mathbf{G}_{n,m}$. b) Normalized experimental reflection (solid line) and transmission (dashed line) spectra for a 2D hcp lattice of PS spheres ($D = 457$ nm diameter). The spectra were acquired under normal ($\theta = 0°$) incident, non-polarized illumination and through the substrate. Z is the normalized wave number.

Expliciting Eq. VI.2, the Bragg resonance wavelength is then given by [221]

$$\lambda = \frac{\sqrt{3}}{2}\frac{D}{\sqrt{n^2+p^2+np}}\left[\sqrt{\epsilon_{eff} - sin(\theta)^2 sin(\phi)^2} - sin(\theta)cos(\phi)\right] \tag{VI.3}$$

where $cos(\phi) = \mathbf{e}_k \cdot \mathbf{e}_G$.

We show in figure VI.2b the normalized reflection and transmission spectra for a 2D hcp lattice of 457 nm diameter PS spheres, acquired for a non-polarized illumination at normal incidence ($\theta = 0°$). Usually a PhC shows macroscopic dimensions so that the Maxwell equations are scale invariant [216]. Plotting the spectra as a function of the normalized wave number $Z = D/\lambda$ thus allows for comparison between systems with different sphere diameters. For instance we easily verify that the transmission spectrum in Fig. VI.2b shows the same features as the one published by L. Landström *et al.* in Ref. [222] for 1.42 μm diameter spheres.

First we see in Fig. VI.2b that the transmitted intensity decreases with decreasing wavelength because of absorption in both the glass substrate and the PS spheres [223]. We then note a dip in transmission at about $Z = 0.8$, corresponding to a slightly shifted peak in reflection. These features were attributed to the first order Bragg scattering and constitute the PBG of the structure [224, 225]. In the Bragg formalism a first order scattering corresponds to $(n, p) \in [(1, 0), (0, 1)]$. Using Eq. VI.3 for $\theta = 0°$, we derive the position of this first order Bragg resonance $Z_{res} = D/\lambda_{res} = 2/\sqrt{3\epsilon_{\text{eff}}} \approx 0.83$ which is in reasonable agreement with the experimental resonance observed in Fig. VI.2b. The presence of the glass substrate, as well as defects in the lattice, may explain the slight shift to the longer wavelength of the experimental Bragg mode with respect to the estimated one [226, 227].

Then we observe in Fig. VI.2b a second peak in reflection at about $Z = 1.1$ along with a dip in transmission. This minimum in the transmission spectrum on the short-wavelength side was attributed to the coupling to higher order modes propagating in the structure [222]. These modes consist in the scattering of light parallel to the sample plane and are evanescent in free space, in a similar way to Rayleigh-Wood anomaly [228–231]. Therefore they are usually named as Rayleigh-Wood anomaly [224, 232].

We now observe the evolution of the reflection spectrum with the incidence angle θ for non-polarized illumination, see figure VI.3. First, we note a minimum in reflection at $\theta \approx 57°$, it corresponds to the Brewster angle between the air and the effective medium [233, 234]. Next we observe that the Rayleigh-Wood anomaly at $Z = 1.1$ shows no dispersion with the incidence angle. Then we see that the Bragg resonance, previously identified at $Z \approx 0.8$ in Fig. VI.2b, splits progessively as θ is increased. For a non-zero incidence angle θ, we see in

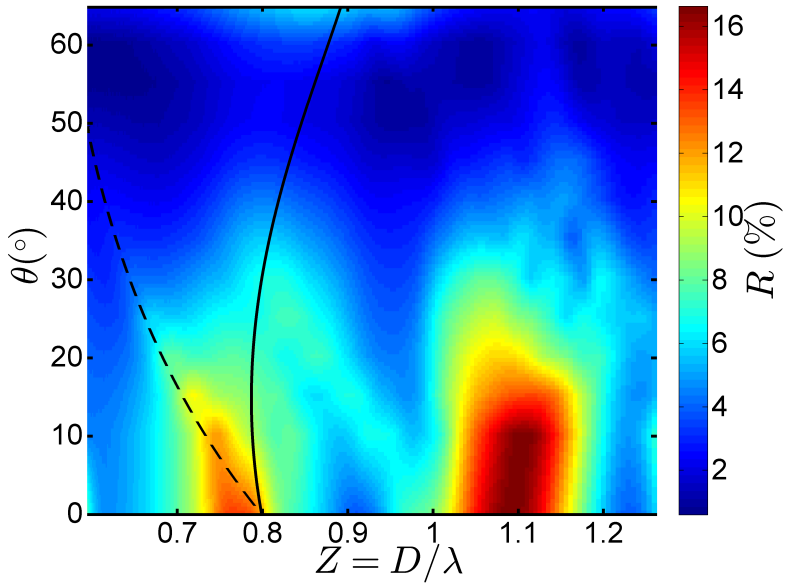

Figure VI.3: Evolution of the experimental reflection spectra from a hcp lattice of PS spheres with the incidence angle θ. The spectra were acquired under non-polarized illumination and through the substrate. Z is the normalized wave number. Black lines are dispersion curves from Eq. VI.3, for $\phi = 5\pi/6$ (dashed line) and $\phi = \pi/2$ (solid line).

Eq. VI.3 that the dispersion curve strongly depends on θ but also on the lattice orientation with respect to the incident wavevector, given by the azimuthal angle ϕ defined in Fig. VI.2a. In practice the reflection and transmission spectra are collected over large area ($3 \times 3\ mm^2$), and as the monolayer is not perfectly arranged, several domain orientations are investigated. As a consequence all azimuthal angles ϕ are potentially present. The measured spectra are thus the result of averaging that may depend on the angle of incidence θ. Nevertheless it has been reported, based on FDTD calculation, that incident light may preferentially couple to specific orientations depending on its polarization (see Fig. VI.1) [221]. More precisely, s-polarization preferentially couples for $\phi = 5\pi/6$ and $\phi = \pi$ while p-polarized light shows a better coupling for $\phi = \pi/2$. Accordingly a good agreement is observed in Fig. VI.3 between the reflection peaks and the dispersion curves plotted for $\phi = 5\pi/6$ (dashed line), thus attributed to s-polarization, and for $\phi = \pi/2$ associated to p-polarization. At small θ FDTD calculation showed that the coupling to guided modes is almost equally averaged over all azimuthal orientations ϕ. This is in agreement with the broad Bragg reflection peak showing poor dispersion with small θ in Fig. VI.3. The evolution of the Bragg resonance with the incidence angle here reported was observed for transmission dips in similar structures [221].

Finally the position of the Bragg resonance and its coupling efficiency can be tuned by deposition of a dielectric layer onto the sphere lattice [221, 222].

VI.1.a.iii Mie scattering

Besides the Bragg scattering, Mie scattering by each PS sphere [88] also contributes to the optical response of the structure. Light scattering by a 500 nm diameter PS sphere exhibits specific eigenmodes described by the spherical harmonics with index l.

Low-order Mie resonances ($l \leq 3$) are spatially extended outside of the sphere, allowing for interactions with its close environment. On one hand, the coupling to the glass substrate modifies the optical response [227], and notably results in a shift of the reflection peak, as noticed previously in Fig. VI.2b. On the other hand, when the Mie modes of two neighboring spheres spatially overlap, light leaked from one sphere can be trapped by another one. The field is then trapped in the structure and results in a local Bloch mode [235]. For an increasing number of spheres in the monolayer, this mode progressively builds up a new photonic band, resulting in a peak in reflection and a dip in transmission [225,236]. The overlap of Bragg and Mie resonances in PhC was then used as a solution to produce optimized PBG [235,237,238]. Nonetheless the Mie resonance of a 457 nm diameter PS sphere is at about $\lambda_{Mie} = 720\ nm$, yielding to $Z_{Mie} = 0.64$. So Mie scattering weakly affects the Bragg mode in the studied structure [224].

On the contrary higher order Mie resonances are confined in the sphere and consist in intraparticle Mie scattering. Their contribution to the far field spectra is thus weak and consists in the geometrical sum of the scattering from each sphere. Accordingly higher order Mie resonances were reported to structure the background of the reflection spectrum with broad and weak peaks [224].

VI.1.b 2D plasmo-photonic crystal

The design of optical devices using dielectric PhC led to some very interesting features such as tunable PBG, but also light guidance [239], light localization [240] and slow light group velocity [241] in the structure.

Nevertheless metallic gratings constitute another approach to control the scattering of light using a periodic structure. In this case the incident light couples to electronic modes: localized or propagating surface plasmons [242]. These plasmonic resonances allow to confine light in subwavelength volumes [14,243], leading interesting features such as omnidirectional absorption [244] or Extraordinary Optical Transmission (EOT) [245,246]. Furthermore the plasmonic modes can strongly couple to photonic modes [247], thus stimulating the introduction of plasmonics in PhC.

To achieve EOT in a 2D plasmo-photonic crystal, the coupling between photonic and

plasmonic resonances should be optimized [234]. This is successfully performed by capping the PS spheres with a thin metal layer [248, 249] as represented in figure VI.4a. In this configuration plasmonic and photonic modes support the same periodicity and interpenetrate each other. In the studied structure, a 50 nm thick gold layer was deposited on the 2D hcp PhC. The metal layer was thick enough to form a periodic arrangement of hemispherical Au caps that are interconnected at the touching points of neighboring spheres [250]. Here we briefly discuss the optical properties of the resulting hybrid structure.

VI.1.b.i Localized surface plasmon polariton modes (LSPP)

The limited volume of each hemispherical metal shell leads to the formation of localized electron oscillations, resulting in a so-called Localized Surface Plasmon Polariton mode (LSPP). These electrons oscillate with specific patterns imposed by the spherical shape of the metal cap. It was reported that the transverse dipolar mode represented in figure VI.4a dominates in the far field response [251].

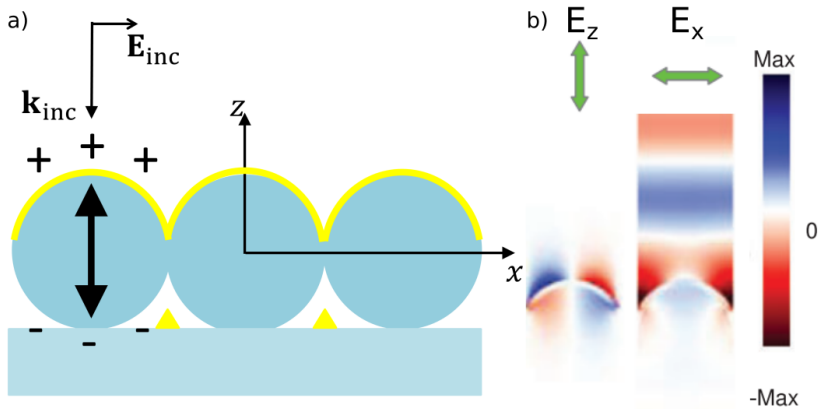

Figure VI.4: a) Schematic of localized plasmon oscillation for the transverse dipolar mode of an hemispherical metal cap. b) Electric near field of the Localized Surface Plasmon Polariton (LSPP) mode, estimated from FDTD simulations of the 2D structure with substrate. The exciting electric field is linearly polarized along x ($\mathbf{E}_{inc}$), propagates along z ($\mathbf{k}_{inc}$), and is detected in the x (E_x) and z (E_z) directions. (Reproduced from Ref. [252])

To understand its effect on the optical response, we reproduce in figure VI.4b a map of the electric near-field, along x and z directions, of the LSPP mode from FDTD calculation in Ref. [252]. As indicated in Fig. VI.4a, the incident electric field propagates along z and is polarized along x. Strikingly we note that the field does not propagate in the structure, but is localized at the dielectric-metal interface, confirming the formation of localized plasmon oscillations. The LSPP resonance thus results in a peak in absorption while it is a dip in transmission and reflection, on the long wavelength side of the Bragg resonance [232, 252].

Finally the localized plasmon resonance is determined by the shape and dimensions of the metal cap and it shows no dispersion with the incidence angle [234].

Besides we note that during the metal deposition, some gold is deposited on the glass substrate through the interstices of the 2D lattice. It results in an array of well separated conical metal islands, as represented in figure VI.4a. These nanocones support LSPP modes that are weakly coupled to the rest of the structure, they thus have a negligible contribution to the structure optical response [250].

VI.1.b.ii Surface plasmon polariton modes (SPP)

If the metal layer is thick enough to form interconnected caps, then the electron oscillation can propagate along the periodic lattice, at the metal-air and metal-dielectric interfaces. In addition to the LSPP, the hybrid structure thus supports Surface Plasmon Polariton modes (SPP) following the metal corrugation. One thus expect the same behavior as observed when light couples with SPP in metal gratings [242, 253]. A SPP mode is then optically excited when its wavevector matches the incident wavevector and the grating reciprocal vector [245, 254]

$$\mathbf{k}_{\mathrm{SPP}} = \frac{2\pi}{\lambda}\sqrt{\epsilon_{\mathrm{eff}}}\mathbf{e}_{k_{\mathrm{SPP}}} = \mathbf{k}_{inc}^{\parallel} + \mathbf{G}_{n,p} \tag{VI.4}$$

where $\epsilon_{\mathrm{eff}} = (1/\epsilon_{Au} + 1/\epsilon_{\mathrm{dielectric}})^{-1}$ is the effective permittivity of the SPP mode [255] and $\epsilon_{\mathrm{dielectric}}$ is the permittivity of air or of the PS monolayer, depending on the interface. Comparing the resonance condition for $\mathbf{k}_{\mathrm{eff}}$ in Eq. VI.2 and for $\mathbf{k}_{\mathrm{SPP}}$ in Eq. VI.4, we note that, as the Bragg and the SPP modes appreciate the same periodicity, they spectrally overlap. Furthermore the structure is designed in such a way that the two modes spatially interpenetrate each other. Hence the coupling between Bragg and SPP modes is very efficient and results in an hybrid mode called Bragg-plasmon or Bloch-SPP mode [232, 248, 252].

In practice when light is coupled to a hybrid Bragg-plasmon mode, instead of being guided in the structure and coherently scattered as observed for the Bragg mode in PhC, the corrugated SPP allows for light out-coupling. Indeed the lifetime of SPP in a corrugated metal film is much smaller than its absorption characteristic time, and is limited by its coupling to the free space [256]. It thus results in a peak in transmission (EOT) and a dip in reflection [248]. This mechanism and the associated features are similar to those reported for EOT on perforated metallic films, confirming the role of plasmon oscillations.

We show in figure VI.5 the evolution of the reflection and transmission spectra of a 2D hcp plasmo-photonic crystal with the incidence angle under non-polarized illumination. First we observe that the Rayleigh-Wood anomaly previously observed for $\theta = 0°$ at $Z = 1.1$ (Fig.

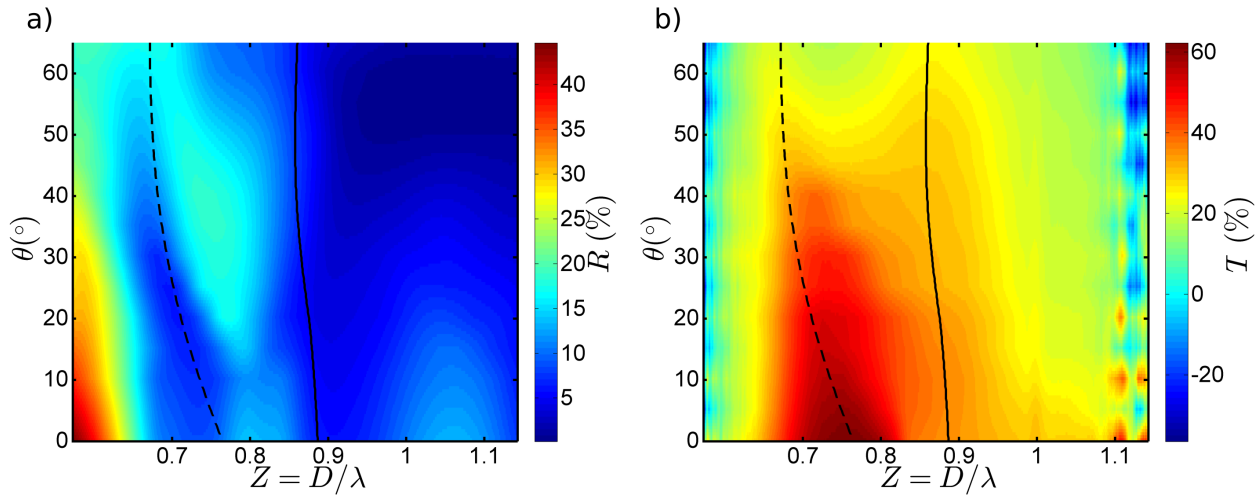

Figure VI.5: Evolution of the experimental a) reflection and b) transmission spectra with the incidence angle θ. The structure is a 2D hcp lattice of PS spheres coated with a 50 nm gold film, as represented in Fig. VI.4a. The spectra were acquired under non-polarized illumination and through the substrate. Z is the normalized wave number. Black lines are dispersion curves from Eq. VI.4 for $\phi = 123°$, with $\epsilon_{dielectric} = \epsilon_{air} \approx 1$ (solid line) and $\epsilon_{dielectric} = \epsilon_{ps} f + \epsilon_{air}(1-f) \approx 1.93$ (dashed line).

VI.2) is slightly shifted to longer wavelength but still corresponds to a peak in reflection with no dispersion with θ.

In agreement with the literature [232, 248] we then observe in Fig. VI.5 a reflection dip and a transmission peak that substitute the reflection peak and the transmission dip observed in Fig. VI.2b for the bare monolayer at $Z \approx 0.8$ and $\theta = 0°$. This dramatic transformation of the optical response with an EOT is the result of the hybridization from Bragg to Bragg SPP mode.

With increasing θ the coupling to this Bragg-SPP mode shows a different dispersion as the one observed for the Bragg scattering in the bare structure (see Fig. VI.2b). Using Eq. VI.4 with $\epsilon_{\text{dielectric}} = \epsilon_{PS} f + \epsilon_{air}(1-f) \approx 1.93$, the best fit was obtained for $\phi = 123°$ (dashed line), showing that the averaging over the azimuthal angle is different between the Bragg and the Bragg-SPP modes. A similar value was estimated by Ding *et al.* in Ref. [255].

Then we observe in Fig. VI.5b another transmission peak at $Z \approx 0.9$ for $\theta = 0°$, with a corresponding dip in reflection in Fig. VI.5a. This second transmission peak was attributed to the coupling to the Bragg-SPP mode formed with the SPP propagating on the gold-air interface [232, 234]. A good agreement was indeed observed using Eq. VI.4 with $\epsilon_{\text{dielectric}} = \epsilon_{air} \approx 1$ and $\phi = 123°$ (solid line).

Finally the optical mode that was investigated in the following published work is the Bragg-SPP mode formed with the SPP on the gold-monolayer interface, i.e. $Z_{res} \approx 0.76$ corresponding to $\lambda_{res} \approx 600\ nm$ for 457 nm spheres.

VI.2 Abstract

We report on the experimental observation of an asymmetric wavelength-dependence of the emission rate enhancement in a two-dimensional plasmo-photonic crystal. This feature strongly contrasts with the traditional Lorentzian line shape exhibited at a resonance by the Purcell factor. The unusual dispersive behavior is shown to be reproducible for different combinations of emitters and structures measured in different geometries. It is further retrieved from finite-difference time-domain simulations and is dominantly attributed to the fact that a hybridized mode, resulting from the coupling of a Bragg and a surface plasmon polariton modes, is coupled to the emitters. Further studies of the emission detuning by hybrid plasmonic/photonic structures are expected to benefit many related fields and notably sensing and bio-sensing technologies.

VI.3 Introduction

The spontaneous decay rate of a quantum emitter is strongly altered by its surrounding environment. The Purcell effect [59] represents the maximum spontaneous rate enhancement for an ideal coupling between a single emitter and a cavity mode, i.e., a perfect spectral, spatial, and polarization matching [59]. A spectral mismatch between the dipole frequency and the cavity resonance reduces the decay rate according to the usual Lorentzian line shape. It is one of the most fundamental effects investigated in quantum electrodynamics. Owing to recent advances in nanotechnology, tremendous applications have emerged and numerous fundamental studies have arisen in order to push the reachable limits of this factor. The control of spontaneous emission by manipulating optical modes with photonic crystals (PhC) has been predicted and achieved in various structures [168, 257–260]. One has recently seen the advent of nano-lasers [261], plasmonic antenna for light [65, 262], plasmon based nano-lasers [27, 263], enhanced single-photon sources [264].

A hybrid optical nano-cavity, consisting of a photonic crystal coupled to a metal surface separated from the PhC by a nano-scale air gap, has been shown to open up opportunities for various applications in enhanced light-matter interactions [265]. When two-dimensional (2D) photonic crystals are made of noble metal (thereby avoiding oxidation), the periodically modulated complex dielectric function of the metallic structures allows for the optical excitation of surface plasmon polaritons (SPP). These SPP propagate along the metallo-dielectric interface due to diffractive coupling [266, 267]. Quantum emitters located in the vicinity of such 2D metallic PhC will experience the Purcell effect [147,165,252]. Their emission can also

be spectrally reshaped [268] or spatially redirected [255, 269]. Such plasmo-photonic systems can also be used in bio-sensing [270, 271], photo-voltaic and photo-catalytic devices [272, 273].

Actually, structures possessing a large area are beneficial to real life photonic and opto-electronic applications. Nanosphere lithography (NSL) has been used to fabricate large plasmo-photonic structures [274–278]. In NSL, convective self-assembly (CSA) produces arrays of colloidal spheres as templates for 2D plasmo-photonic architectures. Their optical properties are usually characterized by the excitation of i) non-dispersive localized surface plasmon polaritons modes (LSPP), ii) photonic modes as the Rayleigh-Wood mode and iii) traveling SPP, which can be excited via momentum transfer of a reciprocal lattice vector, the so-called Bloch-SPP or Bragg-plasmon (BP) mode [232, 234, 248, 250, 252].

In this paper, we use NSL to engineer 2D hybrid colloidal crystals, here after named 2Dhcc structures. Owing to experimental and numerical observations of the UV-visible spectra, we assign unambiguously the transmission maximum of the structure to a BP mode. After dispersing a solution of quantum dots with their emission spectrum spectrally overlapping the BP mode of the 2Dhcc structure, we show that the average emission rate enhancement $< F_P >$ exhibits an asymmetric (non Lorentzian) dispersive behavior with an increase (decrease) of $< F_P >$ as a function of wavelength while reaching (passing over) the BP peak. This asymmetric spectral detuning between the emitter and the BP resonance is further retrieved from numerical simulations of the emission rate enhancement. It is explained in terms of hybridized mode and spatial averaging, bringing the system far from the Purcell regime. While the absolute values of $< F_P >$ are not as spectacularly large as those reported for other structures [279], the observed behavior is well reproduced for different combinations of emitters and structures, pointing to the robustness of our approach.

VI.4 Materials and methods

Latex micro-spheres [diameters $D = 457$ nm and $D = 505$ nm, 2.5% solids (w/v) aqueous suspensions] were supplied by Polysciences. Au (99.999%, 3mm x 6mm) was purchased from Neyco. CdSe@ZnS quantum dots suspended in toluene with emission peaks at either 570 nm, 610 nm and 640 nm were supplied by Aldrich. Glass plates with a size of $2X2$ cm^2 and a thickness of 5 mm were carefully cleaned and treated with UV-ozone for 30 min. Then an opportune ratio of Triton $10-3$ (mass) in water/polystyrene (PS) micro-spheres was deposited on the glass surface and dried under a tilt angle of approximately 10^o under controlled conditions of temperature and humidity ($T = 293$ K, $H = 65\,\%$). After formation of large areas of well-ordered mono-layers of latex nano-spheres, the substrates were covered

with 50 nm of gold by using a Boc-Edwards Auto306 evaporator. The thickness was controlled by an in-situ mounted quartz crystal micro-balance. Then a 20 μl volume of QDs solution (1 % v/v in either water or toluene/ethanol) were randomly spread (drop casted) on the gold coated mono-layers. We estimated that $\approx 10^4$ QDs were deposited on each gold coated PS bead. The AFM image of drop casted QDs on a similar hybrid plasmonic-photonic structure is published elsewhere [252].

Scanning electron micro-graphs (SEM) were recorded on a field-emission scanning electron microscope (FESEM, JEOL JSM-6700F). The transmission spectra of the plasmo-photonic crystals were measured on the whole visible range, collecting the signal from a large (3 mm) area owing to a white light illumination lamp (fiber coupled white light HL-2000-HP-FHSA, Ocean Optics) used in combination with a spectrometer (fiber spectrometer USB2000 + VIS-NIR, Ocean Optics). The spontaneous emission properties of the various quantum dots were recorded with a spectral- and time- resolved set-up consisting of a streak camera (HAMAMATSU Streak Scope C10627) pre-fitted with a spectrograph (Princeton Instruments) with a 150 gr/mm choice of the grating. The excitation light was the frequency doubled output of the $\lambda = 1030$ nm wavelength, 10 MHz repetition rate, 300 fs line width pulses delivered by a diode-pumped Ytterbium femtosecond oscillator from Amplitude systems (t-Pulse 200). The beam was collimated to a 1.5 mW, 100 μm diameter spot to excite the emitters in the targeted nano-structure prior to focus the $530\,nm$ long-pass filtered emission intensity on the entrance slit of the spectrograph.

The transmission (T), reflection (R) and absorption (A) spectra, the modes and the local density of states of the 2Dhcc structures have been simulated by solving Maxwell equations using the three-dimensional finite-difference time-domain (FDTD) method, as implemented in the freely available MEEP software package [280]. By Fourier transforming the response to a short, broadband, spatially extended Gaussian pulse in the far-field of the structures and normalizing with the response of a reference (the glass substrate) for the same excitation conditions, a single simulation yielded the T, R, A spectra over a wide spectrum of frequencies. The resonance modes were obtained by sending a narrow-band, frequency gated, and spatially extended Gaussian pulse in the far-field of the structure and recording the three components of the electric field in time. Finally, in order to compute the emission rate enhancement of the emitters on the nano-structures, we performed Fourier transforms of the response to an impulsive point-dipole TM-polarized source. We then normalized this response with the one obtained for a point-dipole source located near the substrate in the same excitation conditions. In all types of simulations, the wave-vector is normal to the substrate's surface; periodic boundary conditions were implemented laterally while perfectly

matched layers were implemented longitudinally, in the propagation direction. The dielectric permittivities of the glass substrate and the PS spheres were taken as 2.3 and 2.5, respectively. The dielectric permittivity of gold was specified by using a sum of Drude and Drude-Lorentz terms, according to the work performed by Rakic et al. [83]

VI.5 Results and discussion

Mono-layers of polystyrene (PS) beads of either 457 nm or 505 nm have been self-assembled in a compact hexagonal lattice onto a glass substrate according to well-reported procedures [275–277]. Subsequently, these structures have been coated with a 50 nm thick layer of gold, forming 2-dimensional hybrid colloidal crystals (2Dhcc, Figure VI.6: the middle inset shows a scheme of the engineering process). This manufacturing technique, called Nano-Sphere Lithography, is known to allow for the easy, inexpensive fabrication of high quality, large (cm^2) surface areas. Figure VI.6 exhibits such a large area of $100\mu m\ X\ 100\mu m$ with a single crystalline plane of coated beads. As a close inspection reveals, a single crystalline orientation is found from the top left of the figure to the bottom right. If some very slight grooves are frequently visible between two adjacent lines of beads (either caused by attractive capillary forces acting at a late stage of drying or by the presence of a tiny or a big bead slightly disturbing the arrangement, see the bottom left inset recorded at larger magnification), they do no reach the state of dislocations, or grain boundaries, as there are no orientation changes between adjacent domains.

The UV-visible-near IR optical properties of these 2Dhcc structures have been extensively studied in the literature [234,248,250,252]. Here, we aim to focus specifically on the BP mode, and investigate in detail its action on the emission of quantum weakly-coupled excitons. In order to precisely locate the resonance wavelength of this mode, we firstly performed transmission and reflection measurements. Figure VI.7a shows such spectra for a structure based on $D = 457$ nm diameter PS beads. The absorption spectrum, also shown in Fig. VI.7a, has been obtained by applying the usual formula $A(\lambda) = 1 - T(\lambda) - R(\lambda)$. In excellent agreement with the literature [232], a major peak is observed in transmission at 610 nm, which is attributed to the BP mode. On the long wave side of this peak, a significantly reduced transmission, associated with an absorption maximum, is noticed, which can be assigned to a LSPP mode. In order to assess the quality of our samples (in addition to the SEM inspection performed in Fig. VI.6) and the spectral measurements, we performed FDTD simulations of transmission (T), reflection (R), and absorption (A) spectra. These far-field spectra are shown in Fig. VI.7b (dashed, dash-dotted, and dotted lines, respectively). Clearly, the matching of

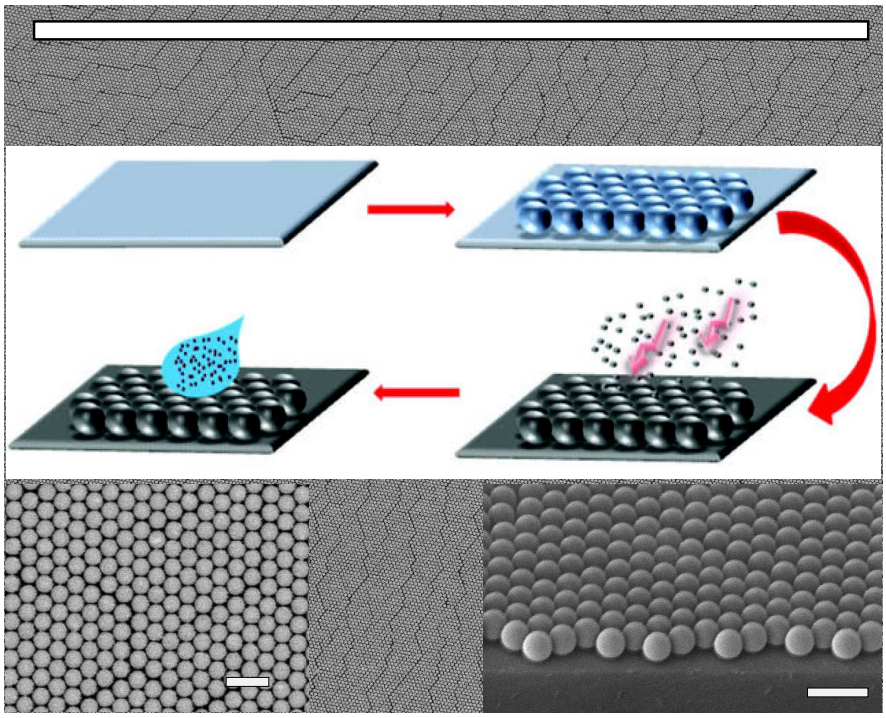

Figure VI.6: SEM micrograph of the 2D hybrid colloidal crystal (2Dhcc) recorded at low magnification (the scale bar is $100\mu m$ *long). The bottom left inset shows a portion of this micrograph obtained at larger magnification (scale bar of* $1\mu m$*). The bottom right inset shows a tilted SEM view, evidencing the formation of a single monolayer during this assembling process. The middle inset shows a scheme of the manufacturing process, consisting in the convective self-assembly (CSA) of an hexagonal mono-layer of polystyrene (PS) beads onto a glass substrate, followed by the evaporation of a thin metal layer (*50 *nm) and the deposition of CdSe@ZnS quantum emitters.*

the Bragg-plasmon resonance wavelength is good between simulations and experiments. The transmission maximum is recovered, centered at 595 nm and coincides with the minimum absorption. This contrasts with the simultaneous observation of transmission and absorption maxima in extraordinary transmission of hole arrays [281]. Concerning the LSPP resonance wavelength, we observe a slight discrepancy between simulations and experiments, which might originate from an imperfect coverage of the gold over-layer in the experiments, as compared to the ideal simulated case.

The simulated H_y and E_z near-field patterns at the transmission maximum, TM-excited at normal incidence, are shown as insets of Fig. VI.7a. The H_y field is directly transmitted through the structure. The field distribution suggests that an interference mechanism (like in planar thin films) contributes to the transmitted band. The E_z map exhibits a periodic pattern in the x direction, indicative of a propagative mode in the plane of the array, with z-polarized light propagating along the x direction. The distance between the two 'lobes', about half the sphere diameter, together with the large spatial extension, support the propagative nature of this mode. The same E_z map reveals a symmetric coupling between the outer and inner surfaces of the shells, again characteristic for long-range propagative modes. These features ascertain the Bragg-plasmon character of the maximum transmission peak [232,249]. The significant reduction of the transmission on the long wave side (Fig. VI.7b) coincide with an absorption maximum at 660 nm, which further signals the attribution of this mode to a LSPP [232].

Let us now proceed to the investigation of the emission properties of QDs spread onto the structure and spectrally overlapping the BP mode. We aim to observe the spectral detuning of the emission rate enhancement between the emitter and BP resonances. An obvious way to achieve this is to i) disperse onto the structure QDs possessing an emission spectrum slightly detuned (on the long wave side) with respect to the transmission maximum, at normal incidence; ii) rotate the sample so that the maximum transmission peak is brought trough the emission spectrum of the emitters. Indeed, owing to an increase of the incidence angle, the main transmission peak is expected to shift to the long wave side, going all the way through the other edge of the emission spectrum, according to the Bragg-plasmon law [221,248]

$$\lambda = \frac{\sqrt{3}D}{2}(\sqrt{\epsilon_{\text{eff}}(\lambda) + sin^2\theta}) \tag{VI.5}$$

where $D = 457nm$ is the diameter of spheres, ϵ_{eff} is the effective permittivity expressed by the plasmonic-dielectric interface mixing rule $\frac{1}{\epsilon_{\text{eff}}(\lambda)} = \frac{1}{\epsilon_{Au}(\lambda)} + \frac{1}{\epsilon_{\text{dielectric}}}$ [255], in which $\epsilon_{\text{dielectric}}$ is defined on a filling factor basis $\epsilon_{\text{dielectric}} = \epsilon_{PS}f + \epsilon_{air}(1-f)$ as estimated in ref. [248].

The 610 nm maximum CdSe@ZnS emitter has precisely its emission spectrum slightly

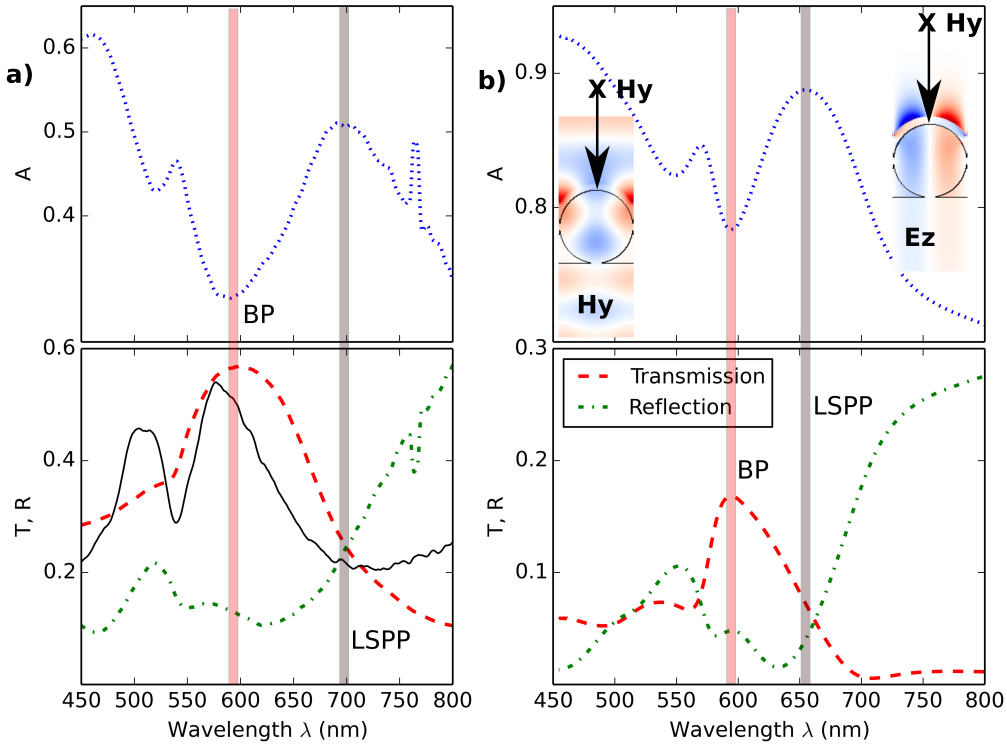

Figure VI.7: Experimental (a) and simulated (b) transmission (T, red dashed), reflection (R, green dash-dotted) and absorption (A, blue dotted) spectra of the 2Dhcc structure coated with a gold thin layer. The reflection spectrum of the bare PS monolayer assembled on the glass substrate is shown for comparison (solid black line). The insets in b) are the H_y and E_z near-field patterns of the 2Dhcc structure TM-excited at the 595 nm wavelength of the BP mode. Light is propagating from top to bottom (z-direction).

red-shifted with respect to the maximum transmission of the BP mode, at normal incidence (Fig. VI.9a). Figure VI.8b shows the 2D (x- and y-axis: spectral and temporal dimensions, respectively) fluorescence diagram measured for such $\lambda_{max} = 610$ nm CdSe@ZnS emitters deposited on the 2Dhcc structure at an incidence angle $\theta = 60°$ (inset). We retrieve the total decay profile, Fig. VI.8a, by projecting this 2D plot on the y-axis. The decay profiles are obtained as a function of wavelength by dividing the x-axis in 5 nm range windows and projecting the resulting diagrams on the y-axis. We then determine the average decay times by performing stretched exponential fits [147] on all 5 nm wavelength -resolved decay profiles. The profiles shown in Fig. VI.8c provide a direct comparison of the decay rates exhibited by the emitters deposited on either the glass substrate (reference, blue circles) or the structured sample (red triangles), in the selected wavelength range 620 nm $< \lambda <$ 625 nm. The estimated average decay times are $< \tau >= 9.16 \pm 0.07$ ns and $< \tau >= 4.87 \pm 0.05$ for the emitters in the reference (solid blue line) sample and in the structure (dashed red line), respectively.

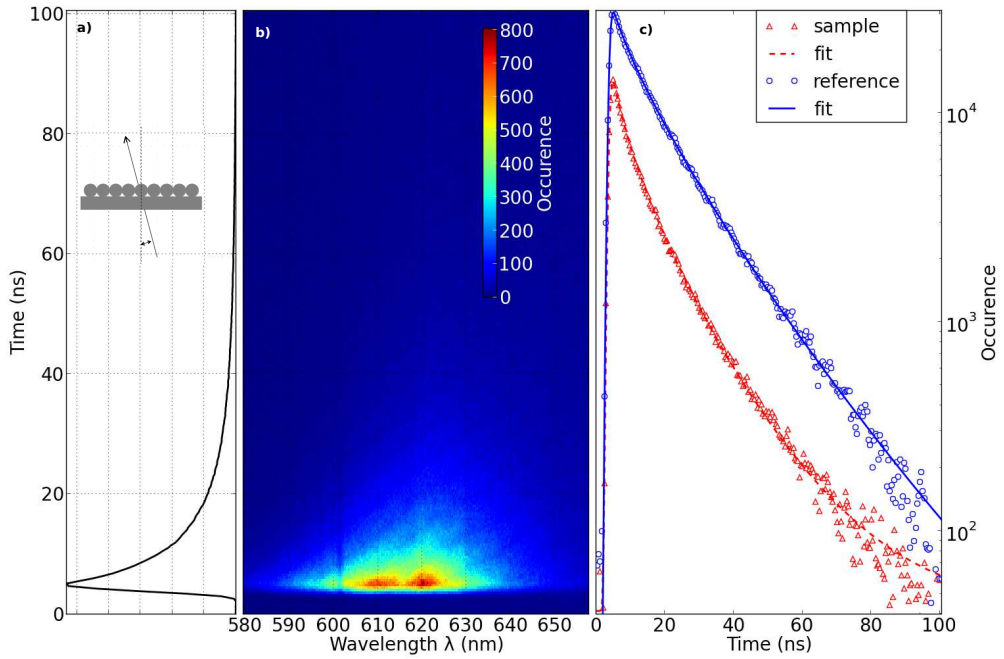

Figure VI.8: Experimental fluorescence decay profile (a) obtained by projecting on the time axis the fluorescence diagram (b) of emitters deposited onto the gold 2Dhcc structure measured at an oblique incidence $\theta = 60°$. c) Decay profiles, for the selected $620-625$ nm wavelength range, of emitters deposited either on the glass substrate (blue circles) used as a reference or on the structured sample (red triangle). The lines are the best fits of a stretched exponential function convoluted with the instrumental response function of the setup.

In order to determine the average emission rate enhancement $< F_P >$ of the CdSe@ZnS quantum dots deposited on the structure, we have divided the decay rates of the quantum emitters on the 2Dhcc structures Γ^{2Dhcc} with respect to the same respective emitters deposited

on glass Γ^{glass}, according to Eq. VI.6 [282].

$$< F_P >= \frac{\Gamma^{2Dhcc}}{\Gamma^{glass}} \tag{VI.6}$$

A $< F_P > \simeq 2$ has been determined for these emitters deposited on the 2Dhcc structure within the selected wavelength range and incidence angle. This way, we determined the average emission rate enhancements for all types of emitters investigated in this paper, in wavelength ranges of 5 nm across their emission spectra. Figure VI.9a shows the transmission spectra of the structure at different incidence angles for unpolarized light. With an increase of θ, the main transmission peak (BP) is indeed red-shifted and its intensity decreases. Considering the coupling condition with a reciprocal vector of an hexagonal structure [248] and taking into account the gold dispersion, we estimated the BP resonance wavelength by resolving eq. VI.5. It shifts from 595 to 680 nm.

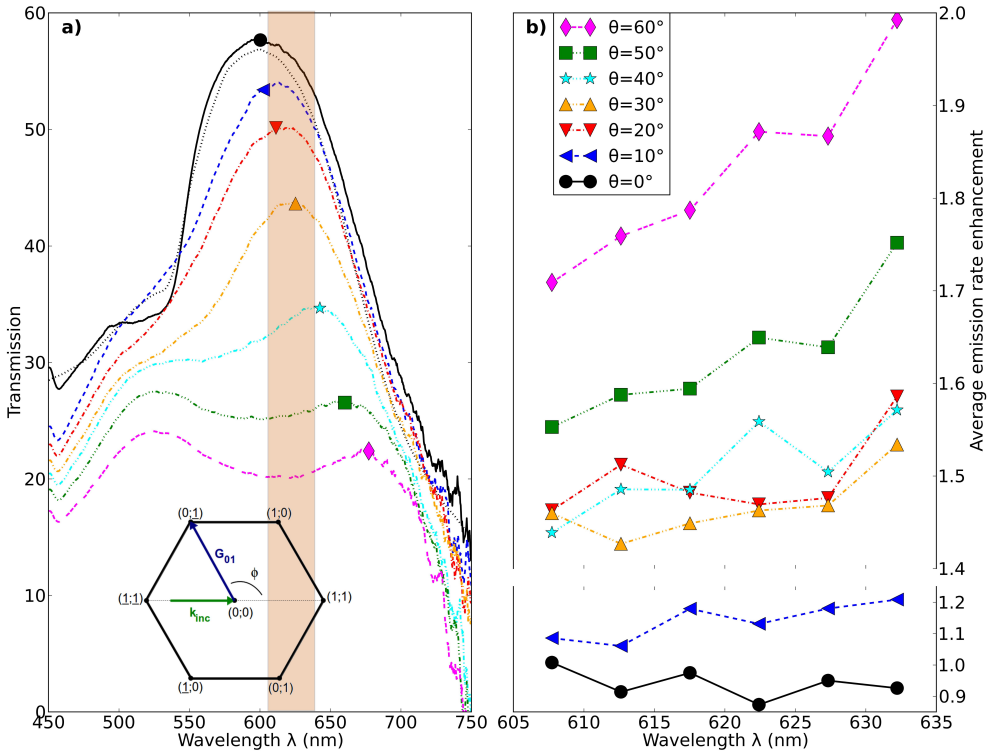

Figure VI.9: a) Experimental transmission spectra (lines) of the 2Dhcc structure for different incidence angles and unpolarized incident light. The symbols indicate the predicted wavelengths of the BP resonances. The shaded area represents the spectral emission range of the used QDs. b) Average emission rate enhancement of the 610 *nm maximum CdSe@ZnS emitters as a function of wavelength for different incidence angles.*

Figure VI.9b shows the wavelength-dependent evolution of the average emission rate enhancement. At $\theta = 60^o$ incidence angle, for which the emission spectrum of the considered emitters is on the blue side of the BP mode, $< F_P >$ rises as a function of wavelength.

Then, as the angle θ is progressively reduced close to 0, dragging the transmission maximum to the short wave side through the emission spectrum, the slope of $< F_P >$ as a function of wavelength decreases progressively prior to be slightly negative at $\theta = 0$. As a whole, very interestingly, we do observe an asymmetric dispersive behavior of the emission rate enhancement with a relatively steep rise of $< F_P >$ while approaching the BP resonance and a smooth decline once passed.

To further demonstrate such observation of an asymmetric, non Lorentzian spectral detuning between the dipole emitter and the BP resonance frequencies, we performed additional measurements. On the one side, we manufactured 2Dhcc structures based on larger PS beads of diameters $D = 505$ nm. After gold deposition, we dispersed a solution of 610 nm maximum CdSe@ZnS quantum emitters onto the structure. Because of the larger lattice parameter, the whole transmission spectrum of the structure is shifted to the long wave side so that the emission spectrum of the quantum dots lies on the blue side of the BP mode. Figure VI.10 shows the numerically (a) and experimentally (c) obtained spectra, with (red up triangles) or without (black solid line) emitters deposited on top of the structure (c), together with the emission spectrum of the latter (b). Clearly, the matching between the simulated and experimental spectra is good with a transmission maximum (absorption minimum) located at 650, 680 nm, respectively. The deposition of the quantum dots on top of the structure did not modify significantly the transmission spectrum (red curve compared to the black one in Fig. VI.10c), preserving the spectral matching of the short wave side of the BP mode and the QDs emission spectrum. After measurement of $< F_P >$, according to the procedure here above described and use of Eq. VI.6, we observe an increase of $< F_P >$ as a function of wavelength while reaching the BP resonance mode from the short wave side (Fig. VI.10d), in full agreement with the results shown in Fig. VI.9b.

On the other side, we have dispersed 570 and 640 nm emission maxima CdSe@ZnS quantum dots on top of the initial 2Dhcc structures (with PS beads of 457 nm diameter). These two types of quantum dots have been chosen since their emission spectra cover nicely one or the other side of the BP mode. Figure VI.11a shows the $< F_P >$ obtained at normal incidence for each of these emitters ($\lambda_{max} = 570$ nm, blue squares; $\lambda_{max} = 640$ nm, red circles). Very remarkably, the wavelength-dependent $< F_P >$ again exhibits a clear asymmetric profile.

In an attempt to understand the origin of the asymmetric line shape, we performed FDTD simulations of the photonic local density of states (LDOS) and emission rate enhancement F_P for single emitters in 4 different configurations. According to ref. [280], the LDOS in the direction l $\in$ x,y,z is

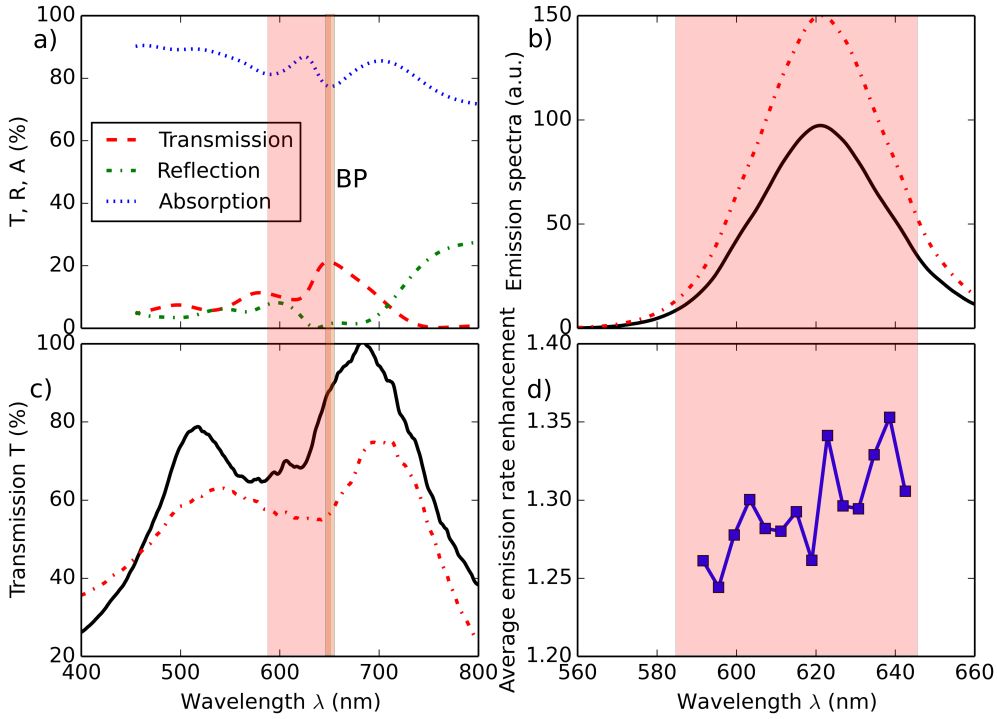

Figure VI.10: FDTD simulated transmission (T), reflection (R) and absorption (A) spectra (a) and experimental transmission spectra (c) of the 2Dhcc structure based on the CSA of 505 *nm diameter beads. In c, the red dashed-dotted curve is the spectrum with emitters randomly spread on top of the structure while the black solid line is the spectrum of the bare structure. Emission spectra (b) of the* 610 *nm maximum emission CdSe@ZnS quantum dots spread onto either a glass substrate (black solid line) or the 2Dhcc structure (red dashed-dotted line) and the corresponding experimentally obtained* $< F_P >$ *(d). The shaded areas represent the spectral emission range of the used QDs.*

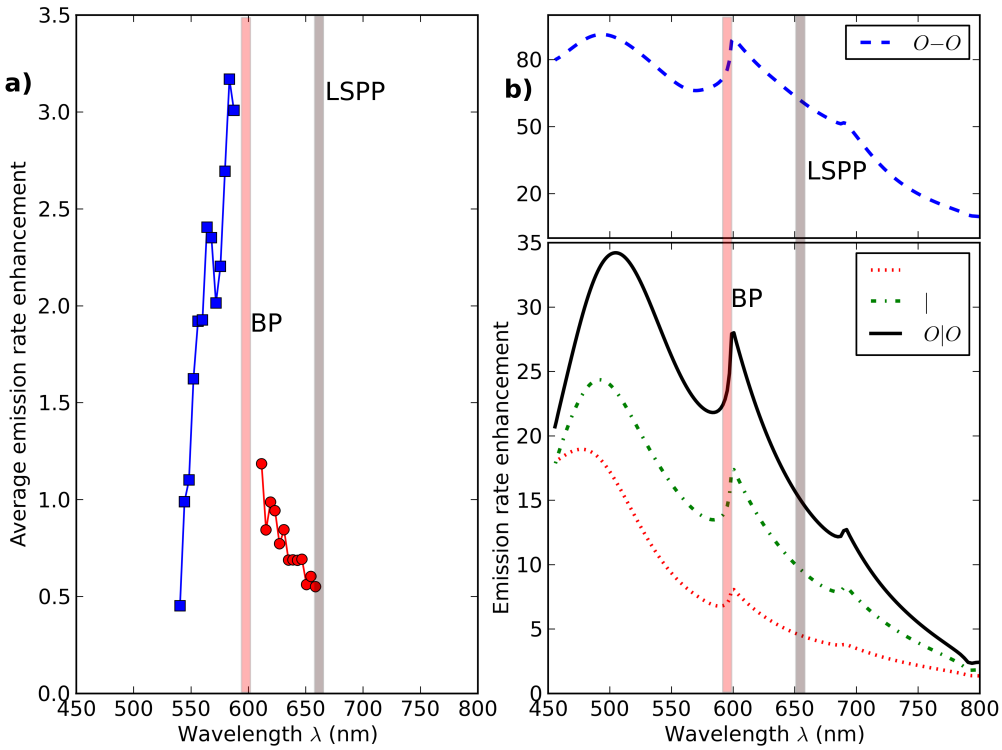

Figure VI.11: Experimentally (a) and numerically (b) determined (average $< F_P >$) emission rate enhancements F of emitters deposited on the 2Dhcc structure. The blue squares and red circles correspond to the measured $< F >$ of the CdSe@ZnS quantum dots with emission at $\lambda_{max} = 570$ and $\lambda_{max} = 640$ nm, respectively, deposited randomly on the structures (a). Red dotted, green dashed-dotted, black solid and blue dashed lines pertain to the simulated F of a single emitter located at 10 nm in front of the air-2Dhcc boundary either in the $-$, $|$, $o-o$, or $o|o$ configuration (b).

$$D_l(\mathbf{x}_0,\omega) = \frac{4}{\pi}\epsilon(\mathbf{x}_0)P_l(\mathbf{x}_0,\omega), \tag{VI.7}$$

where $P_l(\mathbf{x}_0,\omega)$ is the power radiated by an impulsive dipole current source $\mathbf{J} = \mathbf{e}_l\delta(\mathbf{x} - \mathbf{x}_0)p(t)$, located at $\mathbf{x}_0$, $\epsilon(\mathbf{x}_0)$ is the dielectric constant at this point and $\mathbf{e}_l$ is the unit vector in the direction l.

In the FDTD model here employed, accumulating the Fourier transform $\hat{E}_l(\mathbf{x}_0,\omega)$ of the field generated at $\mathbf{x}_0$ by the impulsive broadband dipole current source yielded the complete LDOS spectrum $D_l(\mathbf{x}_0,\omega) = -\frac{2}{\pi}\epsilon(\mathbf{x}_0)\frac{Re[\hat{E}_l(\mathbf{x}_0,\omega)\hat{p}(\omega)^*]}{|\hat{p}(\omega)|^2}$ at $\mathbf{x}_0$ in a single calculation. In each chosen configuration, we computed the LDOS twice, the impulsive dipole current source mimicking the quantum emitter being close to either the 2Dhcc structure or the glass substrate taken as a reference. The emission rate enhancement F_P is finally obtained by dividing the LDOS in the structure with the LDOS in the reference, Eq. VI.8 [282].

$$F_P^l(\mathbf{x}_0,\omega) = \frac{D_l^{2Dhcc}(\mathbf{x}_0,\omega)}{D_l^{glass}(\omega)} \tag{VI.8}$$

The 4 configurations we have chosen are to locate a single quantum emitter at 10 nm far from the structure/substrate either in front of a sphere or just in between two adjacent spheres, where the metallic half-shells meet. In each case, we have considered two different polarizations of the emitters: l ∈ x,z, with x in the plane of the substrate and z normal to it.

Figure VI.11b shows the wavelength-dependent emission rate enhancement for emitters located and polarized in either one of the 4 configurations here above mentioned ($-$, |: x and z polarizations in front of a sphere; $o-o$, $o|o$: x and z polarizations in between two spheres) for the 2Dhcc structure. As expected, the location of the emitter and its polarization matter. The largest F_P have been obtained for the emitter located in between the metallic half-shells, with F of the x-polarized emitter overwhelming by almost one order of magnitude the one of the z-polarized emitter. The x-polarization of the emitter at this location is indeed normal to the half-shell boundaries, a situation well known to lead to an optimized coupling between the dipole and the plasmon resonances. The simulated T, R, A spectra have shown that the BP mode occurs at $\lambda = 595$ nm. The maximum F_P, which is located at precisely the same wavelength, thus marks equally well the BP resonance. For all considered configurations, F_P rises abruptly towards the maximum and decreases more smoothly after passing it, in an asymmetric way, dissimilar to the traditional Lorentzian spectral detuning generally expected between the emitter frequency and the resonance frequency of a single cavity [59].

It is noteworthy to note here that the numerically obtained F_P dispersion profiles (Fig. VI.11b) agree well, qualitatively (in shape and not in absolute values), with the experimentally mea-

sured $< F_P >$ (Figs. VI.11b, VI.9b and VI.10c). Several reasons can be invoked to explain the discrepancy between these exhibited asymmetric profiles and the expected traditional Lorentzian detuning. The Purcell factor generally reported in the literature [59] is based on the assumption that the emitter is at the field maximum (both spectrally and spatially) and that the dipole moment orientation is parallel to the field at this point. Moreover, there is an implicit assumption that the emitter couples to a single mode only. These requirements are not fulfilled in our numerical implementation. Indeed, the emitters are placed at positions that agree with the experimental conditions ($10\,nm$ far from the surface). They neither are located at positions of field maximum nor have a polarization strictly parallel to the field. Furthermore and most importantly, the simulations are not performed in the single mode regime. Other modes (e.g. LSPP) are spectrally close and the Bragg-plasmon mode in itself consists in the hybridization between a plasmonic and a photonic mode. Such a hybridized mode is likely to influence the emission properties of a quantum emitter weakly coupled to it in a way different as would do a traditional single cavity mode.

Experimentally, the situation is complicated by the fact that many emitters are measured simultaneously. Indeed, in the experiments, the emitters are spread onto the samples from a solution. They are thus dispersed everywhere on the sample with their dipole moments randomly oriented. The measurements thus lead to an emission rate enhancement $< F_P >$ averaged over spatial positions and polarizations, where quasi-static corrections add in an asymmetry that is well beyond the Purcell factor regime. The emission rate enhancement determined theoretically F_P and experimentally $< F_P >$ are thus not strictly comparable and an averaging process, depending on all positions, dipole moment orientations and emission frequencies of the N emitters must be considered. This explains the quantitative differences observed in Fig. VI.11b between the amplitudes of the experimental $< F_P >$ and simulated F_P.

VI.6 Conclusion

In conclusion, we have designed several types of hybrid metallo-dielectric structures, by combining commensurate PS colloidal mono-layers and gold over-layers. Specific plasmo-photonic modes appear, which are well-signaled in the UV-visible transmission spectra. The proper assignment of these modes has been performed owing to extensive comparison of the experiments with FDTD simulations. Focusing specifically on the Bragg-plasmon (BP) mode of the various structures, we have measured and simulated the wavelength-dependent emission rate enhancement F_P of emitters spread on top of the structures. We found truly

appealing the fact that both numerical and experimental findings reveal that the spectral dependence of F_P is non Lorentzian. The dominant aspect of this behavior has been attributed to the fact that a hybridized mode, not a pure single mode, is affecting the emission properties of the quantum emitters. The full understanding of emission detuning by hybrid plasmonic/photonic structures exceeds pure academic interest and would provide benefits in many related fields. Notably, a full understanding would require a more detailed study in order to correlate not only spectral overlapping but mainly spatial overlapping, which in turn plays the fundamental role in most light matter interaction mechanisms. We consider single molecule spectroscopy [279] as the most suitable technique to reach this goal. Furthermore, these studies could lead to advancement in sensing and biosensing technologies, with the observation of a F_P asymmetric dispersion profile as a potential sensing trace of a hybridized mode.

Chapter VII

Summary and Outlook

VII.1 Results summary

RECENT theoretical studies [35, 36] suggest that the plasmonic field mainly acts as a communication bus allowing for intense cross-talking between emitters. It leads to the formation of collective states, called superradiant states, which are promising in the field of quantum information. During this doctorate thesis, we investigated the plasmon-mediated superradiance in metallo-dielectric nanohybrids. Typically a collection of fluorescent molecules are distributed around a spherical plasmonic core. The distance between the emitters and the metal core is tuned by controlling the thickness of an intermediate silica shell.

In 2009, the pioneering work of V. Pustovit and T. Shahbazyan [36] identified the mechanism of plasmonic superradiance by considering a fully symmetrical distribution of a collection of emitters around a spherical plasmonic core. As an extension of this theoretical description, we developed an explicit and efficient approach to investigate the superradiance of large collections of molecules near an engineered optical resonance. In particular the computational tool makes no assumption on the emitters position and orientation. Therefore this model allows to derive the ensemble response of a collection of nanohybrids, for which the exact location and orientation of emitters are not known, as it is usually the case in experiments [123, 124]. Besides this model accounts for the presence of a dielectric layer which is usually used to set the emitters at a specific distance to the plasmonic structure [123, 124].

The theoretical investigation first concerned spherical nanohybrids because they were further characterized experimentally. Using the Mie theory, we showed that the optical properties of a spherical metallo-dielectric structure is ruled by the dynamics of Localized Surface Plasmon Polariton (LSPP) modes. The nanohybrid thus represents a rich environment for

the emitters. More precisely the emission of one emitter is enhanced due to the plasmonic core, but at the expense of Ohmic losses in the metal. However for a collection of emitters, both the radiative and non-radiative LSPP modes contribute to the coupling between the emitters. In particular the non-dipolar LSPP modes mainly contribute to non-radiative coupling. Besides these higher order modes promote the interaction between neighbor emitters. Therefore the formation of pure superradiant states, that involve a large proportion of the emitters, is observed when the emitter-emitter interaction is dominated by the dipole LSPP mode. We deduced that the optimal plasmonic core size for the observation of superradiant states is 60 nm.

Then using the theoretical model we predicted that the superradiant decay rate is proportional to the number of emitters and that the associated slope increases if the emitters get closer to the plasmonic core. The largest superradiant decay rates and slopes are expected in the fully symmetrical configuration considered by V. Pustovit and T. Shahbazyan [36, 37]. If the emitters position and orientation are randomly distributed, the trend is still valid, but the values of the superradiance decay rates and slopes are dramatically decreased. Finally averaging over the emitters position and orientation - which are not controlled experimentally - these trends survive.

To go further we treated the superradiance of emitters distributed around a metal nanorod. The geometry of the structure, along with the quasi-normal modes formalism allowed to get a better insight into the plasmonic superradiance phenomenon. First, we have clearly demonstrated that large frequency shifts are mainly due to the direct emitter-emitter interaction; while large decay rates were attributed to the plasmon-mediated interaction. Then from the examination of the induced dipole moments distribution, we deduced that the cooperativity of the superradiant and the subradiant modes is mainly due to the plasmon-mediated interaction. Whereas the direct emitter-emitter interaction results in localized subradiant states with only few emitters optically active. As a consequence, plasmon-mediated superradiance is disrupted when some neighbor emitters are separated by few nanometers. We confirmed that, also for a gold nanorod, the superradiant decay rate is expected to scale with the number of emitters, even after averaging over the emitters position and orientation. Furthermore we introduced the averaged Purcell factor, as an intrinsic property of the cavity. Finally we proposed and verified an analytical expression for the superradiant decay rate in the case of a purely cooperative system, mediated by a single electromagnetic resonance.

The experimental work was devoted to plasmonic superradiance in spherical metallo-dielectric nanohybrids. We reported that the measured decay rate is proportional with the number of emitters. A particular care was taken to identify and limit the influence of the

direct emitter-emitter interaction on the observed fluorescence signal. It yields to a direct and clear evidence of plasmonic superradiance. It is worth noticing that this trend was observed for two systems: different fluorescence molecules and plasmonic core dimensions that were characterized with different approaches: ensemble and single object measurements. Besides, tuning the silica shell thickness allowed us to observe that the slope of the decay rate with respect to the number of emitters increases as the emitters are closer to the plasmonic core. Even though these experimental results are in accordance with the predictions made with the classical model, a quantitative agreement could only be obtained for one emitter. As the experiment was performed at room temperature, we proposed a further interpretation of these results by discussing the effect of temperature-induced dephasing. A simple semi-classical model allowed us to show that a pure dephasing process disrupts the plasmonic superradiance. In particular the slope of the decay rate with the number of emitters is dramatically decreased due to thermal dephasing.

Finally we characterized the wavelength-dependence of the Purcell factor of quantum-dots distributed on a two dimensional plasmonic-photonic crystal. We reported an asymmetrical spectral line shape instead of a Lorentzian line shape, which is expected for the Purcell factor of a single mode with negligible leakage and absorption. These observations were supported by FDTD simulations and were attributed to the coupling of the emitters to a hybridized mode. An asymmetric dispersion profile of the Purcell factor is thus a potential sensing trace of a hybridized mode, which could lead to advancement in sensing and biosensing technologies.

VII.2 Outlook

The results achieved in this doctorate thesis form a first basis for the understanding of plasmonic superradiance in metallo-dielectric nanohybrids. Furthermore we reported a clear and direct evidence that plasmon-mediated superradiance can be performed at room temperature, even with a limited number of molecules. These results open questions about the robustness of plasmon-mediated superradiant states against decoherence mechanisms, paving the way for potential development in quantum optics devices.

As demonstrated both theoretically and experimentally, the plasmonic superradiance phenomenon strongly depends on the emitters position and orientation, as well as the influence of the environment on their transition dipole moment. To investigate how these effects may be tuned to enhance the superradiance features, we propose several outlooks.

VII.2.a Theoretical study of inhomogeneous broadening and spectral diffusion in plasmonic superradiance

In both the classical and the semi-classical theoretical models developed in this manuscript, we considered identical emitters: same resonance frequency and same natural linewidth. However experimentally the molecules were embedded in a polymer matrix at room temperature. Therefore we expect their transition frequencies to be distributed due to inhomogeneous broadening, but also to fluctuate in time due to spectral broadening. Furthermore energy transfers with the environment may offer new non-radiative relaxation channels that modify the molecule linewidth.

Therefore it would be interesting to introduce both a static and a dynamic disorder of the emitters resonance frequencies in the theoretical models. In the case of Dicke superradiance, theoretical [205–207] and experimental [208] studies reported that both effects yield to a disrupted collective emission. As a consequence we expect them to strongly influence the plasmonic superradiance.

VII.2.b Theoretical study of thermal dephasing in plasmonic superradiance

In chapter V we proposed a simple semi-classical model to discuss the effect of thermal dephasing on plasmonic superradiance. In particular we assumed that the transition frequency of each molecule is undergoing rapid and independent fluctuations, as introduced by H. Haken and G. Strobl [209].

This approach showed that approximating the homogeneous dephasing as a stochastic Markovian process overestimates the effects of thermal dephasing. The same observation was reported by F. Spano, J. Kuklinski and S. Mukamel [201] as they tried to explain the results published by S. de Boer and D. Wiersma [200] on the temperature-dependency of superradiant emission in J-aggregates. F. Spano *et al.* managed to interpret S. de Boer *et al.* results by proposing a microscopic approach that introduces the details of the interaction with the phonon modes. In particular they considered how the temporal memory of phonon modes can maintain some coherence between the emitters [202]. Therefore a better understanding of our experimental results may be provided by developing a similar microscopic theory.

VII.2.c Direct correlation between optical and structural properties

Chapters II and III showed that plasmonic superradiance strongly depends on the emitters position and orientation. Furthermore defects in the metal core and the silica shell may also be crucial in the system optical properties. To investigate these effects experimentally it is promising to perform a direct correlation between the optical response of a nanohybrid and its specific structure. The core-shell object can be fully characterized by TEM. However the fluorescent molecules are too small to be observed in TEM. We thus decided to use semiconductor nanocrystals (NC) consisting in a 10 nm diameter cadmium selenide (CdSe) core with a 10 nm thick zinc sulfide (ZnS) shell (Invitrogen). Hence their atomic number ($Z \approx 30$) and dimensions are large enough to observe them in TEM.

In semiconductors, light absorption generally leads to the excitation of an electron in the conduction band, leaving a hole in the valence band. In a NC the electron is bound to the hole by the Coulomb interaction, forming a quasi-particle: the exciton. The recombination of the electron-hole pair can result in the emission of a photon. Unlike fluorescent molecules, nanocrystals are synthesized by nucleation and growth of precursor agents [283]. Thus there is a dispersity in size, shape and crystallinity from one NC to another. Therefore an ensemble of NC shows an intrinsic inhomogeneous distribution of the transition frequency and the lifetime, regardless of their environment. Furthermore the emission of light can be quenched by the presence of charges trapped at the NC surface, that lead to non-radiative recombination. The quantum yield of these emitters is thus dependent on the quality of the passivating ZnS shell. The commercial NC used in this study show a 65 % quantum yield with an emission peak at 585 nm. The main recombination mechanism of excitons is thus radiative in these NC. Their average lifetime in water was deduced from ensemble measurements: $27 \pm 2\ ns$. However after three weeks in water, the average lifetime dropped to $2.9 \pm 0.5\ ns$. This value was confirmed by a statistical study on single NC in a PVA matrix. It reveals that the NC surface state deteriorates in water even though it is soluble in aqueous solution. Nevertheless the NC lifetime is stable after three weeks. We then studied the effect of the binding on an amino-functionalized silica surface by grafting few NC - typically 10 NC as estimated from TEM observation - on a silica sphere. Right after the binding process we observed that the NC lifetime is already $2.9 \pm 0.5\ ns$ in water and that the lifetime is stable in time. Hence after binding to the silica surface, the emitter is the NC in a stable but degraded state, with a low quantum yield: 7 ± 1 %.

In order to correlate directly the optical properties with the structure the substrate must

be compatible with both the optical and electronic observation techniques. We identified a grid of silicon nitride (Si_3N_4) as an optimal solution. On the one hand it is transparent at optical frequency and so it does not induce important fluorescence quenching - while the usual carbon film does [284]. Single object measurements on NC dispersed on the Si_3N_4 grid yields a 2.7 ± 0.4 *ns* average lifetime. On the other hand silicon nitride is a sufficiently good conductor and robust enough for observation in electronic tomography.

To study plasmonic superradiance these nanocrystals were grafted on a core-shell gold-silica nanohybrid. The metal core diameter is 100 ± 5 *nm* to have a matching with the quantum dot exciton line. The silica shell is 21 ± 4 *nm* thick. A collaboration with Ovidiu Ersen and Simona Moldovan at the IPCMS (Strasbourg, France) has enabled us to access a 3 dimensional (3D) structural characterization of these metallo-dielectric nanohybrids. After the acquisition of fluorescence temporal decay of single nanohybrids, the grids were sent to O. Ersen who carried out an electron tomography analysis by using a JEOL 2100F S/TEM microscope in STEM mode. Acquisitions of the tilt images series were performed from +60 to -60 degrees, with projections taken every 2.5°. The 3D volume reconstructions have been computed using the TOMO3D software [285] Visualization and quantitative analysis of the final volumes were carried out by using ImageJ software. We show in figure VII.1a the 3D reconstruction of one nanohybrid decorated with 22 CdSe/ZnS NC.

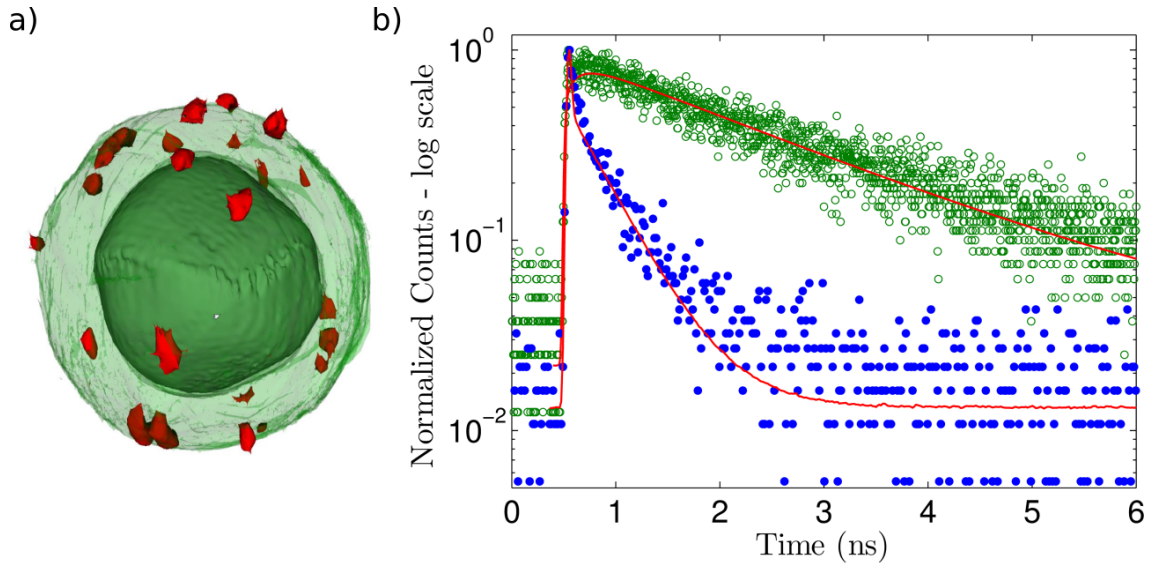

Figure VII.1: a) Three dimensional reconstruction of one nanohybrid decorated with 22 CdSe/ZnS nanocrystals (NC). The green structure consists in a 100 ± 5 *nm diameter gold core coated with a* 21 ± 4 *nm silica shell. The red dots represent the NC. b) Temporal decay profile of the fluorescence signal from the nanohybrid (blue circles) represented in a) and from a single NC (green circles), deposited on a silicon nitride grid. Solid red lines represent the fits to the experimental data.*

Clearly the 3D electron tomography allows to unambiguously estimate the number of NC

and their position. We also have access to the exact shape, dimensions and defects of the gold core and the silica shell. From the electronic microscopy images we estimate that the gold core diameter is $100 \pm 5\ nm$ and the silica shell thickness is $21 \pm 4\ nm$. Prior to the structure characterization, the fluorescence temporal decay profile of this nanohybrid was acquired.

Figure VII.1b compares the experimental fluorescence decay profile of this nanohybrid, with the fluorescence decay profile of a single NC on the grid. Using a monoexponential model, we estimate that the nanohybrid decay time is $0.4 \pm 0.1\ ns$. The decay rate enhancement is thus about 7 ± 2. In order to interpret this result, the theoretical model would need to account for the pure dephasing processes as well as for the presence of the silicon nitride film.

Appendix A

Binding yield of Atto-based nanohybrids

We show the experimentally measured binding yield of the Atto-based nanohybrids with different silica shell thicknesses. We deduce the number of Atto532 molecules per nanohybrid and the average distance between neighbor emitters. The gold core is a $57 \pm 3\ nm$ diameter nanosphere.

Silica shell thickness (nm)	Binding yield η_{bind} (%)	Number of Atto532 per NP	Average distance between emitters (nm)
10 ± 3	91	274	8
10 ± 3	92	184	10
10 ± 3	92	46	20
10 ± 3	94	24	28
13 ± 2	99	297	9
13 ± 2	99	198	10
13 ± 2	98	98	15
13 ± 2	99	49	21
13 ± 2	98	25	29
13 ± 2	99	10	46
18 ± 2	92	276	10
18 ± 2	97	194	12
18 ± 2	97	97	17
18 ± 2	90	45	25
18 ± 2	88	22	35
24 ± 3	92	276	11
24 ± 3	96	192	14
24 ± 3	92	92	19
24 ± 3	96	48	27
24 ± 3	95	24	39
24 ± 3	95	9	62
37 ± 3	94	282	14
37 ± 3	93	186	17
37 ± 3	92	92	24
37 ± 3	92	23	49
57 ± 6	73	218	21
57 ± 6	67	134	26
57 ± 6	76	76	35
57 ± 6	77	39	49

Appendix B

Estimation of the excitation regime

In chapter V we experimentally study the plasmonic superradiance in metallo-dielectric spherical nanohybrids. For Atto-based nanohybrids, the experiment consists in the acquisition of a fluorescence temporal decay profile of a single nanohybrid in confocal configuration. A short laser pulse was focused on a nanohybrid by using an oil immersion objective (1.45 numerical aperture). Here we estimate the probability that one of the molecules located near the nanohybrid is excited by the excitation pulse.

The average excitation power introduced into the overfilled objective was $P_{avg} = 150\ nW$ at $\lambda_{exc} = 532\ nm$. The oil immersion objective focused the excitation beam on a $\Phi = 250\ nm$ diameter pattern, yielding to a $I_{avg} = 210 W/cm^2$ incident average power density in the sample plane. For a $\Delta t = 140$ fs pulse duration with a repetition rate of $\nu_{rate} = 80$ MHz, the peak power density is then

$$I_{peak} = \frac{I_{avg}}{\nu_{rate}\Delta t} = 19 MW.cm^{-2} \tag{B.1}$$

We deduce the incident electric field

$$E_{peak} = \sqrt{\frac{2I_{peak}}{c\epsilon_0 n_{PVA}}} = 9.8 MV.m^{-1} \tag{B.2}$$

where n_{PVA} is the hosting medium (PVA) refractive index. This electric field at the molecules position will be enhanced by the presence of the plasmonic nanohybrid. To estimate this field enhancement, we consider the smallest experimentally studied silica shell: $d = 11\ nm$. For larger silica shell thicknesses the molecules are more distant from the metal core and the field enhancement is thus smaller. The nanohybrid is illuminated by a linearly polarized plane wave at $\lambda = 532\ nm$, as represented in figure B.1a where we define spherical coordinates (θ, ϕ). Figure B.1b then represents the calculated distribution of the electric field enhancement $F_{E\|}$ at the silica surface, which is where the molecules are located. The electric field was projected on the tangential plane since Atto532 molecules are preferentially oriented parallel to the particle surface.

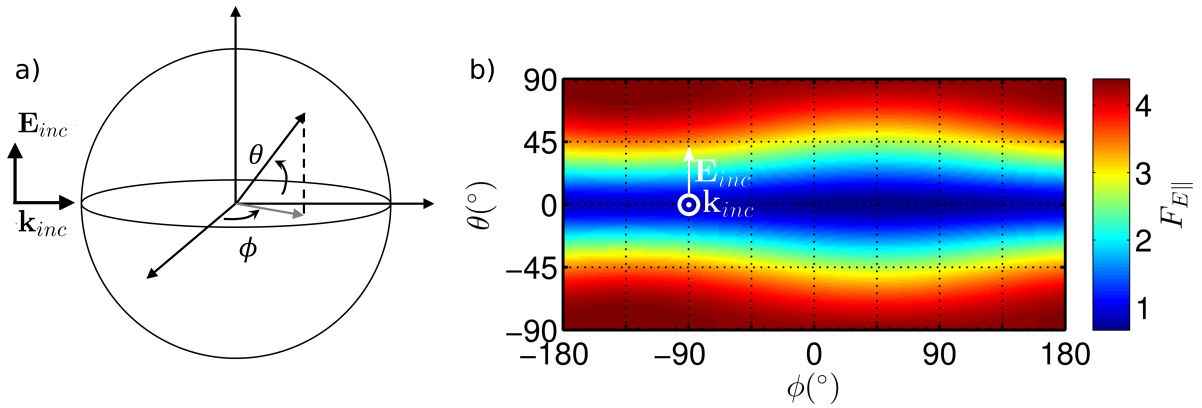

Figure B.1: A 57 nm diameter gold sphere coated with a 10 nm silica shell is illuminated by a linearly polarized plane wave $\mathbf{E}_{inc}$ at $\lambda = 532$ nm. We consider spherical coordinates (θ, ϕ) as represented in a). The incident wave propagates from the direction $\theta = 0°$,$\phi = -90°$, as represented by the white arrows in b). We show the calculated distribution of the electric field enhancement $F_{E\|}$ at the silica surface. The electric field was projected on the tangential plane since the molecules are preferentially oriented parallel to the particle surface.

The incident plane wave propagates from the direction $\theta = 0°$,$\phi = -90°$. Since the excitation wavelength matches the dipolar LSPP mode, we observe in Fig. B.1 two lobes in the field distribution at $\theta = -90°$ and $\theta = 90°$. The maximum electric field enhancement in the tangential plane at $d = 11$ nm from the core surface is then 4.3 and the average enhancement is about 2.7. These values are in accordance with the literature [95, 286].

Therefore the average intensity experienced by a molecule near the plasmonic nanohybrid is

$$I_{avg}^{Au@SiO_2@Atto} = \frac{1}{2} c\epsilon_0 n_{PVA} F_{E\|}^2 E_{peak}^2 = 140 MW.cm^{-2}. \tag{B.3}$$

Atto532 molar extinction coefficient at $\lambda_{exc} = 532$ nm is $\epsilon_{Atto} = 1.15 \cdot 10^5 M^{-1} cm^{-1}$ so the absorption cross section is [287]

$$\sigma_{abs}^{Atto} = \frac{2303 \epsilon_{Atto}}{N_A} = 4.39 \cdot 10^{-16} cm^2 = 0.044 nm^2 \tag{B.4}$$

We deduce the average probability to excite one Atto532 molecule per excitation pulse

$$N_{exc}^{Au@SiO_2@Atto} = \sigma_{abs}^{Atto} \frac{\lambda}{hc} I_{avg}^{Au@SiO_2@Atto} \Delta t = 2.3\% \tag{B.5}$$

At $d = 11$ nm from the plasmonic core, the weak excitation approximation is thus valid for less than 45 emitters per nanohybrid. In the case discussed in section V.2.d in chapter V, $d = 18$ nm and then the weak excitation approximation is valid for less than 100 emitters per nanohybrid. For a decorated silica sphere in absence of plasmonic core, the average

probability to excite one Atto532 molecule per pulse is

$$N_{exc}^{SiO_2@Atto} = 0.1\% \tag{B.6}$$

Appendix C

Derivation of the average decay rate

In this appendix we provide details on the derivation of the average decay rate Γ, in particular we demonstrate Eq.V.6 given in chapter V. We consider N Two-Level Systems (TLS) with identical transition frequency ω_0 and natural population decay rate γ_p. We denote by $|e_l\rangle$ and $|g_l\rangle$ the excited and ground state of the TLS l, respectively. The TLS are distributed around a spherical plasmonic nanohybrid.

The system relaxation is directly related to the probability that one TLS is excited at time t, given by

$$\chi_e(t) = \sum_{l=1}^{N} \left\langle \hat{\sigma}_l^+ \hat{\sigma}_l^- \right\rangle \tag{C.1}$$

where $\hat{\sigma}_l^+$ and $\hat{\sigma}_l^-$ are the raising and lowering operators for the TLS l.

From $\chi_e(t)$, we will deduce the average decay rate by [199]

$$\Gamma = \left[\int_0^\infty dt \chi_e(t) \right]^{-1} \tag{C.2}$$

In the Heisenberg picture, the time evolution of an operator $\hat{\mathcal{O}}$ is then given by the master equation

$$\partial_t \hat{\mathcal{O}} = \frac{i}{\hbar}[\hat{H}, \hat{\mathcal{O}}] + \mathrm{Tr}(\hat{\mathcal{O}}\mathcal{L}) \tag{C.3}$$

The Hamiltonian of the molecular system can be written as [45]

$$\hat{H} = \hbar\omega_0 \sum_{l=1}^{N} (\hat{\sigma}_l^+ \hat{\sigma}_l^-) + \sum_{l=1, j\neq l}^{N,N} \hbar g_{lj} (\hat{\sigma}_l^+ \hat{\sigma}_j^- + \hat{\sigma}_j^+ \hat{\sigma}_l^-) \tag{C.4}$$

where g_{lj} describes the coherent coupling between the TLS l and j, in the presence of the nanohybrid.

The dissipative part of the master equation from Eq. C.3 consists in the following Liouville

operator

$$\begin{aligned}\mathcal{L}\hat{\rho} = &-\sum_{l=1}^{N}\frac{F_P\gamma_p}{2}(\hat{\sigma}_l^+\hat{\sigma}_l^-\hat{\rho}+\hat{\rho}\hat{\sigma}_l^+\hat{\sigma}_l^- - 2\hat{\sigma}_l^-\hat{\rho}\hat{\sigma}_l^+)\\ &-\sum_{l=1}^{N}\gamma^*(\hat{\sigma}_l^+\hat{\sigma}_l^-\hat{\rho}+\hat{\rho}\hat{\sigma}_l^+\hat{\sigma}_l^- - 2\hat{\sigma}_l^+\hat{\sigma}_l^-\hat{\rho}\hat{\sigma}_l^+\hat{\sigma}_l^-)\\ &-\sum_{l=1,j\neq i}^{N}\frac{\gamma_{lj}}{2}(\hat{\sigma}_j^+\hat{\sigma}_l^-\hat{\rho}+\hat{\rho}\hat{\sigma}_j^+\hat{\sigma}_l^- - 2\hat{\sigma}_l^-\hat{\rho}\hat{\sigma}_j^+ + \hat{\sigma}_l^+\hat{\sigma}_j^-\hat{\rho}+\hat{\rho}\hat{\sigma}_l^+\hat{\sigma}_j^- - 2\hat{\sigma}_j^-\hat{\rho}\hat{\sigma}_l^+)\end{aligned} \tag{C.5}$$

where F_P is the Purcell factor of the nanohybrid. The first term of Eq. C.5 accounts for the coupling to the vacuum field bath of each TLS, modified by the Purcell effect. The second term describes the coupling to the phonon bath by assuming that the electronic transition frequency of each TLS is undergoing rapid fluctuations at a dephasing rate γ^*, according to a Markovian process [209]. It induces a relaxation of the interTLS coherences at the dephasing rate γ^* , without associated population decay [72, 288]. The third term of Eq. C.5 accounts for the incoherent interaction between the TLS γ_{lj}.

To account for the plasmon-mediated interaction, we use the classical estimation of the local electromagnetic field. The coherent g_{lj} and the incoherent γ_{lj} coupling terms, which are induced by the environment, are thus deduced from the classical Green function [31]

$$g_{lj} = \frac{\omega_0^2}{\hbar\epsilon_0 c^2}\boldsymbol{\mu}_l^*\cdot\mathrm{Re}\Big\{\overleftrightarrow{\mathbf{G}}(\mathbf{r}_l,\mathbf{r}_j,\omega)\Big\}\cdot\boldsymbol{\mu}_j \tag{C.6}$$

$$\gamma_{lj} = 2\frac{\omega_0^2}{\hbar\epsilon_0 c^2}\boldsymbol{\mu}_l^*\cdot\mathrm{Im}\Big\{\overleftrightarrow{\mathbf{G}}(\mathbf{r}_l,\mathbf{r}_j,\omega_0)\Big\}\cdot\boldsymbol{\mu}_j \tag{C.7}$$

The master equation from Eq. C.3 then yields to the following closed system of equations [289]

$$\partial_t\left\langle\hat{\sigma}_l^+\hat{\sigma}_l^-\right\rangle = -F_P\gamma_p\left\langle\hat{\sigma}_l^+\hat{\sigma}_l^-\right\rangle - \sum_{j\neq l}^{N}\frac{\gamma_{lj}}{2}\Big(\left\langle\hat{\sigma}_j^+\hat{\sigma}_l^-\right\rangle + \left\langle\hat{\sigma}_l^+\hat{\sigma}_j^-\right\rangle\Big) - i\sum_{j\neq l}^{N}g_{lj}\Big(\left\langle\hat{\sigma}_l^+\hat{\sigma}_j^-\right\rangle - \left\langle\hat{\sigma}_j^+\hat{\sigma}_l^-\right\rangle\Big) \tag{C.8}$$

$$\begin{aligned}\partial_t\left\langle\hat{\sigma}_j^+\hat{\sigma}_l^-\right\rangle = &-(F_P\gamma_p+2\gamma^*)\left\langle\hat{\sigma}_j^+\hat{\sigma}_l^-\right\rangle - \frac{\gamma_{lj}}{2}\Big(\left\langle\hat{\sigma}_l^+\hat{\sigma}_l^-\right\rangle + \left\langle\hat{\sigma}_j^+\hat{\sigma}_j^-\right\rangle - 4\left\langle\hat{\sigma}_l^+\hat{\sigma}_l^-\hat{\sigma}_j^+\hat{\sigma}_j^- >\right\rangle\Big)\\ &+\sum_{m\neq l,m\neq j}^{N}\Big(\gamma_{lm}\left\langle\hat{\sigma}_j^+\hat{\sigma}_m^-\hat{\sigma}_l^z\right\rangle + \gamma_{jm}\left\langle\hat{\sigma}_l^-\hat{\sigma}_m^+\hat{\sigma}_j^z\right\rangle\Big)\\ &-ig_{lj}\Big(\left\langle\hat{\sigma}_j^+\hat{\sigma}_j^-\right\rangle - \left\langle\hat{\sigma}_l^+\hat{\sigma}_l^-\right\rangle\Big) - \sum_{m\neq l,m\neq j}^{N}2i\Big(g_{jm}\left\langle\hat{\sigma}_m^+\hat{\sigma}_l^-\hat{\sigma}_j^z\right\rangle - g_{lm}\left\langle\hat{\sigma}_j^+\hat{\sigma}_m^-\hat{\sigma}_l^z\right\rangle\Big)\end{aligned} \tag{C.9}$$

where $\hat{\sigma}_l^z = [\hat{\sigma}_l^+, \hat{\sigma}_l^-]/2$ is the energy operator.

We then assume that the system was observed under the weak excitation regime, as discussed in appendix B. It yields that only one TLS is excited at time $t = 0$ following the excitation pulse. We express this condition as $\langle \sigma^z \rangle = -1/2$ for all the TLS [290] except for the excited TLS which has $\langle \sigma^z \rangle = +1/2$. The molecular system can then be described in the Hilbert subspace represented by the left part of figure C.1. It consists in N excited states where only one TLS is excited $|g_1, ..., g_{l-1}, e_l, g_{l+1}.., g_N\rangle$ and 1 ground state $|g\rangle = |g_1, ..., g_N\rangle$ where all the TLS are in their ground state.

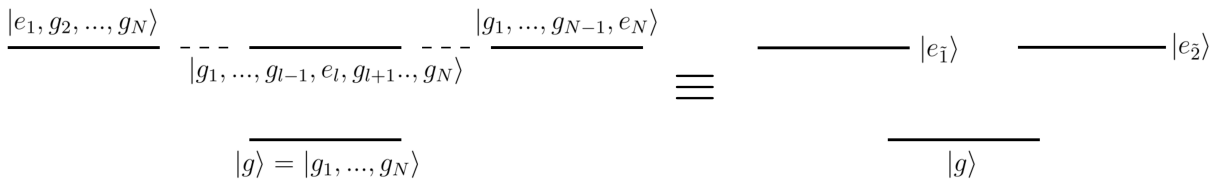

Figure C.1: Left part: schematic representation of the N+1 states which describe the molecular system in the weak excitation approximation. Right part: schematic representation of the 3 states introduced for a weakly excited symmetrical molecular system: identical TLS and identical coupling between all the TLS. The state $|e_{\tilde{1}}\rangle$ represents the TLS which is initially excited and the state $|e_{\tilde{2}}\rangle$ represents the N-1 indistinguishable other TLS.

For simplicity we consider a perfectly symmetrical system where all the TLS are identically coupled. In such a configuration, the molecular system can be described in a smaller subspace. Let us denote by $|e_{\tilde{1}}\rangle$ the state where one TLS is excited, namely the TLS which is excited by the excitation pulse at time $t = 0$. Because of the symmetry, this TLS interacts identically with the $N-1$ non-excited TLS. These non-excited TLS are thus indistinguishable such that the corresponding $N-1$ excited states $|g_1, ..., g_{l-1}, e_l, g_{l+1}.., g_N\rangle$ with $l \neq \tilde{1}$ can be gathered in one degenerated state denoted by $|e_{\tilde{2}}\rangle$. Therefore the system is equivalent to two interacting TLS, as represented by the right part of figure C.1: the TLS $\tilde{1}$ which is initially excited and the TLS $\tilde{2}$ which is not initially excited. Accordingly we define $|e_{\tilde{1}}\rangle$ and $|g_{\tilde{1}}\rangle$ as the excited and the ground state of the TLS $\tilde{1}$, respectively. And similarly, $|e_{\tilde{2}}\rangle$ and $|g_{\tilde{2}}\rangle$ are the excited and the ground state of the TLS $\tilde{2}$, respectively. We then define the operators

$$\begin{aligned} \hat{\sigma}_{\tilde{1}}^+ &= |e_{\tilde{1}}\rangle \langle g_{\tilde{1}}| & \hat{\sigma}_{\tilde{2}}^+ &= |e_{\tilde{2}}\rangle \langle g_{\tilde{2}}| \\ \hat{\sigma}_{\tilde{1}}^- &= |g_{\tilde{1}}\rangle \langle e_{\tilde{1}}| & \hat{\sigma}_{\tilde{2}}^- &= |g_{\tilde{2}}\rangle \langle e_{\tilde{2}}| \end{aligned} \tag{C.10}$$

The corresponding coherent and incoherent coupling constants are $g_{\tilde{1}\tilde{2}}$ and $\gamma_{\tilde{1}\tilde{2}}$, respectively. These hypotheses allow us to considerably simplify the system from Eqs. (C.8,C.9), which

becomes

$$\partial_t \left\langle \hat{\sigma}_{\tilde{1}}^+ \hat{\sigma}_{\tilde{1}}^- > \right\rangle = - F_P \gamma_p \left\langle \hat{\sigma}_{\tilde{1}}^+ \hat{\sigma}_{\tilde{1}}^- \right\rangle - (N-1)\gamma_{\tilde{1}\tilde{2}} \,\mathrm{Re}\Big\{ \left\langle \hat{\sigma}_{\tilde{1}}^+ \hat{\sigma}_{\tilde{2}}^- \right\rangle \Big\} + 2(N-1) g_{\tilde{1}\tilde{2}} \,\mathrm{Im}\Big\{ \left\langle \hat{\sigma}_{\tilde{1}}^+ \hat{\sigma}_{\tilde{2}}^- \right\rangle \Big\} \tag{C.11}$$

$$\begin{aligned} \partial_t \left\langle \hat{\sigma}_{\tilde{1}}^+ \hat{\sigma}_{\tilde{2}}^- \right\rangle = &- \left(F_P \gamma_p + 2\gamma^*\right) \left\langle \hat{\sigma}_{\tilde{1}}^+ \hat{\sigma}_{\tilde{2}}^- \right\rangle - \gamma_{\tilde{1}\tilde{2}} \left\langle \hat{\sigma}_{\tilde{1}}^+ \hat{\sigma}_{\tilde{1}}^- \right\rangle \\ &- (N-2)\gamma_{\tilde{1}\tilde{2}} \,\mathrm{Re}\Big\{ \left\langle \hat{\sigma}_{\tilde{1}}^+ \hat{\sigma}_{\tilde{2}}^- \right\rangle \Big\} + 2(N-2) g_{\tilde{1}\tilde{2}} \,\mathrm{Im}\Big\{ \left\langle \hat{\sigma}_{\tilde{1}}^+ \hat{\sigma}_{\tilde{2}}^- \right\rangle \Big\} \end{aligned} \tag{C.12}$$

It can then be reduced in the matricial form

$$\begin{bmatrix} \partial_t \left\langle \hat{\sigma}_{\tilde{1}}^+ \hat{\sigma}_{\tilde{1}}^- \right\rangle \\ \partial_t \,\mathrm{Re}\{ \left\langle \hat{\sigma}_{\tilde{1}}^+ \hat{\sigma}_{\tilde{2}}^- \right\rangle \} \\ \partial_t \,\mathrm{Im}\{ \left\langle \hat{\sigma}_{\tilde{1}}^+ \hat{\sigma}_{\tilde{2}}^- \right\rangle \} \end{bmatrix} = \begin{pmatrix} -F_P\gamma_p & -(N-1)\gamma_{\tilde{1}\tilde{2}} & 2(N-1)g_{\tilde{1}\tilde{2}} \\ -\gamma_{\tilde{1}\tilde{2}} & -F_P\gamma_p - 2\gamma^* - (N-2)\gamma_{\tilde{1}\tilde{2}} & 2(N-2)g_{\tilde{1}\tilde{2}} \\ 0 & 0 & -F_P\gamma_p - 2\gamma^*) \end{pmatrix} \begin{bmatrix} \left\langle \hat{\sigma}_{\tilde{1}}^+ \hat{\sigma}_{\tilde{1}}^- \right\rangle \\ \mathrm{Re}\{ \left\langle \hat{\sigma}_{\tilde{1}}^+ \hat{\sigma}_{\tilde{2}}^- > \right\rangle \} \\ \mathrm{Im}\{ \left\langle \hat{\sigma}_{\tilde{1}}^+ \hat{\sigma}_{\tilde{2}}^- > \right\rangle \} \end{bmatrix} \tag{C.13}$$

The 3 eigenvalues of this system from Eq. C.13 are

$$\begin{pmatrix} -F_P\gamma_p - \gamma^* - \frac{1}{2}(N-2)\gamma_{\tilde{1}\tilde{2}} \pm \sqrt{\gamma^{*2} + \frac{N^2}{4}\gamma_{\tilde{1}\tilde{2}}^2 + (N-2)\gamma_{\tilde{1}\tilde{2}}\gamma^*} \\ F_P\gamma_p - 2\gamma^* \end{pmatrix} \tag{C.14}$$

Following a short pulsed excitation, the initial state at time $t = 0$ is [199]

$$\begin{pmatrix} \left\langle \hat{\sigma}_{\tilde{1}}^+ \hat{\sigma}_{\tilde{1}}^- \right\rangle_{t=0} \\ \left\langle \hat{\sigma}_{\tilde{1}}^+ \hat{\sigma}_{\tilde{2}}^- \right\rangle_{t=0} \end{pmatrix} = \begin{pmatrix} 1 \\ 1 \end{pmatrix} \tag{C.15}$$

Solving the system from Eq. C.13 with the initial conditions from Eq. C.15, we derive the probability that one TLS is excited at time t

$$\begin{aligned} \chi_e(t) = \left\langle \hat{\sigma}_{\tilde{1}}^+ \hat{\sigma}_{\tilde{1}}^- \right\rangle = &\frac{1}{2}\Big[1 + \frac{\gamma^* - \frac{N}{2}\gamma_{\tilde{1}\tilde{2}}}{\kappa}\Big] exp\Big[(-F_P\gamma_p - \gamma^* - \frac{1}{2}(N-2)\gamma_{\tilde{1}\tilde{2}} + \kappa)t\Big] \\ &+ \frac{1}{2}\Big[1 - \frac{\gamma^* - \frac{N}{2}\gamma_{\tilde{1}\tilde{2}}}{\kappa}\Big] exp\Big[(-F_P\gamma_p - \gamma^* - \frac{1}{2}(N-2)\gamma_{\tilde{1}\tilde{2}} - \kappa)t\Big] \end{aligned} \tag{C.16}$$

where $\kappa = \sqrt{\gamma^{*2} + \frac{N^2}{4}\gamma_{\tilde{1}\tilde{2}}^2 + (N-2)\gamma_{\tilde{1}\tilde{2}}\gamma^*}$.

We deduce the average decay rate of a collection of N identical TLS that are identically coupled in the weak excitation regime

$$\Gamma = \Big[\int_0^\infty dt \chi_e(t)\Big]^{-1} = F_P\gamma_p + (N-1)\gamma_{\tilde{1}\tilde{2}}\Big(\frac{F_P\gamma_p - \gamma_{\tilde{1}\tilde{2}}}{F_P\gamma_p - \gamma_{\tilde{1}\tilde{2}} + 2\gamma^*}\Big) \tag{C.17}$$

Applying Eqs. C.16 and C.17 to the case of $N = 2$ TLS, we find the result published by J. Grad *et al.* in Ref. [199].

Bibliography

[1] J. A. J. Gowlett, The discovery of fire by humans: a long and convoluted process. *Phil.Trans. R. Soc. B* **371**, 20150164 (2016).

[2] T. H. Maiman, Stimulated optical radiation in ruby. *Nature* **187**, 493 (1960).

[3] H. H. Hopkins and N. S. Kapany, A flexible fibrescope, using static scanning. *Nature* **173**, 39 (1954).

[4] R. H. Dicke, Coherence in spontaneous radiation processes. *Phys. Rev.* **93**, 99 (1954).

[5] N. Skribanowitz, I. P. Herman, J. C. MacGillivray, and M. S. Feld, Observation of Dicke superradiance in optically pumped HF gas. *Phys. Rev. Lett.* **30**, 309 (1973).

[6] M. Gross, C. Fabre, P. Pillet, and S. Haroche, Observation of near-infrared Dicke superradiance on cascading transitions in atomic sodium. *Phys. Rev. Lett.* **36**, 1035 (1976).

[7] M. Gross and S. Haroche, Superradiance: An essay on the theory of collective spontaneous emission. *Phys. Rep.* **93**, 301 (1982).

[8] C. Hettich, C. Schmitt, J. Zitzmann, S. Kühn, I. Gerhardt, and V. Sandoghdar, Nanometer resolution and coherent optical dipole coupling of two individual molecules. *Science* **298**, 385 (2002).

[9] J. Hernando, J. P. Hoogenboom, E. M. H. P. van Dijk, J. J. García-López, M. Crego-Calama, D. N. Reinhoudt, N. F. van Hulst, and M. F. García-Parajó, Single molecule photobleaching probes the exciton wave function in a multichromophoric system. *Phys. Rev. Lett.* **93**, 236404 (2004).

[10] S. Inouye, A. P. Chikkatur, D. M. Stamper-Kurn, J. Stenger, D. E. Pritchard, and W. Ketterle, Superradiant Rayleigh scattering from a Bose-Einstein condensate. *Science* **285**, 571 (1999).

[11] A. V. Andreev, V. I. Emel'yanov, and Y. A. Il'inskii, Collective spontaneous emission (Dicke superradiance). *Usp. Fiz. Nauk* **131**, 653 (1980).

[12] M. O. Scully and A. A. Svidzinsky, The super of superradiance. *Science* **325**, 1510 (2009).

[13] R. H. Ritchie, Plasma losses by fast electrons in thin films. *Phys. Rev.* **106**, 874 (1957).

[14] W. L. Barnes, A. Dereux, and T. W. Ebbesen, Surface plasmon subwavelength optics. *Nature* **424**, 824 (2003).

[15] D. K. Gramotnev and S. I. Bozhevolnyi, Plasmonics beyond the diffraction limit. *Nature Photonics* **4**, 83 (2010).

[16] S. Nie and S. R. Emory, Probing single molecules and single nanoparticles by surface-enhanced Raman scattering. *Science* **275**, 1102 (1997).

[17] M. Bompart, Y. De Wilde, and K. Haupt, Chemical nanosensors based on composite molecularly imprinted polymer particles and surface-enhanced raman scattering. *Adv. Mater.* **22**, 2343 (2010).

[18] E. Betzig, J. K. Trautman, T. D. Harris, J. S. Weiner, and R. L. Kostelak, Breaking the diffraction barrier: Optical microscopy on a nanometric scale. *Science* **251**, 1468 (1991).

[19] J.-J. Greffet and R. Carminati, Image formation in near-field optics. *Progress in Surface Science* **56**, 133 (1997).

[20] F. Formanek, Y. De Wilde, and L. Aigouy, Analysis of the measured signals in apertureless near-field optical microscopy. *Ultramicroscopy* **103**, 133 (2005).

[21] R. Kolesov, B. Grotz, G. Balasubramanian, R. Stöhr, A. Nicolet, P. Hemmer, F. Jelezko, and J. Wrachtrup, Wave-particle duality of single surface plasmon polaritons. *Nature Physics* **5**, 470 (2009).

[22] A. V. Akimov, A. Mukherjee, C. L. Yu, D. E. Chang, A. S. Zibrov, P. R. Hemmer, H. Park, and M. D. Lukin, Generation of single optical plasmons in metallic nanowires coupled to quantum dots. *Nature* **450**, 402 (2007).

[23] R. W. Heeres, L. P. Kouwenhoven, and V. Zwiller, Quantum interference in plasmonic circuits. *Nature Nanotechnology* **8**, 719 (2013).

[24] M.-C. Dheur, E. Devaux, T. W. Ebbesen, A. Baron, J.-C. Rodier, J.-P. Hugonin, P. Lalanne, J.-J. Greffet, G. Messin, and F. Marquier, Single-plasmon interferences. *Science Advances* **2**, e1501574 (2016).

[25] D. Bouchet, E. Lhuillier, S. Ithurria, A. Gulinatti, I. Rech, R. Carminati, Y. De Wilde, and V. Krachmalnicoff, Correlated spontaneous emission of fluorescent emitters mediated by single plasmons. *arXiv:1609.09687v1* (2016).

[26] D. J. Bergman and M. I. Stockman, Surface plasmon amplification by stimulated emission of radiation: Quantum generation of coherent surface plasmons in nanosystems. *Phys. Rev. Lett.* **90**, 027402 (2003).

[27] M. A. Noginov, G. Zhu, A. M. Belgrave, R. Bakker, V. M. Shalaev, E. Narimanov, S. Stout, E. Herz, T. Suteewong, and U. Wiesner, Demonstration of a spaser-based nanolaser. *Nature* **460**, 1110 (2009).

[28] E. Altewischer, M. P. van Exter, and J. P. Woerdman, Plasmon-assisted transmission of entangled photons. *Nature* **418**, 304 (2002).

[29] E. Moreno, F. J. García-Vidal, D. Erni, J. I. Cirac, and L. Martín-Moreno, Theory of plasmon-assisted transmission of entangled photons. *Phys. Rev. Lett.* **92**, 236801 (2004).

[30] L. Olislager, W. Kubo, T. Tanaka, S. Ungureanu, R. A. L. Vallée, B. Kolaric, P. Emplit, and S. Massar, Propagation and survival of frequency-bin entangled photons in metallic nanostructures. *Nanophotonics* **4**, 324 (2015).

[31] D. Martín-Cano, A. González-Tudela, L. Martín-Moreno, F. J. García-Vidal, C. Tejedor, and E. Moreno, Dissipation-driven generation of two-qubit entanglement mediated by plasmonic waveguides. *Phys. Rev. B* **84**, 235306 (2011).

[32] A. González-Tudela, D. Martín-Cano, E. Moreno, L. Martín-Moreno, C. Tejedor, and F. J. García-Vidal, Entanglement of two qubits mediated by one-dimensional plasmonic waveguides. *Phys. Rev. Lett.* **106**, 020501 (2011).

[33] F. Verstraete, M. M. Wolf, and J. I. Cirac, Quantum computation and quantum-state engineering driven by dissipation. *Nature Physics* **5**, 633 (2009).

[34] D. E. Chang, A. S. Sørensen, E. A. Demler, and M. Lukin, A single-photon transistor using nanoscale surface plasmons. *Nature Physics* **3**, 807 (2007).

[35] D. Martín-Cano, L. Martín-Moreno, F. J. García-Vidal, and E. Moreno, Resonance energy transfer and superradiance mediated by plasmonic nanowaveguides. *Nano Lett.* **10**, 3129 (2010).

[36] V. N. Pustovit and T. V. Shahbazyan, Cooperative emission of light by an ensemble of dipoles near a metal nanoparticle: The plasmonic Dicke effect. *Phys. Rev. Lett.* **102**, 077401 (2009).

[37] V. N. Pustovit and T. V. Shahbazyan, Plasmon-mediated superradiance near metal nanostructures. *Phys. Rev. B* **82**, 075429 (2010).

[38] H. Ditlbacher, A. Hohenau, D. Wagner, U. Kreibig, M. Rogers, F. Hofer, F. R. Aussenegg, and J. R. Krenn, Silver nanowires as surface plasmon resonators. *Phys. Rev. Lett.* **95**, 257403 (2005).

[39] B. Valeur and M. N. Berberan-Santos, *Molecular Fluorescence*, John Wiley & Sons, 2012.

[40] Dirac P. A. M., *The Principles of Quantum Mechanics*, Oxford University Press, 1982, 4th edition.

[41] G. Grynberg, A. Aspect, and C. Fabre, *Introduction to Quantum Optics*, Cambridge University Press, 2010, 1st edition.

[42] J. D. Jackson, *Classical Electrodynamics*, John Wiley & Sons, 1962.

[43] L.Novotny and B. Hecht, *Principle of Nano-Optics*, Cambridge University Press, 2012.

[44] T. Basché, S. Kummer, and C. Bräuchle, Excitation and Emission Spectroscopy and Quantum Optical Measurements, in *Single-Molecule Optical Detection, Imaging and Spectroscopy*, edited by T. Basché, W. E. Moerner, M. Orrit, and U. P. Wild, Wiley-VCH, 1996, 1st edition.

[45] G. V. Varada and G. S. Agarwal, Two-photon resonance induced by the dipole-dipole interaction. *Phys. Rev. A* **45**, 6721 (1992).

[46] L. Mandel and E. Wolf, *Optical Coherence and Quantum Optics*, Cambridge University Press, 1995.

[47] U. Akram, Z. Ficek, and S. Swain, Decoherence and coherent population transfer between two coupled systems. *Phys. Rev. A* **62**, 013413 (2000).

[48] N. E. Rehler and J. H. Eberly, Superradiance. *Phys. Rev. A* **3**, 1735 (1971).

[49] G. S. Agarwal, Quantum statistical theories of spontaneous emission and their relation to other approaches, in *Quantum Optics*, Springer Berlin Heidelberg, 1974.

[50] A. Auffèves, D. Gerace, S. Portolan, A. Drezet, and M. França Santos, Few emitters in a cavity: From cooperative emission to individualization. *New Journal of Physics* **13**, 093020 (2011).

[51] V. V. Temnov and U. Woggon, Photon statistics in the cooperative spontaneous emission. *Opt. Express* **17**, 5774 (2009).

[52] J. G. Bohnet, Z. Chen, J. M. Weiner, D. Meiser, M. J. Holland, and J. K. Thompson, A steady-state superradiant laser with less than one intracavity photon. *Nature* **484**, 78 (2012).

[53] Q. H. F. Vrehen and M. F. H. Schuurmans, Direct measurement of the effective initial tipping angle in superfluorescence. *Phys. Rev. Lett.* **42**, 224 (1979).

[54] H. A. M. Leymann, A. Foerster, F. Jahnke, J. Wiersig, and C. Gies, Sub- and superradiance in nanolasers. *Phys. Rev. Applied* **4**, 044018 (2015).

[55] B. R. Mollow, Power spectrum of light scattered by two-level systems. *Phys. Rev.* **188**, 1969 (1969).

[56] E. Fermi, *Nuclear Physics*, University of Chicago Press, 1950.

[57] W. Heitler, *The Quantum Theory of Radiation*, Oxford University Press, 1954, 3rd edition.

[58] R. Pierrat and R. Carminati, Spontaneous decay rate of a dipole emitter in a strongly scattering disordered environment. *Phys. Rev. A* **81**, 063802 (2010).

[59] E. M. Purcell, Spontaneous emission probabilities at radio frequencies. *Phys. Rev.* **69**, 681 (1946).

[60] K. H. Drexhage, M. Fleck, H. Kuhn, F. P. Schafer, and W. Sperling, Beeinflussung der Fluoreszenz eines Europium-Chelates durch einen Spiegel. *Ber. Bunsenges. Phys. Chem.* **70**, 1179 (1966).

[61] R. R. Chance, A. H. Miller, A. Prock, and R. Silbey, Fluorescence and energy transfer near interfaces: The complete and quantitative description of the Eu+3/mirror systems. *J. Chem. Phys.* **63**, 1589 (1975).

[62] A. Cazé, R. Pierrat, and R. Carminati, Radiative and non-radiative local density of states on disordered plasmonic films. *Photonics and Nanostructures - Fundamentals and Applications* **10**, 339 (2012).

[63] G. Vaubel, H. Baessler, and D. Möbius, Reaction of singlet excitons at an anthracene/metal interface: Energy transfer. *Chem. Phys. Lett.* **10**, 334 (1971).

[64] J. N. Farahani, D. W. Pohl, H.-J. Eisler, and B. Hecht, Single quantum dot coupled to a scanning optical antenna: A tunable superemitter. *Phys. Rev. Lett.* **95**, 017402 (2005).

[65] L. Novotny and N. van Hulst, Antennas for light. *Nature Photonics* **5**, 83 (2011).

[66] C. Sönnichsen, T. Franzl, T. Wilk, G. Von Plessen, J. Feldmann, O. Wilson, and P. Mulvaney, Drastic reduction of plasmon damping in gold nanorods. *Phys. Rev. Lett.* **88**, 077402 (2002).

[67] W. Zhang, A. O. Govorov, and G. W. Bryant, Semiconductor-metal nanoparticle molecules: Hybrid excitons and the nonlinear Fano effect. *Phys. Rev. Lett.* **97**, 146804 (2006).

[68] D. Dzsotjan, A. S. Sørensen, and M. Fleischhauer, Quantum emitters coupled to surface plasmons of a nanowire: A Green's function approach. *Phys. Rev. B* **82**, 075427 (2010).

[69] S. Hughes and H. Kamada, Single-quantum-dot strong coupling in a semiconductor photonic crystal nanocavity side coupled to a waveguide. *Phys. Rev. B* **70**, 195313 (2004).

[70] A. Delga, J. Feist, J. Bravo-Abad, and F. J. García-Vidal, Quantum emitters near a metal nanoparticle: strong coupling and quenching. *Phys. Rev. Lett.* **112**, 253601 (2014).

[71] F. Le Kien, S. D. Gupta, K. P. Nayak, and K. Hakuta, Nanofiber-mediated radiative transfer between two distant atoms. *Phys. Rev. A* **72**, 063815 (2005).

[72] R. Esteban, J. Aizpurua, and G. W. Bryant, Strong coupling of single emitters interacting with phononic infrared antennae. *New Journal of Physics* **16**, 013052 (2014).

[73] H. T. Dung, L. Knöll, and D.-G. Welsch, Resonant dipole-dipole interaction in the presence of dispersing and absorbing surroundings. *Phys. Rev. A* **66**, 063810 (2002).

[74] R. D. Artuso and G. W. Bryant, Quantum dot-quantum dot interactions mediated by a metal nanoparticle: Towards a fully quantum model. *Phys. Rev. B* **87**, 125423 (2013).

[75] A. Goban, C. L. Hung, J. D. Hood, S. P. Yu, J. A. Muniz, O. Painter, and H. J. Kimble, Superradiance for atoms trapped along a photonic crystal waveguide. *Phys. Rev. Lett.* **115**, 063601 (2015).

[76] A. Goban, C.-L. Hung, S.-P. Yu, J. D. Hood, J. a. Muniz, J. H. Lee, M. J. Martin, a. C. McClung, K. S. Choi, D. E. Chang, O. Painter, and H. J. Kimble, Atom-light interactions in photonic crystals. *Nature communications* **5**, 3808 (2014).

[77] M. V. Shestakov, E. Fron, L. F. Chibotaru, and V. V. Moshchalkov, Plasmonic Dicke effect in Ag-nanoclusters-doped oxyfluoride glasses. *J. Phys. Chem. C* **119**, 20051 (2015).

[78] M. Praveena, A. Mukherjee, M. Venkatapathi, and J. K. Basu, Plasmon-mediated emergence of collective emission and enhanced quantum efficiency in quantum dot films. *Phys. Rev. B* **92**, 235403 (2015).

[79] B. R. Cooper, H. Ehrenreich, and H. R. Philipp, Optical properties of noble metals. II. *Phys. Rev.* **138**, 494 (1965).

[80] P. Drude, Zur Elektronentheorie der Metalle. *Annalen der Physik* **306**, 566 (1900).

[81] R. N. Gurzhi, Mutual electron correlations in metal optics. *Sov. Phys. JETP* **35**, 673 (1959).

[82] P. B. Johnson and R. W. Christy, Optical constants of the noble metals. *Phys. Rev. B* **6**, 4370 (1972).

[83] A. D. Rakić, A. B. Djurišić, J. M. Elazar, and M. L. Majewski, Optical properties of metallic films for vertical-cavity optoelectronic devices. *Applied Optics* **37**, 5271 (1998).

[84] E. D. Palik, *Handbook of Optical Constants of Solids*, Part II. Academic Press, 1985.

[85] M. Meier and A. Wokaun, Enhanced fields on large metal particles: dynamic depolarization. *Opt. Lett.* **8**, 581 (1983).

[86] A. Moroz, Depolarization field of spheroidal particles. *J. Opt. Soc. Am. B* **26**, 517 (2009).

[87] K. L. Kelly, E. Coronado, L. L. Zhao, and G. C. Schatz, The optical properties of metal nanoparticles: The influence of size, shape, and dielectric environment. *J. Phys. Chem. B* **107**, 668 (2003).

[88] C. F. Bohren and D. R. Huffman (editors), *Absorption and Scattering of Light by Small Particles*, John Wiley & Sons, 1983.

[89] E. C. Le Ru, W. R. C. Somerville, and B. Auguié, Radiative correction in approximate treatments of electromagnetic scattering by point and body scatterers. *Phys. Rev. A* **87**, 012504 (2013).

[90] B. T. Draine, The discrete-dipole approximation and its application to interstellar graphite grains. *Astrophysical Journal* **333**, 848 (1988).

[91] A. Lakhtakia, Macroscopic theory of the coupled dipole approximation method. *Opt. Commun.* **79**, 1 (1990).

[92] R. Carminati, J.-J. Greffet, C. Henkel, and J. M. Vigoureux, Radiative and non-radiative decay of a single molecule close to a metallic nanoparticle. *Opt. Commun.* **261**, 368 (2006).

[93] G. Mie, Beiträge zur Optik trüber Medien, speziell kolloidaler Metallösungen. *Annalen der Physik* **330**, 377 (1908).

[94] H. Horvath, Gustav Mie and the scattering and absorption of light by particles: Historic developments and basics. *Journal of Quantitative Spectroscopy and Radiative Transfer* **110**, 787 (2009).

[95] G. Sun and J. B. Khurgin, Plasmonic enhancement of optical properties by isolated and coupled metal nanoparticles, in *Plasmonics and Plasmonic Metamaterials : Analysis and Applications*, edited by G. Shvets and I. Tsukerman, World Scientific Publishing Company, 2011, chapter 1.

[96] P. D. Howes, R. Chandrawati, and M. M. Stevens, Colloidal nanoparticles as advanced biological sensors. *Science* **346**, 1247390 (2014).

[97] H. Fröhlich, *Theory of Dielectrics: Dielectric Constant and Dielectric Loss*, Oxford University Press, 1987, 2nd edition.

[98] S. Underwood and P. Mulvaney, Effect of the solution refractive index on the color of gold colloids. *Langmuir* **10**, 3427 (1994).

[99] F. J. García de Abajo, Multiple scattering of radiation in clusters of dielectrics. *Phys. Rev. B* **60**, 6086 (1999).

[100] L. M. Liz-Marzán, M. Giersig, and P. Mulvaney, Synthesis of nanosized gold-silica core-shell particles. *Langmuir* **12**, 4329 (1996).

[101] J. Rodríguez-Fernández, I. Pastoriza-Santos, J. Pérez-Juste, F. J. García De Abajo, and L. M. Liz-Marzán, The effect of silica coating on the optical response of sub-micrometer gold spheres. *J. Phys. Chem. C* **111**, 13361 (2007).

[102] D. R. Lide, *Handbook of Chemistry and Physics*, CRC Press, 2009, 90th edition.

[103] J. Gersten and A. Nitzan, Spectroscopic properties of molecules interacting with small dielectric particles. *J. Chem. Phys.* **75**, 1139 (1981).

[104] R. Ruppin, Decay of an excited molecule near a small metal sphere. *J. Chem. Phys.* **76**, 1681 (1982).

[105] H. Chew, Transition rates of atoms near spherical surfaces. *J. Chem. Phys.* **87**, 1355 (1987).

[106] Y. S. Kim, P. T. Leung, and T. F. George, Classical decay rates for molecules in the presence of a spherical surface: A complete treatment. *Surface Science* **195**, 1 (1988).

[107] P. Anger, P. Bharadwaj, and L. Novotny, Enhancement and quenching of single-molecule fluorescence. *Phys. Rev. Lett.* **96**, 113002 (2006).

[108] Y. Chen, K. Munechika, and D. S. Ginger, Dependence of fluorescence intensity on the spectral overlap between fluorophores and plasmon resonant single silver nanoparticles. *Nano Lett.* **7**, 690 (2007).

[109] S. Kühn, U. Håkanson, L. Rogobete, and V. Sandoghdar, Enhancement of single-molecule fluorescence using a gold nanoparticle as an optical nanoantenna. *Phys. Rev. Lett.* **97**, 017402 (2006).

[110] H. Mertens, A. F. Koenderink, and A. Polman, Plasmon-enhanced luminescence near noble-metal nanospheres: Comparison of exact theory and an improved Gersten and Nitzan model. *Phys. Rev. B* **76**, 115123 (2007).

[111] G. Colas des Francs, A. Bouhelier, E. Finot, J. C. Weeber, A. Dereux, C. Girard, and E. Dujardin, Fluorescence relaxation in the near-field of a mesoscopic metallic particle: distance dependence and role of plasmon modes. *Opt. Express* **16**, 17654 (2008).

[112] A. Ridolfo, O. D. Stefano, N. Fina, R. Saija, and S. Savasta, Quantum plasmonics with quantum dot-metal nanoparticle molecules: Influence of the Fano effect on photon statistics. *Phys. Rev. Lett.* **105**, 263601 (2010).

[113] V. N. Pustovit, Enhanced fluorescence of a molecular dipole near metal nanoparticle. *Physica* **405B**, 754 (2010).

[114] V. N. Pustovit and T. V. Shahbazyan, Fluorescence quenching near small metal nanoparticles. *J. Chem. Phys.* **136**, 204701 (2012).

[115] C. Van Vlack, P. T. Kristensen, and S. Hughes, Spontaneous emission spectra and quantum light-matter interactions from a strongly coupled quantum dot metal-nanoparticle system. *Phys. Rev. B* **85**, 075303 (2012).

[116] H. Y. Chung, P. T. Leung, and D. P. Tsai, Molecular fluorescence in the vicinity of a charged metallic nanoparticle. *Opt. Express* **21**, 26483 (2013).

[117] M. Sukharev, N. Freifeld, and A. Nitzan, Numerical calculations of radiative and nonradiative relaxation of molecules near metal particles. *J. Phys. Chem. C* **118**, 10545 (2014).

[118] J.-J. Greffet, Nanoantennas for light emission. *Science* **308**, 1561 (2005).

[119] L. Gao, F. Lemarchand, and M. Lequime, Refractive index determination of SiO2 layer in the UV/Vis/NIR range: Spectrophotometric reverse engineering on single and bi-layer designs. *J. Europ. Opt. Soc. Rap. Public.* **8**, 13010 (2013).

[120] M. Thomas, J.-J. Greffet, R. Carminati, and J. R. Arias-Gonzalez, Single-molecule spontaneous emission close to absorbing nanostructures. *Appl. Phys. Lett.* **85**, 3863 (2004).

[121] H. R. Haakh, S. Faez, and V. Sandoghdar, Polaritonic states in a dielectric nanoguide: localization and strong coupling. *arXiv: 1510.07979* (2015).

[122] M. Venkatapathi, Collective eigenstates of emission in an N-entity heterostructure and the evaluation of its Green tensors and self-energy components. *J. Opt. Soc. Am. B* **31**, 3153 (2014).

[123] P. Reineck, D. Gómez, S. H. Ng, M. Karg, T. Bell, P. Mulvaney, and U. Bach, Distance and wavelength dependent quenching of molecular fluorescence by Au@SiO2 core-shell nanoparticles. *ACS Nano* **7**, 6636 (2013).

[124] N. S. Abadeer, M. R. Brennan, W. L. Wilson, and C. J. Murphy, Distance and plasmon wavelength dependent fluorescence of molecules bound to silica-coated gold nanorods. *ACS nano* **8**, 8392 (2014).

[125] W. Rudin, *Real and Complex Analysis*, McGraw-Hill Education, 1986, 3rd edition.

[126] J. D. Faires and R. L. Burden, *Numerical Methods*, Brooks Cole, 2003, 3rd edition.

[127] R. Friedberg, S. R. Hartmann, and J. T. Manassah, Frequency shifts in emission and absorption by resonant systems ot two-level atoms. *Phys. Rep.* **7**, 101 (1973).

[128] F. W. Cummings, Spontaneous emission from a single two-level atom in the presence of N initially unexcited identical atoms. *Phys. Rev. A* **33**, 1683 (1986).

[129] T. Förster, Transfer mechanisms of electronic excitation. *Discuss. Faraday Soc.* **27**, 7 (1959).

[130] P. Morse and H. Feshback, *Methods of Theoretical Physics*, McGraw-Hill Book Company, 1953.

[131] P. T. Leung, K. M. Pang, and K. Young, Two-component wave formalism in spherical open systems. *J. Phys. A: Math. Gen.* **39**, 247 (2005).

[132] A. H. Barnett, S. P. Smith, M. Olshanii, K. S. Johnson, A. W. Adams, and M. Prentiss, Substrate-based atom waveguide using guided two-color evanescent light fields. *Phys. Rev. A* **61**, 023608 (2000).

[133] C. Sauvan, J. P. Hugonin, I. S. Maksymov, and P. Lalanne, Theory of the spontaneous optical emission of nanosize photonic and plasmon resonators. *Phys. Rev. Lett.* **110**, 237401 (2013).

[134] P. Lalanne, C. Sauvan, and J. Hugonin, Photon confinement in photonic crystal nanocavities. *Laser & Photon. Rev* **2**, 514 (2008).

[135] K. Srinivasan, P. E. Barclay, O. Painter, J. Chen, A. Y. Cho, and C. Gmachl, Experimental demonstration of a high quality factor photonic crystal microcavity. *Appl. Phys. Lett.* **83**, 1915 (2003).

[136] Y. Akahane, T. Asano, B.-S. Song, and S. Noda, High-Q photonic nanocavity in a two-dimensional photonic crystal. *Nature* **425**, 944 (2003).

[137] Q. Bai, M. Perrin, C. Sauvan, J.-P. Hugonin, and P. Lalanne, Efficient and intuitive method for the analysis of light scattering by a resonant nanostructure. *Opt. Express* **21**, 27371 (2013).

[138] J. Yang, M. Perrin, and P. Lalanne, Analytical formalism for the interaction of two-level quantum systems with metal nanoresonators. *Phys. Rev. X* **5**, 021008 (2015).

[139] P. T. Kristensen, G. Rong-Chun, and H. Stephen, Normalization of quasinormal modes in leaky optical cavities and plasmonic resonators. *Phys. Rev. A* **92**, 053810 (2015).

[140] E. A. Muljarov and W. Langbein, Comment on " Normalization of quasinormal modes in leaky optical cavities and plasmonic resonators ". *arXiv:1602.07278v1* (2016).

[141] P. T. Kristensen, G. Rong-Chun, and H. Stephen, Reply to " Comment on " Normalization of quasinormal modes in leaky optical cavities and plasmonic resonators " ". *arXiv:1605.08702v1* (2016).

[142] U. Fano, Effects of configuration interaction on intensities and phase shifts. *Phys. Rev.* **124**, 1866 (1961).

[143] X.-W. Chen, V. Sandoghdar, and M. Agio, Coherent interaction of light with a metallic structure coupled to a single quantum emitter: From superabsorption to cloaking. *Phys. Rev. Lett.* **110**, 153605 (2013).

[144] R. J. Bell and P. Dean, Atomic vibrations in vitreous silica. *Discuss. Faraday Soc.* **50**, 55 (1970).

[145] B. Kramer and A. Mackinnon, Localization: theory and experiment. *Rep. Prog. Phys.* **56**, 1469 (1993).

[146] C. E. Máximo, N. Piovella, P. W. Courteille, R. Kaiser, and R. Bachelard, Spatial and temporal localization of light in two dimensions. *Phys. Rev. A* **92**, 062702 (2015).

[147] M. Ferrié, Design de particules plasmoniques pour le contrôle de l'absorption et de l'émission de lumière. *Thèse de l'Université de Bordeaux I* (2011).

[148] K. R. Brown, D. G. Walter, and M. J. Natan, Seeding of colloidal Au nanoparticle solutions. 2. Improved control of particle size and shape. *Chem. Mater.* **12**, 306 (2000).

[149] N. G. Bastus, J. Comenge, and V. Puntes, Kinetically controlled seeded growth synthesis of citrate-stabilized gold nanoparticles of up to 200 nm: Size focusing versus ostwald ripening. *Langmuir* **27**, 11098 (2011).

[150] C. Graf, D. L. J. Vossen, A. Imhof, and A. van Blaaderen, A general method to coat colloidal particles with silica. *Langmuir* **19**, 6693 (2003).

[151] W. Stöber, A. Fink, and E. Bohn, Controlled growth of monodisperse silica spheres in the micron size range. *Journal of Colloid and Interface Science* **26**, 62 (1968).

[152] S. Kang, S. I. Hong, C. R. Choe, M. Park, S. Rim, and J. Kim, Preparation and characterization of epoxy composites filled with functionalized nanosilica particles obtained via sol–gel process. *Polymer* **42**, 879 (2001).

[153] J. Rheims, J. Köser, and T. Wriedt, Refractive-index measurements in the near-IR using an Abbe refractometer. *Meas. Sci. Technol.* **8**, 601 (1997).

[154] C. Ayala-Orozco, J. G. Liu, M. W. Knight, Y. Wang, J. K. Day, P. Nordlander, and N. J. Halas, Fluorescence enhancement of molecules inside a gold nanomatryoshka. *Nano Lett.* **14**, 2926 (2014).

[155] F. L. Arbeloa, P. R. Ojeda, and I. L. Arbeloa, Fluorescence self-quenching of the molecular forms of Rhodamine B in aqueous and ethanolic solutions. *Journal of Luminescence* **44**, 105 (1989).

[156] Atto-Tec GmbH, Siegen, Germany. Information available online at www.atto-tec.com.

[157] W. C. Galley and R. M. Purkey, Role of heterogeneity of the solvation site in electronic spectra in solution. *Proc. Natl. Acad. Sci. U. S. A.* **67**, 1116 (1970).

[158] C. H. Brito Cruz, R. L. Fork, W. H. Knox, and C. V. Shank, Spectral hole burning in large molecules probed with 10 fs optical pulses. *Chem. Phys. Lett.* **132**, 341 (1986).

[159] P. C. Becker, H. L. Fragnito, J. Y. Bigot, C. H. Brito Cruz, R. L. Fork, and C. V. Shank, Femtosecond photon echoes from molecules in solution. *Phys. Rev. Lett.* **63**, 505 (1989).

[160] R. Zhang, T.-S. Yang, and A. B. Myers, Femtosecond incoherent photon echo from rhodamine B in propylene glycol. Inhomogeneous broadening and spectral diffusion at room temperature. *Chem. Phys. Lett.* **211**, 541 (1993).

[161] A. van Blaaderen and A. Vrij, Synthesis and characterization of colloidal dispersions of fluorescent, monodisperse silica spheres. *Langmuir* **8**, 2921 (1992).

[162] C. Graf, Q. Gao, I. Schütz, C. N. Noufele, W. Ruan, U. Posselt, E. Korotianskiy, D. Nordmeyer, F. Rancan, S. Hadam, A. Vogt, J. Lademann, V. Haucke, and E. Rühl, Surface functionalization of silica nanoparticles supports colloidal stability in physiological media and facilitates internalization in cells. *Langmuir* **28**, 7598 (2012).

[163] Q. A. Best, R. Xu, M. E. McCarroll, L. Wang, and D. J. Dyer, Design and investigation of a series of rhodamine-based fluorescent probes for optical measurements of pH. *Organic Letters* **12**, 3219 (2010).

[164] L. M. Bollinger and G. E. Thomas, Measurement of the time dependence of scintillation intensity by a delayed-coincidence method. *Review of Scientific Instruments* **32**, 1044 (1961).

[165] R. A. L. Vallée, M. Ferrié, H. Saadaoui, and S. Ravaine, Broadband spontaneous emission rate enhancement through the design of plasmonic nanoantennas. *Opt. Mater. Express* **2**, 566 (2012).

[166] A. F. van Driel, I. S. Nikolaev, P. Vergeer, P. Lodahl, D. Vanmaekelbergh, and W. L. Vos, Statistical analysis of time-resolved emission from ensembles of semiconductor quantum dots: Interpretation of exponential decay models. *Phys. Rev. B* **75**, 035329 (2007).

[167] I. S. Nikolaev, P. Lodahl, A. F. van Driel, A. F. Koenderink, and W. L. Vos, Strongly nonexponential time-resolved fluorescence of quantum-dot ensembles in three-dimensional photonic crystals. *Phys. Rev. B* **75**, 115302 (2007).

[168] R. A. L. Vallée, K. Baert, B. Kolaric, M. Van der Auweraer, and K. Clays, Nonexponential decay of spontaneous emission from an ensemble of molecules in photonic crystals. *Phys. Rev. B* **76**, 045113 (2007).

[169] M. N. Berberan-Santos, E. N. Bodunov, and J. M. G. Martinho, Luminescence kinetics of chromophores attached to the ends of a flexible polymer chain. *Optics and Spectroscopy* **89**, 876 (2000).

[170] Y. S. Liu and W. R. Ware, Photophysics of polycyclic aromatic hydrocarbons adsorbed on silica gel surfaces. 1. Fluorescence lifetime distribution analysis: an ill-conditioned problem. *J. Phys. Chem.* **97**, 5980 (1993).

[171] B. Mollay and H. F. Kauffmann, Dynamics of energy transfer in aromatic polymers, in *Disorder effects on relaxational processes*, edited by R. Richert and A. Blumen, Springer-Verlag, 1994, 509.

[172] M. N. Berberan-Santos, E. N. Bodunov, and B. Valeur, Mathematical functions for the analysis of luminescence decays with underlying distributions. *Chemical Physics* **315**, 171 (2005).

[173] R. Kohlrausch, Theorie des elektrischen Rückstandes in der Leidener Flasche. *Annalen der Physik* **167**, 179 (1854).

[174] G. Williams and D. C. Watts, Non-symmetrical dielectric relaxation behaviour arising from a simple empirical decay function. *Transactions of the Faraday Society* **66**, 80 (1970).

[175] C. P. Lindsey and G. D. Patterson, Detailed comparison of the Williams–Watts and Cole–Davidson functions. *J. Chem. Phys.* **73**, 3348 (1980).

[176] M. Minsky, Memoirs on inventing the confocal scanning microscope. *Scanning* **10**, 128 (1988).

[177] J. Mieloszyk, R. Drabent, and J. Siódmiak, Phosphorescence and fluorescence of poly(vinyl alcohol) films. *Journal of Applied Polymer Science* **34**, 1577 (1987).

[178] L. Piatkowski, E. Gellings, and N. F. van Hulst, Broadband single-molecule excitation spectroscopy. *Nature Communications* **7**, 10411 (2016).

[179] C. B. Walsh and E. I. Franses, Ultrathin PMMA films spin-coated from toluene solutions. *Thin Solid Films* **429**, 71 (2003).

[180] S. Mahendia, A. K. Tomar, P. K. Goyal, and S. Kumar, Tuning of refractive index of poly(vinyl alcohol): Effect of embedding Cu and Ag nanoparticles. *J Appl Phys.* **113**, 073103 (2013).

[181] N. Sultanova, S. Kasarova, and I. Nikolov, Dispersion properties of optical polymers. *Acta Physica Polonica A* **116**, 585 (2009).

[182] A. Köhler, Ein neues Beleuchtungsverfahren für mikrophotographische Zwecke. *Zeitschrift für wissenschaftliche Mikroskopie und für Mikroskopische Technik* **10**, 433 (1893).

[183] M. Locquin and M. Langeron, *Handbook of Microscopy*, Butterworth-Heinemann, 1983.

[184] Y. Wu, X. Wu, R. Lu, J. Zhang, L. Toro, and E. Stefani, Resonant scanning with large field of view reduces photobleaching and enhances fluorescence yield in STED microscopy. *Scientific Reports* **5**, 14766 (2015).

[185] T.-J. Yim, Y. Wang, and X. Zhang, Synthesis of a gold nanoparticle dimer plasmonic resonator through two-phase-mediated functionalization. *Nanotechnology* **19**, 435605 (2008).

[186] W. Rechberger, A. Hohenau, A. Leitner, J. R. Krenn, B. Lamprecht, and F. R. Aussenegg, Optical properties of two interacting gold nanoparticles. *Opt. Commun.* **220**, 137 (2003).

[187] P. Nordlander, C. Oubre, E. Prodan, K. Li, and M. I. Stockman, Plasmon hybridization in nanoparticle dimers. *Nano Lett.* **4**, 899 (2004).

[188] E. Prodan, C. Radloff, N. J. Halas, and P. Nordlander, A hybridization model for the plasmon response of complex nanostructures. *Science* **302**, 419 (2003).

[189] E. Abbe, Beiträge zur theorie des mikroskops und der mikroskopischen wahrnehmung. *Archiv für mikroskopische Anatomie* **9**, 413 (1873).

[190] L. Rayleigh, On the theory of optical images, with special reference to the microscope. *J. R. Microsc. Soc.* **23**, 474 (1903).

[191] R. Jain, M. Mathur, S. Sikarwar, and A. Mittal, Removal of the hazardous dye rhodamine B through photocatalytic and adsorption treatments. *Journal of Environmental Management* **85**, 956 (2007).

[192] Q. H. F. Vrehen, Spectral distribution of the stimulated emission of a rhodamine B dye laser. *Opt. Commun.* **3**, 144 (1971).

[193] T. Förster, Zwischenmolekulare Energiewanderung und Fluoreszenz. *Annalen der Physik* **437**, 55 (1948).

[194] M. D. Galanin and L. V. Levshin, Quenching of fluorescence of solutions by absorbing substances. *Zhur. Eksptl. i Teoret. Fiz.* **21**, 121 (1951).

[195] A. Reisch, P. Didier, L. Richert, S. Oncul, Y. Arntz, Y. Mély, and A. S. Klymchenko, Collective fluorescence switching of counterion-assembled dyes in polymer nanoparticles. *Nature Communications* **5**, 4089 (2014).

[196] S. Kedenburg, M. Vieweg, T. Gissibl, and H. Giessen, Linear refractive index and absorption measurements of nonlinear optical liquids in the visible and near-infrared spectral region. *Opt. Mater. Express* **2**, 1588 (2012).

[197] M. Ferrié, M. Pinna, S. Ravaine, and R. A. L. Vallée, Wavelength-dependent emission enhancement through the design of active plasmonic nanoantennas. *Opt. Express* **19**, 17697 (2011).

[198] C.-L. Hsieh, S. Spindler, J. Ehrig, and V. Sandoghdar, Tracking single particles on supported lipid membranes: Multimobility diffusion and nanoscopic confinement. *J. Phys. Chem. B* **118**, 1545 (2014).

[199] J. Grad, G. Hernandez, and S. Mukamel, Radiative decay and energy transfer in molecular aggregates: The role of intermolecular dephasing. *Phys. Rev. A* **37**, 3835 (1988).

[200] S. de Boer and D. A. Wiersma, Dephasing-Induced damping of superradiant emission in J-aggregates. *Chem. Phys. Lett.* **165**, 45 (1990).

[201] F. C. Spano, J. R. Kuklinski, and S. Mukamel, Temperature-dependent superradiant decay of excitons in small aggregates. *Phys. Rev. Lett.* **65**, 211 (1990).

[202] F. C. Spano, J. R. Kuklinski, and S. Mukamel, Cooperative radiative dynamics in molecular aggregates. *J. Chem. Phys.* **94**, 7534 (1991).

[203] M. Bednarz, V. a. Malyshev, and J. Knoester, Temperature dependent fluorescence in disordered Frenkel chains: Interplay of equilibration and local band-edge level structure. *Phys. Rev. Lett.* **91**, 217401 (2003).

[204] D. J. Heijs, V. A. Malyshev, and J. Knoester, Decoherence of excitons in multichromophore systems: Thermal line broadening and destruction of superradiant emission. *Phys. Rev. Lett.* **95**, 177402 (2005).

[205] T. V. Shahbazyan, M. E. Raikh, and Z. V. Vardeny, Mesoscopic Cooperative Emission From a Disordered System. *Phys. Rev. B* **61**, 13266 (2000).

[206] F. C. Spano and S. Mukamel, Superradiance in molecular aggregates. *J. Chem. Phys.* **91**, 683 (1989).

[207] F. Šanda and S. Mukamel, Cooperative effects in photon statistics of molecular dimers with spectral diffusion. *J. Chem. Phys.* **124**, 124103 (2006).

[208] J. Hernando, E. M. H. P. van Dijk, J. P. Hoogenboom, G.-L. J.-J., D. N. Reinhoudt, M. Crego-calama, M. F. Garcia-Parajo, and N. F. van Hulst, Effect of disorder on ultrafast exciton dynamics probed by single molecule spectroscopy. *Phys. Rev. Lett.* **97**, 216403 (2006).

[209] H. Haken and G. Strobl, An exactly solvable model for coherent and incoherent exciton motion. *Z. Physik* **262**, 135 (1973).

[210] R. Métivier, F. Nolde, K. Müllen, and T. Basché, Electronic excitation energy transfer between two single molecules embedded in a polymer host. *Phys. Rev. Lett.* **047802**, 1 (2007).

[211] M. Lippitz, C. G. Hübner, T. Christ, H. Eichner, P. Bordat, A. Herrmann, K. Müllen, and T. Basché, Coherent electronic coupling versus localization in individual molecular dimers. *Phys. Rev. Lett.* **92**, 103001 (2004).

[212] S. Link, C. Burda, M. Mohamed, B. Nikoobakht, and M. El-Sayed, Femtosecond transient-absorption dynamics of colloidal gold nanorods: Shape independence of the electron-phonon relaxation time. *Phys. Rev. B* **61**, 6086 (2000).

[213] M. B. Mohamed, T. S. Ahmadi, S. Link, M. Braun, and M. A. El-Sayed, Hot electron and phonon dynamics of gold nanoparticles embedded in a gel matrix. *Chem. Phys. Lett.* **343**, 55 (2001).

[214] H. Portales, L. Saviot, E. Duval, M. Fujii, S. Hayashi, N. Del Fatti, and F. Vallée, Resonant Raman scattering by breathing modes of metal nanoparticles. *J. Chem. Phys.* **115**, 3444 (2001).

[215] X. Huang and M. A. El-Sayed, Gold nanoparticles: Optical properties and implementations in cancer diagnosis and photothermal therapy. *Journal of Advanced Research* **1**, 13 (2010).

[216] J. D. Joannopoulos, S. G. Johnson, J. N. Winn, and R. D. Meade (editors), *Photonic crystals: molding the flow of light*, Princeton University Press, 2008, 2nd edition.

[217] P. Fauché, S. Ungureanu, B. Kolaric, and R. A. L. Vallée, Emitters as probes of a complex plasmo-photonic mode. *J. Mater. Chem. C* **2**, 10362 (2014).

[218] X. Ma, J. Q. Lu, R. S. Brock, K. M. Jacobs, P. Yang, and X.-H. Hu, Determination of complex refractive index of polystyrene microspheres from 370 to 1610 nm. *Phys. Med. Biol.* **48**, 4165 (2003).

[219] F. Bloch, Über die Quantenmechanik der Elektronen in Kristallgittern. *Zeitschrift für Physik* **52**, 555 (1929).

[220] W. H. Bragg and W. L. Bragg, The reflection of X-rays by crystals. *Proc. R. Soc. Lond. A* **88**, 428 (1913).

[221] L. Landström, N. Arnold, D. Brodoceanu, K. Piglmayer, and D. Bäuerle, Photonic properties of silicon-coated monolayers of colloidal silica microspheres. *Appl. Phys. A* **83**, 271 (2006).

[222] L. Landström, D. Brodoceanu, N. Arnold, K. Piglmayer, and D. Bäuerle, Photonic properties of silicon-coated colloidal monolayers. *Appl. Phys. A* **81**, 911 (2005).

[223] C. Farcau, E. Vinteler, and S. Astilean, Experimental and theoretical investigation of optical properties of colloidal photonic crystal films. *Journal of Optoelectronics and Advanced Materials* **10**, 3165 (2008).

[224] M. Inoue, K. Ohtaka, and S. Yanagawa, Light scattering from macroscopic spherical bodies. II. Reflectivity of light and electromagnetic localized state in a periodic monolayer of dielectric spheres. *Phys. Rev. B* **25**, 689 (1982).

[225] H. T. Miyazaki, H. Miyazaki, K. Ohtaka, and T. Sato, Photonic band in two-dimensional lattices of micrometer-sized spheres mechanically arranged under a scanning electron microscope. *J Appl Phys.* **87**, 7152 (2000).

[226] Y. Kurokawa, H. Miyazaki, and Y. Jimba, Light scattering from a monolayer of periodically arrayed dielectric spheres on dielectric substrates. *Phys. Rev. B* **65**, 201102 (2002).

[227] Y. Kurokawa, H. Miyazaki, and Y. Jimba, Optical band structure and near-field intensity of a periodically arrayed monolayer of dielectric spheres on dielectric substrate of finite thickness. *Phys. Rev. B* **69**, 155117 (2004).

[228] R. W. Wood, On a remarkable case of uneven distribution of light in a diffraction grating spectrum. *Proc. Phys. Soc. Lond.* **18**, 269 (1902).

[229] L. Rayleigh, On the dynamical theory of gratings. *Proc. R. Soc. Lond. A* **79**, 399 (1907).

[230] U. Fano, Zur Theorie der Intensitätsanomalien der Beugung. *Annalen der Physik* **32**, 393 (1938).

[231] E. W. Palmer, M. C. Hutley, A. Franks, J. F. Verrill, and B. Gale, Diffraction gratings (manufacture). *Reports on Progress in Physics* **38**, 975 (1975).

[232] C. Farcau, M. Giloan, E. Vinteler, and S. Astilean, Understanding plasmon resonances of metal-coated colloidal crystal monolayers. *Appl. Phys. B* **106**, 849 (2012).

[233] D. Brewster, On the Laws Which Regulate the Absorption of Polarised Light by Doubly Refracting Crystal. *Philosophical Transactions of the Royal Society of London* **109**, 11 (1819).

[234] S. G. Romanov, A. V. Korovin, A. Regensburger, and U. Peschel, Hybrid colloidal plasmonic-photonic crystals. *Adv. Mater.* **23**, 2515 (2011).

[235] L. Shi, X. Jiang, and C. Li, Effects induced by Mie resonance in two-dimensional photonic crystals. *J. Phys.: Condens. Matter* **19**, 176214 (2007).

[236] H. Miyazaki and K. Ohtaka, Near-field images of a monolayer of periodically arrayed dielectric spheres. *Phys. Rev. B* **58**, 6920 (1998).

[237] L. Rayleigh, On the maintenance of vibrations by forces of double frequency, and on the propagation of waves through a medium endowed with a periodic structure. *Philosophical Magazine Series 5* **24**, 145 (1887).

[238] M. Florescu, S. Torquato, and P. J. Steinhardt, Complete band gaps in two-dimensional photonic quasicrystals. *Phys. Rev. B* **80**, 155112 (2009).

[239] D. Chigrin, S. Enoch, C. M. Sotomayor Torres, and G. Tayeb, Self-guiding in two-dimensional photonic crystals. *Opt. Express* **11**, 1203 (2003).

[240] S. John, Strong localization of photons in certain disordered dielectric superlattices. *Phys. Rev. Lett.* **58**, 2486 (1987).

[241] T. Baba, Slow light in photonic crystals. *Nature Photonics* **2**, 465 (2008).

[242] R. H. Ritchie, E. T. Arakawa, J. J. Cowan, and R. N. Hamm, Surface-plasmon resonance effect in grating diffraction. *Phys. Rev. Lett.* **21**, 1530 (1968).

[243] J. R. Krenn, A. Dereux, J. C. Weeber, E. Bourillot, Y. Lacroute, J. P. Goudonnet, G. Schider, W. Gotschy, A. Leitner, F. R. Aussenegg, and C. Girard, Squeezing the optical near-field zone by plasmon coupling of metallic nanoparticles. *Phys. Rev. Lett.* **82**, 2590 (1999).

[244] T. V. Teperik, F. J. García de Abajo, A. G. Borisov, M. Abdelsalam, P. N. Bartlett, Y. Sugawara, and J. J. Baumberg, Omnidirectional absorption in nanostructured metal surfaces. *Nature Photonics* **2**, 299 (2008).

[245] T. W. Ebbesen, H. J. Lezec, H. F. Ghaemi, T. Thio, and P. A. Wolff, Extraordinary optical transmission through sub-wavelength hole arrays. *Nature* **391**, 667 (1998).

[246] H. J. Lezec, A. Degiron, E. Devaux, R. A. Linke, L. Martin-Moreno, F. J. García-Vidal, and T. W. Ebbesen, Beaming light from a subwavelength aperture. *Science* **297**, 820 (2002).

[247] A. Christ, S. G. Tikhodeev, N. A. Gippius, J. Kuhl, and H. Giessen, Waveguide-plasmon polaritons: strong coupling of photonic and electronic resonances in a metallic photonic crystal slab. *Phys. Rev. Lett.* **91**, 183901 (2003).

[248] L. Landström, D. Brodoceanu, K. Piglmayer, and D. Bäuerle, Extraordinary optical transmission through metal-coated colloidal monolayers. *Appl. Phys. A* **84**, 373 (2006).

[249] L. Landström, D. Brodoceanu, D. Bäuerle, F. J. García-Vidal, S. G. Rodrigo, and L. Martin-Moreno, Extraordinary transmission through metal-coated monolayers of microspheres. *Opt. Express* **17**, 761 (2009).

[250] P. Zhan, Z. L. Wang, H. Dong, J. Sun, J. Wu, H.-T. Wang, S. N. Zhu, N. B. Ming, and J. Zi, The anomalous infrared transmission of gold films on two-dimensional colloidal crystals. *Adv. Mater.* **18**, 1612 (2006).

[251] A. I. Maaroof, M. B. Cortie, N. Harris, and L. Wieczorek, Mie and Bragg plasmons in subwavelength silver semi-shells. *Small* **4**, 2292 (2008).

[252] S. Ungureanu, B. Kolaric, J. Chen, R. Hillenbrand, and R. A. L. Vallée, Far-field disentanglement of modes in hybrid plasmonic-photonic crystals by fluorescence nano-reporters. *Nanophotonics* **2**, 173 (2013).

[253] Y. J. Chen, E. . Koteles, R. J. Seymour, G. J. Sonek, and Ballantyne J M, Surface plasmons on gratings: Coupling in the minigap regions. *Solid State Commun.* **46**, 95 (1983).

[254] H. F. Ghaemi, T. Thio, D. E. Grupp, T. W. Ebbesen, and H. J. Lezec, Surface plasmons enhance optical transmission through subwavelength holes. *Phys. Rev. B* **58**, 6779 (1998).

[255] B. Ding, C. Hrelescu, N. Arnold, G. Isic, and T. A. Klar, Spectral and directional reshaping of fluorescence in large area self-assembled plasmonic–photonic crystals. *Nano Lett.* **13**, 378 (2013).

[256] I. Ursu, I. Mihailescu, A. Prokhorov, V. Konov, and V. Tokarev, On the role of the periodical structures induced by powerful laser irradiation of metallic surfaces in the energy coupling process. *Physica* **132C**, 395 (1985).

[257] E. Yablonovitch, Inhibited spontaneous emission in solid-state physics and electronics. *Phys. Rev. Lett.* **58**, 2059 (1987).

[258] P. Lodahl, A. Floris van Driel, I. S. Nikolaev, A. Irman, K. Overgaag, D. Vanmaekelbergh, and W. L. Vos, Controlling the dynamics of spontaneous emission from quantum dots by photonic crystals. *Nature* **430**, 654 (2004).

[259] S. Noda, M. Fujita, and T. Asano, Spontaneous-emission control by photonic crystals and nanocavities. *Nature Photonics* **1**, 449 (2007).

[260] K. Aoki, D. Guimard, M. Nishioka, M. Nomura, S. Iwamoto, and Y. Arakawa, Coupling of quantum-dot light emission with a three-dimensional photonic-crystal nanocavity. *Nature Photonics* **2**, 688 (2008).

[261] M. Khajavikhan, A. Simic, M. Katz, J. H. Lee, B. Slutsky, A. Mizrahi, V. Lomakin, and Y. Fainman, Thresholdless nanoscale coaxial lasers. *Nature* **482**, 204 (2012).

[262] T. H. Taminiau, F. D. Stefani, F. B. Segerink, and N. F. van Hulst, Optical antennas direct single-molecule emission. *Nature Photonics* **2**, 234 (2008).

[263] R. F. Oulton, V. J. Sorger, T. Zentgraf, R.-M. Ma, C. Gladden, L. Dai, G. Bartal, and X. Zhang, Plasmon lasers at deep subwavelength scale. *Nature* **461**, 629 (2009).

[264] J. T. Choy, B. J. M. Hausmann, T. M. Babinec, I. Bulu, M. Khan, P. Maletinsky, A. Yacoby, and M. Lončar, Enhanced single-photon emission from a diamond–silver aperture. *Nature Photonics* **5**, 738 (2011).

[265] X. Yang, A. Ishikawa, X. Yin, and X. Zhang, Hybrid photonic-plasmonic crystal nanocavities. *ACS Nano* **5**, 2831 (2011).

[266] B. Lamprecht, G. Schider, R. T. Lechner, H. Ditlbacher, J. R. Krenn, A. Leitner, and F. R. Aussenegg, Metal nanoparticle gratings: Influence of dipolar particle interaction on the plasmon resonance. *Phys. Rev. Lett.* **84**, 4721 (2000).

[267] B. Auguié and W. L. Barnes, Collective resonances in gold nanoparticle arrays. *Phys. Rev. Lett.* **101**, 143902 (2008).

[268] M. Ringler, A. Schwemer, M. Wunderlich, A. Nichtl, K. Kürzinger, T. Klar, and J. Feldmann, Shaping emission spectra of fluorescent molecules with single plasmonic nanoresonators. *Phys. Rev. Lett.* **100**, 203002 (2008).

[269] S. G. Romanov, A. V. Fokin, and R. M. De La Rue, Anisotropic photoluminescence in incomplete three-dimensional photonic band-gap environments. *Appl. Phys. Lett.* **74**, 1821 (1999).

[270] J. N. Anker, W. P. Hall, O. Lyandres, N. C. Shah, J. Zhao, and R. P. van Duyne, Biosensing with plasmonic nanosensors. *Nature Materials* **7**, 442 (2008).

[271] A. V. Kabashin, P. Evans, S. Pastkovsky, W. Hendren, G. A. Wurtz, R. Atkinson, R. Pollard, V. A. Podolskiy, and A. V. Zayats, Plasmonic nanorod metamaterials for biosensing. *Nature Materials* **8**, 867 (2009).

[272] H. A. Atwater and A. Polman, Plasmonics for improved photovoltaic devices. *Nature Materials* **9**, 205 (2010).

[273] C. Clavero, Plasmon-induced hot-electron generation at nanoparticle/metal-oxide interfaces for photovoltaic and photocatalytic devices. *Nature Photonics* **8**, 95 (2014).

[274] U. C. Fischer and H. P. Zingsheim, Submicroscopic pattern replication with visible light. *J. Vac. Sci. Technol.* **19**, 881 (1981).

[275] J. C. Hulteen and R. P. van Duyne, Nanosphere lithography: A materials general fabrication process for periodic particle array surfaces. *J. Vac. Sci. Technol. A* **13**, 1553 (1995).

[276] J. C. Hulteen, D. A. Treichel, M. T. Smith, M. L. Duval, T. R. Jensen, and R. P. van Duyne, Nanosphere lithography: Size-tunable silver nanoparticle and surface cluster arrays. *J. Phys. Chem. B* **103**, 3854 (1999).

[277] C. L. Haynes and R. P. Van Duyne, Nanosphere lithography: A versatile nanofabrication tool for studies of size-dependent nanoparticle optics. *J. Phys. Chem. B* **105**, 5599 (2001).

[278] R. Morarescu, H. Shen, R. A. L. Vallée, B. Maes, B. Kolaric, and P. Damman, Exploiting the localized surface plasmon modes in gold triangular nanoparticles for sensing applications. *J. Mater. Chem.* **22**, 11537 (2012).

[279] A. Kinkhabwala, Z. Yu, S. Fan, Y. Avlasevich, K. Müllen, and W. E. Moerner, Large single-molecule fluorescence enhancements produced by a bowtie nanoantenna. *Nature Photonics* **3**, 654 (2009).

[280] A. Taflove, A. Oskooi, and S. G. Johnson (editors), *Advances in FDTD Computational Electrodynamics: Photonics and Nanotechnology*, Artech House, Inc., 2013.

[281] W. L. Barnes, W. A. Murray, J. Dintinger, E. Devaux, and T. W. Ebbesen, Surface plasmon polaritons and their role in the enhanced transmission of light through periodic arrays of subwavelength holes in a metal film. *Phys. Rev. Lett.* **92**, 107401 (2004).

[282] M. Agio, Optical antennas as nanoscale resonators. *Nanoscale* **4**, 692 (2012).

[283] C. B. Murray, D. J. Norris, and M. G. Bawendi, Synthesis and characterization of nearly monodisperse CdE (E = S, Se, Te) semiconductor nanocrystallites. *J. Am. Chem. Soc.* **115**, 8706 (1993).

[284] S. Jander, A. Kornowski, and H. Weller, Energy transfer from CdSe/CdS nanorods to amorphous carbon. *Nano Lett.* **11**, 5179 (2011).

[285] C. Messaoudi, T. Boudier, C. O. S. Sorzano, and S. Marco, TomoJ: tomography software for three-dimensional reconstruction in transmission electron microscopy. *BMC Bioinformatics* **8**, 288 (2007).

[286] S. Foteinopoulou, J. P. Vigneron, and C. Vandenbem, Optical near-field excitations on plasmonic nanoparticle-based structures. *Opt. Express* **15**, 4253 (2007).

[287] C. A. Leatherdale, W.-K. Woo, F. V. Mikulec, and M. G. Bawendi, On the absorption cross section of CdSe nanocrystal quantum dots. *J. Phys. Chem. B* **106**, 7619 (2002).

[288] M. Boissonneault, J. M. Gambetta, and A. Blais, Dispersive regime of circuit QED: Photon-dependent qubit dephasing and relaxation rates. *Phys. Rev. A* **79**, 013819 (2009).

[289] Z. Ficek, R. Tanas, and S. Kielich, Cooperative Effects in the spontaneous emission from two non-identical atoms. *Optica Acta* **33**, 1149 (1986).

[290] Z. Ficek, R. Tanaś, and S. Kielich, Quantum beats and superradiant effects in the spontaneous emission from two nonidentical atoms. *Physica* **146A**, 452 (1987).

Plasmonic superradiance in metallo-dielectric nanohybrids

Abstract: Hybridization of quantum emitters and plasmonic nanostructures has attracted much attention over the last years, due to their potential use as plasmon-based nanolasers or to achieve long-range quantum bit entanglement. Recent theoretical studies suggest that the plasmonic field can induce efficient cross-talking between emitters and lead to the formation of collective superradiant states. In this thesis, we developed a theoretical model able to analyse collective effects in large ensemble of dipoles coupled by an electromagnetic nanoresonator. We experimentally investigated the plasmon-mediated superradiance of organic emitters grafted at a well-controlled distance from a metal nanosphere at room temperature. We report on the measured decay rates of these hybrid structures at the ensemble and single object levels. We find that the decay rate increases i) with the number of emitters and ii) as the spacing between the emitters and the metal core decreases, a direct and clear evidence of plasmonic superradiance. This trend was observed for two types of hybrid structures, differing both by the size of the metal core and the type of organic dye used as emitter. The observation of plasmonic superradiance at room temperature opens questions about the robustness of these collective states against decoherence mechanisms. This robustness is of major interest for potential applications of quantum systems at room temperature.

Keywords: superradiance, surface plasmon, energy transfer, decoherence

Superradiance plasmonique dans des nanohybrides métallo-diélectriques

Résumé : Placer des nanostructures plasmoniques à proximité d'émetteurs quantiques est une approche prometteuse pour concevoir des nanolasers plasmoniques ou réaliser l'intrication de bits quantiques à longue distance. Des études théoriques récentes suggèrent que le champ plasmonique peut induire un couplage efficace entre émetteurs et mener à la formation d'états collectifs superradiants. Dans ce travail de thèse, nous avons développé un modèle théorique afin d'analyser les effets collectifs pour un ensemble de dipoles couplés à un nanorésonateur électromagnétique. Nous avons étudié expérimentalement la superradiance plasmonique d'émetteurs organiques greffés à une distance contrôlée d'une nanosphère metallique, à température ambiante. Nous avons mesuré le taux de relaxation de ces structures hybrides, en ensemble et à l'échelle de l'objet unique. Nous observons que le taux de relaxation augmente i) avec le nombre d'émetteurs et ii) lorsque la distance entre les émetteurs et le coeur métallique diminue, une preuve directe et claire de la superradiance plasmonique. Cette tendance a été observée pour deux types de structure hybride, différentes par la taille du coeur métallique et par le type de molécule utilisée comme émetteur. L'observation de la superradiance plasmonique à température ambiante ouvre des questions sur la robustesse d'un état superradiant contre des mécanismes de décohérence. Cette robustesse présente un intérêt majeur pour des applications potentielles de systèmes quantiques à température ambiante.

Mots clés : superradiance, plasmon de surface, transfert d'énergie, decohérence

---

Unité de Recherche
Centre de Recherche Paul Pascal - CNRS, UPR 8641
115, avenue Albert Schweitzer, 33600 PESSAC